INCREASING THE SPECIFIC SPEED OF SIMPLE MICROHYDRO PROPELLER TURBINES

Adam Michael Fuller

A thesis submitted in partial fulfilment
of the requirements
for the Degree of
Doctor of Philosophy
in Mechanical Engineering
in the University of Canterbury

University of Canterbury
2011

Contents

List of Figures

List of Tables

Acknowledgements

I should recognize the University technicians, who have been a source of skill and wisdom throughout my research. Graeme Harris endured lots of questions and gave me a place to tinker. Ken Brown is one of the most pleasant people I've ever had a chance to work with and an excellent machinist. Ken handled the vast majority of my machining and fabrication jobs. Three years ago I was unsure if I would ever get along with Scott Aimies, but he turned out OK. Eric Cox was never shy about helping on a search or with lifting. Ron Tinker let me camp in the boiler room pretty much indefinitely. Jimmy McLean was very kind about periodically reminding me which lever does what on a lathe. Dave Read injected rays of humor and sarcasm into the mechanical engineering lab wing. Julian Philips was totally accommodating when it came to all things electrical. Ian Sheppard in the Civil Engineering gave me lots of help and a fairly wide berth when it came to setting up my prototype in the fluids lab.

Also, thanks to the people who write the software I use, which has become an indispensable part of my daily life: typesetting is done with with LaTeX, so many thanks go to Don Knuth and Leslie Lamport; GNU Octave was used throughout my research for parsing, calculating, and plotting of all sorts; everything I write has been edited in the excellent Vim editor by Bram Moolenar. Thanks to the army of contributors that make free and open source software great.

Back home, thanks to mom, dad, and brother, who have given me so much long-distance love, wisdom, and good old-fashioned humor in the past years: you all deserve a shiny star and my eternal love, not that that's new. Thanks to Kim, who probably never guessed her ticket would wind up exporting me for four years. Thanks and love to all the family and friends who I left back home and have kept in touch. Thanks for putting up with my decision to temporarily relocate, and I look forward to seeing you all again.

Here in my adopted home base, thanks to the beautiful and varied Kiwi, American, Iranian, Chilean, Columbian, British, Trinidadian, German, French, and Japanese friends, hosts, and partners that I've had the joy of knowing here, and who have shared these islands with me.

And to Keith, thanks for keeping in touch since 2006 and making this chapter of my life a possibility.

Abstract

The late University of Canterbury civil engineering lecturer Peter Giddens developed a range of simple microhydro turbines, with publications from as early as the 1980s. He considered that a range of simple but well-designed turbines which covered the gamut of possible small sites would be more useful than any single turbine. He started with radial inflow turbines, then set about extending their range of applicability by increasing specific speed. That extension was continued by the research in this thesis, which aimed to produce a design with a minimum efficiency of 70 % at a specific speed of at least 600 (rev/min, kW, m). Achieving those targets would differentiate it from existing microhydro designs. In order to reach those performance targets, the volute, runner, and draft tube were examined through experiment and computational fluid dynamics models to characterize past designs and test the validity of their embodied assumptions. A prototype with a design specific speed of 650 was built and fully characterized by dynamometer testing.

Measurements of the outlet velocity distribution of two of Peter Giddens's volutes confirmed that single tangential inlet volutes are not torque-free when certain geometric conditions are met; swirl increased through those volutes by 70 % or more depending on the design. A new overall turbine design was proposed, where axial flow enters the runner and swirling flows leaves it. This required the design of a novel volute. Through computational analysis, the effect of swirling flow entering the conical draft tube was shown to affect its pressure recovery: negatively for draft tubes with small angles, positively for larger angles. It was shown that the peak pressure recovery of an optimum draft tube was not likely to be improved upon by the use of swirl, and since there was uncertainty in the analysis, a conservative draft tube was specified for the prototype. A flat-bladed runner was designed for the prototype and computational modeling indicated its performance would be sensitive to small changes in flow angle. Despite that sensitivity — an intrinsic property of high specific speed runner velocity triangles — the computational model was shown to give good predictions of the runner flow characteristics, although not its efficiency. Finally, a 1.2 kW prototype was built and achieved a peak net efficiency of 64 % as defined by the American Society of Mechanical Engineers at a net head of 2.07 m, a flowrate of 94 L/s, and a runner shaft speed of 1670 rev/min, corresponding to a specific speed of 740. Maximum measured runner efficiency of 87 % also occurred at those conditions. Compared to existing designs, that performance extended the operational envelope of microhydro turbines considerably. A three-zone computational model of the entire prototype was assembled and trialled, but not validated.

It is concluded that for efficient high specific speed turbines, volute swirl characteristics must be known with confidence, as the volute sets the conditions at the leading edge for peak runner efficiency. A simple but efficient runner may be made using flat blades, showing the potential for this geometry even when made by limited workshops. Adding a free-vortex tangential velocity distribution to the inlet flow of a stalled conical draft tube may increase its pressure recovery, although it is not likely to exceed the best performance obtainable with axial inlet flow. Therefore taking measures to reduce the peak fluid velocity entering the draft tube could be more beneficial to overall performance than seeking outright improvements in draft tube pressure recovery.

Nomenclature

Due to some overlap in naming conventions between chapters, the nomenclature of each chapter is outlined separately.

Chapter 1

d_t	runner tip diameter
D	representative diameter
g	local acceleration due to gravity
H_n	turbine net head
H_r	runner total head
$\dot{m}$	mass flowrate
n	turbine rotor rotational speed [rev/s]
n_q	European specific speed
n_s	rigorous SI dimensionless specific speed
n'_s	specific speed[34] [rev]
N	turbine rotor rotational speed [rev/min]
N_S	standard specific speed adopted in this thesis, also used to label a particular turbine design, e.g. N_S650
P_r	runner shaft power
Q	volumetric flowrate
r	radius
T	runner torque
V_a	axial velocity
V_t	tangential velocity
Δ	difference
η_n	turbine net efficiency
η_r	runner efficiency
ρ	density
ω	turbine rotor angular velocity, rad/s

Subscripts

i	runner inlet
o	runner outlet

Chapter 2

A	area
$f()$	a function of
DAQ	data acquisition
F_{AM}	angular momentum ratio
g	acceleration due to gravity
H	turbine head
$k\omega$SST	k-omega shear stress transport turbulence model
K_v	total pressure loss coefficient attributed to volute
n	mesh cell count
N	turbine rotor rotational speed [rev/min]
N_S	turbine specific speed [rev/min, kW, m]
N_R	Reynolds number
p	pressure
P	power
PC	personal computer
Q	volumetric flowrate
r	radius
r'	effective inlet radius
$\overline{r}$	area-weighted average radius
RSM ($k\omega$)	Reynolds stress model, using the $k\omega$ turbulence model
STIV	single tangential inlet volute
T	runner torque
V	velocity
Z	a linear dimension parallel to the volute centerline
α	flow angle relative to radial, equivalent to $\phi - \psi$, positive CW when viewed from top [°]
Δ	difference
η	turbine gross efficiency
ρ	density
θ	probe azimuth position, positive CCW when viewed from top [°]
ϕ	probe rotation relative to radial, positive CW when viewed from top [°]

ψ	yaw angle, flow relative to probe tip, positive CCW when viewed from top [°]
ω	turbine rotor angular velocity, rad/s

Subscripts

C	yawmeter center port
d	dynamic
d′	indicated dynamic, $p_C - p_s$
i	volute or control volume inlet
L	yawmeter left port
n	surface normal
o	volute or control volume outlet
r	radial
R	yawmeter right port
s	static
t	total (pressure) or tangential (velocity)
LE	rotor leading edge

Chapter 3

A	diffuser nominal cross-sectional area
A_R	ratio of diffuser outlet to inlet nominal area
B_S	swirl bias
C_p	pressure recovery coefficient
$C_{pax.}$	ideal pressure recovery coefficient neglecting reduction of tangential velocity
$C_{psw.}$	ideal pressure recovery coefficient including reduction of tangential velocity
d	diffuser diameter
C_{p_i}	ideal pressure recovery coefficient for axial flow
FOU	first order upwind
H_n	turbine net head
k	turbulence kinetic energy
L_R	ratio of diffuser length to inlet radius
L_o	diffuser outlet pipe length
N	diffuser length
p	static pressure
$\overline{p}$	area-weighted average static pressure
p_d	dynamic pressure
p_t	total pressure
Q	volumetric flowrate
R_h	runner hub radius
R_c	centerline computational domain cutout radius
RSM	Reynolds stress model
SO	second order
SOU	second order upwind
V, $\lvert V \rvert$	velocity magnitude
V_a	axial velocity
V_r	radial velocity
V_t	tangential velocity
V_{ti}	runner inlet tangential velocity
V_{to}	runner outlet tangential velocity
y^+	non-dimensional cell-center-to-wall distance
$\vec{V}$	velocity vector
α	absolute angle of flow relative to axial direction
θ_d	diffuser conical half-angle
ω	turbulence specific dissipation rate
ρ	fluid density
μ_T	turbulent viscosity

Subscripts

1	diffuser inlet station
2	diffuser outlet station

Chapter 4

d, D	representative diameter
g	local acceleration due to gravity
FOU	first order upwind
H_n	turbine net head
H_r	total head across runner
i1	the desktop runner blade design
i2	the first runner design iteration to be analyzed
i3	the second runner design iteration to be analyzed, which was used for the N_S650 prototype
k	turbulence kinetic energy
KU	peripheral velocity coefficient
l	blade length, chord
N_S	turbine specific speed
N	runner rotation rate, rev/min
P_r	runner shaft power
Q	volumetric flowrate
r	radial distance from runner axis
s	peripheral distance between blade at a particular radius
std.	standard discretization scheme
T_r	runner torque
U	blade peripheral velocity
V_a	axial velocity

V_r	radial velocity
V_t	tangential velocity
$\hat{V}$	the direction of $\vec{V}$
Z	number of blades on runner
α	local blade angle of attack
β	local blade angle with the axis-normal plane
β'	local mean flow angle with axis-normal plane
δ	trailing edge deviation
η_n	turbine net total-to-static efficiency
η_r	runner total-to-total efficiency
ψ	blade setup angle
Ψ	Zweifel blade loading coefficient
θ	runner azimuth angular coordinate, positive in direction of rotation
ω	runner angular velocity, rad/min, or turbulence specific dissipation rate

Subscripts

1	runner leading edge
2	runner trailing edge
abs	relative to stationary frame
h	runner hub
t	runner tip
rel	relative to rotating frame of runner

Chapter 5

AoA	angle of attack at runner leading edge
BEP	best efficiency point
D	representative diameter
E	total local energy of flow, sum of Bernoulli terms
g	acceleration due to gravity
$F_{\text{l.c.}}$	force on load cell
$F_{\text{cal.}}$	calibration force
H_n	turbine net total-to-static head
H_r	runner total-to-total head
$m_{\text{cal.}}$	calibration mass
N	runner rotation rate, rev/min
n_{11}	unit speed[30]
p	local static pressure
Q	volumetric flowrate
$r_{\text{l.c.}}$	loadcell moment arm
$r_{\text{cal.}}$	calibration weight moment arm
T_{drag}	torque to overcome bearing drag
T_{gross}	shaft torque at braking motor
V	velocity
z	elevation
α	absolute angle of flow relative to axial direction
η_n	turbine net efficiency
η_r	runner efficiency
η_t	'turbine', or Giddens, efficiency
ρ	fluid density
θ_d	conical diffuser half-angle
ω	runner angular velocity, rad/s

Subscripts

0	upstream of volute
1	runner leading edge
2	runner trailing edge
2b	downstream end of runner hub
3	draft tube exit
4	tailwater free surface
dyn	dynamic component
l.c.	load cell

Chapter 1

Context and introduction

This thesis relates to increasing the specific speed of a simple propeller water turbine. This is another way of saying that given a turbine of constant power, speed, and efficiency, there is an increase in flowrate and a decrease in head. Making these performance changes requires changes to the three main turbine components: the volute, runner, and draft tube.

Specific speed is a convenient way to describe the overall shape of a turbine. It non-dimensionally expresses the combination of head, speed, and power at which a particular design performs best. Specific speed may be used as a helpful "shape factor" to select the most appropriate turbine for a given site. A turbine with a large specific speed will efficiently extract energy from a low head, large flowrate stream. Designs such as Francis, Pelton, propeller, and tubular have become associated with the ranges of specific speeds where they are usually applied.

This thesis would not be complete without a description of Peter Giddens's influence on the project. The late University of Canterbury civil engineering lecturer developed an extensive range of simple microhydro turbines, with publications from as early as the 1980s.[25] He considered that a range of simple but consistently well-designed turbines which covered the gamut of possible small sites would be more useful than any single turbine.[4, 5] He started with radial inflow turbines for high heads, then set about extending their range of applicability by increasing specific speed to address low-head sites.[7, 6] His latest propeller turbine design achieved a specific speed of 544 and a peak efficiency of approximately 70 %. His convention of labeling designs by their nominal specific speed has been continued in this thesis. For example, his most recent propeller achieved a specific speed at peak efficiency of 544, and is thus labeled N_S544. 'Giddens volutes' refer to designs of his which, uniquely, lacked guide vanes but provided reasonably uniform swirling flow entering the runner. His designs have been implemented within New Zealand and as far away as Sri Lanka. He passed away in Christchurch, New Zealand in 2006.

The research in this thesis overcomes the technical barriers to increasing specific speed of a water turbine without betraying Peter Giddens's tenets of simplicity and functionality.

1.1 Chapter signposts

Rather than group the work under headings such as "design", "methods", and "results", the components of the turbine are treated in their own chapters, in the order in which they were studied. This order has the benefit that conclusions of one chapter lead to the questions addressed in the next. The volute chapter is based on experimental work of the author which led to a journal paper[24]; it first draws conclusions about the Giddens designs, then its conclusions lead directly to the creation of the volute used in the N_S650 prototype. By contrast, the draft tube and runner chapters are based on computational studies performed by the author and published in a conference paper.[23] The conclusions of both those chapters were made before the prototype had been built and tested. Only after the final research chapter which presents the measured performance of a 1.2 kW prototype were those conclusions able to be evaluated.

First, this chapter lays out the context and foundation for the later research chapters, introducing the state of the art in microhydro with a literature review of relevant topics, dissecting the wording of the title, and explaining why small water turbines are rightfully treated differently than large ones. It gives examples of turbines which are similar in one or more ways to the N_S650.

Chapter 2 identifies a flaw in the volutes which Mr. Giddens designed for propeller turbines. The chapter is framed around a paper published by the author in Experimental Thermal and Fluid Science[24], which presented measured velocity distributions over the outlet of two of Peter Giddens's volute designs, concluding that the volutes cannot be assumed torque-free.

Chapter 3 addresses the effect of weakly swirling inlet flow on the pressure recovery performance of a straight conical diffuser. The available literature on diffusing flow was inconclusive as to the sign and magnitude of the effect of swirl on pressure recovery, so a computational study was undertaken which compares swirling and non-swirling inlet flow over a range of diffuser cone angles.

The idea of using flat blades for efficient propeller turbines appeared in print as early as 1980[34], followed later by Mr. Giddens in the 1990s, although his work remained unpublished until recently.[6] Rather than twist, the geometry of the intersection of a plane and a cylinder is exploited to produce an airfoil with apparent camber to cylindrical streamtubes from a flat blade with the correct leading and trailing edge angles. Chapter 4 presents this method of blade design in detail, and then analyzes a runner designed by it to a specific speed of 650. Challenges emerge which are a consequence of the proportions of the high specific speed turbine velocity diagram; the geometric accuracy required during fabrication of the runner may be too fine.

Chapter 5 documents the results of dynamometer testing carried out on a prototype turbine designed with the above research in mind.

1.2 Design scope

This section defines the envelope that guides later research, and finally the N_S650 design. The turbines considered here are:

simple relative to large-scale turbines in terms of their geometry, construction, and operation. The key Giddens design tenet was simplicity since turbines must be simple if they are to be built locally and maintained by the end user. They are designed to operate at peak efficiency at a single speed with minimal maintenance. Their geometry is fully fixed to minimize mechanical complexity. Mechanical transmission of power to the load is direct to reduce opportunities for bearing failure and lubrication requirements, and guide vanes or any other stationary flow-spanning structures are foregone to avoid clogging with debris.

Microhydro describes the size of a turbine in terms of its power output. The term itself has been variously used to describe turbines producing within a range with a minimum of 1 kW to 10 kW up to a maximum of 35 kW to 100 kW. The term 'microhydro' could be replaced with 'community' or 'household' in many cases due to its frequent applications at that scale. For this thesis, about 2 kW to 35 kW is the range of interest.

Propeller describes the general shape of the one moving part, the runner. The fluid path through a propeller turbine is largely axial, and propeller turbines are sometimes referred to as 'axial-flow' to distinguish them from designs where the flow through the runner has a larger radial component. The propeller design corresponds to a high specific speed, so increasing specific speed may be viewed as enhancing the properties that make propeller turbines unique.

This short list of properties has further implications. For example, consider a common application of microhydro turbines, which is to provide alternating current mains electricity. Two distinct solutions exist to provide constant-frequency alternating current power supply from a turbine under a range of loads:

1. generate direct current power or rectify to DC, charge a storage battery, then electronically invert, or

2. drive an induction or synchronous motor as a generator, producing alternating current at mains frequency directly.

The first option is handicapped by the losses introduced by storage and inversion, although it does buffer the electrical load from fluctuations in turbine speed and power. The second option is potentially more efficient, but with the added challenges that electrical frequency is proportional to turbine speed, and therefore must be tightly controlled to produce quality power. The latter option is chosen for the Giddens turbines and this prototype.

Prior to the advent of electronic speed controllers, the most complicated and expensive component of a small turbine would have been the mechanical governor. However, the maturity of digital power electronics has provided an economical answer to the challenge of governing small turbines: electronic ballast governors.[28] In a typical installation, the electronic controller senses the frequency output of the generator and if the frequency is above the target it switches in more resistance from a bank of resistors to slow the turbine down. If the frequency is too low, it reduces the impedence of the electrical load on the generator and the runner speeds up. This loop is performed several times per second so that the effects of discrete switching are not noticeable. This balancing of real user loads with ballast loads ensures that the electrical quality is high at all times, ready for a user load to be switched on. This arrangement means that the turbine is operating at its best hydraulic efficiency at all times. The requirement for the ballast resistors is to be able to absorb the full output of the turbine. There is no reason the ballast load cannot contribute to a useful purpose such as water or space heating.

While the electrical design of a microhydro installation is of great importance to the end user, it is outside the scope of this thesis. In this study the load is assumed to be a generator, which is a directly driven 4-pole induction motor and as such requires a nominal 1500 rev/min to produce 50 Hz alternating current output.

Microhydro turbines are usually run-of-river, meaning there is no storage reservoir, and the turbine flowrate is limited to the flowrate of the stream at any given time. Depending on the size of the parent stream, the turbine flow may be a significant portion of the total stream flow. While an ideal, simplified stream would have a constant flowrate all year round, real streams exhibit significant variation with the seasons and from year to year. These variations are illustrated by a flow duration curve, showing during what proportion of the total sample period the flowrate exceeded a particular value. Figure 1.1 is an example from Camp Stream in the Southern Alps.

Fixed-geometry turbines running at a constant speed require careful study of at least one year of hydrological data, and are generally given a design flowrate of the minimum expected stream flow less any required flows reserved for other purposes; this is labeled the available flowrate, Q_a, and is shown in Figure 1.1. This does have the downside of not capturing all available energy, but is a necessary simplification. Accurately estimating Q_a before turbine design begins is a critically important measurement, as is the measurement of gross head, H_g, but hydrology and survey are out of the scope of this thesis. In this study, a turbine is intended to operate at a fixed flowrate, meaning

$$Q = Q_a = \text{const.}. \tag{1.1}$$

In the absence of adjustable turbine geometry, the flowrate which a turbine passes will be a unique function of turbine head. As the speed is fixed by the controller, and the site head will not likely vary appreciably, the scale of the turbine needs to be such that the design flowrate is passed under these precise conditions, otherwise the relatively narrow peak of efficiency of the fully-fixed propeller turbine will not be utilized. From the perspective of the turbine manufacturer, a fully-fixed turbine greatly reduces mechanical complexity and simplifies construction. However, the same decision works against the designer,

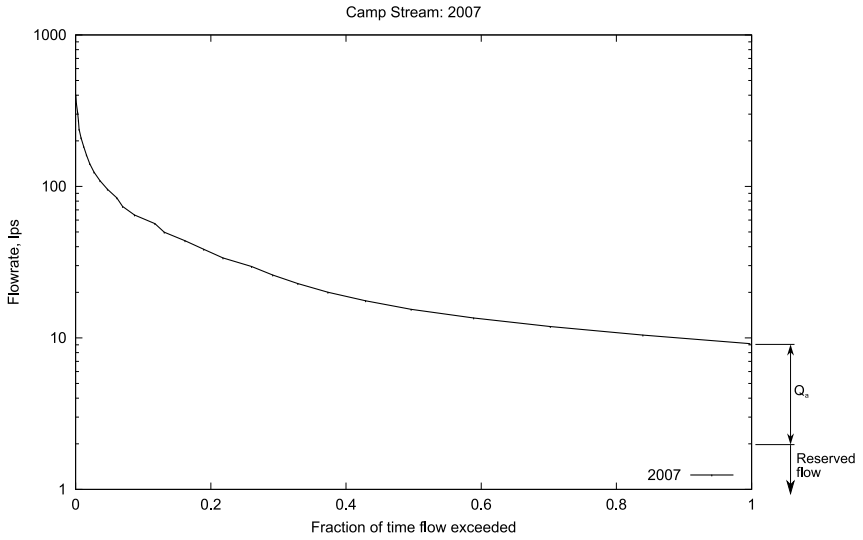

Figure 1.1: A typical mountain stream flow duration curve

who must ensure that the geometry specified will result in a turbine operating at peak efficiency. Once built, there will be little room to correct off-design operation.

In short, what begins as a short list of labels — simple, microhydro, propeller — has actually defined the workspace of the chapters to come. For example, in the volute chapter, one could argue that adding guide vanes would improve efficiency over varying conditions and make volute design and runner fabrication less critical. At a larger scale this would be reasonable, but guide vanes add considerable mechanical complexity, require monitoring of conditions to govern their actuation, and tend to catch debris which flows through the turbine, and are therefore not necessarily reasonable for a water turbine which is to be financed, built, and maintained by the user. Regarding the runner, the application of twist to the blades — which would require casting or computerized machining — or even actuated blades — which have been applied to the design of large-scale Kaplan turbines since their invention over one hundred years ago — would be out of place in even a modern a microhydro installation. Instead, designing for peak efficiency at fixed conditions allows for good efficiency with minimal complexity. Constraints such as these will appear throughout the research and go on to shape the prototype.

Finally, to summarize the design constraints imposed by the microhydro scale plus those additional constraints valued by Mr. Giddens:

- fixed-speed, full-power operation
- direct-drive transmission
- no guide vanes or other flow-spanning structures
- flat runner blades

1.3 Literature review

A review of scholarly work on the topics of turbine volute swirl characteristics, the effect of swirling inlet flow on conical diffuser pressure recovery, and methods for simplifying runner geometry will now be presented.

The assumption that the angular momentum of a fluid stream is unchanged as it moves through a volute, often labeled the free-vortex assumption, is applied as a matter of course to volutes in pump and turbine design.[38, 30, 10, 64, 21, 33] The effects of the volute on the angular momentum of the fluid flowing through it may be separated into viscous and inviscid. A net static pressure torque caused

by the shape of the volute interior has the potential to increase angular momentum considerably.[24] The retarding effect of wall friction of angular momentum has a relatively small effect.[64] Velocity surveys of some volutes reveal that the free-vortex assumption is well-founded.[52] Such volutes are of a traditional shape, and are not necessarily geometrically simple enough to be applied to microhydro designs. Simplified Giddens volutes have different proportions, especially in the tongue region.[24] The proportions of the single tangential inlet volute have been classified, although no correlation between the internal geometry of the volute and its effect on angular momentum were proposed.[36] The free-vortex assumption was made for all the Giddens propeller turbine volutes.[6] Through model experiments of two of those volutes, it was concluded that while well-designed pure swirl volutes may exhibit negligible momentum change, contraction swirl volutes such as the Giddens N_S176 andN_S544 will exhibit an increase in angular momentum.[36, 24]

It is stated that a turbine must be designed for zero runner exit swirl to maximize efficiency.[58] Axial runner exhaust does minimize the velocity magnitude of flow leaving the runner, reducing exit losses.[38] This neglects the nature of the turbine as a system of components, and that it is the sum of all components' losses, not just the losses due to exit velocity, which must be minimized in order to maximize efficiency. A design in which axial flow enters the runner allows the volute to be simplified, but at the expense of a swirl component which increases the velocity entering the draft tube. Some authors claim swirl will have a positive effect on pressure recovery.[30, 52, 39, 59] Others disagree.[66]

Research into the application of flat blades to simple but efficient turbine runners has been quite limited.[6] Researchers may suggest using sheet metal as the blade material in the interest of simplicity, only later to suggest bending and twisting to achieve the correct shape, so that the advantage of the idea is reduced.[34, 17, 16] Even if flat blades are used, the leading and trailing edges are sometimes left straight, and the spanwise variation of conditions are ignored.[50] An important paper on the topic, which includes a rigorous introduction to the geometry of the flat blade as well as measured efficiency values, was found which would seem to predate the University of Canterbury research.[34] Kercan and Bizjak actually stop short of truly flat blades, instead obtaining the requisite variation in blade angle along the leading edge by rolling the blade material. Noticeable features of the blade shape when flat blades are rigorously designed to match the relative flow angles are large sweep and anhedral angles. The effects of these geometric properties on turbine blade performance are a deep topic all to themselves, although the research here simply accepts them as a consequence of the blade design.[49, 57]

The relatively generous coverage in the literature of those topics above is a testament to their relevance within the field of turbine design. By comparison, when it comes to published work on specific turbine designs, results are relatively sparse. Advancements in even moderately-sized turbines may be profitable, and are therefore rarely published. At the microhydro end of the turbine spectrum, the motivation is rarely academic, and so publishing results of those designs is not a priority. Despite this, there are a number of turbine research projects which have published results.[13, 58, 45, 27, 16, 6]

Theses written on various aspects of microhydro turbine design or performance are also available.[29, 69, 22] The latter, which happens be another related to Mr. Giddens turbines, is of particular interest due to the quality of its investigation and commonality with the present research.

1.4 Matching microhydro users and turbines

Consider the typical American household, which according to the Energy Information Administration requires an average electrical power of 1.28 kW, or roughly one hairdryer running continuously. Assuming a combined generator and transmission efficiency, $\eta_g\eta_m$, of 80 % and a turbine efficiency, η_t, of 70 %, Table 1.1 shows the different combinations of turbine head and flowrate, Q, which would meet that need. Adding the runner speed constraint of $N = 1550\,\mathrm{rev/min}$ gives the specific speed of each turbine, illustrating the wide range of specific speeds required to exploit such a range of sites. An alternate

definition of specific speed sometimes used in Europe,

$$n_q = \frac{N\sqrt{Q}}{H_n^{\frac{3}{4}}},$$

and the dimensionless parameter which is the basis of all specific speeds,

$$n_s' = \frac{n\sqrt{P_r}}{\sqrt{\rho}\,(gH_n)^{\frac{5}{4}}},$$

where n is speed in rev/s, are included for reference. Assuming reasonable values of unit flow and unit speed[30] allows the calculation of an indicative runner diameter, d_t, which illustrates the increasing size per kW with increasing specific speed when speed is held constant. The final column of Table 1.1 is the fraction of turbine head entering the draft tube as dynamic head, which correlates strongly with specific speed. The importance of this trend is revisited in Chapter 3. The fourth column clearly shows how a range of specific speeds are needed to cover a variety of sites.

Design	H_n, m	Q, L/s	N_S	n_q	n_s'	d_t, mm	$\frac{V_a^2}{2gH_n}$
propeller	2	120	820	315	0.80	210	0.66
propeller	2.4	100	650	250	0.63	200	0.49
propeller	5	50	260	100	0.25	160	0.14
mixed-flow	10	23	110	40	0.11	130	0.05
radial-flow	20	12	50	18	0.05	100	0.01
Pelton	50	5	15	6	0.014	75	0.003
Pelton	100	2.5	6	2.5	0.006	60	0.001

Table 1.1: Required parameters to supply electricity to an average American household at $\eta_n = 0.7$ and $N = 1550$ rev/min over a range of heads

Users of small turbines are varied. They include

- communities looking for a first, or more dependable or economical source of electricity,
- farmers, tramping huts, ski lodges or other remotely located off-grid loads near suitable streams,
- developed nations attempting to reduce environmental impact and utilize existing renewable resources and infrastructure, and
- wastewater treatment and irrigation works where low-head water is a by-product of some primary activity.

1.5 Representative designs

To illustrate the variety of designs under the heading of small, low-head hydro, some examples are given of recent commercial and academic work. Not all designs shown are strictly intended for microhydro-scale installations.

The StraflowMatrix turbine unit made by VA Tech HYDRO GmbH, shown in Figure 1.2 is characterized by a generator configuration where the rotor coils are arranged around the periphery of the runner shroud, while the earlier HydroMatrix uses a more conventional bulb configuration.[51, 332] Units exist from 546 kW to 700 kW, generating under 5.5 m to 30.5 m of head. Square, self-contained turbine units designed for a fixed flowrate are stackable in rectangular arrays to meet various flowrate requirements.

Japanese manufacturer Toshiba markets a four-model microhydro lineup generating from 1 kW to 200 kW under heads from 2 m to 15 m with three standard propellers per model. An example is shown in Figure 1.3. The intended market is mainly city utilities and waste management facilities where residual

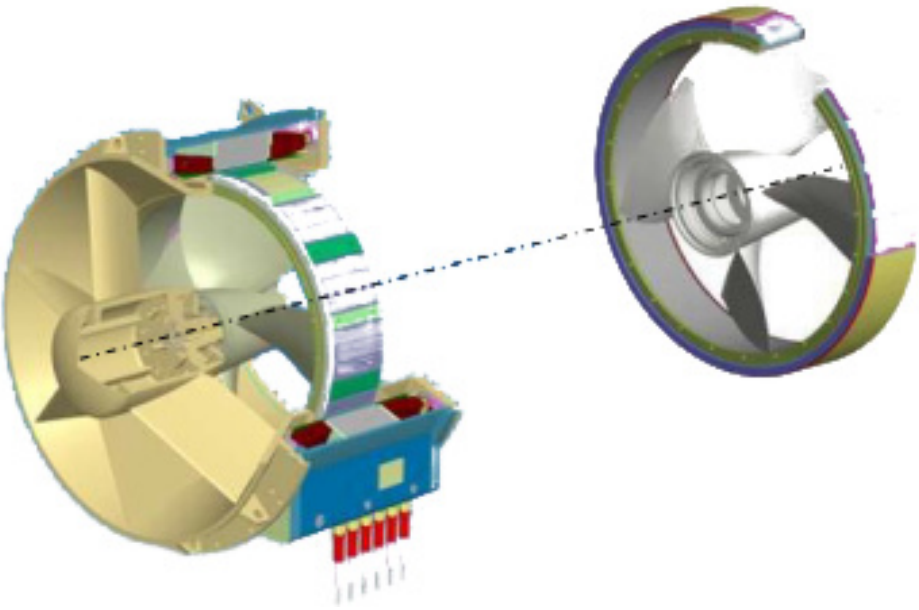

Figure 1.2: VA Tech HYDRO StraflowMatrix/HydroMatrix, flow is from left to right

head exists in an industrial environment and the recovered energy can easily be injected back into the grid. The product literature states the turbines' ability to operate off-grid.[61, 54]

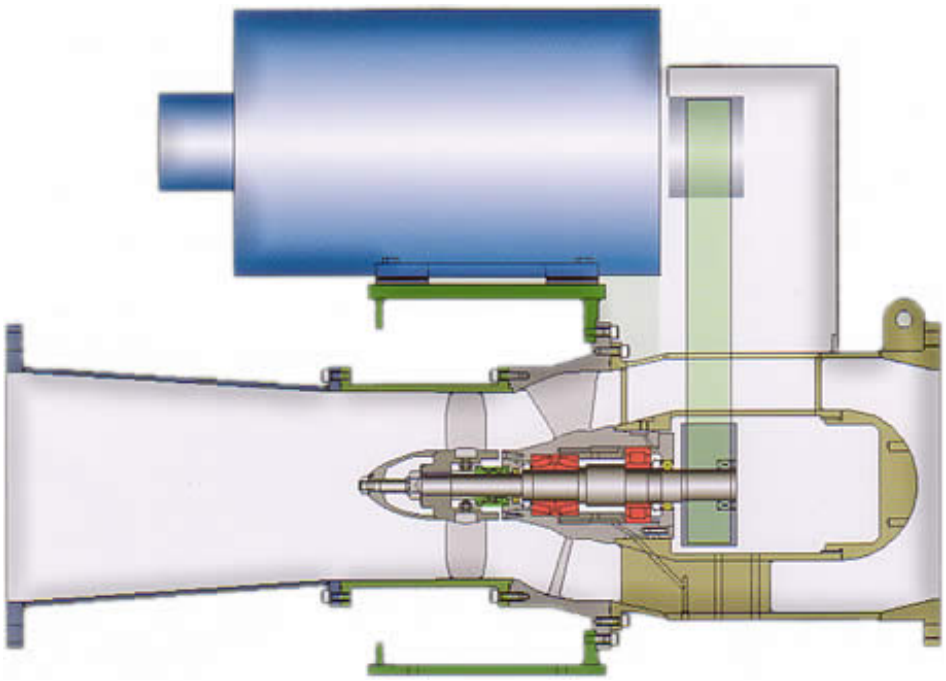

Figure 1.3: Toshiba Hydro-eKIDS, flow is from right to left

UK firm IT Power has developed a 10 kW belt-driven propeller turbine compatible with a 3 m head, shown in Figure 1.4, in a siphon configuration which operates fully above the headwater to reduce civil works complexity and protect the turbine from flooding damage, but requires priming by external means for startup.[48]

The Very Low Head, or VLH, turbine developed by Canadian firm MJ2 Technologies S.A.R.L. is different from most other low head designs. Rather than attempting a smaller size and higher speed turbine to achieve a more compact machine, the designers have opted for a large through-flow area and

Figure 1.4: IT Power siphon propeller turbine, flow is from a headwater to the right, through the conical draft tube to the tailwater channel on the left

low peak-efficiency speed which keep runner exit velocities to a minimum which avoids the need for a draft tube. Power ranges from 100 kW to 500 kW, and heads from 1.4 m to 2.8 m. Water-to-wire efficiencies are around 79% for the smaller turbines. Testing took place at the University of Laval.[60] The low speed of the runner requires special many-poled generators, but one benefit is lowered fish mortality.

The 'Vaneless' turbine, whose volute is shown in Figure 1.6 has been designed by Swiderski Engineering/Rapid-Eau also with low fish-mortality in mind. The omission of flow-spanning vanes, however, should also translate to reduced susceptibility to clogging by entrained leaves and other trash, which is an important requirement for micro-scale turbines. No test results are available. Testing took place at the University of Laval.

Exmork, Energy Systems and Design, and Yueniao are three companies which manufacture or supply a similar class of turbine: a one-piece unit consisting of a runner and guide vanes connected to a directly-driven generator by a rigid frame, which is meant to be directly fitted to a circular orifice in the bottom of an open race. Power output ranges from 300 W to 1 kW utilizing a head from 1.5 m to 4 m. An example is shown in Figure 1.7. They are generally unregulated and produce either standard AC directly or DC power for charging battery banks. Exmork (`http://www.exmork.com`) is a Chinese manufacturer whose products are distributed in Canada by PowerPal and in Europe by Kleinstwasserkraft Klopp. PowerPal (`http://www.powerpal.com`) is a Canadian company who manufactures in Vietnam and imports. Energy Systems and Design (`http://www.microhydropower.com`) is a Canadian company that produces a 1 kW turbine similar to PowerPal. Yueniao (`http://www.yueniao.com/`) is a Chinese manufacturer who produces a similar 1 kW turbine.

Using pumps as turbines (PAT), for example as shown in Figure 1.8, provides an alternative to purpose-built turbines in the case where pumps are available at competitive prices.[43] When used as turbines, the pumps cover approximately the same head and flow range as during normal pump operation, although there is an efficiency penalty. High specific speed axial-flow pumps, which also operate at relatively high specific speeds as turbines, are more expensive per-kilowatt than their lower specific speed, centrifugal counterparts. If the efficiency handicap of operating in reverse is overcome, the simplicity of a single unit containing turbine and generator is attractive.[65, 64]

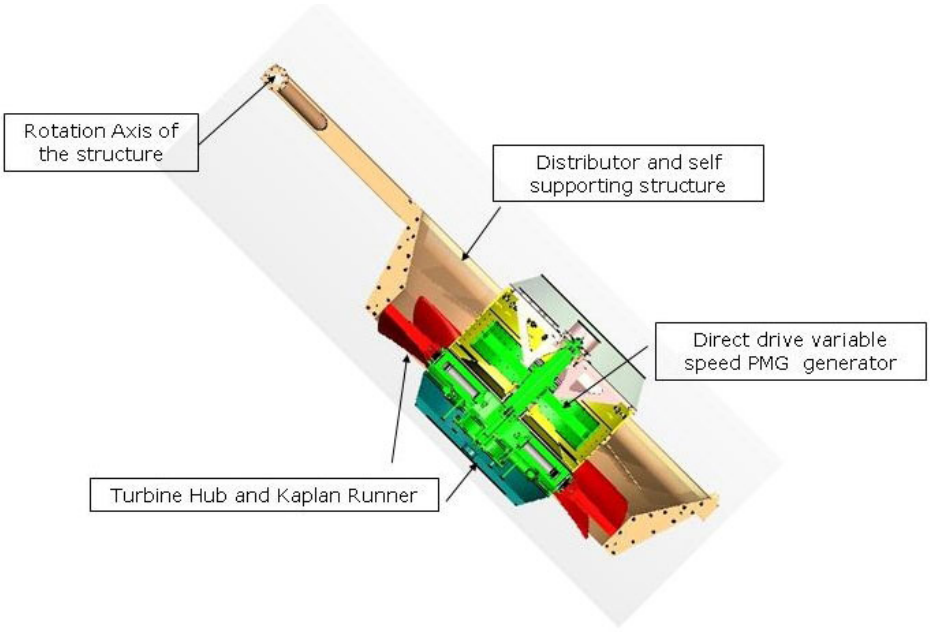

Figure 1.5: MJ2 Technologies Very Low Head turbine, flow is from upper right to lower left

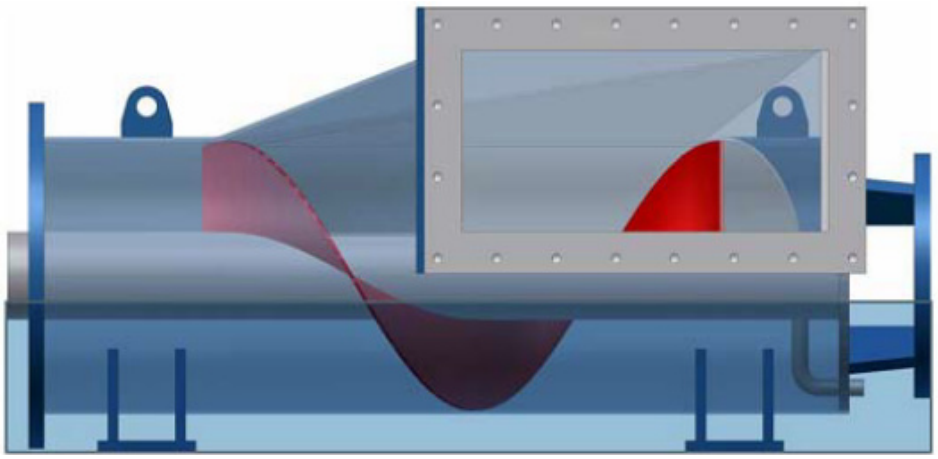

Figure 1.6: Swiderski Engineering/Rapid-Eau Vaneless turbine, flow enters the volute through the rectangular opening and leaves for the runner to the left

Figure 1.7: Sub-kilowatt turbines, flow is top to bottom in the picture shown

Figure 1.8: Pump as turbine, flow enters the volute by the tangential pump outlet and leaves through the pump eye

UK firm Western Renewable has developed the Archimedean screw, shown in Figure 1.9, into a relatively novel method of making electrical energy from a low-head hydro source. The principle was discovered by Archimedes in the third century BC as a useful method of pumping water. It is comparable to traditional waterwheels in that it requires considerable civil works and a significant speed increase in order to generate 50 Hz AC power, which came about when shaft output was directly used for mechanical work, which could utilize the slow rotational speeds directly. It is available commercially to generate between 5.5 kW and 63 kW under 1.6 m to 8 m of head.

Figure 1.9: Western Renewable Archimedean screw, flow is top to bottom along the channel by parcels which are separated by the helical blade of the runner

Named after late civil engineering professor Peter Giddens who spearheaded the project, The University of Canterbury mechanical engineering department has developed a range of radial, mixed-flow, and more recently, axial-flow propeller turbines designed for simple construction and reliable use in remote locations. An example propeller volute is shown in Figure 1.10. As with all tangential inlet turbines, the flow enters tangentially, swirls to the smaller radius of the runner, increasing its tangential velocity, exiting axially into the runner. Guide vanes are absent. Prototypes exist from 1.4 kW to 4.1 kW under heads of 3.4 m to 10.7 m of head.

The turbines developed of Mr. Giddens are more than historical backdrop to this research. The successes and shortcomings of his designs set targets in terms of specific speed and efficiency. Figure 1.11 gives the range of conditions, in terms of head and flowrate, which existing Giddens designs can cover. Each contour of specific speed has been validated by a prototype in the range of 1 kW to 3 kW; the other dots along each line are the result of geometric scaling to meet other conditions at the same specific speed.[6] The figure clearly illustrates how extending the range of specific speed translates to more sites which may be developed. But just what is specific speed?

1.6 Specific speed

When comparing different turbine designs, specific speed is a useful parameter for grouping families of turbines, that is turbines of similar shape but different size and speed. The non-dimensional form of specific speed is given in Equation 1.2. Consistent units, such as base SI, must be used, with units of

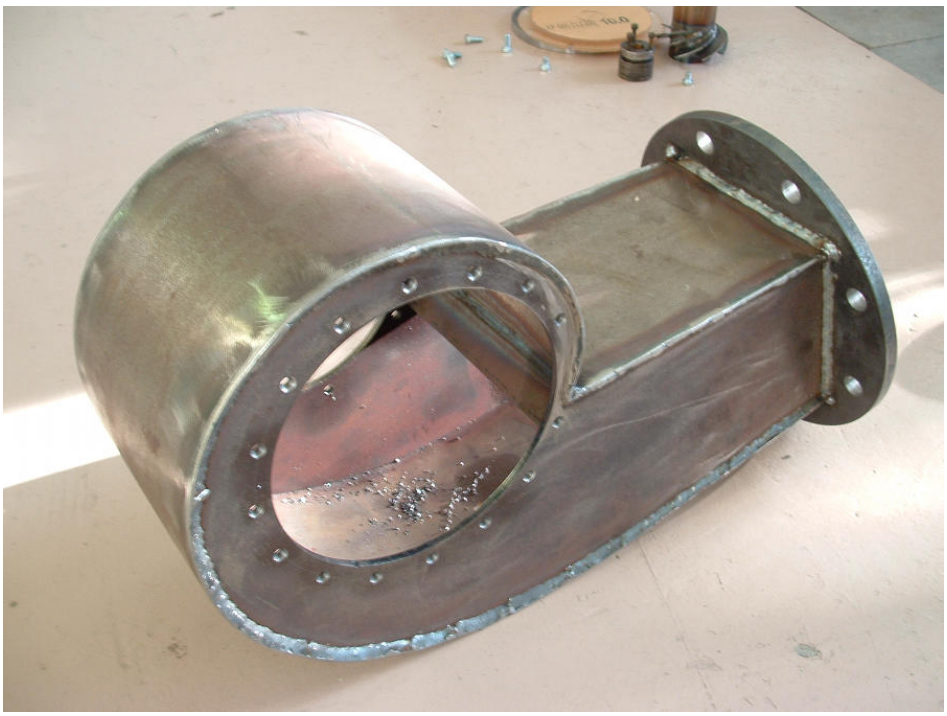

Figure 1.10: University of Canterbury Giddens turbine

rad/s for ω.

$$n_S = \frac{\omega\sqrt{P}}{\sqrt{\rho}\,(gH)^{\frac{5}{4}}}, \tag{1.2}$$

However, as a parameter used extensively across the breadth of the topic of turbomachinery, it appears in various convenient forms. The form adopted in this thesis is given in Equation 1.3,

$$N_S = \frac{N\sqrt{P_r}}{H_n^{\frac{5}{4}}}. \tag{1.3}$$

where N is runner speed in rev/min, P_r denotes shaft power in kW, and H_n is the turbine net head in m.

1.6.1 Derivation from similarity

Specific speed allows the similarity of two operating conditions to be compared since it derives from three fundamental types of similarity.

Geometric similarity says that the shapes of the turbines in the two sets of conditions must be similar, that is all homologous angles and ratios are equal,

kinematic similarity says that all velocities must change proportional to one another, and

dynamic similarity says that the proportion between a fluid acceleration and its corresponding reaction force should remain constant.

The form of a physical thing is described in two parts: its shape and its size. Geometric similarity is achieved when two shapes are the same, for example, when a turbine is precisely scaled up or down. See Equation 1.4.

$$\beta = \text{const.}, \quad \frac{d_h}{d_t} = \text{const.}, \quad \ldots \tag{1.4}$$

Regarding kinematic similarity, there are really only two velocities of interest in the idealized turbine: that of the flow and of the runner. Regardless of their magnitudes, if the ratio of these two is kept constant

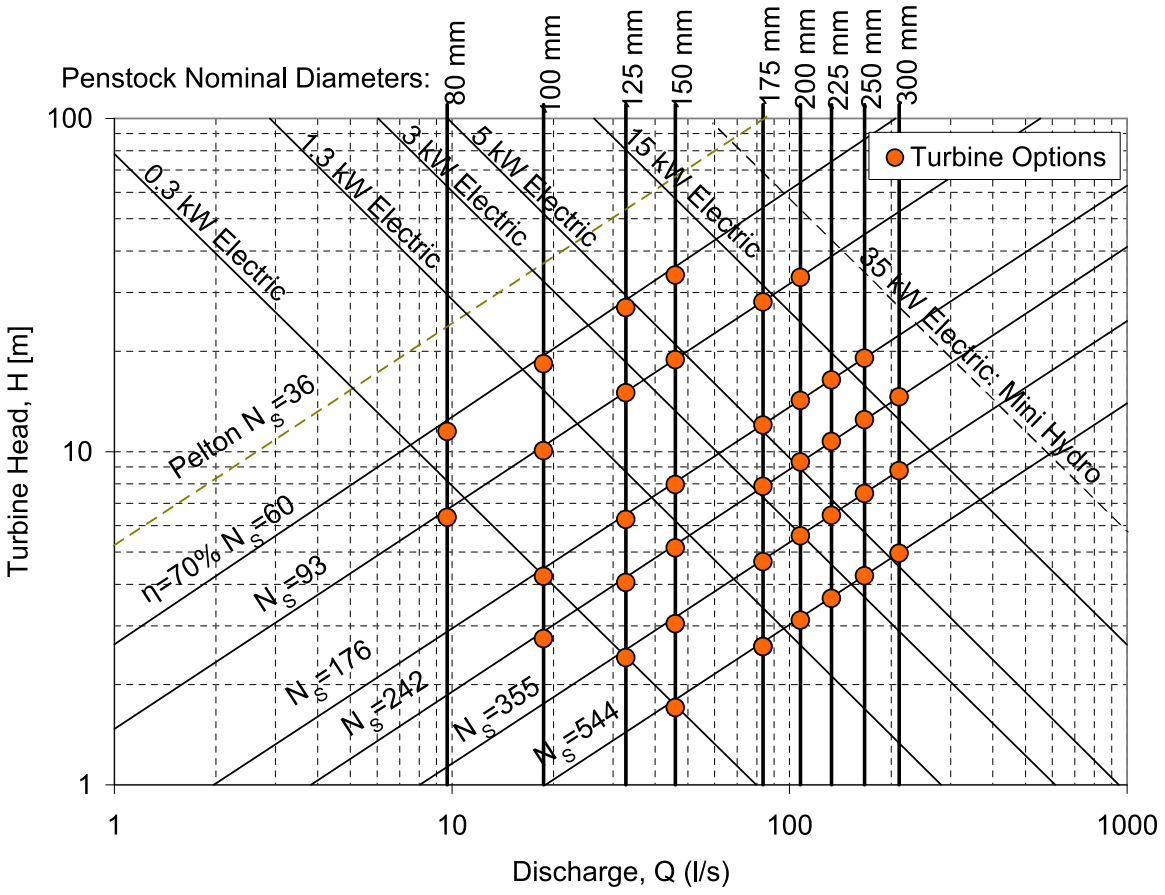

Figure 1.11: Giddens turbines' operational envelope

for two different conditions, it is said that these two conditions are kinematically similar. The velocity of the flow at any point in a turbine will be proportional to flowrate divided by an area, and an area will be proportional to any length squared, so this may be substituted for velocity. Similarly, the velocity of a point on the runner will be proportional to its rotation rate and its diameter. The condition for kinematic similarity is then given in Equation 1.5.

$$\frac{Q}{ND^3} = \text{const.} \tag{1.5}$$

Dynamic similarity derives from Newton's second law of motion, Equation 1.6.

$$F = \frac{d\,(mV)}{dt} \tag{1.6}$$

The second law relates a force to a change in momentum. Dynamic similarity is the condition of maintaining a constant ratio of the left and right-hand sides of Equation 1.6. Assuming dynamic similarity is obeyed, all forces in the system change proportionally to one another. This allows the left-hand side to be written in terms of turbine head: $F \propto \rho g H D^2$. Similarly, the right-hand side is written in terms of the momentum change in the runner: $\frac{d(mV)}{dt} = \dot{m}\Delta V \propto \rho V D^2 V = \rho N^2 D^4$. A constant ratio of these two results is the condition for dynamic similarity, given in Equation 1.7.

$$\frac{gH}{N^2D^2} = \text{const.} \tag{1.7}$$

Raising Equation 1.7 to the $-\frac{3}{2}$ power and multiplying by Equation 1.5 allows for the elimination of D, giving the intermediate result in Equation 1.8.

$$\frac{Q}{ND^3}\left(\frac{gH}{N^2D^2}\right)^{\frac{-3}{2}} = \frac{N^2Q}{(gH)^{\frac{3}{2}}} = \text{const.} \tag{1.8}$$

Taking the square root of Equation 1.8 gives an expression which is proportional to speed, known as specific speed. Equation 1.9 is an alternative but equivalent formulation of Equation 1.3. Variations in g are negligible, so it is omitted in practice.

$$\frac{N\sqrt{Q}}{(gH)^{\frac{3}{4}}} = \text{const.} \tag{1.9}$$

Equation 1.3 is a statement of kinematic and dynamic similarity between two different operating conditions for a geometrically similar machine. The same result may also be obtained by dimensional analysis.

1.6.2 Effects of its increase on turbine parameters

Angular momentum is what the runner changes in the passing flow in order to extract work. This is succinctly presented in the Euler turbomachinery equation, Equation 1.10, which states that the runner torque is equal to the product of mass flowrate through the runner, and the change in the value of rV_t across it.

$$T = \dot{m}\Delta(rV_t) \tag{1.10}$$

The relationship between torque and turbine head is revealed if Equation 1.10 is multiplied by runner angular velocity, ω, resulting in several representations of runner power, shown in Equation 1.11,

$$P = \eta_r g\rho Q H_r = \omega T = \omega\rho Q\left((rV_t)_i - (rV_t)_o\right) \tag{1.11}$$

where η_r is runner efficiency, and then divided through by $\dot{m}$, giving Equation 1.12,

$$\eta_r H_r = \frac{\omega}{g}\left((rV_t)_i - (rV_t)_o\right) \tag{1.12}$$

which shows that torque and head alike are both proportional to the change in rV_t across the runner.

With these relations in mind, consider a 'rubber' propeller turbine of fixed P and ω, where the up and down arrows in the following equations represent an increase or decrease of the adjacent quantity. The initial perturbation is to slightly increase flowrate, while all subsequent adjustments are those required to fit the stated constraints. The list is meant to be read in order from top to bottom, and shows why, all other things being equal, the change of swirl across high specific speed turbines is less.

1. $P_r = \eta_r \rho g Q^{\uparrow} H_{r\downarrow}$, Q is increased and the change in H_r is inversely proportional.
2. $N_{S\uparrow} = \frac{N\sqrt{\eta_r \rho g Q^{\uparrow}}}{{H_r}^{3/4}_{\downarrow}}$, N_S increases.
3. $P = T\omega$, P and ω are constants, so T is unchanged.
4. $T = \rho Q^{\uparrow}\Delta(rV_t)_{\downarrow}$, $\Delta(rV_t)$ changes inversely proportional to Q, as shown in Equations 1.10 through 1.12.

This analysis shows that at a constant power and speed, several things must change in the design to achieve an increase in specific speed:

1. a larger flowrate under less head will require a larger cross-sectional area, so one or both of a smaller hub-to-tip ratio, or a larger tip diameter; and

2. to maintain a constant torque, the increase in flowrate must be accompanied by a proportional decrease in $\Delta(rV_t)$. The increase in r exacerbates the effects of the decrease in ΔV_t on the shape of the runner velocity diagram.

So, considering the mid-span section, the axial velocity is unchanged or increased, blade peripheral velocity is definitely increased, and the change in tangential velocity across the runner shrinks in comparison to all other velocity components. Having defined specific speed and the effects of increasing it, the obstacles to increasing it will now be identified and addressed.

Chapter 2

Giddens volutes

It is hypothesized that the reason later Giddens turbines did not achieve their target specific speed was an increase in angular momentum of the flow through the turbine volute which connects the penstock to the runner. This would have increased runner torque at a given flowrate and speed, and thereby contributed to a reduced specific speed. Single tangential inlet volutes (STIVs) are commonly assumed not to affect the angular momentum of the flow, although the validity of this assumption will be shown to depend on the proportions of the volute tongue region. This chapter will show by measurement of the outlet velocity distribution of two Giddens STIVs that they are unable to provide outlet flow with the precise amount of weak swirl required for high specific speed operation. Rather than modifying STIV geometry to produce the correct swirl, a novel volute is proposed which will produce approximately uniform axial outlet flow instead.

2.1 Volute design theory

The turbine volute forms a sealed join between some form of water supply — an open channel or a penstock — and the runner annulus. An efficient volute achieves this change in direction and cross-sectional shape with a minimum of turbulence and non-uniformity, and provides a predictable outlet velocity distribution to match the runner leading edge blade angle.

Regarding the design of volutes, Wilson discouragingly states in his book on the design of efficient turbomachines that "we know of no proven design methods for turbine ... snail-shell scrolls; many have been published, and some may be effective."[66, p.358] Reconciling the dismissive tone of this quote with the reality that water turbines have been refined to very high efficiencies leads to the consideration of whether a method must be proven to be effective.

An example of an unproven but effective method is the simple torque-free assumption which Mr. Giddens applied to design volutes for a series of microhydro turbines. He started with a philosophy that small water turbines should be exceptionally simple, low-maintenance, and economical, but at the same time properly designed, which was translated into a list of technical constraints based on his practical experience with such turbines.

One of the most notable of these constraints was that flow-spanning structures, including guide vanes, should be omitted in order to prevent small turbines from clogging with leaves. Guide vanes are used in water turbines to control the degree of swirl entering the runner,[53] and are commonly thought of as an essential component of an efficient turbine.[58, 33] Omitting guide vanes means that the swirl present at the runner leading edge is governed by the shape of the volute itself. Mr. Giddens assumed, as is common, that the flow through the volute was subjected to no significant torque.[6, 33]

In turbomachinery design, matching the flow direction to rotor blade leading edge angles is a common goal to minimize losses. While the through-velocity is known from the flowrate and passage cross-sectional area, the swirl component is the result of subtle influences originating upstream. Furthermore, for

fixed-geometry turbines which must operate at a fixed speed, e.g. microhydro turbines without guide vanes directly driving a generator, the high-efficiency region of the efficiency versus speed curve is relatively narrow, so matching the volute exit flow angle to the rotor leading edge blade angle is imperative to designing turbines which operate at maximum peak efficiency.[62]

From the perspective of swirling flow requirements, turbines might be considered distinct from other applications of swirling flow such as cyclone separators[26, 35], combustors[26, 2, 3], and chemical mixing chambers[36] which use very similar geometry, but have no rotor and therefore less stringent demands on swirl strength to perform satisfactorily. In most turbine applications where precise flow angles are required, guide vanes are used to set the flow direction with more certainty. A notable exception is the common automotive turbocharger, whose rotor operates at a wide range of speeds and therefore would not necessarily benefit from a fixed flow angle, although the relative benefits of vaned versus vaneless volutes remain under debate.[66, 54, 53] In vaned volute designs, the torque-free assumption is often made with little or no modification between the guide vane trailing edge and the rotor leading edge.[54]

In the absence of guide vanes, it is the volute's shape alone which determines how well the incoming linear flow of a single inlet is transformed into uniform, swirling flow entering the runner annulus. The torque-free assumption would appear to be the only candidate for a volute 'design method' in the literature[30, 10, 64, 21, 33], but this chapter goes some way to showing the limits of its use.

For an example of a volute which is quite nearly torque-free, see the excellent paper by Malak *et al.*[37], which reports detailed velocity measurements throughout the body of a lower specific speed turbine's radial-inflow volute. That paper's focus, however, was more on the secondary flows within the volute body itself, and the data resolution across the outlet section is not as high as was measured here. On the other hand, examples may be found of turbine volutes designed by the free-vortex assumption which give disappointing results.[31]

The torque-free assumption, and the estimates of flow behavior that come from it are variously labeled 'ideal'[33], 'free-vortex'[62], 'conservation of angular momentum'[10], or as a method for selecting stay-vane angle in large hydro turbines[30]. The assumption is predicated on the fact that the net pressure torque on the fluid within the implied control volume is in fact negligible. Also, torque due to wall shear stress must be a relatively small fraction of total angular momentum flux, which is typically the case when the flow is fully turbulent. Whether or not simply slicing through the pipe supplying the volute provides a representative upstream boundary to a zero-torque control volume depends on the design of the volute.

Due to its several appearances in the literature, it is worth noting that it is common to modify the zero-torque assumption with an empirical coefficient that reflects the loss of angular momentum due to wall shear stress[33, 62], despite its typically small effect. The quoted reasonable ranges of such a coefficient are wide enough, and the descriptions of the designs to which they apply vague enough, that the coefficient is clearly one which needs to be determined by experimentation, partially negating its usefulness in an analytical relation.

Beyond this simple one-dimensional approach, analytical two-dimensional methods of design exist to specify the azimuthal variation of casing geometry, but they are in fact underpinned by the zero-torque assumption.[21] Not surprisingly, no analytical method exists to predict outlet flow from a general volute design.

2.2 STIV terminology

The effects of a volute on angular momentum are a result of the internal geometry, and the proportions of the junction between the inlet pipe and volute body in particular, known as the tongue. Legentilhomme and Legrand introduced a naming convention appropriate for describing volute inlets and how the dimensions of the inlet pipe and volute might effect volute exit swirl, but stopped short of proposing a quantitative correlation.[36] Shown in Figure 2.1, pure, contraction, and expansion swirl flow describe whether inlet

diameter is equal to, greater than, or less than, respectively, the main volute radius minus outlet pipe radius. The angle of the tongue is acute for expansion swirl, becoming less acute for pure and contraction swirl.

That same paper quantifies the influence of viscosity on reducing swirl, called decaying swirl flow, as the flow travels the length of the main volute, swirling through the annular space between the outlet pipe and the main volute wall.

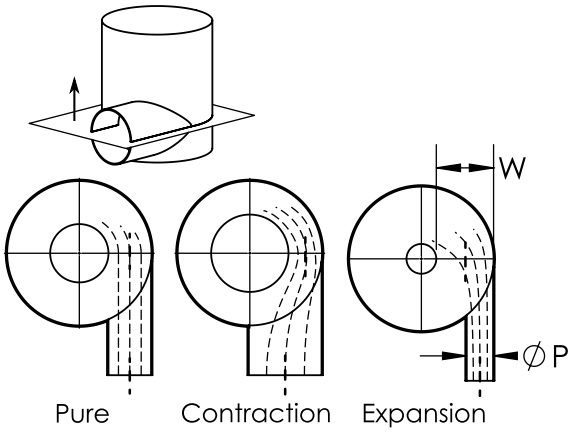

Figure 2.1: Pure, contraction, and expansion swirl as defined by Legentilhomme and Legrand

2.3 Introduction to volute velocimetry

In this chapter, the focus is on the performance of contraction-swirl STIVs from two Peter Giddens propeller turbines: the N_S176 and N_S544.[6] In particular, each volute is to be characterized by its ratio of inlet to outlet angular momentum flux, F_{AM}, and the total pressure loss normalized by its inlet dynamic pressure, K_v. To simplify the experiment, the working fluid is air. Both F_{AM} and K_v should be insensitive to Reynolds number as measurements take place well into the fully turbulent regime, and an effort has been made to match the Reynolds numbers achieved in microhydro turbines, which are on the order of 10^5. Mach numbers in the region of the velocity probe are less than 0.1.

2.4 Velocimetry experimental setup

For each volute, a survey of the time-averaged exit velocity distribution was sensed using a three-port yawmeter with electronic pressure transducers which were sampled with high-speed computerized data acquisition. Each velocity measurement was accompanied by an average flowrate, measured by sampling the throat wall pressure of a calibrated bellmouth on the apparatus inlet, shown in Figure 2.2. The flow was turbulent, with random fluctuations of periods up to approximately 1 s. By collecting many samples over long enough period for each data point, a repeatable average was obtained. The experimental setup consisted of the volute itself, a fan connected to the volute outlet to generate airflow by suction, and a length of inlet pipe with a bellmouth contraction. The following sections describe the experimental setup in detail.

2.4.1 Apparatus

Figure 2.2 shows the main components of the measurement setup for the N_S176 volute model, with part of the inlet and volute cut away to show internal components. Figure 2.3 shows the N_S176 model as it was tested in the lab. The setup for the N_S544 volute was functionally equivalent. Figure 2.4 shows a view of

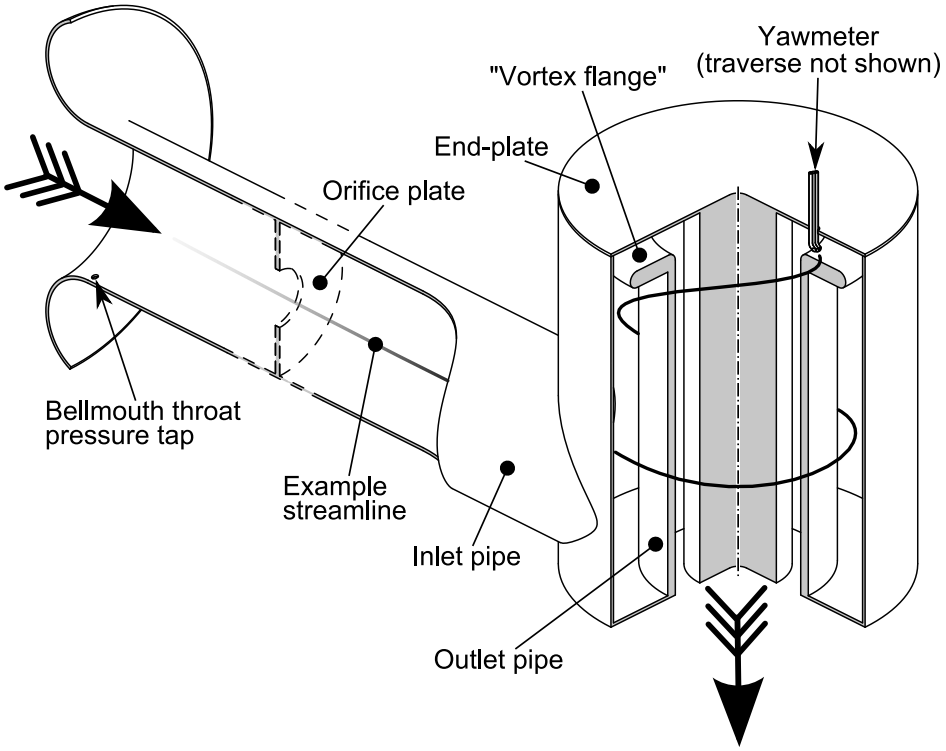

Figure 2.2: N_S176 volute velocity measurement apparatus schematic with relative position of key elements, including temporary orifice plate for bellmouth calibration, shown, with tailed arrows indicating general flow direction

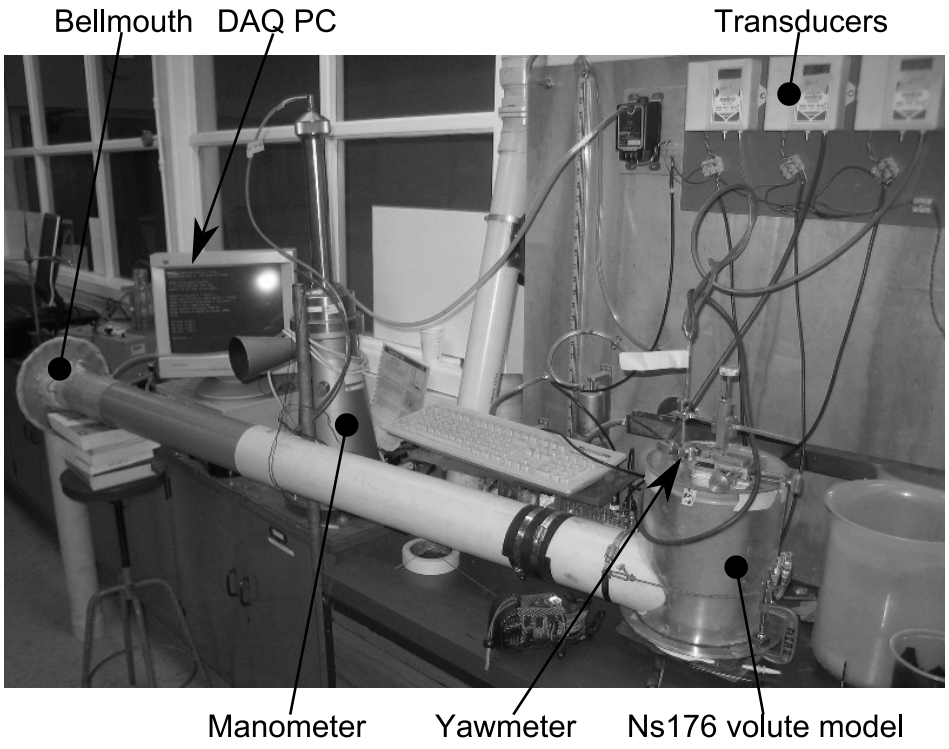

Figure 2.3: N_S176 model set up for velocimetry. A fan drew air through the volute through a hole in the benchtop on which the model sat.

main components, without the velocimetry equipment, and with the suction duct not yet connected to the volute outlet.

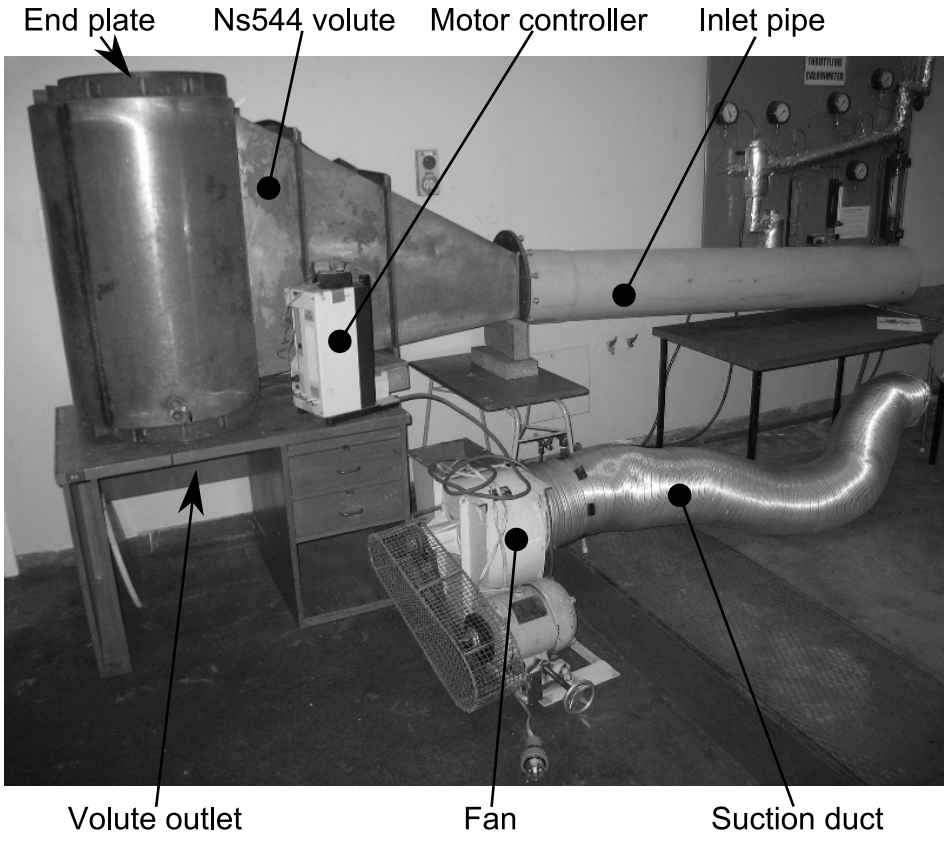

Figure 2.4: N_S544 main apparatus

The fluid path was an open circuit, beginning with a smooth contraction open to atmosphere followed by a straight inlet length connected to the volute itself, whose outlet was connected to a source of vacuum, in this case, a fan, which exhausted to atmosphere. The radial-inflow section upstream of the axial-flow outlet section between the end-plant and vortex flange was where the measurements took place. The axial section had a stationary cylinder along the centerline, simulating a rotor hub.

Air was chosen as the working fluid for the resulting simplified plumbing and the fact that Reynolds numbers on the order of the those of the volutes' corresponding water turbines were achievable with the available pumping equipment.

Inlet

The inlet configuration while taking measurements consisted of a bellmouth open to atmosphere followed by a straight length of tubing leading to the volute. The bellmouth provided uniform flow to the inlet pipe, and its throat depression was also used to measure instantaneous flowrate. This flowrate was captured, along with the three yawmeter port pressures, for each data point. This allowed any point-to-point unsteadiness to be corrected for by multiplying each yawmeter velocity magnitude by the ratio of its corresponding inlet velocity to the mean inlet velocity over the entire run. In order to ensure the accuracy of the bellmouth, which is an unstandardized device for flowrate measurement[11], it was calibrated in line with an orifice plate constructed to ISO 5167[32]. The orifice plate was removed while taking yawmeter measurements.

Yawmeter

The yawmeter was constructed of three ∅1.23 mm outer-diameter stainless steel hypodermic tubes, bent into an L-shape, with the outer two tubes ground back at 45° from the center tube, which was left blunt. The tip of the probe was 10 mm from the centerline of the probe stem. The probe was calibrated to return yaw angle, static pressure, and dynamic pressure by measuring all three port pressures of the probe as it was swept through a range of angles, facing into a jet of air exhausting to atmosphere, so that $p = 0$. When viewed from upstream, the left, center, and right ports are named L, C, and R. The probe is shown in place in Figure 2.5 with ports labeled. In general, the center port did not sense total pressure exactly

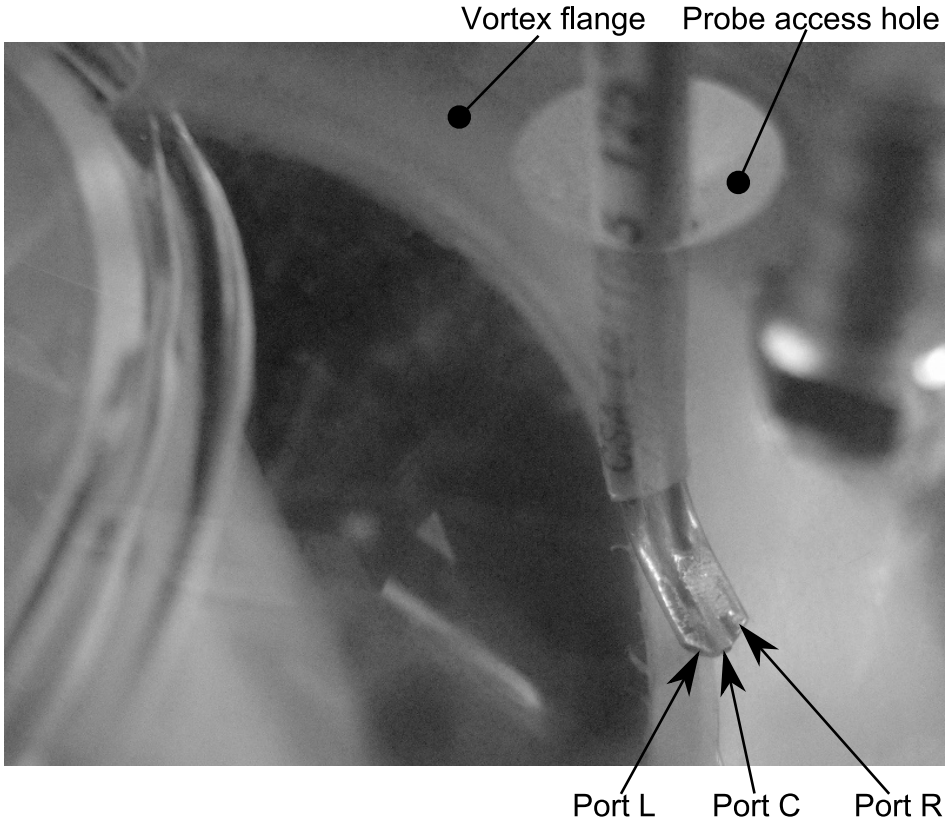

Figure 2.5: Yawmeter installed through chamfered access hole in endplate in the N_S176 model, as viewed from outside endplate

but something less than it. This new pressure, $p_C - p_s$, was named the indicated dynamic pressure, or $p_{d'}$. Indicated dynamic pressure was the value by which $p_L - p_R$ and $p_C - p_L$ are nondimensionalized and related to ψ and p_d. Since $p_{d'}/p_d$ was also a function of ψ, an iterative procedure was required to arrive at values of ψ, p_d, and p_s. The combination of the yawmeter range of ±20° and a traverse capable of positioning the probe at an arbitrary angle allowed all measurements to be taken well within the linear range shown in Figure 2.7. Figure 2.6 shows the probe mounted to the calibration jet apparatus.

As the three yawmeter ports lay on a plane, the yawmeter was not capable of resolving an out-of-plane velocity component, which was assumed small following tuft observations of the region of interest. Consequently, Figure 2.8 is representative of the effect of any out-of-plane component on the sensed pressures; within −10° to 10° the error of dynamic pressure was less than about 5 %. The ratio of the difference of the outer two ports to the center port was found to be linear over a conservative range of −20° to 20° and independent of Reynolds number for the ranges tested. The results of several calibration runs are shown in Figures 2.7 and 2.8. The asymmetry of probe response was due to imperfect construction, which was accounted for with calibration.

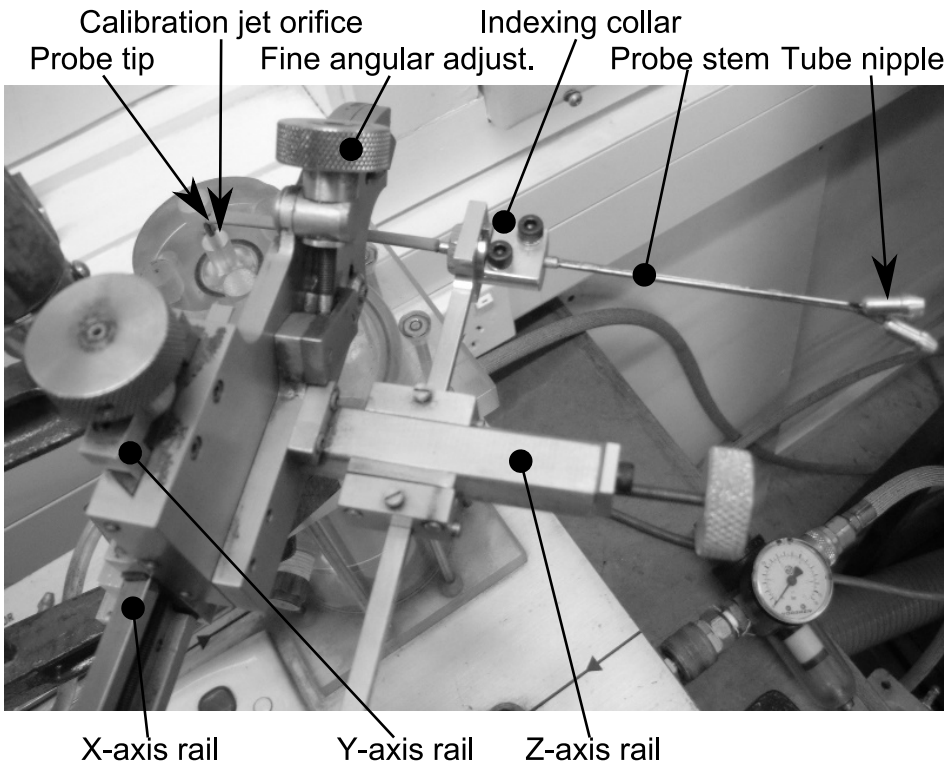

Figure 2.6: Yawmeter installed over calibration jet

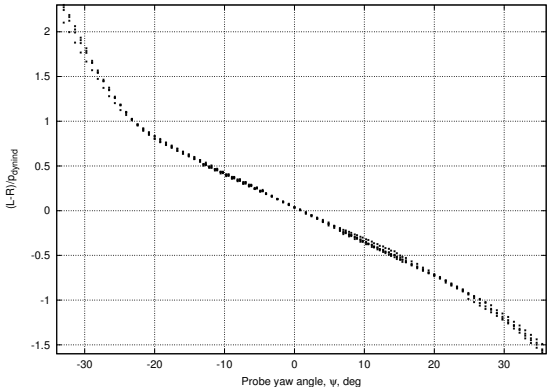

Figure 2.7: The difference of the two outer port pressures as a fraction of indicated dynamic pressure

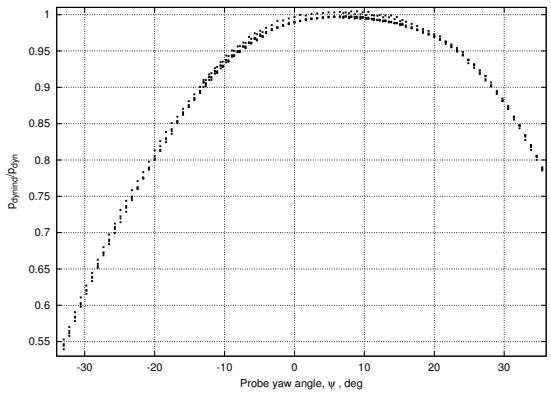

Figure 2.8: The fraction of true dynamic pressure sensed on the center yawmeter port

Traverse

As the flow was shown to be generally steady, but varied in space, provisions were made to traverse the yawmeter over an entire cross-section of the flow passage to allow measurement of flow angle and magnitude at any position.

Positioning of the probe was done with a manual 4-axis traverse (X, Y, and Z linear and Z rotation), the Z axis being parallel to the probe shaft, although only the Z linear and rotation axes were used. The Z rotation of the traverse, known as a goniometer, was limited to approximately $-15°$ to $15°$, so an indexing collar with $20°$ increments was designed to allow the probe to sweep a full circle, if needed. The traverse was fixed to the end-plate of the volutes, and could be rotated freely to allow repositioning the probe to a different azimuth location.

Geometry and orientation

The volutes were oriented such that measurements took place from above as shown in Figure 2.2. The angles describing flow direction and probe orientation and location are presented in Figure 2.9. The angle between the flow and radial, α, is given by absolute probe angle, ϕ, minus relative flow yaw angle, ψ.

Probe azimuth location θ was positive counter-clockwise when viewed from above, as in Figure 2.9. The nominal radius for measurement was the probe shaft radius, r_o. The affect of ϕ and the length of the probe head on actual the actual value of r was taken into account.

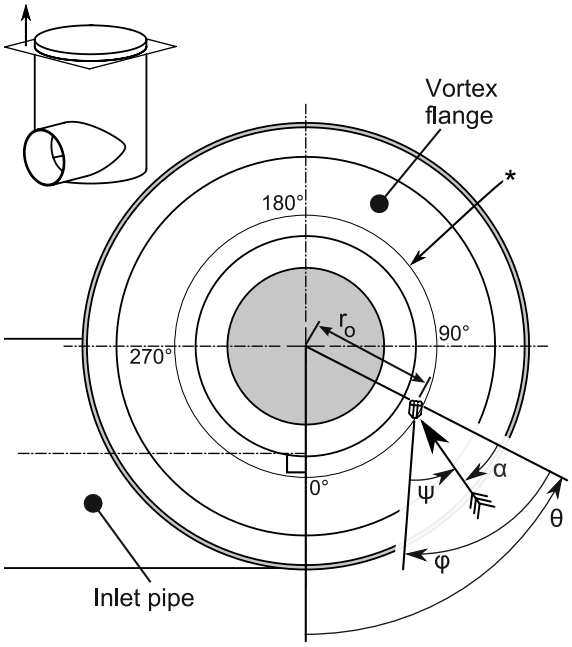

Figure 2.9: Important volute velocimetry angles. Here * indicates the projection of the measurement domain, the imaginary cylindrical surface on which the measurements apply, along Z.

The collection of measured points therefore lay on an imaginary, nominally cylindrical surface referred to as the 'measurement domain'. Table 2.1 gives the dimensions which describe each volute's measurement domain, and the spatial resolution of the measurements, where the dimensions tabulated are defined in Figures 2.9 and 2.10.

All measurements took place with the yawmeter shaft at a constant radius of $r_o = 54.4\,\text{mm}$ and 130 mm and the probe tip was traversed across the 21.1 mm and 64.9 mm gaps between vortex flange and end-plate, shown in Figure 2.10, by a manually-operated traverse at 12 evenly-spaced azimuth locations, where dimensions are quoted for the N_S176 and N_S544, respectively.

The key dimensions for both the N_S176 and N_S544 volutes are presented in Figure 2.11, while Figure 2.12 clarifies potential ambiguity and introduces additional dimensions necessary to fully describe

	Volute	
Volute	N_S176	N_S544
r_o, mm	54.5	130
S, mm	21.1	64.9
ΔZ, mm	1.4	6.3
$\Delta\theta$, $^\circ$	30	30

Table 2.1: Probe traverse parameters

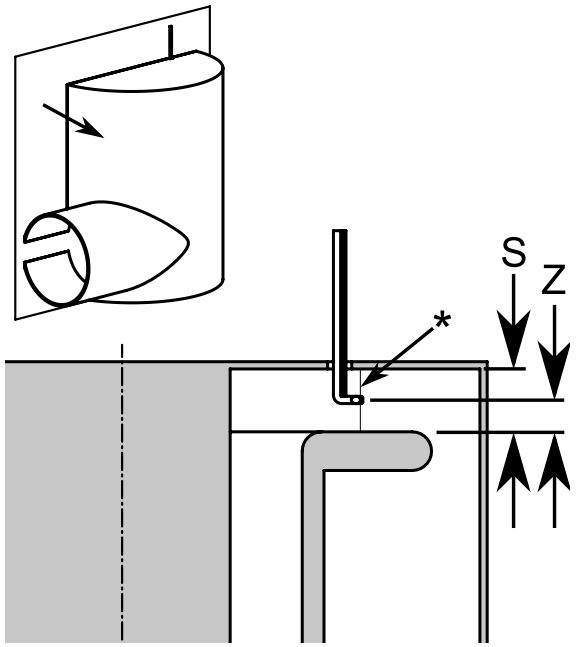

Figure 2.10: Volute velocimetry probe Z location. Here * indicates the meridional projection of the measurement domain, the nominal cylindrical surface on which the measurements were taken.

the N_S544. Dimension names are consistent with those given in Alexander, *et al.*[6], except '⌀D′' where the prime indicates the *outer* diameter of the outlet pipe.

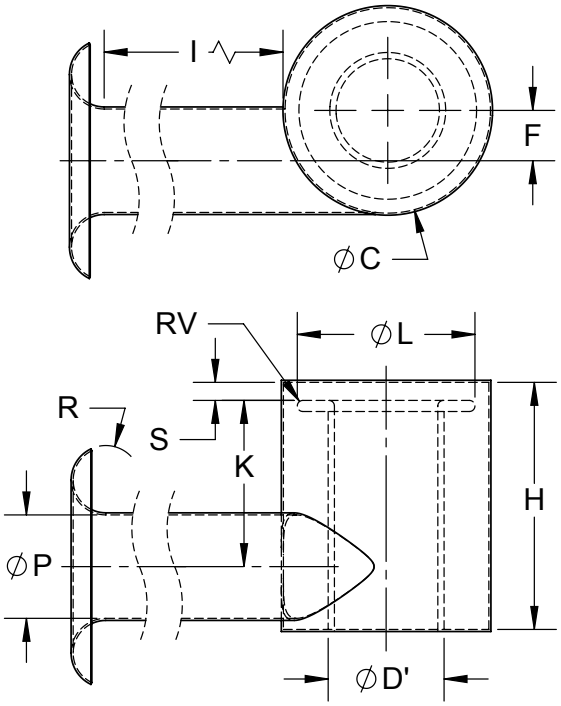

Figure 2.11: Key dimensions

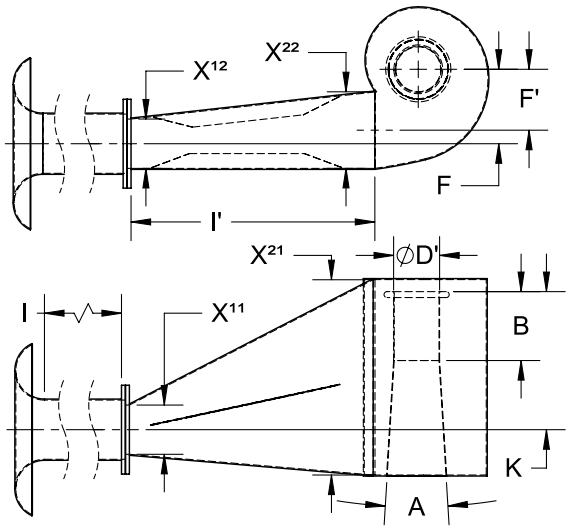

Figure 2.12: Additional dimensions

Volute dimensions are tabulated in Table 2.2.

2.4.2 Measurement

On each of the two volutes, two-dimensional time-averaged velocity measurements were conducted using a three-port yawmeter, known as a cobra probe, in the thin radial-inflow passageway just upstream of where the rotor would be located in a functioning turbine. The velocity magnitude and angle for each measurement point were extracted from pressures measured from the yawmeter. The pressures were captured simultaneously using a data acquisition (DAQ) board installed in a personal computer (PC).

	Volute	
Dimension	N_S176	N_S544
A, °		7
B, mm		319
⌀C, mm	189	
⌀D′, mm	110	233
F, mm	41.5	377
F′, mm		309
H, mm	232	1000
RI, mm	45	70
I, mm	1000	3000
I′, mm		1235
⌀L, mm	159	330
⌀P, mm	104	305
S, mm	21.1	64.9
RV, mm	3.3	15
X^{11}, mm		260
X^{12}, mm		260
X^{21}, mm		1000
X^{22}, mm		397

Table 2.2: Dimensions

Each data point was the average of 2000 samples taken over 20 seconds. The spatial resolution required to capture important flow features was not known beforehand. Twelve azimuth stations for both volutes, and 11 and 15 Z stations for the N_S176 and N_S544 volutes, respectively—132 and 180 stations in total—were shown to be sufficient to capture time-averaged flow features.

The probe azimuth position was set by rotating the end-plate of the volute, to which the traverse and yawmeter were fixed. At each azimuth position, the linear Z traverse was used to step the probe incrementally across the gap between end-plate and vortex flange. For each data point, before initiating data capture, the Z rotation of the probe was adjusted to provide a relative flow angle that was well within the linear region indicated from probe calibration. This was made possible by adjusting the probe angle until the pressures were near equal as indicated by the pressure transducer displays.

For each data point, the indexing collar position, Z rotation fine adjustment, Z linear position, and azimuth station were recorded which, combined with the traverse base's orientation relative to the shaft of the yawmeter, gave the absolute orientation of the yawmeter. After processing the data, the yawmeter angle was combined with the flow angle relative to the probe to give the absolute angle of the flow, so that velocities could be reported in terms of their radial and tangential components, and the flowrate and angular momentum flux could be integrated over the measurement domain.

2.4.3 Method of velocimetry resolution

In addition to the resolving velocity magnitude and yaw angle of the flow relative to the probe, it was required to sense the local static pressure for each measured point. Solving for these three variables from the measured pressures on the three ports of the yawmeter required an iterative procedure.

There was a need to deduce the local static pressure, in order to subtract it from all three ports and resolve yaw angle using the data given in Figure 2.7. The ratio of the difference between the center port and one of the side ports to dynamic pressure was correlated to dynamic pressure. Since neither dynamic pressure or yaw angle were known beforehand, an iterative process was used with an initial condition to resolve the value of ψ, p, and p_d.

The three correlations needed to solve for yaw angle and dynamic pressure were

1. a function that related yaw angle to the ratio of $L-R$ to indicated dynamic pressure, $\psi = f\left(\frac{p_L - p_R}{p_d{}'}\right)$, where f is linear (see Figure 2.7),

2. a function that related the ratio of indicated dynamic pressure to true dynamic pressure to yaw angle, $\frac{p_d}{p_{d'}} = f(\psi)$, where f is parabolic (see Figure 2.8), and

3. a function that related the ratio of the center minus a side port to indicated dynamic pressure to yaw angle, $\frac{p_C - p_L}{p_{d'}} = f(\psi)$, where f is linear.

The structure of the iterative process was to assume a yaw angle of zero,

1. update the indicated dynamic pressure using the relationship between center-minus-side and yaw angle,

2. update the true local dynamic pressure using the relationship between center and true total pressure,

3. update yaw angle using the relationship between $\frac{p_L - p_R}{p_{d'}}$ and yaw angle,

4. return to the top with new yaw angle and repeat until change between iterations is small.

Local static pressure was the center port minus the indicated dynamic pressure, and total pressure was static pressure plus dynamic pressure.

2.5 Computational analysis setup

Steady flow through the Giddens N_S176 and N_S544 volute geometry and flow conditions during measurement was modeled in Fluent (Fluent, Inc., Lebanon, NH, USA) using the inviscid model, the $k\omega$ shear stress transport ($k\omega$SST) turbulence model, and the Reynolds stress model (RSM) modeling turbulence intensity and dissipation with $k\omega$ (RSM ($k\omega$)). The computational domains and coordinate systems are shown in Figure 2.13. Agreement between the real and simulated cases are covered in the following sections.

Although unsteadiness was observed during measurement of both volutes, steady-state numerical analysis was chosen since the most pressing questions were with regard to their time-averaged behavior. All final numerical results relied upon the pressure staggering option (PRESTO!) in Fluent for pressure terms and a second-order upwind discretization scheme for momentum terms. These discretization schemes gave results for swirl strength that were < 0.03 different from the 3rd order MUSCL scheme available in Fluent in terms of F_{AM}. Turbulence scalars used a first order upwind discretization scheme, after the value of F_{AM} was found to be insensitive to discretization order.

For both volutes, the inlet profiles of all relevant properties for the $k\omega$SST and RSM ($k\omega$) cases were taken from the outlet surface of a 15-diameters-long straight-pipe analysis. The straight-pipe analyses (one for each volute and fluid model) were run separately from the volute analysis, the profiles saved from the pipe's outlet surface, and applied to the volute's inlet surface. The inlet conditions to the straight-pipe domain were a uniform velocity and a uniform turbulence intensity. The inviscid model cases had a uniform inlet velocity normal surface applied at the inlet, and zero shear stress applied on all wall boundaries. The outlet boundary in all cases was an "outflow" type, in Fluent parlance, which set all gradients normal to the outlet to zero, approximating fully developed pipe flow.

The final mesh used for the N_S176 analyses whose results are presented here comprised 6.8×10^5 total cells, created using the Hexcore meshing scheme in Gambit (Fluent, Inc., Lebanon, NH, USA) with prism boundary cells. Its boundary cells were several layers of extruded triangular prisms, patched to a regular cartesian hexahedra core by several cell-widths of unstructured tetrahedra.

A view of the N_S176 mesh lying on a meridional plane is shown in Figure 2.14. The N_S544 numerical simulations were also based on a Hexcore mesh, with a total cell count of 2.6×10^6. No refinements were made to the N_S544 mesh.

Figure 2.15 shows the mesh convergence history, as evaluated on the N_S176 volute using the inviscid and $k\omega$SST fluid models. For both models, the coarsest mesh was deemed adequate. This gives an

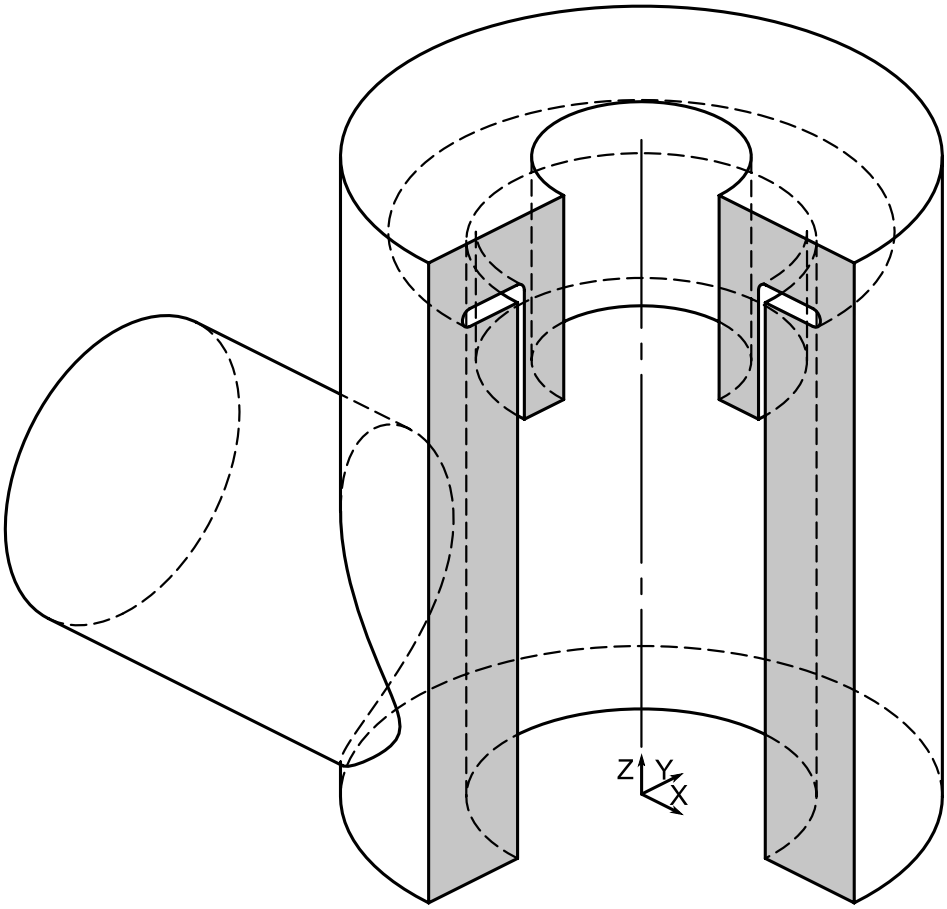

(a) N_S176

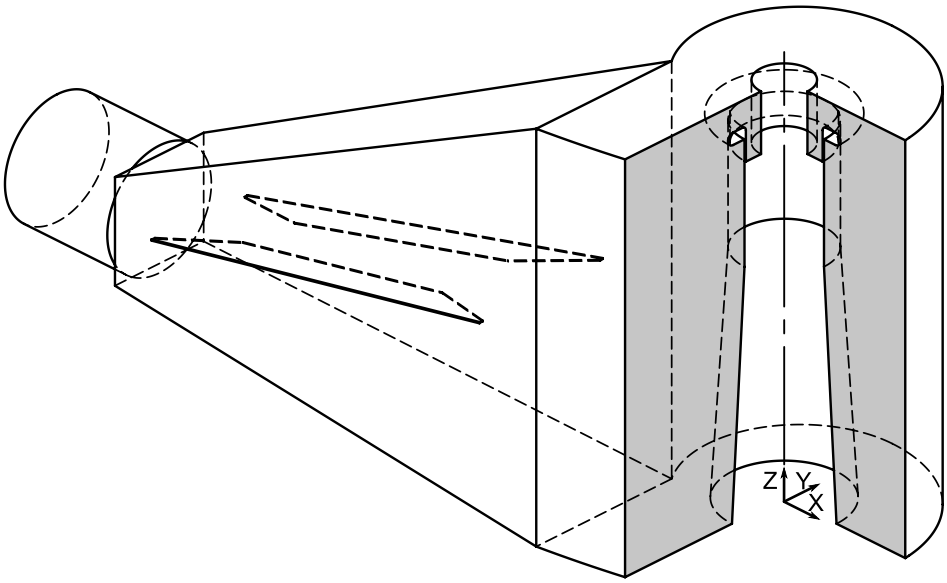

(b) N_S544

Figure 2.13: Numerical computational domains, cut away to show internal features

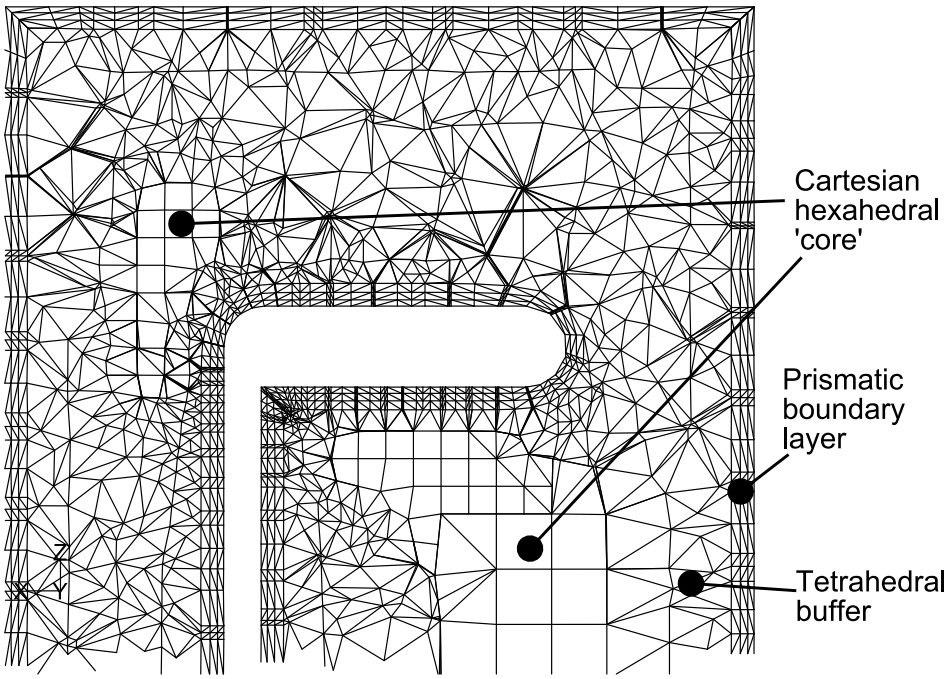

Figure 2.14: A two-dimensional meridional slice through the nominal N_S176 CFD mesh showing key cell type regions

estimated mesh convergence error, in terms of F_{AM}, of 0.02 for the inviscid results and less than 0.01 for the $k\omega$SST results. A separate mesh convergence study was not done for the RSM ($k\omega$) model, since the results were deemed suitably similar to the $k\omega$SST results. Given the similar physics and Reynolds numbers of the N_S176 and N_S544 volutes, the same initial cell height, growth rate, number of prismatic boundary cells, and number of tetrahedral buffer layers were then used to generate a mesh for the N_S544.

Figure 2.16 shows the numerical behavior of F_{AM} over all studies' final iterations.

2.6 Velocimetry results

2.6.1 Summary

The key results for the two volutes investigated were angular momentum flux factor, defined in Equation 2.1

$$F_{AM} = \frac{\oint_o \rho r V_t V_n \, dA}{\oint_i \rho r V_t V_n \, dA} \tag{2.1}$$

and total pressure loss coefficient, defined in Equation 2.2

$$K_v = \frac{\overline{p_t}_i - \overline{p_t}_o}{\overline{p_d}_i} \tag{2.2}$$

where an overbar indicates an area-weighted average of the variable underneath. Table 2.3 gives a summary of the most important results, where Reynolds numbers are from bulk inlet conditions, 'Meas.' indicates measured values, and $k\omega$, 'Inviscid', and 'RSM' indicate the use of the $k\omega$SST turbulence model, the inviscid flow model, and the RSM ($k\omega$) turbulence model, respectively. For the N_S176 volute, the inlet angular momentum is calculated using the mean velocity and offset within the penstock, as in Equation 2.3.

$$\oint_i \rho r V_t V_n \, dA \underset{\mathrm{N_S176}}{\approx} \rho \frac{4Q^2}{\pi \left(\varnothing \mathrm{P}\right)^2} \mathrm{F} \tag{2.3}$$

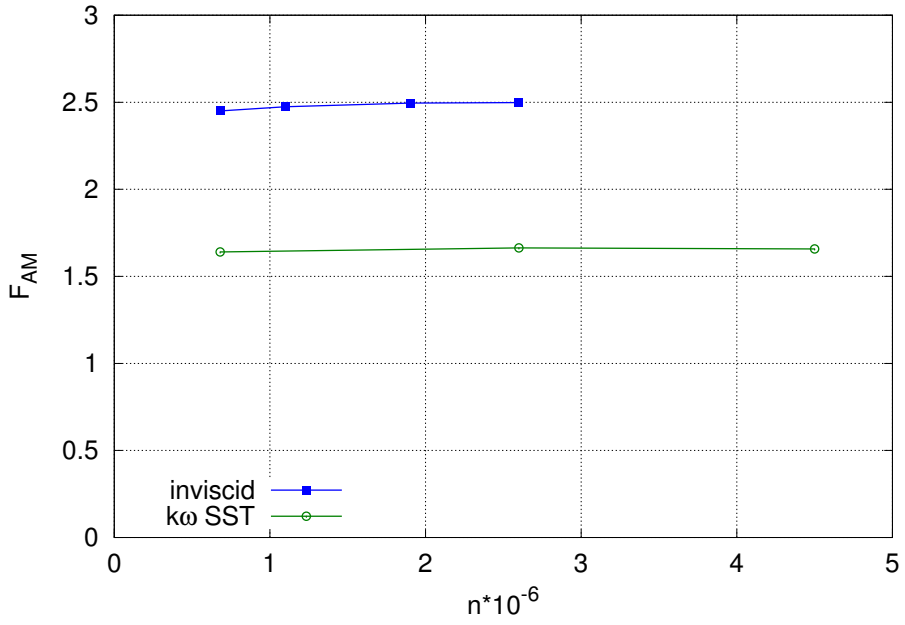

(a) Convergence of F_{AM}

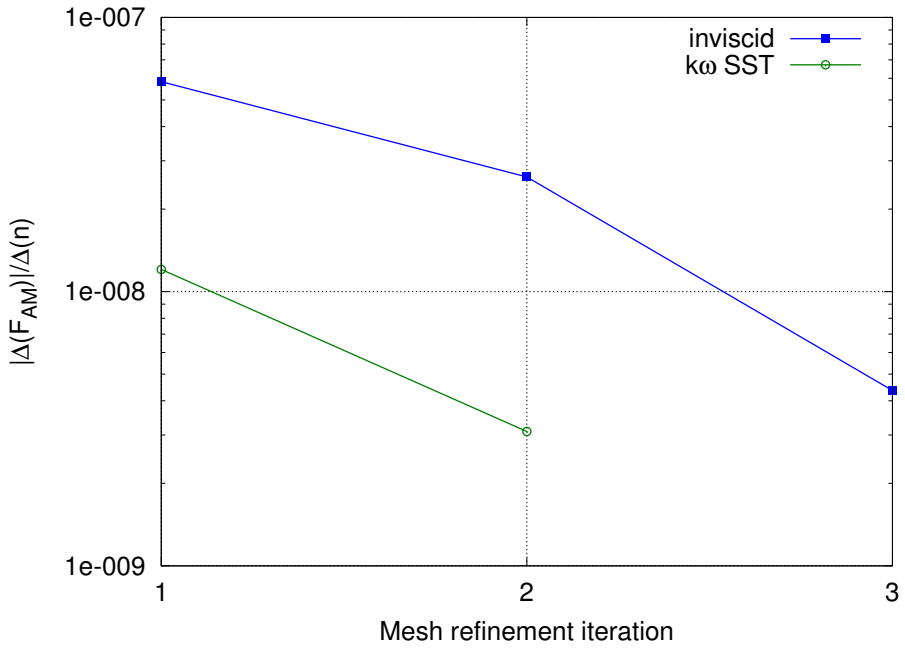

(b) Differences in F_{AM} with increasing cell count

Figure 2.15: N_S176 volute mesh convergence analysis

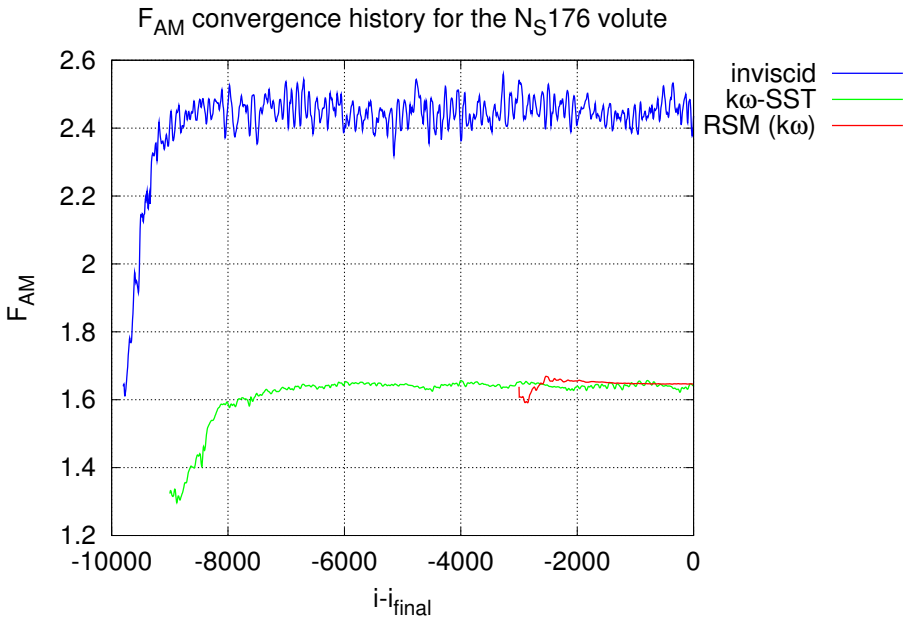

(a) N_S176

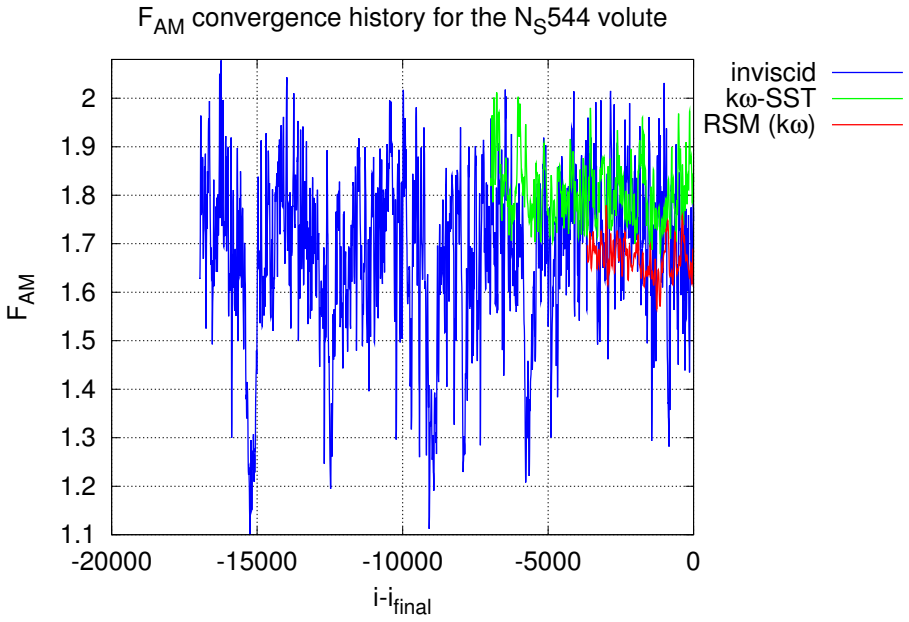

(b) N_S544

Figure 2.16: Comparison of numerical convergence histories of F_{AM} over final iterations

	N_{Ri}		F_{AM}				K_v			
Volute	air	water	Meas.	$k\omega$	RSM	Inviscid	Meas.	$k\omega$	RSM	Inviscid
N_S176	8.3×10^4	1.8×10^5	1.78	1.64	1.65	2.45	1.52	1.31	1.33	0.76
N_S544	1.8×10^5	5.1×10^5	1.94	1.83	1.70	1.71	1.22	1.04	1.07	0.76

Table 2.3: Results comparison

For the N_S544 volute, V_{ti} was taken as the mean value not in the penstock, but through the downstream end of the inlet diffuser with height, width, and offset from Figure 2.12 of X^{21}, X^{22}, and F', respectively, as in Equation 2.4.

$$\oint_i \rho r V_t V_n \, dA \underset{N_S544}{\approx} \rho \frac{Q^2}{X^{21} X^{22}} F \tag{2.4}$$

This reflects the assumption embodied in the design that the diffuser would perform ideally. The flow models whose predicted values of F_{AM} and K_v were closest to measured values were selected for detailed comparison with the measurements. Although the $k\omega$SST and RSM ($k\omega$) models gave similar results on both volutes, the RSM ($k\omega$) was closest for the N_S176 volute and the $k\omega$SST gave the best results for the N_S544 volute.

Measured values of F_{AM} and K_v were confirmed to be independent of Reynolds numbers from near zero up to the Reynolds number of interest by increasing fan speed in steps and observing that the ratio of transducer outputs did not change significantly. This was not surprising since all observations took place well into the fully-turbulent flow regime. Nominal Reynolds numbers based on inlet pipe conditions are given for the experiment taken in air, as well as what would occur in the corresponding microhydro turbine. Experimental Reynolds numbers were limited in both cases by fan flowrate at the maximum operating speed. Higher specific speed fans would address this shortcoming and allow larger Reynolds numbers for the same fan power.

All data presented in this chapter were from a single run per volute which had the smallest discrepancy between the integrated and bellmouth flowrates. The ratio of integrated outlet to bellmouth-indicated inlet flowrate for the runs whose data is presented is 1.008 and 0.988 for the N_S176 and N_S544 volute, respectively.

2.6.2 N_S176

Figures 2.18 and 2.19 show the tangential and radial velocity components across the N_S176 measurement domain. All numerical results shown for the N_S176 volute were obtained with an unmodified RSM ($k\omega$) turbulence model, and streamlines of the converged solution are shown in Figure 2.17. The mean inlet pipe velocity for the run presented was 11.79 m/s. Once again, the deviation from the ideal case was clear: at the same radius, a range of tangential velocities existed. This may be attributed in part to the fact that the flow entered the volute at a range of radii, and each fluid particle travels downstream to the measurement domain retaining some semblance of that initial swirl strength. Such effects could be useful in explaining the pattern of radial velocities right around the measurement domain in Figure 2.19, characterized by a sharp decline in radial velocity nearest the vortex flange — which may be attributed to the wake of the vortex flange — balanced by the peak in radial velocity for many of the azimuth stations just away from the vortex flange — which may be attributed to the acceleration of flow around the vortex flange's inner radius as it is turned downward to the axial direction. By contrast, the increase in radial velocity approaching the end-plate was less intuitive.

The tangential velocity profiles also exhibited similar properties at a range of azimuth angles around the measurement domain, with azimuth station profiles falling into two broad categories: ones with relatively constant values of V_t and ones where V_t increased more or less proportionally to the distance away from flange. Spanwise variations in tangential velocity were difficult to explain due to a lack of

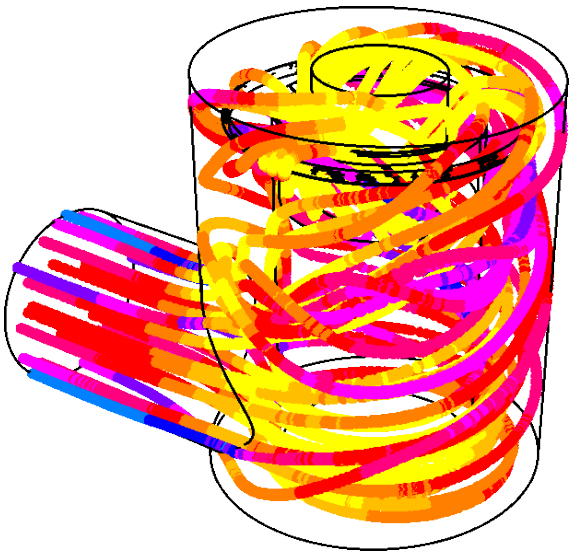

Figure 2.17: N_S176 streamlines from the RSM steady solution

torque-creating influences, apart from the aforementioned range of inlet radii entering the volute. Perhaps cross-inlet streamlines propagated downstream, remaining relatively coherent, with the smaller-offset streamlines winding up nearer to the vortex flange, with corresponding smaller tangential velocities, and the larger-offset streamlines staying outside and crossing the measurement domain nearer to the end-plate.

Figure 2.20 shows the derived flow angles relative to radial, illustrating the wide variation—35° to 58° on the end-plate and 22° to 63° on the vortex flange—over the full range of θ and z on the measurement domain, indicating the magnitude of error which would be incurred by estimating the flowrate or swirl strength from a single velocity measurement or tuft reading.

To highlight deviations from circumferentially uniformity, the points from each azimuth location were combined. Figure 2.21 shows the measured and numerical circumferential distributions of mass flux variation through the measurement domain as a percentage of the surface average mass flux. About the measurement domain, an approximately sinusoidal mass flux pattern became evident that could be described as two instances of an approximately ±10 % deviation in mass flux from mean, each occupying 180° of azimuth.

Figure 2.22 shows the measured and numerical circumferential distributions of swirl strength through the measurement domain as a percentage of the measurement domain's average swirl strength. About the measurement domain, an approximately sinusoidal swirl strength pattern has become evident that could be described as two instances of an approximately ±10 % deviation in swirl strength from mean, each occupying 180° of azimuth.

Note that the variations in the flow and swirl components were nearly in phase. Flowrate peaks occur near 90° and 240°, with troughs at 180° and 330°. Swirl peaks occurred at 90° and 240°, with one trough between 150° and 180°, and the other near 300°.

The presence of an axial velocity component deviation from the plane of the probe on the order of 10° was noted prior to testing using a tufted wand. Its presence was neglected as Figure 2.8 shows the relative insensitivity of pitot-type probes to small out-of-plane deflections. An axial component would have had a small effect on the integrated flowrate calculation. This axial component was greatest near the rounded transition between the vortex flange and the axial outlet passage, and decayed rapidly in magnitude toward the volute end-plate.

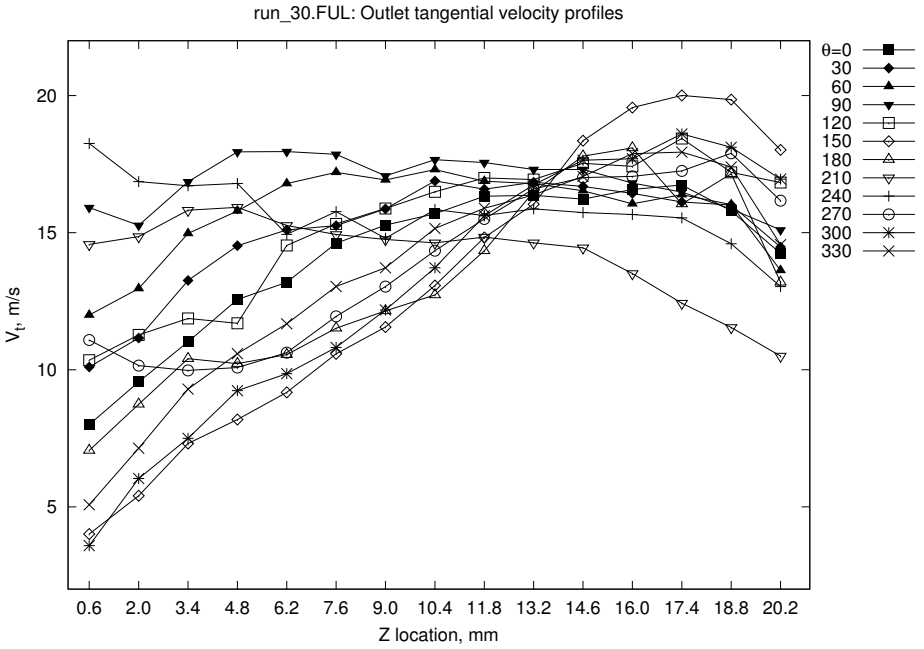

(a) Measured

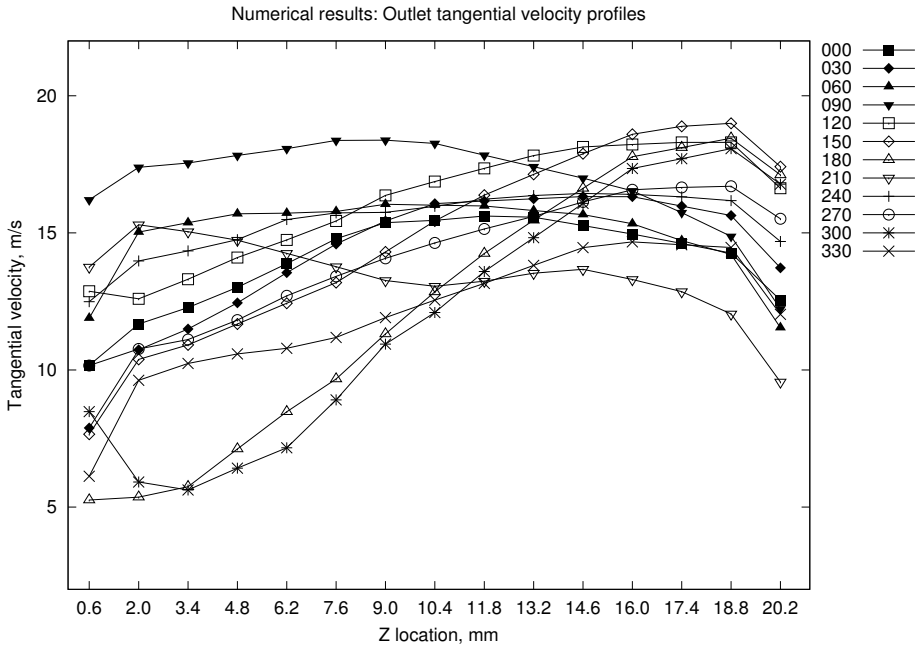

(b) RSM

Figure 2.18: N_S176 circumferential distribution of tangential velocity, series labels are azimuth location, θ

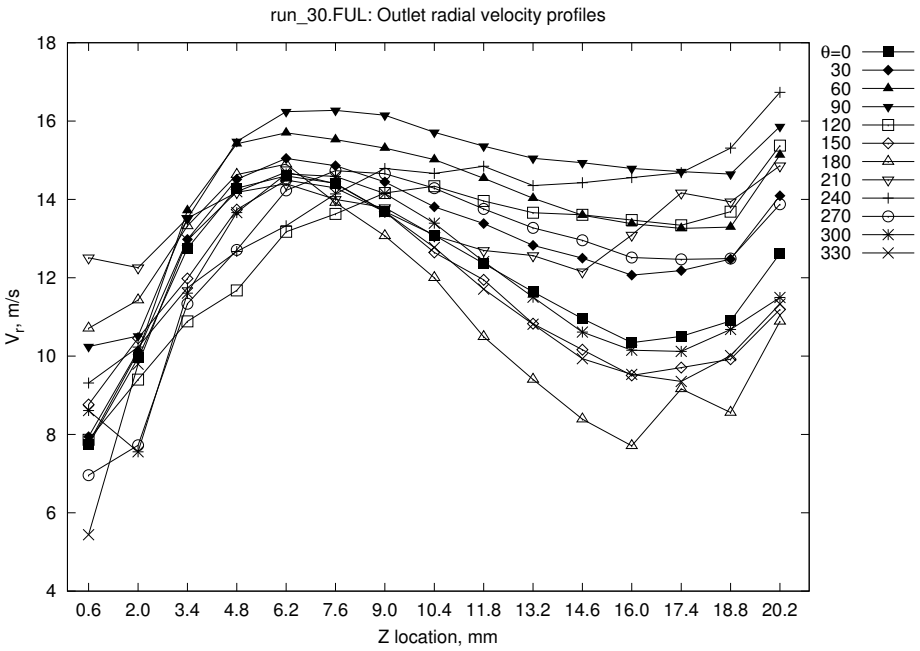

(a) Measured

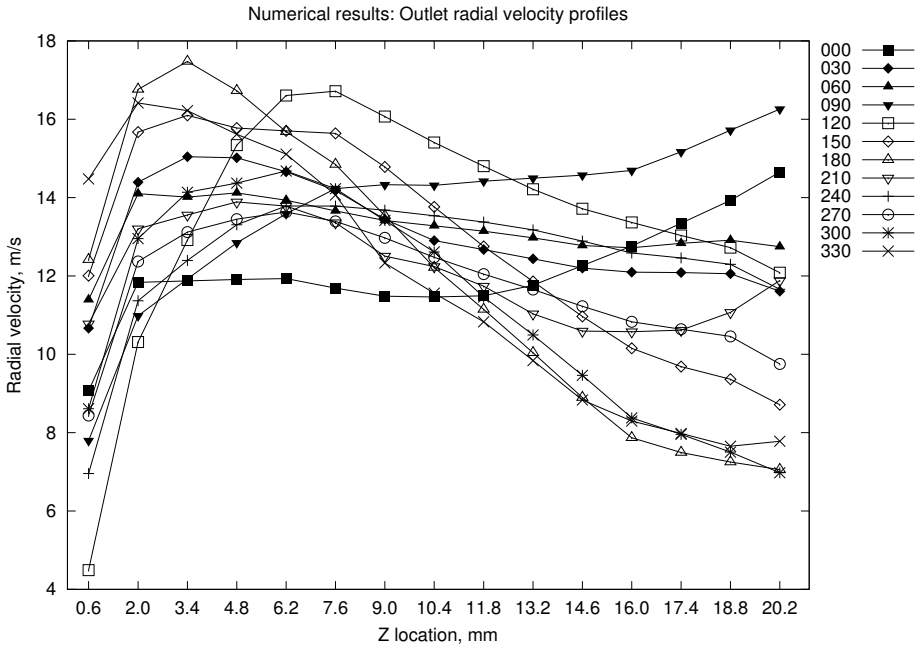

(b) RSM

Figure 2.19: N_S176 circumferential distribution of radial velocity, series labels are azimuth location, θ

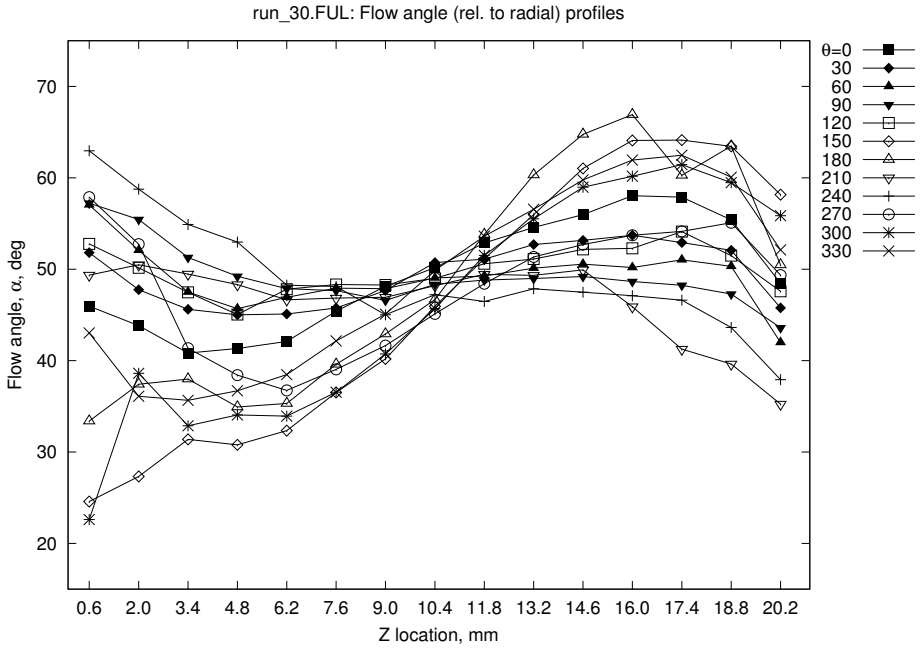

(a) Measured

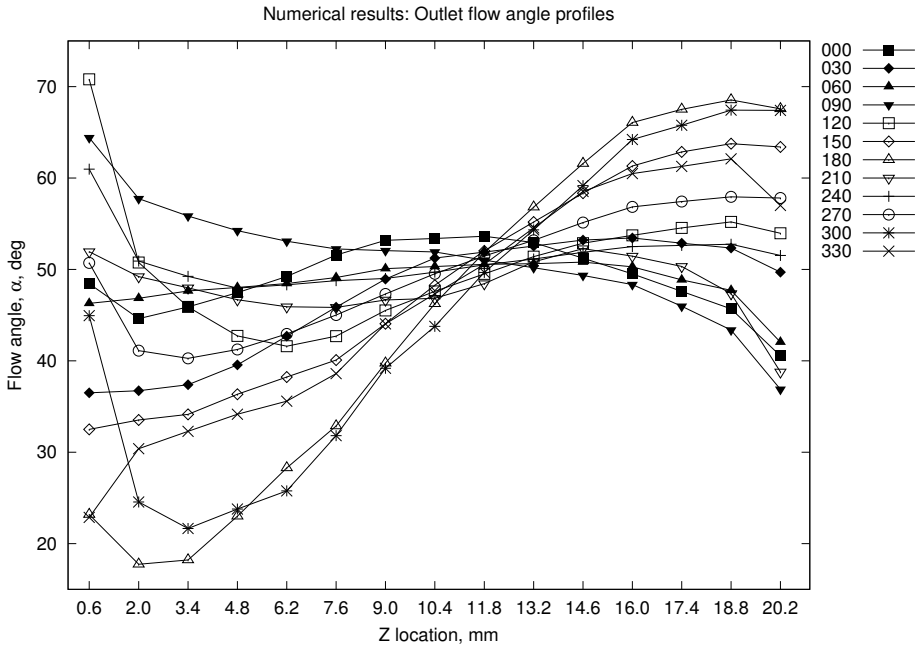

(b) RSM

Figure 2.20: N_S176 circumferential distribution of flow angle, series labels are azimuth location, θ

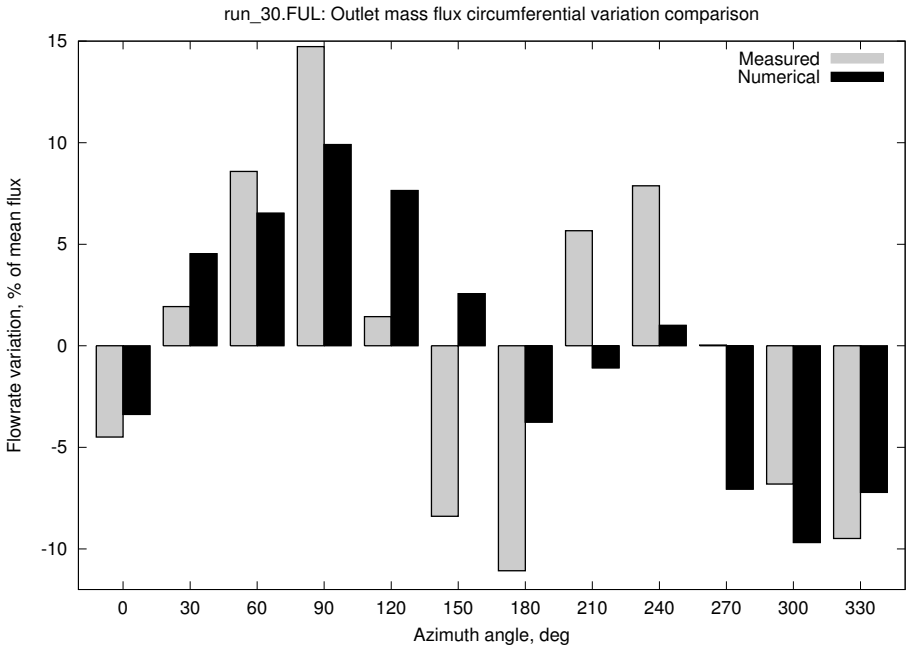

Figure 2.21: N_S176 circumferential distribution of mass flux, with comparison to corresponding RSM numerical results.

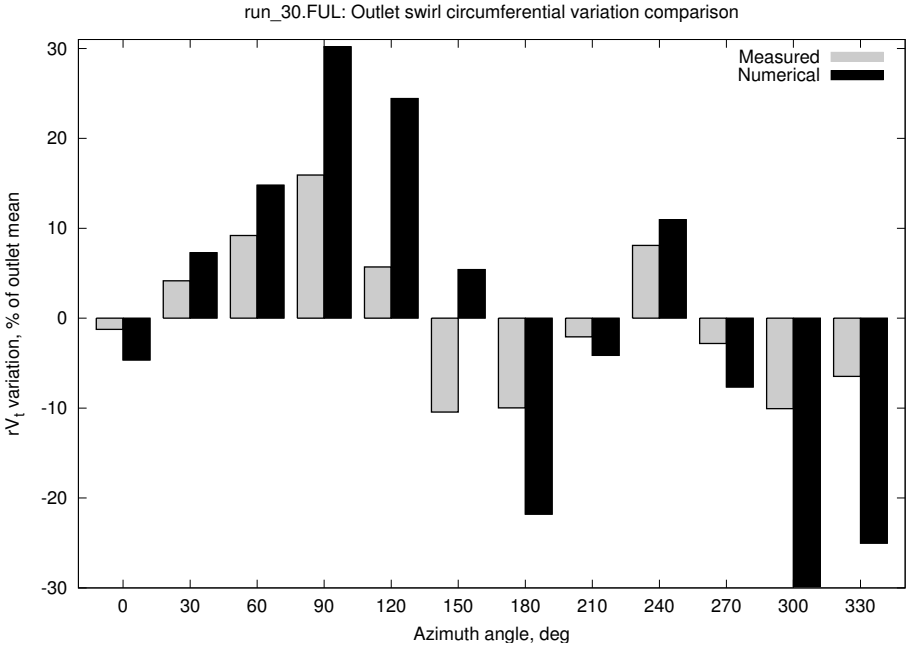

Figure 2.22: N_S176 circumferential distribution of rV_t, with comparison to corresponding RSM numerical results.

2.6.3 N_S544

Figures 2.24 and 2.25 show the tangential and radial velocity components across the N_S544 measurement domain, with corresponding numerical results using an unmodified $k\omega$ turbulence model, and streamlines of the converged solution are shown in Figure 2.23. The mean inlet pipe velocity for the run presented was 8.77 m/s.

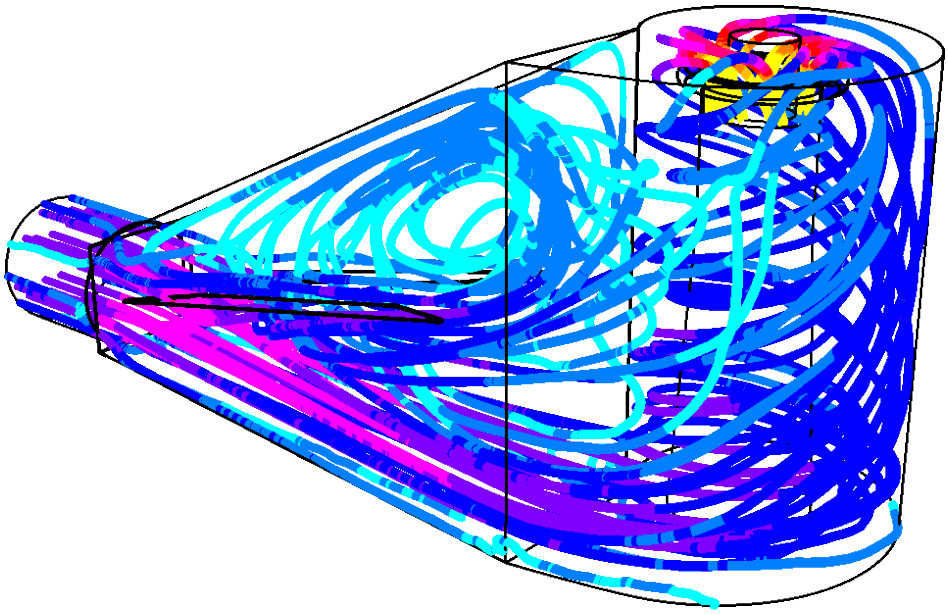

Figure 2.23: N_S544 streamlines from the $k\omega$ steady solution

Figure 2.26 shows the derived flow angles relative to radial, illustrating the wide variation — 8° to 40° on the end-plate and 8° to 27° on the vortex flange — over the full range of θ and z on the measurement domain, again indicating the uncertainty of estimating the flowrate or swirl strength from a single velocity measurement or tuft reading. The erratic behavior that appears across 30° and 60° was in fact a repeatable feature of all measurement runs.

To highlight deviations from the ideal circumferentially uniform case, the different Z point from each azimuth location were combined. Figure 2.27 shows the measured and numerical circumferential distributions of mass flux through the measurement domain as a percentage of the measurement domain's average mass flux. At the point where measurements were taken, an approximately sinusoidal mass flux pattern became evident that could be described as a single instance of a ±20 % deviation in mass flux from mean.

Figure 2.28 shows the measured and numerical circumferential distributions of swirl strength through the measurement domain as a percentage of the measurement domain's average swirl strength. At the point where measurements were taken, an approximately sinusoidal swirl strength pattern became evident that could be described as one instance of a ±30 % deviation in swirl strength from mean.

Note that the flow and swirl variations were almost 180° out of phase. The measured flow peak and trough occurred at 90° and 0° respectively, while the measured swirl peak and trough occurred at 300° and 60° degrees, respectively.

2.6.4 Uncertainty

The main uncertainties associated with the measurements presented are summarized in Table 2.4. An explanation of each item follows. Estimated precision for probe rotation was based on one eighth of a turn of the rotational stage knob at 0.8° per turn, azimuth was based on visually aligning a mark on the end-plate with a mark on the volute wall, Z position was based on one eighth of a turn of the Z

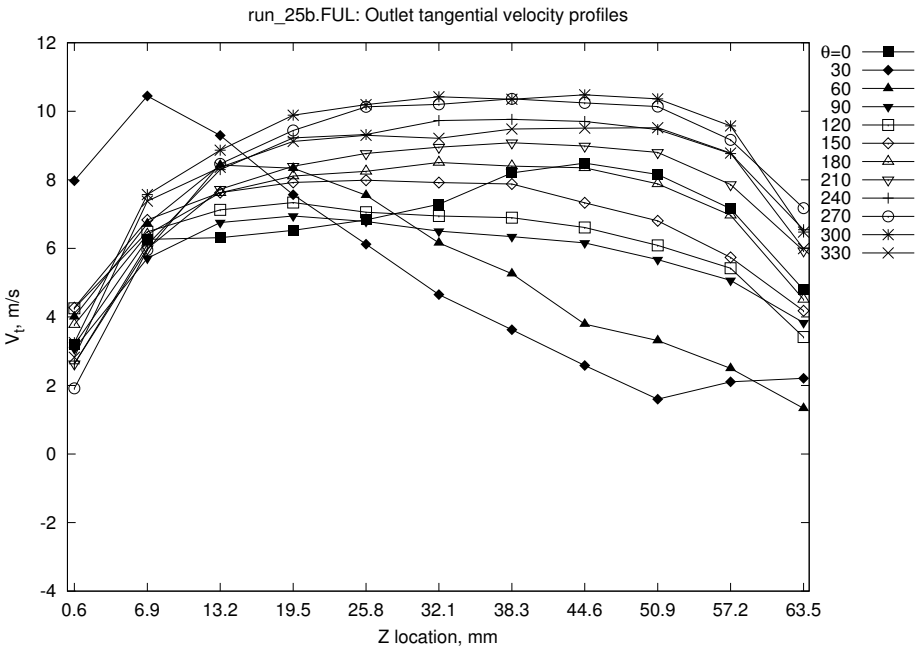

(a) Measured

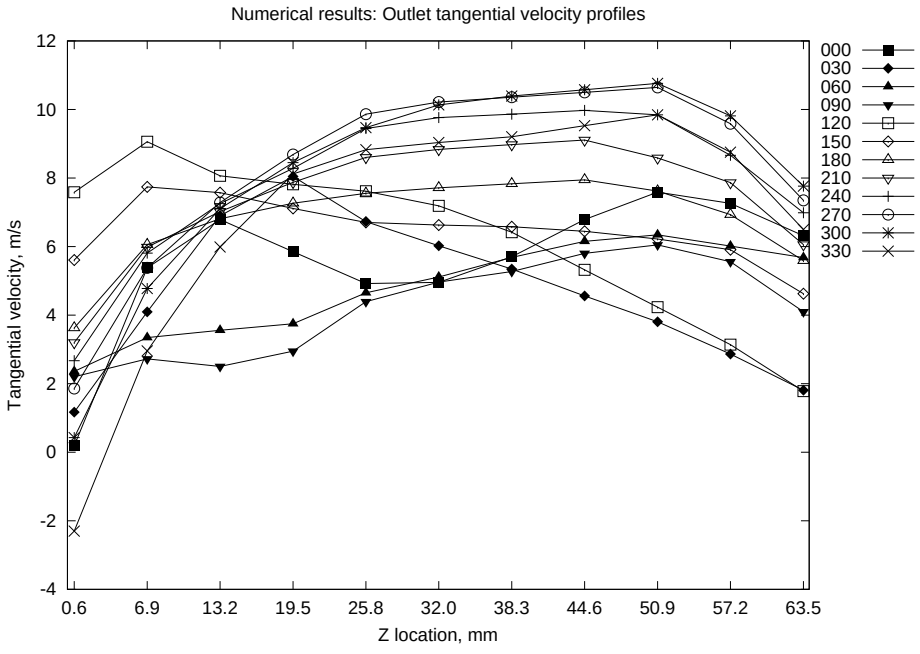

(b) $k\omega$

Figure 2.24: N_S544 circumferential distribution of tangential velocity, series labels are azimuth location, θ

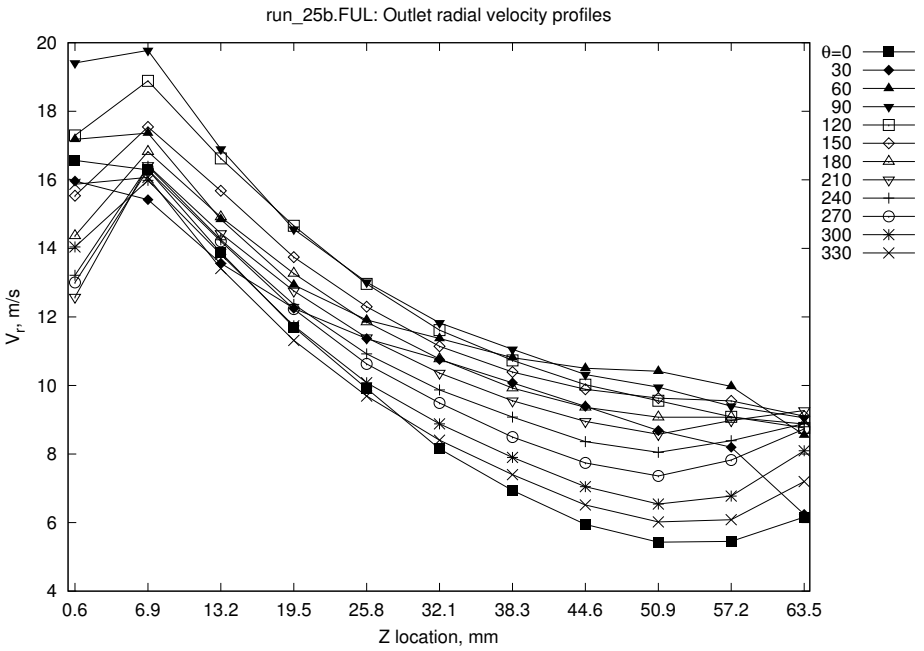

(a) Measured

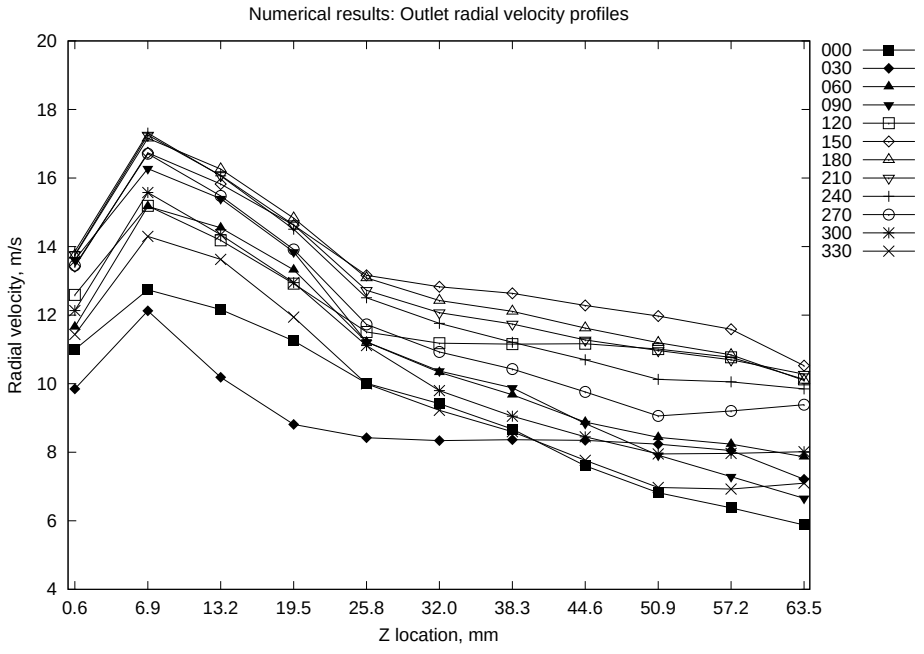

(b) $k\omega$

Figure 2.25: N_S544 circumferential distribution of radial velocity, series labels are azimuth location, θ

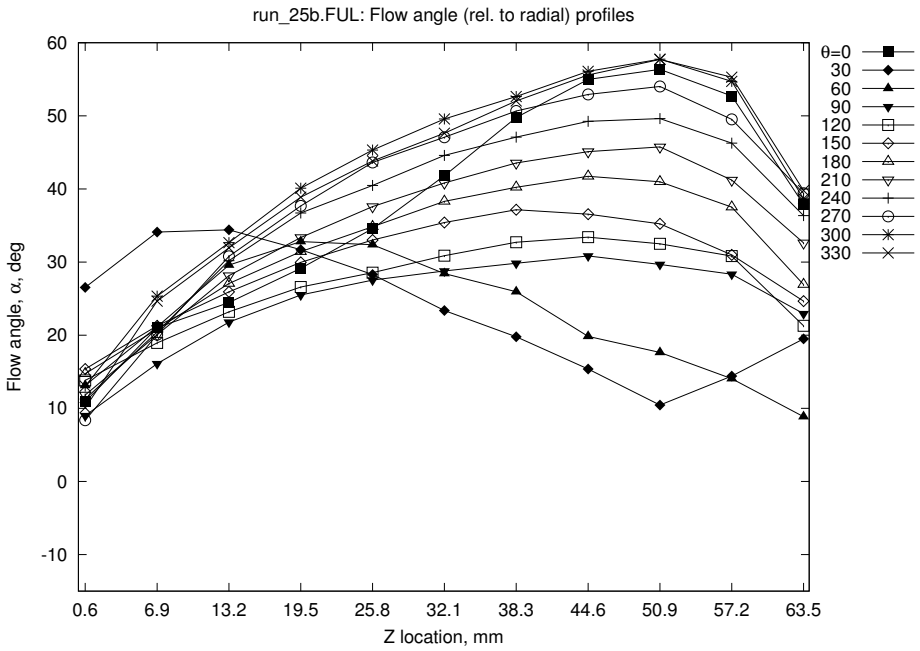

(a) Measured

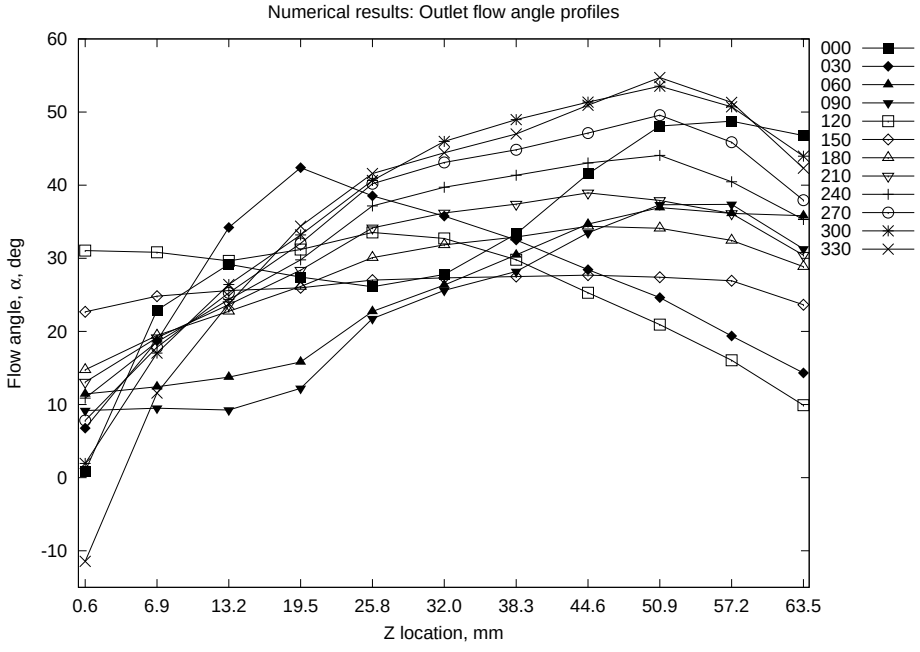

(b) $k\omega$

Figure 2.26: N_S544 circumferential distribution of flow angle, series labels are azimuth location, θ

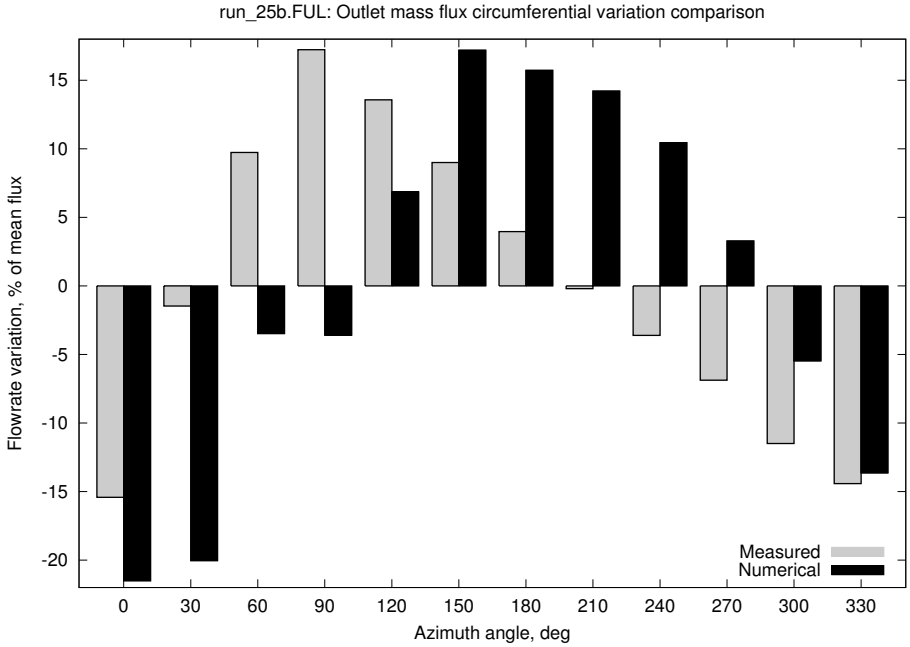

Figure 2.27: N_S544 circumferential distribution of mass flux, with comparison to corresponding $k\omega$ numerical results.

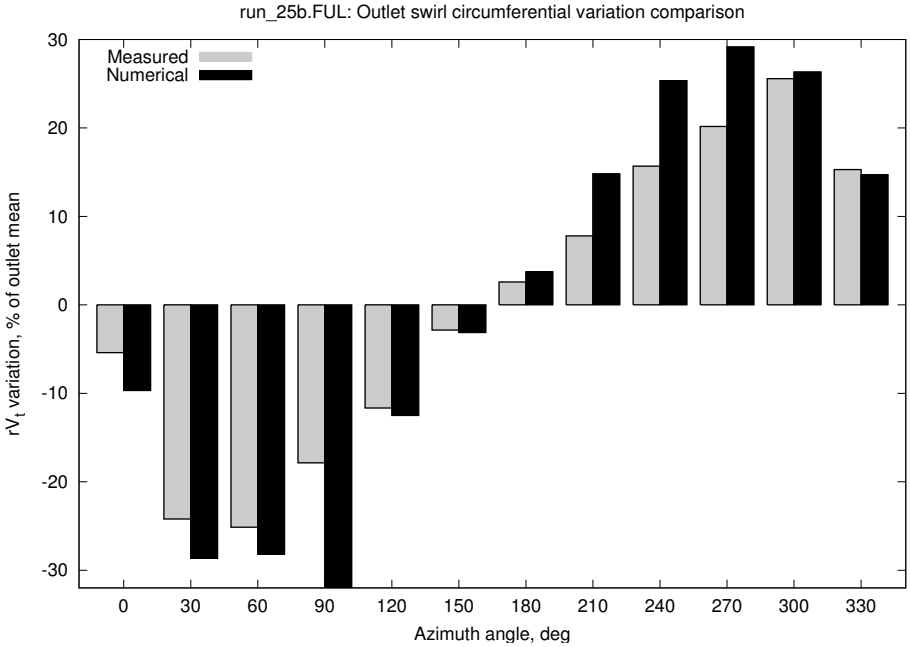

Figure 2.28: N_S544 circumferential distribution of rV_t, with comparison to corresponding $k\omega$ numerical results.

Quantity	Precision
Probe rotation	$\pm 1^\circ$
Probe azimuth	$\pm 3^\circ$
Probe Z position	± 0.1 mm
Flowrate (integrated)	$\pm 5\,\%$
Flowrate (bellmouth)	$\pm 0.3\,\%$
Yaw angle	$\pm 0.8^\circ$
All pressures	± 1 Pa
N_S176 F_{AM}	$\pm 0.3\,\%$
N_S176 K_v	$\pm 0.5\,\%$
N_S544 F_{AM}	$\pm 1.4\,\%$
N_S544 K_v	$\pm 5.5\,\%$

Table 2.4: Measurement uncertainties

	Standard deviation		
Volute	$k\omega$	RSM	Inviscid
N_S176	0.0003	0.006	0.036
N_S544	0.064	0.036	0.165

Table 2.5: Numerical F_{AM} standard deviation

traverse knob at 0.7 mm per turn, integrated flowrate was based on the difference between integrated and bellmouth flowrates over 6 consecutive runs, bellmouth flowrate was based on the stated uncertainty of the ISO 5167 orifice plate used to calibrate it, yaw angle was based on maximum data scatter of calibration data taken at a range of Reynolds numbers surrounding those occurring during measurement, and pressure uncertainty was based on the precision of the manometer used to calibrate the pressure transducers. Listed uncertainties were symmetrical except probe rotation which had a potential bias on the order of $\pm 2^\circ$. Uncertainty values tabulated for F_{AM} and K_v, were deduced from the scatter of values produced from at least four identical measurement runs.

In some of the numerical cases, after the residuals ceased subsiding, there were still significant fluctuations in the value of F_{AM}. Although the numerical F_{AM} results reported in Table 2.3 were averaged over a period of iterations significantly longer than the longest observed fluctuations, a high-frequency fluctuation could still cast doubt on the value of an average. In an effort to quantify these fluctuations, the values given in Table 2.5 indicate the standard deviation of the set of values of F_{AM} which were averaged to provide the single value of reported in Table 2.3. In general, the N_S544 numerical model did not converge as well as did the N_S176.

2.7 Discussion of velocimetry results

2.7.1 N_S176 surface flow visualization

Close agreement of the location and relative extent of the two major stagnation lines within the volute was achieved between the numerical and physical model. A viscous mixture of oil and aluminum dioxide powder was applied to the volute interior surfaces and allowed to flow under the influence of the passing air, revealing flow structures adjacent to those surfaces. The first stagnation line was visible on the outlet pipe wall while looking down the axis of the inlet pipe as in Figure 2.29. Although the stagnation line initially appeared to be due to the left-most inlet streamline directly stagnating upon initial entry to the volute body, the numerical model suggested that the stagnation line was actually the terminus of streamlines that have been around the volute once, and were then turned into the outlet pipe wall by fresh streamlines.

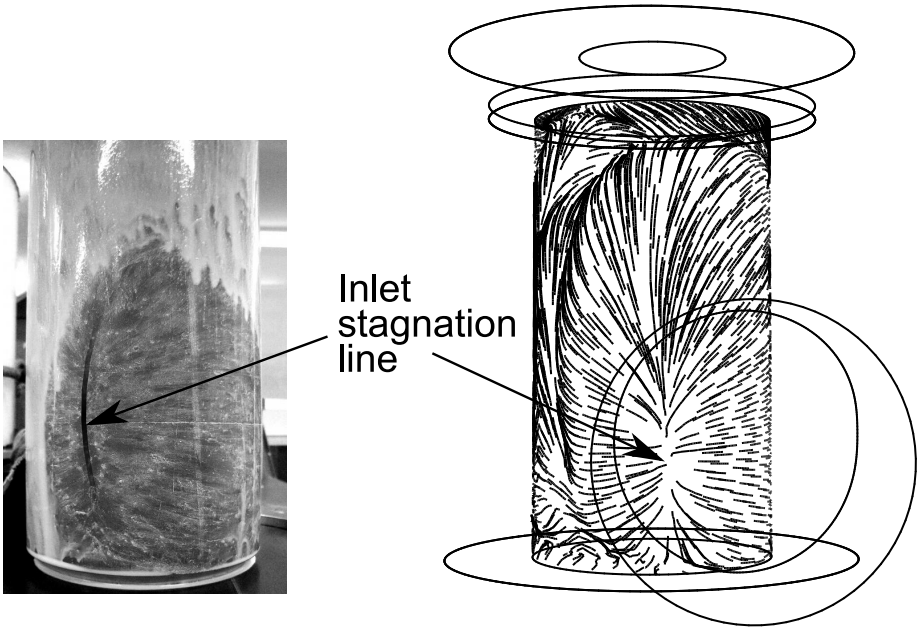

Figure 2.29: Views of the stagnation line on outlet pipe wall down the length of the inlet pipe (the outlet pipe has been removed from the experimental volute in this photograph) showing agreement between physical and numerical models. Somewhat counter-intuitively, the stagnation line is the terminus of streamlines that have made nearly a complete circuit of the volute, not come directly from the inlet pipe onto the outlet pipe wall.

The second stagnation line was present around the entire circumference of the vortex flange's surface facing the end plate, at about one third to one half the flange's width inward from the flange's outer edge, as shown in Figure 2.30. The flow was only stagnated in the radial direction, and flow at radii greater than the stagnation line continued around circumferentially while moving radially outward to be swept back inward again. The recirculating region in the photo was the region toward the vortex flange outer edge which was whiter due to the aluminum dioxide congregating there. The labels in the photo are on the outside of the end-plate. If anything, the $k\omega$SST model tended to slightly over-predict the extent of the stagnated region. This region of recirculating flow was first detected, prior to any measurements taking place, by use of a tufted wand and it was the presence of this recirculation which encouraged the use of the smallest-radius yawmeter position possible. The flange-adjacent measurements would have been contaminated by stagnant flow at a greater radius and by an increasing axial velocity component at a smaller radius.

The video clip in Figure 2.31 highlights the same stagnant region near the vortex flange surface.

2.7.2 N_S176 internal turning

In an effort to reduce the value of rV_t entering the runner and drive specific-speed up without resorting to guide vanes, the N_S176 inlet offset (labeled 'F' in Figure 2.11) was reduced to such an extent that the two key factors listed below prevented the continued proportionality of r_i and $(rV_t)_o$:

1. the runner and its casing, the outlet pipe, caused an obstruction which forced the flow to turn to a larger radius, $\overline{r_i}'$, and

2. the angle of the tongue region, the pinch-point where the inlet pipe joined the volute wall, was large enough that recirculating streamlines rejoin fresh streamlines from the inlet pipe at nearly a right angle, which also turned the flow to a larger radius.

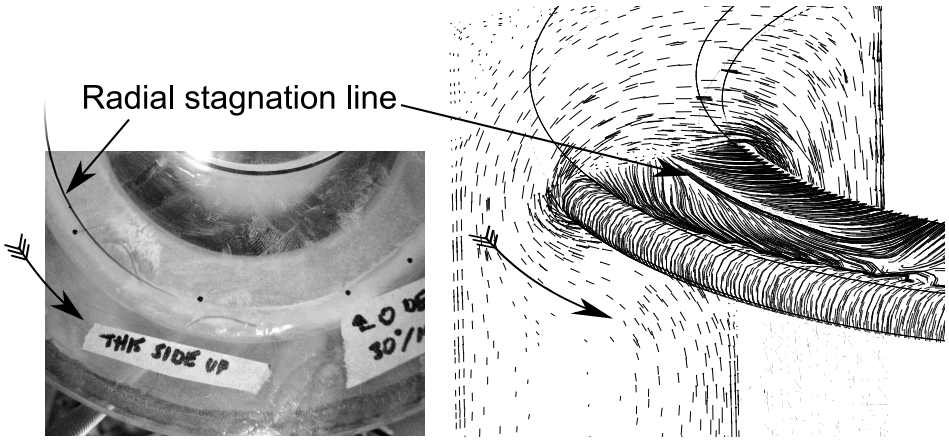

Figure 2.30: Views of the vortex flange radial stagnation line from above showing agreement between physical and numerical models. Tailed arrows indicate the direction of flow. The flow is coming up and over the outer edge of the vortex flange and the flange's outer radius is too to prevent a region of recirculation just beyond the edge. Recirculating flow occupies a third to half the radial span of the vortex flange.

There is an inline video here. If your PDF viewer can play inline video, click to activate or use the controls in the caption. Alternatively, open the target video with an external program.

Figure 2.31: Visualizing flow in vortex flange gap with tufted wand (`../common/MVI_4697.mp4`) Show controls / Play / Pause / Stop / Close

Figure 2.32 illustrates the essence of why contraction-swirl STIVs blindly designed by the zero-torque assumption tend to undershoot their design specific speed: the effective radius of the nearest suitable inlet surface upstream of the rotor is greater than the inlet pipe offset, $\overline{r_i}' > \overline{r_i}$. The streamtube travels from surface A_i to A_i', increasing in both velocity and radius. In the case of the N_S176 volute design, the ratio $\frac{\overline{r_i}'}{\overline{r_i}}$ is 1.79, which is of a similar magnitude to the volute's measured value of F_{AM} of 2.06. Visualization of the streamlines passing through the volute helps avoid an unrealistic torque-free control volume, since streamline curvature as seen in Figure 2.32b indicates a momentum-increasing pressure gradient across the incoming streamtube.

2.7.3 N_S544 upstream diffusing

Accurate prediction of both exit swirl and total pressure loss of the N_S544 volute using numerical simulation was made more difficult by its design, which incorporated an upstream diffuser to reduce inlet rV_t. In that case, the angle of the diffuser was much larger than the generally accepted value of 7°, as well as diffusing asymmetrically, which meant that in operation the diffuser experienced immediate separation and little diffusion. The uncertainty surrounding the amount of diffusion that took place over the length I' in Figure 2.12 meant the representative volute inlet rV_t and pressure loss incurred due to gross separation were not known with precision. The wide range of numerical results shown in Table 2.3 from different fluid models highlights the difficult nature of simulating diffusing flow. The uncertainty and non-uniformity of a diffuser outlet velocity distribution are reasons the diffuser has been eliminated from the design.

The N_S544 volute offers two possible representative inlets: the inlet pipe terminus or the rectangular surface connecting the inlet diffuser to the volute proper. The inlet diffuser was assumed to diffuse perfectly, that is, to a uniform velocity distribution, in which case the inlet diffuser exit plane makes a logical definition of volute inlet. In reality, the inlet diffuser exit velocity distribution will fall between the two extremes of jet flow and perfect diffusion, making the definition of F_{AM} in the case of the N_S544 somewhat arbitrary. Figure 2.33 shows the predicted outlet flow of the upstream diffuser of the N_S544 volute and its dependence on turbulence modeling. All models tested indicated the same general departure from an ideal diffuser; the flow ignored the upper diffuser wall and vanes and passed as a largely undisturbed jet to the volute body. An ideal diffuser of area ratio 5.9 would have a uniform exit velocity of $\frac{\overline{V_i}}{5.9} = 0.17\overline{V_i}$.

2.7.4 Reasons why a volute may not be torque-free

Conservation of angular momentum is a robust principle, but in the case of the two STIVs analyzed, it was Giddens's assumption that the volute exerted negligible torque on the fluid, combined with the choice of upstream extent of control volume led to the break-down of its applicability.

A control volume applied to a volute will have one inlet and one outlet. Applying conservation of angular momentum through the control volume and assuming there is no net torque requires that the control volute encompass no torque-inducing features.

For a typical radial-inflow turbine volute, the inlet boundary may usually be defined as several diameters upstream of the tongue region, in a straight section of the inlet pipe. This station will have approximately uniform conditions, and importantly, a known value of $(rV_t)_i$. To validate the assumptions defined above, the designer must satisfy himself that the streamlines within the control volume under analysis will not be turned by the presence of torque-inducing pressure gradients.

The two volutes analyzed here were shown to exert a momentum-increasing torque on the flow by turning the flow to a larger radius in the tongue region which transitions between the inlet pipe and the volute interior. Because this change in angular momentum happens within the control volume which was used when designing them, they may no longer be assumed torque-free.

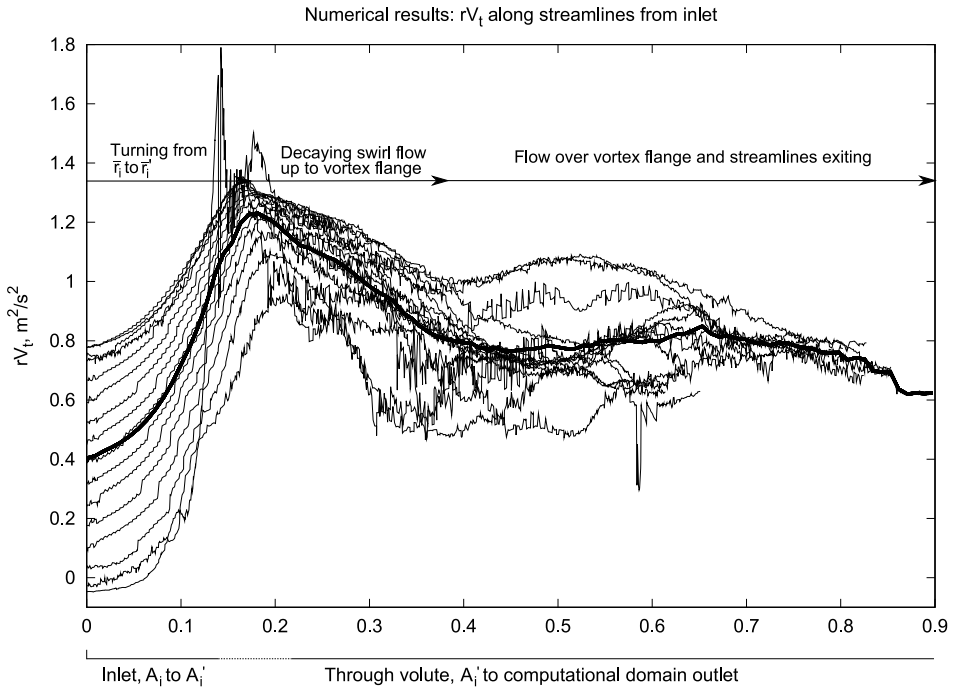

(a) rV_t variation along streamlines through the N_S176 volute emanating from cross-inlet rake, with their mean shown as a heavier line

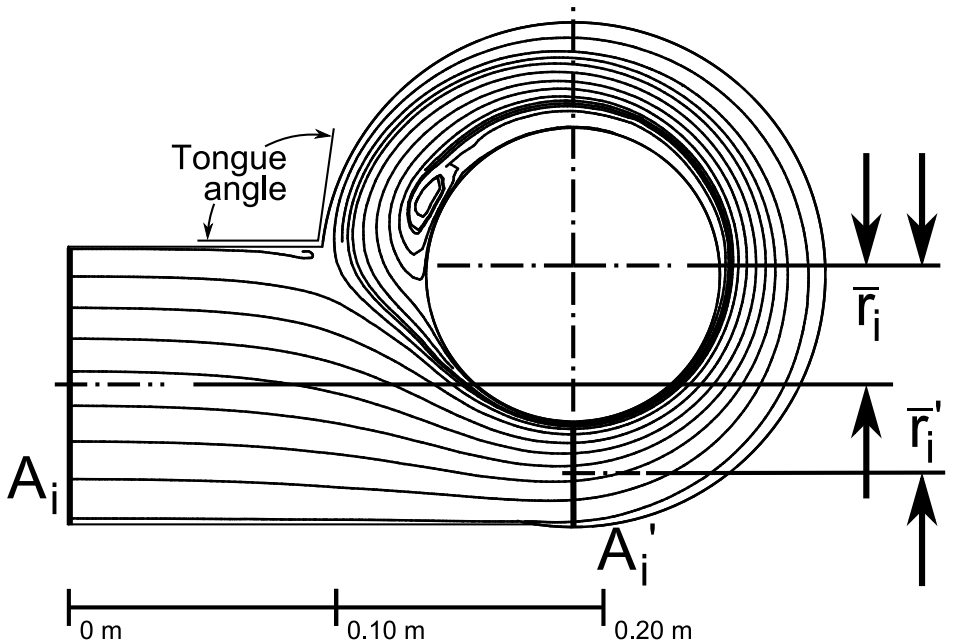

(b) In-plane streamlines in a cut-plane passing through the N_S176 volute's inlet at mid-Z

Figure 2.32: The effect of internal turning in the N_S176 volute on bulk streamtube rV_t: an initial increase as the flow is turned from the inlet pipe, represented by its mean radial offset, $\overline{r_i}$, to the space between the main volute wall and outlet pipe, represented by a more meaningful streamtube offset inside the volute, $\overline{r_i}'$, which is coincident with the peak of mean rV_t in sub-figure (a) near 0.2 m along the streamlines, followed by a steady decay due to the effect of wall shear stress

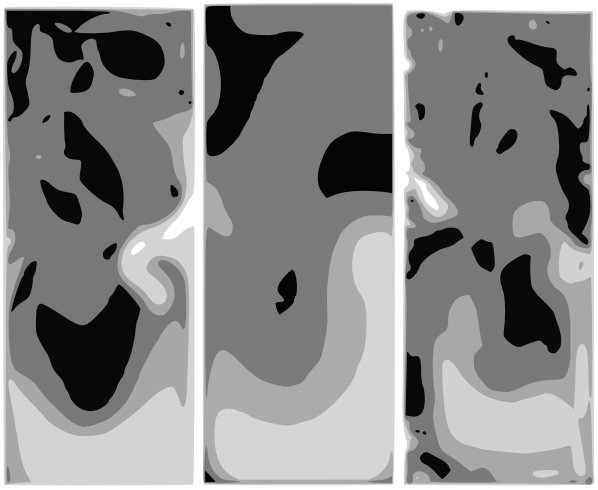

(a) Inviscid (b) $k\omega$ (c) RSM

Figure 2.33: Velocity contours over N_S544 inlet diffuser outlet plane, where the color limits and boundaries are 0, 0.16, 0.33, 0.49, 0.66, and $0.82\overline{V_i}$ from black to white, respectively

2.8 Conclusions on Giddens volutes

In both volutes, which were of the contraction-swirl type, the exit swirl component was measured to be at least 1.7 times what would be predicted by the torque-free assumption. The best computational results generally agreed with the measured result. The computational models of flow through the two volutes were validated based on F_{AM}.

Postprocessing revealed the velocity magnitude along streamlines passing through the N_S176 volute as shown in Figure 2.32 and suggested three main sources of torque on the flow passing through contraction-swirl STIVs. These three factors combined to invalidate the torque-free assumption for the two volutes considered for this experiment.

1. When present, diffusers installed upstream of a volute will reduce angular momentum, but to an unknown degree.

2. Angular momentum increased between the inlet pipe and the volute outlet due to the mean streamtube radius increasing as well as the mean streamtube velocity increasing or staying constant. This inviscid phenomenon was due to a pressure gradient across the width of the inlet pipe near the inlet-annulus transition, and ultimately the contraction-swirl inlet geometry.

3. Angular momentum decreased as it swirled in the annular space before leaving along the volute axis. This viscous phenomenon was attributable to wall shear stress.

Regarding the first point, the diffuser in the N_S544 volute was an example of an overly-agressive design. The divergent angle of the upper and lower wall Flow separated immediately on its upper wall and it achieved negligible deceleration of the flow. In this case, the diffuser was seen to be of limited value and a hindrance to analysis of the volute swirl characteristics. In any case it is preferable to avoid unnecessary diffusion and have monotonic acceleration between the inlet and the leading edge, and then monotonic deceleration from the runner trailing edge to the tailwater.

Regarding the second point, a contraction swirl STIV should be avoided due to the unpredictable effect on swirl. If a contraction swirl volute is required, the angular momentum of the flow will likely increase through the volute, i.e. $F_{AM} > 1$. As a first approximation, $F_{AM} \approx \frac{\overline{r_i}'}{\overline{r_i}}$, referring to Figure 2.32.

Regarding the third point, the axial length of the volute should be minimized in order to keep the effect of wall shear stress on gross angular momentum small.

The effect of each of these factors on angular momentum may be approximated analytically or estimated empirically, but the factors are best avoided altogether to keep the volute a simple and efficient component.

2.9 A novel volute

Following a period of brainstorming on what a volute which addresses the aforementioned issues might look like, the design shown in Figure 2.35a was conceived and analyzed using Fluentwithin CFX Workbench (Ansys, Inc., Canonsburg, PA, USA) to determine its outlet flow distribution and pressure loss. Figure 2.34 is an interactive 3D model of the volute.

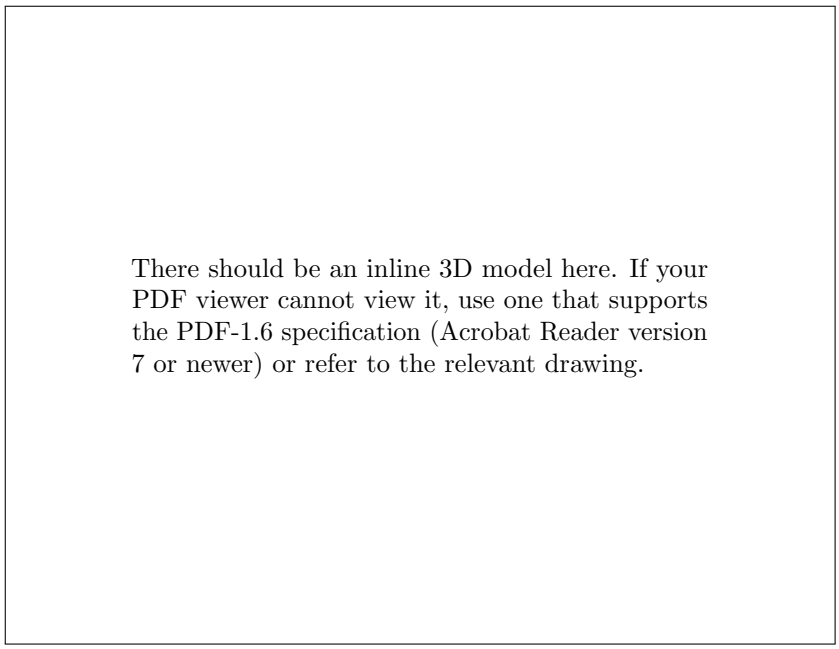

Figure 2.34: Volute model (`../common/volute_try2_no_hw.U3D`) Show controls / Close

The steady computational analysis utilized the $k\omega$ turbulence model, and the inlet turbulence intensity was set to 2 % of the mean velocity. The working fluid was water, with a Reynolds number based on mean conditions in the annular outlet passage of approximately 2.5×10^5. Wall functions were used in the near wall region, with an appropriate $\overline{y^+}$ of 100.[1] The geometry in Figure 2.35a was meshed using the Hexcore scheme in Gambit.

Some modifications were required to achieve a uniform, steady, axial outlet velocity distribution. The main features of the finalized volute are summarized here:

A large rectangular inlet replaced a penstock connection. The head of the N_S650 was low enough that the turbine may be placed at the headwater, terminating an open channel. This had the advantage that the streamlines were accelerated through the volute, improving its efficiency.

A pinched end rather than a square or semi-circular shape was required to avoid unsteady vortex shedding caused by flow past the runner mast. The shape remained simple enough to be rolled from sheet.

A 'flow-fence' was required to redistribute flow more uniformly between the upstream and downstream side of the runner mast. The height and angle of this were varied while monitoring the resulting outlet velocity distribution.

A large radius contraction into the runner annulus requires a complex curve, but it was proposed that the shape could be well-approximated by sculpting a concrete insert with the steel volute. Due to the high velocities entering the runner volute, a smooth contraction is essential.

Computational results of the final design iteration included streamlines, shown in Figure 2.35b and 2.35c, and outlet velocity distributions, shown in Figure 2.35d and 2.35e. The predicted total pressure loss, normalized by mean outlet dynamic pressure, was 0.7. The steady computation was numerically well-behaved and all normalized residuals converged to less than 10^{-3}.

Following the rapid design and analysis of a volute which appeared to overcome the unpredictability and loss of the N_S176 and N_S544 volutes, focus turned to how the decision to bias swirl away from the volute and into the draft tube would affect draft tube pressure recovery.

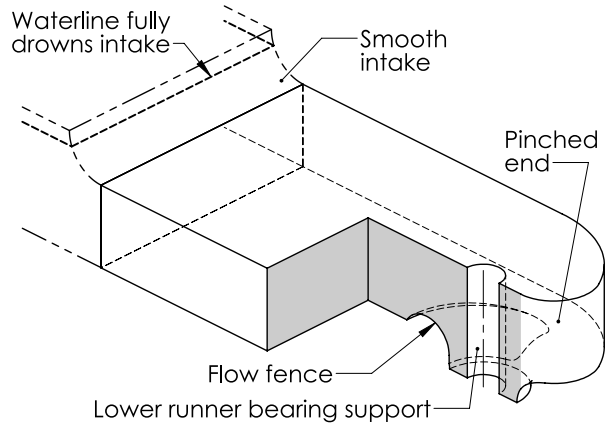

(a) Features of the adapted volute

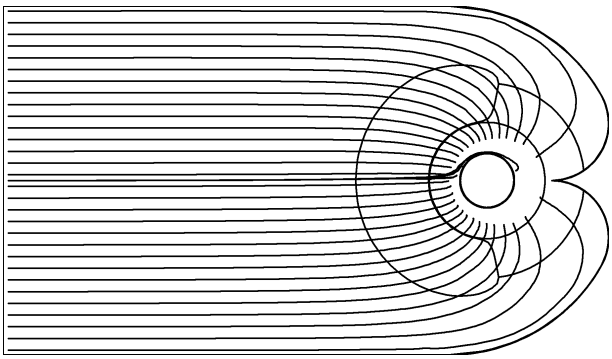

(b) CFD streamlines of the adapted volute from above

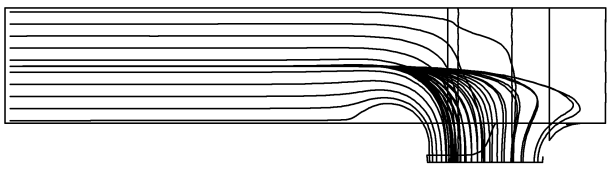

(c) CFD streamlines of the adapted volute from the side

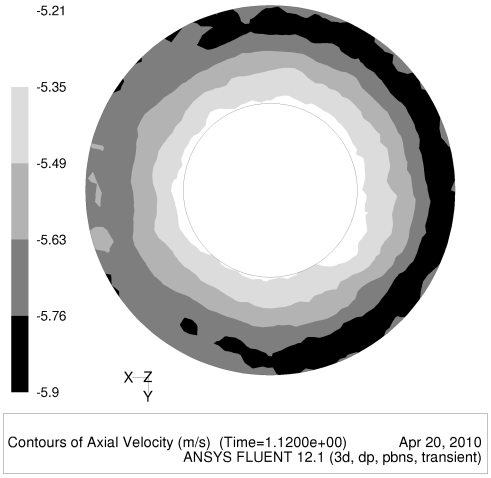

(d) Adapted volute outlet axial velocity contours, where positive is upstream

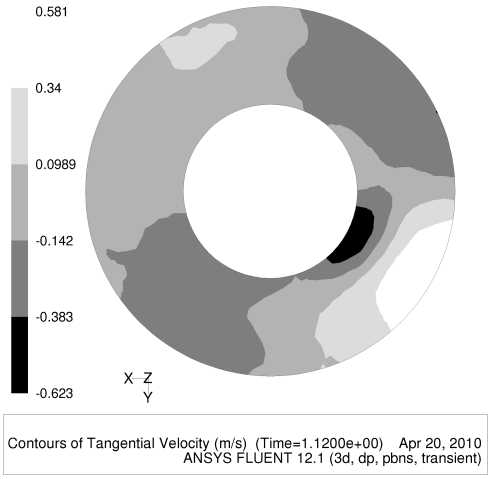

(e) Adapted volute outlet tangential velocity contours, where positive is counter-clockwise. The x-axis points towards the volute inlet, and the y-axis points to the right for streamlines entering the volute.

Figure 2.35: Adapted volute design, cut away to show internal detail. The flow-fence helps distribute flow evenly around the runner annulus while incurring minimal loss. The 'pinch' of the double-radius end was required to prevent the formation of an unsteady vortex street behind the bearing support. A smooth, fully-drowned intake should be used to minimize loss and inlet velocity profile variation.

Chapter 3

The conical draft tube

A net angular momentum change across the runner is the mechanism by which a turbine extracts energy from a fluid stream. In water turbines, swirling flow typically enters the runner from the volute or guide vanes, and leaves axially into the draft tube which minimizes the velocity leaving the runner. It was hypothesized that the swirl may be biased instead into the draft tube maintaining the same net angular momentum difference without an overall penalty. The literature disagreed on the effect of inlet swirl on conical diffuser pressure recovery.[52, 66] Furthermore, the sensitivity of pressure recovery to changes in inlet conditions reduced the generality of available data. Analysis of the diffuser geometry and conditions particular to the N_S650 prototype was therefore proposed to clarify the effect of swirl. Computational study on the effect of swirl on conical draft tubes using N_S650 boundary conditions confirmed claims in the literature that swirl may improve the pressure recovery of otherwise stalled diffusers, although it was unlikely that swirl would improve the maximum possible pressure recovery obtained with uniform axial inlet flow and a diffuser full angle of $2\theta_d \approx 7°$.[52]

This chapter introduces the purpose and theory of the conical diffuser including the effect of an increase in area on the swirl component, explains the origin of the zero-exit-swirl paradigm for water turbines and why its relevance shrinks with increasing specific speed, presents a computational analysis of the effect of swirling inlet flow on the pressure recovery of a conical diffuser for a range of cone angles, and concludes that in light of poor numerical convergence and the uncertainty in the literature, a conservative design is preferred for the N_S650 prototype.

Diffusers, known as draft tubes in the context of hydraulic turbines, are found in fluid circuits wherever the energy of a high-velocity flow is worth conserving. This is relevant because in high specific speed turbines, the dynamic head in the runner is a significant fraction of the net head. If this energy is mishandled it is easily lost, and the overall efficiency of the turbine suffers.

The head and flowrate of a site are fixed, but design speed, which is the machine's contribution to specific speed, may be varied. For a machine turning a mill under a low head and large flowrate, a waterwheel may provide the most useful high-torque, low-speed power directly. When 50 Hz or 60 Hz alternating current electrical power is the desired output, N, and therefore specific speed is maximized because it reduces the size of the machinery and the number of generator poles required. The downside of increasing specific speed is higher fluid velocity.

Figure 3.1 shows how the dynamic head in a turbine grows with specific speed, with measured data of Mr. Giddens's propeller turbines and the N_S650 prototype overlaid. The curve is similar to that found in the European Small Hydro Association's design guide[9]. The entire range of specific speeds shown on Figure 3.1 may be handled by propeller turbines, which shows why even lower specific speed designs, such as radial, mixed-flow, and Pelton wheels, may perform efficiently with no draft tube at all. The importance of the draft tube grows quickly as specific speed approaches 650, where roughly half of the site energy requires diffusion to recover.

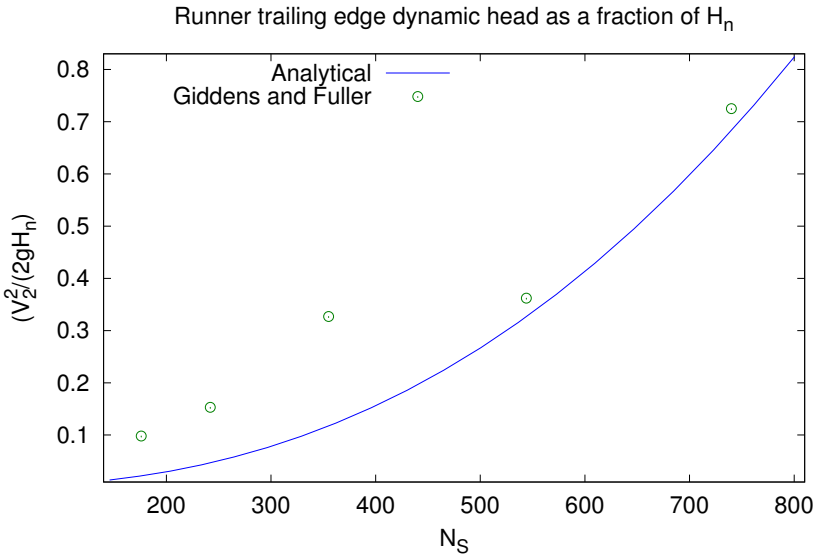

Figure 3.1: How dynamic head grows with specific speed

3.1 Diffuser theory

A diffuser is a stationary component which reduces the velocity of the fluid flowing through it. The resulting pressure increase may be approximated by assuming no energy loss and applying conservation of mass and conservation of energy between the diffuser inlet and outlet. The outlet of a propeller turbine is annular, meaning the conical diffuser is most appropriate. Figure 3.2 shows the shape and basic dimensions of such a diffuser. Conical diffuser proportions are described by length and area ratios, given in Equations 3.1 and 3.2.

$$L_R = \frac{N}{R_1} \tag{3.1}$$

$$A_R = \left(\frac{R_2}{R_1}\right)^2 \tag{3.2}$$

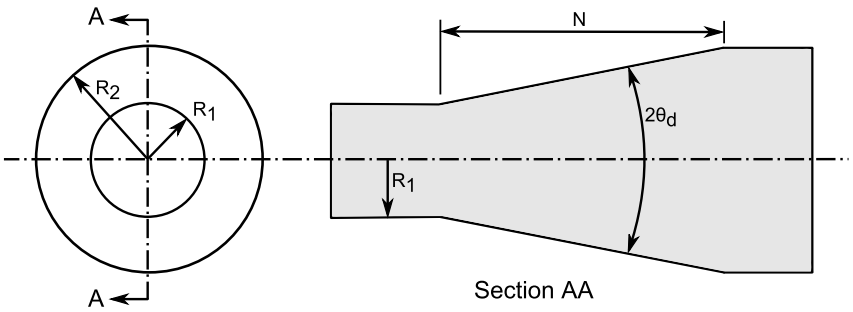

Figure 3.2: Conical diffuser geometry, where flow is from left to right in the section view

3.1.1 Ideal diffusion of the axial velocity component

The fluid velocity downstream of a propeller turbine is generally axial, meaning the energy embodied in tangential velocity is small. However in the case of the N_S650 prototype, with $B_S = 1$, the tangential velocity entering the diffuser will be non-zero by design. The parameter B_S will be introduced later in Section 3.2. Diffusion of the tangential component is separable and for now the focus is on the axial

velocity component only.

Water is an incompressible fluid, meaning $Q_1 = Q_2$, and if mean conditions are taken over the inlet and outlet, $V_1 A_1 = V_2 A_2$. In the ideal case no energy is added or lost through the diffuser, so the state of the fluid along streamlines is given by the Bernoulli equation, Equation 3.3.

$$z + \frac{p}{\rho g} + \frac{V^2}{2g} = \text{constant} \tag{3.3}$$

Decreasing stream velocity through the diffuser results in an increase in static pressure. This increase in static pressure along streamlines is relative, however. Since the diffuser exit is submerged in the tailwater and the exit flow is subsonic and shock-free, the absolute static pressure at the diffuser exit remains equal to the hydrostatic pressure at that depth in the tailwater. The change of static pressure through the diffuser appears as a decrease in the static pressure at the diffuser inlet. This decrease in pressure on the downstream side of the runner is the energy-saving function of the draft tube; dynamic head which would otherwise be exhausted into the tailwater is effectively added to the static head which acts across the runner.

The pressure recovery coefficient, C_p, defined in Equation 3.4, is the ratio of the static pressure increase to inlet dynamic pressure, where an overbar indicates the area-weighted average of the variable underneath. It is the most important performance measure of the draft tube.

$$C_p = \frac{\overline{p}_2 - \overline{p}_1}{\overline{p_{d1}}}, \tag{3.4}$$

The two limits of diffuser performance are:

$\boldsymbol{C_p = 0}$ which is a throttling valve, where total pressure decreases by the difference in mean dynamic pressure from inlet to outlet and static pressure is unchanged, and

$\boldsymbol{C_p = 1}$ which is an ideal diffuser that decelerates the inlet flow to a uniform outlet velocity distribution of zero velocity with no loss of total pressure causing static pressure to increase by the dynamic pressure at the diffuser entrance.

An ideal diffuser may be considered a control volume with one inlet and one outlet, where the ideal pressure recovery coefficient, C_{p_i}, is a function of A_R alone, as defined in Equation 3.5. Equation 3.5 is derived from Equation 3.3 and will always give the maximum attainable pressure recovery due to the velocity components in the meridional plane for any diffuser of a given area ratio. A common area ratio for an industrial diffuser is 4, with an ideal pressure recovery of approximately 0.94, meaning 6 % of inlet dynamic head remains at the exit. By comparison, large water turbines commonly have diffusers with area ratios up to 6 or 8.

$$C_{p_i} = 1 - \frac{1}{{A_R}^2} \tag{3.5}$$

For real diffusers, A_R is not the only independent variable of interest; A_R determines the maximum expected pressure recovery, while several other factors will cause the real pressure recovery to be less. Low Reynolds numbers, low turbulence, circumferential non-uniformity, and thick boundary layers should all be avoided at the inlet to a diffusing section, as they all exacerbate regions of low-velocity fluid near the wall, encouraging boundary layer separation which counteracts pressure recovery.[40] At a Reynolds number of 10^6, comprehensive performance maps of conical diffusers with axial inlet flow are available.[40] The data are presented as contour plots of C_p versus A_R and L_R. Another good reference is published by Creare.[47] Other properties affecting C_p are wall roughness, the smoothness of the transition from inlet pipe to conical section, downstream components, and vibration to name a few.

The optimum cone angle of a diffuser with axial inlet flow is about $2\theta_d = 7°$.[40] In larger turbines, space for the draft tube is limited, leading to the addition of bends or smaller area ratios. For microhydro turbines, such a limitation does not necessarily exist. The length of the draft tube as a function of runner

diameter, diffuser angle, and area ratio is given in Equation 3.6.

$$N = \frac{d_1\left(\sqrt{A_R} - 1\right)}{2\tan\theta_d} \tag{3.6}$$

In the case of the N_S650 prototype, the length of a diffuser with an area ratio of 4 was slightly less H_n, so it was reasonable to place the turbine near the headwater and orient the draft tube vertically underneath.

3.1.2 Ideal diffusion of the tangential velocity component

The main function of the conical diffuser is to reduce the axial velocity component. The required increase in area also increases the mean radius of the fluid stream. If the flow entering the diffuser is swirling, this increase in radius causes a reduction of the tangential velocity component, due to conservation of angular momentum. This section discusses this phenomenon, and updates Equation 3.5 to include its effect. No mention of this effect was found in the literature.

Although the draft tube exerts no torque on the flow, by increasing the mass moment of inertia of the fluid stream its tangential velocity will decrease to conserve angular momentum. Axial velocity is reduced in inverse proportion to cross-sectional area. By the same increase in area, the mean radius of the fluid stream is increased proportional to diameter, which is proportional to the square root of area. This increases the stream's mass moment of inertia, decreasing its tangential velocity proportionally, conserving angular momentum.

Equation 3.5 applies for axial flow and must be amended to include the reduction of the tangential velocity just described. Returning to Bernoulli's equation, C_{p_i} for one-dimensional, horizontal, swirling, inviscid flow through a conical diffuser will now be derived as a function of area ratio and the angle the incoming flow makes with the axial direction. Equation 3.4 is restated here as the starting point.

$$C_p = \frac{\overline{p}_2 - \overline{p}_1}{\overline{p_d}_1}$$

Total pressure is defined as the sum of static and dynamic pressure, where dynamic pressure depends on the absolute magnitude of the velocity vector.

$$p_t = p + \frac{\rho|V|^2}{2} \tag{3.7}$$

Next, Equation 3.7 is substituted for the two instances of p in Equation 3.4, and the equation comes to define the ideal case, given the stated assumptions about constant total pressure.

$$C_{p_i} = \frac{p_{t2} - \frac{\rho|V_2|^2}{2} - p_{t1} - \frac{\rho|V_1|^2}{2}}{\frac{\rho|V_1|^2}{2}} \tag{3.8}$$

which simplifies to

$$C_{p_i} = 1 - \left(\frac{|V_2|}{|V_1|}\right)^2 \tag{3.9}$$

Equation 3.9 is valid for axial or swirling flow, and would lead to Equation 3.5 if only the axial velocity component were considered. Next, $|V|$ is replaced by the axial and tangential velocity components, both written in terms of the diameter. Conservation of angular momentum is used to write the exit tangential velocity in terms of the inlet tangential velocity and the diameter ratio.

$$C_{p_i} = 1 - \frac{\left(\frac{4Q}{\pi d_2^2}\right)^2 + \left(\frac{d_1}{d_2}V_{t1}\right)^2}{\left(\frac{4Q}{\pi d_1^2}\right)^2 + V_{t1}^2} \tag{3.10}$$

Rather than leave V_a and V_t as separate components, V_t is rewritten as a function of V_a and α, which is

the angle that $\vec{V}$ makes with the axial direction.

$$\tan(\alpha) = \frac{V_t}{V_a} \tag{3.11}$$

The relation of Equation 3.11 is then substituted into the instances of V_a in Equation 3.10.

$$C_{p_i} = 1 - \frac{\left(\frac{4Q}{\pi d_2^2}\right)^2 + \left(\frac{d_1}{d_2}\frac{4Q}{\pi d_1^2}\tan\alpha\right)^2}{\left(\frac{4Q}{\pi d_1^2}\right)^2 + \left(\frac{4Q}{\pi d_1^2}\tan\alpha\right)^2} \tag{3.12}$$

Finally, the pressure recovery of an ideal conical diffuser with swirling inlet flow is given in Equation 3.13, where A_R is the diffuser's area ratio, $\left(\frac{R_2}{R_1}\right)^2$.

$$C_{p,\mathrm{sw.}_i}, = 1 - \frac{1}{A_R}\frac{1 + A_R\tan^2\alpha)}{1 + \tan^2\alpha} \tag{3.13}$$

It collapses to Equation 3.5 when $\alpha = 0$.

Figure 3.3 presents the theoretical error of using the original, axial-flow formulation over a range of area ratios and swirl angles. Applying this data to the N_S650, where the absolute flow angle leaving the runner at mid-span is approximately 20°, and $A_R = 4$, the old formulation of C_{p_i} would predict about 0.02 too low. Since the dynamic head at the diffuser inlet is a little over half of turbine net head, this difference made to net efficiency is on the order of 1 %.

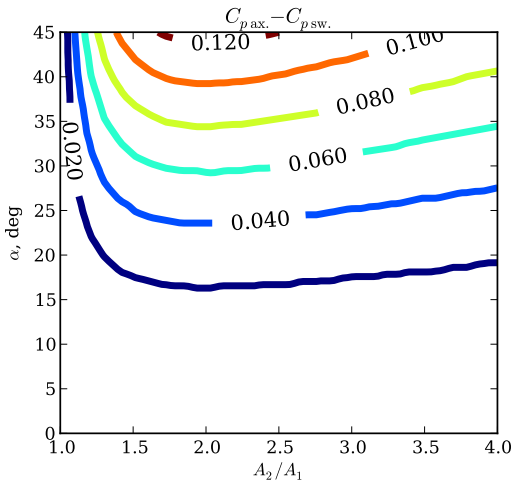

Figure 3.3: Error of using axial formulation of C_{p_i} with swirling inlet flow

3.2 The zero-exit-swirl paradigm and swirl bias

Turbines extract work by changing the angular momentum of a fluid stream opposite to the rotation of the runner. The torque on the runner is proportional to this momentum difference, which is independent of the absolute angular momentum of the fluid stream. For the same flowrate and torque, a runner may be designed for a range of inlet and outlet swirls, as long as the difference between them remains constant. However, it is unusual for a water turbine to operate with anything other than axial flow leaving the runner on-design. Massey states, "The properties of the [reaction turbine] are such that, at the 'design point', the absolute velocity of the fluid leaving the runner has little, if any, whirl component." A reasonable label for this common design goal is the 'zero-exit-swirl paradigm'. The primary function of the paradigm is to minimize the absolute velocity of the fluid leaving the runner, minimizing the energy needing to be

recovered by the draft tube, and improving efficiency overall. Another expression of the paradigm is,

> ...the use of guide vanes immediately upstream of the runner is essential for achieving high efficiencies due to the reduction in draft tube swirl. Guide vanes induce swirl immediately preceding the runner, such that the fluid momentum change occurring across the runner results in a reduced tangential component of velocity in the draft tube, and hence reduced swirl loss.[58]

The designer still has the basic decision when specifying the volute, runner, and draft tube of how to bias the angular momentum difference across the runner. For example, say a turbine design specifies a runner torque of 1 N m. The change in angular momentum of the fluid stream as it passes through the runner is −1 N m, to satisfy the conservation of angular momentum. The zero-exit-swirl paradigm suggests that with no swirl leaving the runner, the angular momentum of the stream at the trailing edge should be 0 N m. The required angular momentum at the leading edge is then found from $0 - (-1) = 1$. Another way to achieve the same torque is to set angular momentum of the stream at the leading edge to 0 N m. The downstream angular momentum is then found from $0 - 1 = -1$. Both cases produce the same torque. The designer must be confident that the volute will produce the required runner inlet flow, and that the draft tube will accept the resulting exit flow without detriment to its performance.

A new parameter, swirl bias, abbreviated B_S, has been defined by the author to embody this design choice. Swirl bias is defined as the ratio of the runner outlet angular momentum to its total angular momentum change. It succinctly describes how this design choice affects all three components. It compliments the other parameters of 'reaction factor' and 'work coefficient' that describe the proportions of a 'simple' turbomachine stage velocity diagram.[66] A simple stage is one that is annular in shape with straight hub and casing walls, with negligible radial velocity, and with incompressible flow. Under these simplifications, the definition of swirl bias reduces to Equation 3.14.

$$B_S = \frac{V_{to}}{V_{to} - V_{ti}} \tag{3.14}$$

where the subscripts i and o denote the runner's inlet and outlet, respectively, and where V_t is positive in the runner's direction of rotation.

Figure 3.4 illustrates different values of swirl bias for a simple stage.

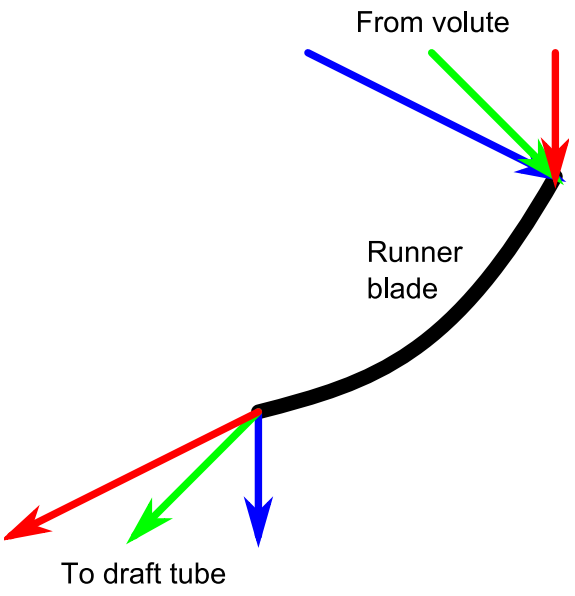

Figure 3.4: Absolute velocity vectors of flow through a generic runner at a range of swirl bias: $B_S = 1$ (in red), $B_S = 0.5$ (in green), and $B_S = 0$ (in blue)

There are two main reasons why the zero-exit-swirl paradigm may be foregone, and in particular why $B_S = 1$ makes sense for the N_S650 prototype or other high specific speed turbines. First, as specific speed increases, the difference between $B_S = 0$ and $B_S = 1$ in terms of exhaust energy shrinks. Figure 3.5 addresses the assertion that changing from $B_S = 0$ to $B_S = 1$ will increase the losses due to increased velocity entering the draft tube. The figure shows, for propeller turbines covering a range of specific speeds, that although the draft tube inlet dynamic head as a fraction of net head increases with specific speed, the difference between the $B_S = 0$ and $B_S = 1$ case shrinks. In fact, at a specific speed of 650, the difference between the two is several times less than the total kinetic energy. By comparison, designing for $B_S = 1$ at a specific speed of 300 would double the fraction of net head entering the draft tube versus the $B_S = 0$ case. The line for $B_S = 0$ is the same data as was shown in Figure 3.1. As specific speed increases, the advantage of designing for $B_S = 0$ shrinks.

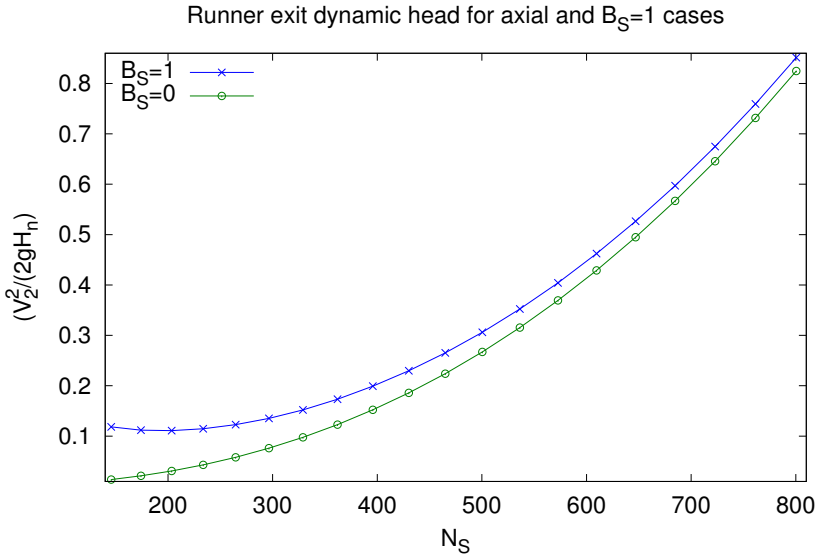

Figure 3.5: Dynamic head entering draft tube as a fraction of net head for $B_S = 0$ and $B_S = 1$

The quote at the beginning of this section recommending the use of guide vanes was taken from a paper regarding a propeller turbine of $N_S = 369$.[58] Figure 3.1 shows that the penalty due to loss of swirl energy at that specific speed is roughly $0.05H_n$, or a reduction of 5 % of net efficiency. If the turbine is to operate at fixed conditions, and the loss incurred by the volute or guide vanes is more than the penalty estimated as the difference between the two lines in Figure 3.5, then $B_S = 1$ is justified.

Secondly, swirl entering the draft tube on-design may actually improve the diffuser C_p.[52] While an ideal diffuser produces a uniform outlet velocity distribution, the uniformity of outlet flow in real diffusers downstream of turbines is hampered by two factors:

1. boundary layer separation from the diffuser wall results in near-wall fluid slowing or recirculating,[40] and

2. the presence of the hub encourages slow and possibly recirculating flow along the centerline.[55]

Swirl has been proposed as a method of energizing the flow near the wall, that is, increasing the turbulent mixing between the turbulent and laminar regions. The energy cost of this mixing, due to the dissipation of energy by turbulent eddies, may be smaller than the energy savings resulting from an increased overall C_p.[52]

To paraphrase the discord in the literature on the effect of swirl on diffuser pressure recovery, two quotes are presented. Wilson states,

> A small degree of swirl in the inlet flow of a diffuser may cause a sharp drop in performance and perhaps complete flow breakdown[66].

But Senoo disagrees,

> By adding a moderate swirl the displacement thickness of boundary layer along diffuser wall became smaller ... , as a result the pressure recovery was increased.[52]

Those quotes typify the literature review[66, 52, 30, 56, 39, 42, 59, 12, 14, 41, 46] on the effect of swirl on conical diffuser performance, which prompted the computational analysis which follows.

3.3 Computational analysis

The setup and results of a series of computational analyses of a conical diffuser will now be presented. The results are intended to show the effect of swirling inlet flow versus the normal axial flow, i.e. $B_S = 1$ versus $B_S = 0$, on a conical diffuser of a range of cone angles in order to help select an appropriate value of θ_d for the N_S650, and also determine if $B_S = 1$ is a viable design option.

Despite the sources of diffuser performance data available in the literature, which give pressure recovery values for different Reynolds number, length ratio, area ratio, and even several different inlet velocity profiles, i.e. fully-developed or following a smooth contraction, the inlet conditions of the N_S650 diffuser are different yet again. There are three main factors which differentiate the available data from the current scenario:

1. the swirling flow of a $B_S = 1$ design,
2. the presence of a runner hub just upstream, meaning the inlet flow is far from uniform, and
3. the unsteadiness of flow leaving a rotating runner.

The following computational analysis will address the first two factors. Unsteady inlet conditions was judged to be of secondary importance and not worth the additional modeling effort.

3.3.1 Computational domain

The computational domain considered here encompassed the part of the turbine between the trailing edge of the runner and the tailwater. This included the annular space of the runner, followed by an expansion to the circular cross-section of the diffuser, followed by the more gradual expansion of the diffuser itself, then a straight section, and finally an outlet of circular cross-section. Figure 3.6 shows the geometry of the diffuser computational domain as used for the subsequent analyses. During analysis θ took values of 3.5°, 5°, 7.5°, and 10°. All other proportions remained fixed: $\frac{L_o}{R_1} = 8$, $\frac{R_h}{R_1} = 0.5$, $\frac{R_c}{R_1} = 0.176$, $\left(\frac{R_2}{R_1}\right)^2 = 3$.

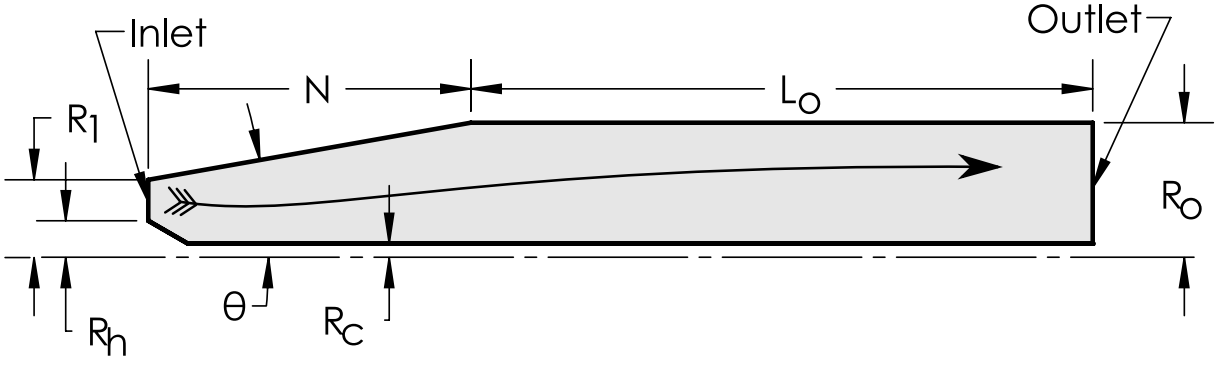

Figure 3.6: Diffuser computational domain geometry shown to scale, where $\theta_d = 10°$

The region between the runner trailing edge and draft tube outlet contains two distinct parts: the sudden expansion following the truncation of the hub and the gradually increasing area of the diffuser proper. Here, it was proposed to treat these two parts separately. The reason for this was that while the gradual expansion of the diffuser should efficiently recover pressure, sudden expansion may be expected to produce very little pressure recovery for the same change in area. The mechanics behind efficient diffuser operation may be approximated by frictionless flow whereas the dissipation which happens following a sudden expansion is inherently viscous and turbulent. Diffuser area ratios quoted here were calculated from Equation 3.2, and do not use the true, annular inlet area. The magnitude of dynamic head entering the diffuser in the N_S650 means the worst-case losses due to the sudden expansion from the runner annulus to the diffuser's circular cross-section are roughly one third of net head. Chapter 5 concludes that reducing these sudden expansion losses is one of the best candidates for raising overall efficiency.

3.3.2 Modeling simplifications

Turbulent flow through an adverse pressure gradient is likely to be unsteady on a range of timescales and original attempts at modeling the flow as steady were unsucessful. First-order transient analysis was employed with a timestep of 0.05 s.

Given the computational requirements of analyzing eight cases, with resolved boundary layers, for thousands of time steps, a fully three-dimensional model was not acceptable. The domain was instead represented as two-dimensional and axisymmetric. A limitation of the CFX Workbench mesher, which was used to generate the meshes, meant that technically each mesh was a 1° wedge, one cell thick, with rotationally periodic boundaries on both of the wedge cut faces.

The origin of problems obtaining converged solutions were early on traced to the cells adjacent to the centerline. Unrealistic values of turbulent kinetic energy appeared in near-centerline cells just downstream of the hub and propagated downstream, corrupting most of the domain. For this reason, cells near the centerline were removed from subsequent meshes, and a tapered transition was added between the hub and the centerline. This improved the stability of the calculations considerably. The radius of the region removed was 15 mm, compared to the outlet radius of 147 mm, leading to an area reduction at the diffuser outlet of 1 %.

3.3.3 Boundary conditions

The diffuser computational domain was bounded by four types of surfaces, each with its own boundary conditions:

velocity inlet which defined axial, tangential, and radial velocity components, and turbulence properties,

outflow which accepted no inputs and was the suitable exit boundary for zones with a velocity inlet,

periodic which enforced the condition of axisymmetry, and

wall which formed the diffuser wall and also the centerline-cutout.

Velocity components and turbulence properties on the diffuser velocity inlet surface were defined as a function of radius only. The distributions were circumferentially averaged from the runner zone outlet upstream. Since the domain was axisymmetric, these boundary conditions were steady. Exploring the effect of a $B_S = 1$ design required two sets of inlet conditions: one representing the $B_S = 1$ case and one representing the $B_S = 0$ case. The boundary conditions in both cases were taken from the N_S650 $B_S = 1$ runner. The $B_S = 1$ cases used all three velocity components and turbulence parameters; the $B_S = 0$ cases set tangential velocity to zero everywhere on the inlet, otherwise it was the same. Figure 3.7 shows the velocity profiles used. Table 3.1 summarizes the two sets of boundary conditions.

B_S	$\overline{\alpha}$, °	N_R
1	17	2.2×10^5
0	0	2.3×10^5

Table 3.1: Diffuser inlet condition summary: B_S turbine swirl bias, $\overline{\alpha}$ mean absolute flow angle off-axial, N_R inlet Reynolds number defined using annulus width and mean inlet velocity magnitude

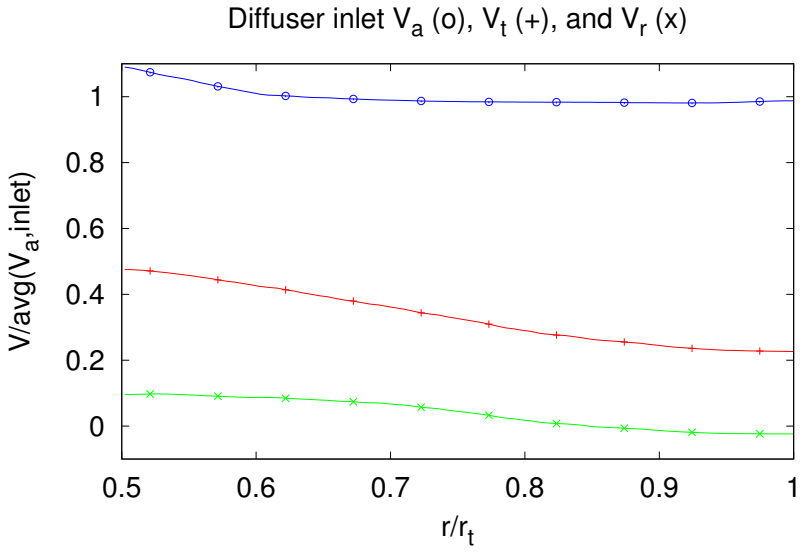

Figure 3.7: Draft tube inlet velocity distributions, normalized by mean axial velocity of 4.98 m/s

Figure 3.8 indicates the range of α seen at the diffuser inlet in the $B_S = 1$ case. The uniform-rV_t, or free-vortex, tangential velocity distribution, together with a nearly uniform axial velocity distribution, produced an absolute flow angle, α, roughly twice as large at the hub as at the tip.

The outflow boundary at the diffuser exit accepted no input. "Outflow boundary conditions in FLUENT are used to model flow exits where the details of the flow velocity and pressure are not known prior to solution of the flow problem."[1]

The periodic boundary-pair enforced a zero pressure gradient, and also a zero net flowrate which was consistent with rotational symmetry. Applying the periodic boundary condition to a domain which was one cell thick was equivalent to axisymmetry.

The diffuser wall was assumed no-slip. The walls which formed the taper downstream of the hub and the centerline cutout were assigned a shear stress of zero.

3.3.4 Fluid model

The fluid model in all cases was a variant of the Reynolds stress model (RSM). The key feature of the RSM is that the turbulent viscosity, the macro effect of turbulence, was not assumed isotropic as in more economical two-equation models. Resolving this anisotropy required a term for each of the six orthogonal shear stress terms, plus a scalar representing turbulent dissipation. Near a wall, the orientation of turbulence was perhaps somewhat organized by the lack of a wall-normal velocity, as well as the application of a shear stress on the fluid which is always facing upstream.[19] It was expected that this more rigorous modeling of turbulence in the near-wall region where boundary layer separation originates would yield better predictions of the velocity field downstream, and therefore the pressure field and C_p at the diffuser exit.

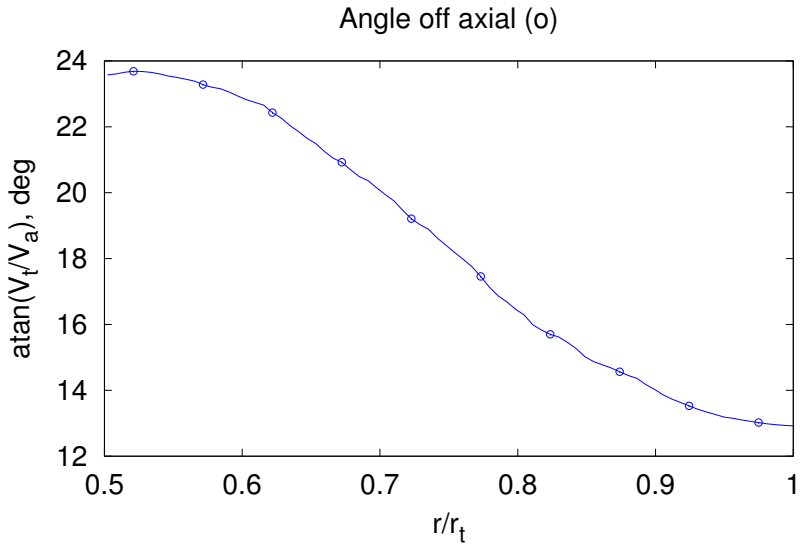

Figure 3.8: Diffuser inlet flow angle, α, for $B_S = 1$, comparable distribution to Wilson and Senoo. $B_S = 0$ is a uniform 0°.

					Discretization scheme			
$2\theta_d$	B_S	Fluid model	Cells	$\overline{y^+}$	Press.	Mom.	ω	RS
7°	0	RSM	90×10^3	0.2	SO	SOU	SOU	FOU
7°	1	RSM	90×10^3	0.2	SO	SOU	SOU	FOU
10°	0	RSM	57×10^3	0.1	SO	SOU	SOU	FOU
10°	1	RSM	57×10^3	0.1	SO	SOU	SOU	FOU
15°	0	RSM	57×10^3	0.1	SO	SOU	SOU	FOU
15°	1	RSM	57×10^3	0.1	SO	SOU	SOU	FOU
20°	0	RSM	46×10^3	0.5	SO	SOU	SOU	FOU
20°	1	RSM	46×10^3	0.5	SO	SOU	SOU	FOU

Table 3.2: Summary of diffuser computational analyses: $2\theta_d$ diffuser full angle, B_S runner swirl bias, $\overline{y^+}$ domain-averaged non-dimensional wall-adjacent cell height, *Press.* pressure, *Mom.* momentum, ω specific dissipation rate, *SO* second order, *FOU* first order upwind, *SOU* second order upwind, *RS* Reynolds stresses, *RSM* Reynolds stress method

3.3.5 Discretization of equations

Discretization refers to the way conditions in one cell are communicated to other neighboring cells; it makes assumptions about the real variation between cells that is being modeled. Higher-order discretization schemes should more realistically model large gradients between cells. The second-order discretization scheme (SO) was used for the pressure equation, second-order upwind (SOU) for momentum and ω, and first-order upwind (FOU) for the Reynolds stresses.

3.3.6 Meshes and wall treatment

The near-wall mesh is very important when modeling a component with an adverse pressure gradient where boundary layers grow and may then separate. When numerically modeling a wall-bounded turbulent flow, there were two options: to model the effects of the laminar-affected boundary layer on the adjacent turbulent flow or to resolve it. Despite the larger mesh size, the decision was made to resolve the boundary layer on the diffuser wall, that is, place cells near enough to the wall that there are several within the viscous sublayer. Table 3.2 summarizes $\overline{y^+}$ and other important parameters of the analyses carried out on the diffuser.

3.3.7 Results

The following results were obtained after nearly two thousand transient time steps and utilized increased under-relaxation to achieve numerical stability. In terms of C_p, all cases converged to a roughly steady state where the value of C_p at the final timestep was a good approximation of the time-averaged value. Figure 3.9 shows the values from the final timestep of each case.

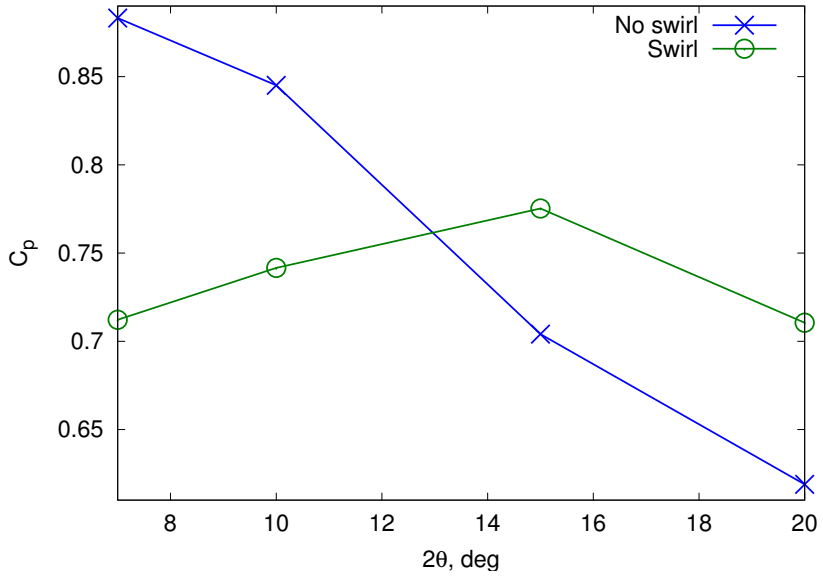

Figure 3.9: Computationally-predicted conical diffuser pressure recovery

Each $B_S = 1$ case resulted in slightly larger residuals than their corresponding $B_S = 0$ case. Diffuser angle was the biggest factor affecting convergence; the $2\theta_d = 7°$ and 10° converged to well below the accepted 10^{-3} criterion, but $2\theta_d = 15°$ and 20° cases failed to converge, limiting the usefulness of those data. Figure 3.10 traces the evolution of the continuity residual of each case over the last round of timesteps.

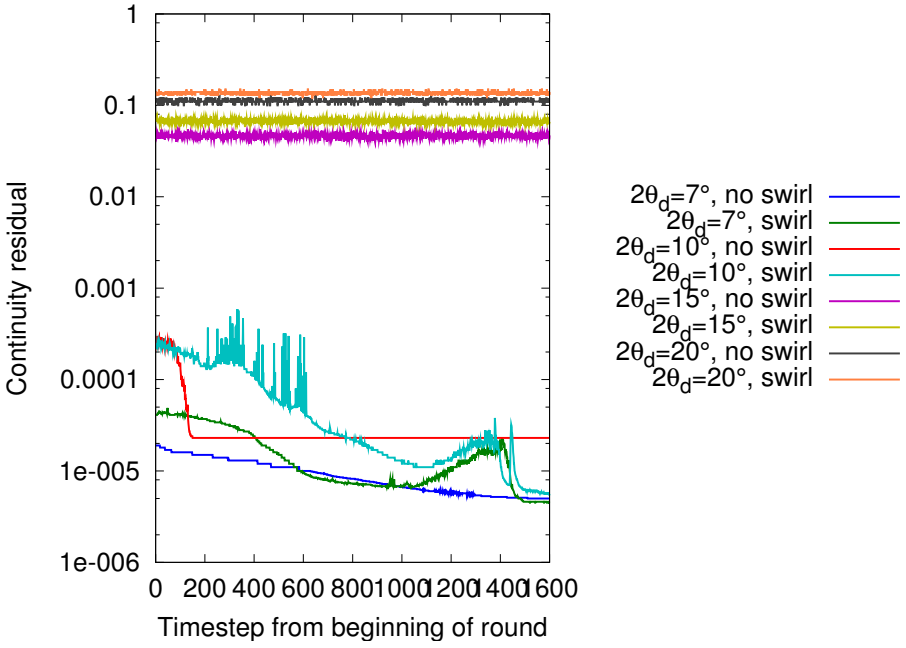

Figure 3.10: Numerical convergence history of diffuser continuity residual

Equation	Under-relaxation	
	Default	Round 14
Pressure	0.3	0.3
ρ	1.0	1.0
Body forces	1.0	0.8
Momentum	0.7	0.6
ω	0.8	0.4
μ_T	1.0	0.9
Reynolds stresses	0.5	0.6

Table 3.3: Under-relaxation summary: ρ density, ω specific dissipation rate, μ_T turbulent viscosity

There are three key points from Figure 3.9 to note:

1. The four $B_S = 0$ cases indicated good pressure recovery near $\theta_d = 3.5°$ and fully stalled flow at larger angles, as expected.[40]

2. The peak pressure recovery when $B_S = 1$ occurred at a larger value of θ_d than for $B_S = 0$, as was hoped.

3. Although $B_S = 1$ offered higher pressure recovery at larger values of θ_d, the peak C_p obtained was almost 0.1 less than in the case of axial flow.

The value of p_d used in the calculation of C_p was based on the magnitude of $\vec{V}_i$, not V_a.

Figures 3.11 and 3.12 present the streamlines corresponding to the results in Figure 3.9. In all cases, the flow immediately separated from the tapered runner hub, leading to a stagnant region along the centerline. Along the diffuser wall, Figure 3.11 shows how, without swirl, increasing $2\theta_d$ beyond 7° led to steadily growing boundary layer thickness. Between $2\theta_d = 10°$ and 15°, the boundary layer completely detached, creating a large region of recirculating flow. Downstream of this region, flow near the wall was more lethargic. Further increasing $2\theta_d$ to 20° moved the separation point further upstream, and the subsequent reattachment point further downstream.

Adding a swirl component to the inlet flow led to noticeable changes in the streamline patterns. Although the stagnant region along the centerline was larger than for $B_S = 0$, the boundary layer along the diffuser wall stayed thin and attached at larger values of $2\theta_d$, not changing appreciably up to 15°, then separating before 20°. In all $B_S = 1$ cases in Figure 3.12, the stagnant region along the centerline appeared larger than for $B_S = 0$. This may be an exaggeration since the number of streamlines shown along the centerline was very sensitive to small changes in the flow field near the separation point on the runner hub.

The uniformity of a diffuser outlet velocity distribution is related to the efficiency of its pressure recovery. Figure 3.13 gives the distributions of velocity magnitude from the final timestep of each of the eight analyses. Velocity was normalized by the mean outlet axial velocity which was 1.47 m/s in all cases. In good agreement with Figure 3.9, the $B_S = 0$, $2\theta_d = 7°$ case showed the velocity distribution closest to uniform. In contrast, $B_S = 0$, $2\theta_d = 20°$ showed the most distorted outlet flow with nearly stagnant flow near the wall and velocities near the centerline approximately 2.5 times the mean axial velocity. The other axial-flow cases, $2\theta_d = 10°$ and 15°, fell between those two cases, and all four $B_S = 0$ distributions crossed at almost exactly the same point near $r/R_2 = 0.6$. As mentioned earlier the convergence of the continuity residual of the $2\theta_d = 15°$ and 20° cases did not reach the 10^{-3} criteria, which led to outlet velocity distributions in Figure 3.13 indicating significant inlet-to-outlet flowrate discrepancies.

Figure 3.14 illustrates the evolution of C_p over many timesteps. Table 3.3 gives the final values of under-relaxation applied to each of the relevant equations.

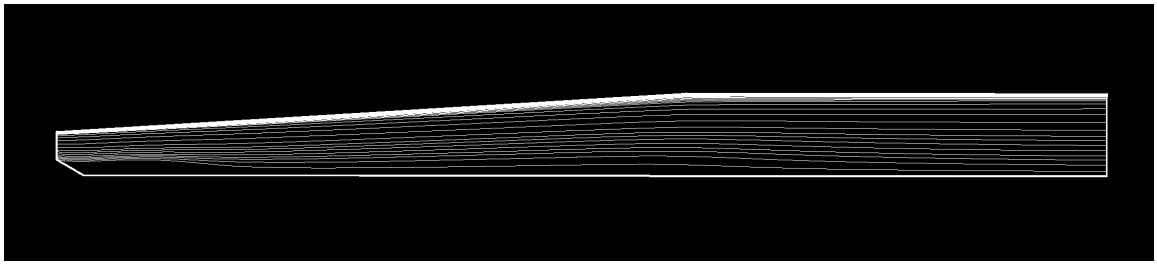

(a) $2\theta_d = 7^\circ$

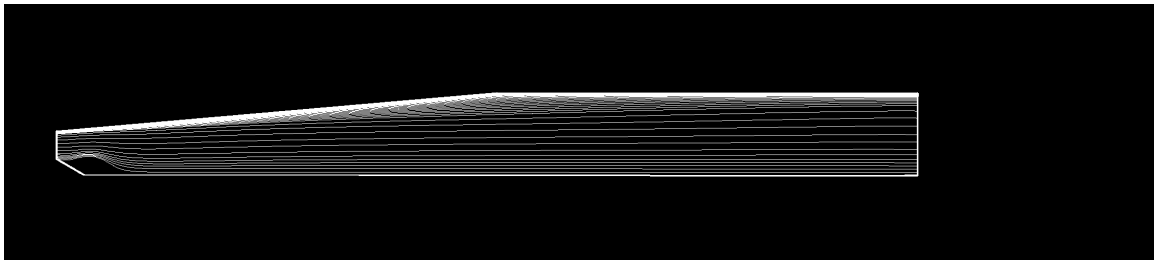

(b) $2\theta_d = 10^\circ$

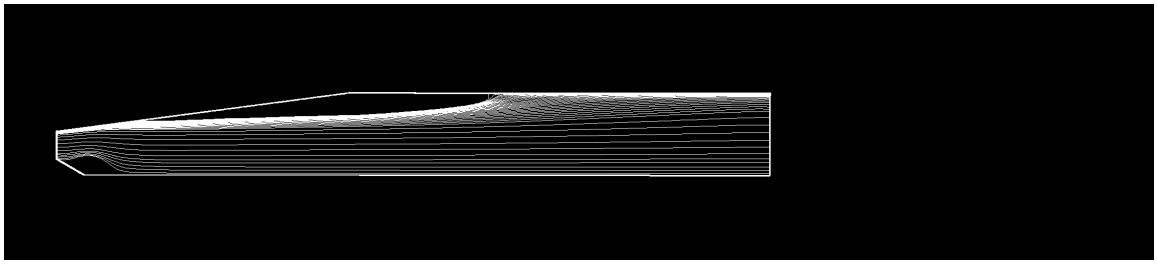

(c) $2\theta_d = 15^\circ$

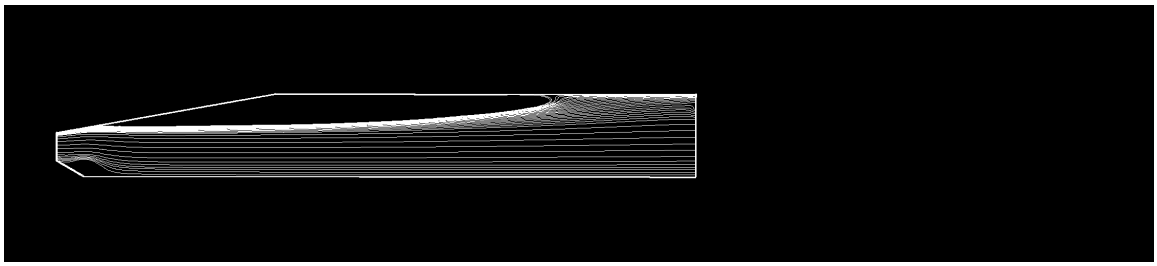

(d) $2\theta_d = 20^\circ$

Figure 3.11: Diffuser streamlines, $B_S = 0$

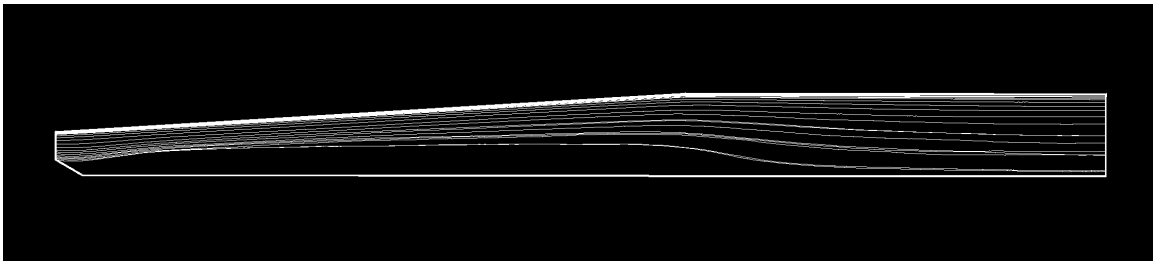

(a) $2\theta_d = 7°$

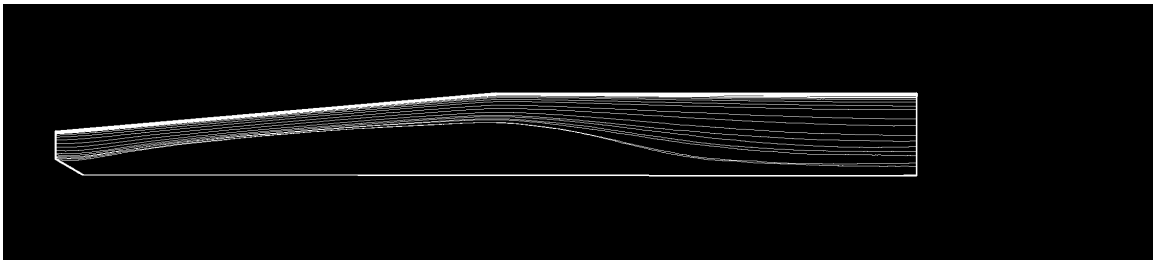

(b) $2\theta_d = 10°$

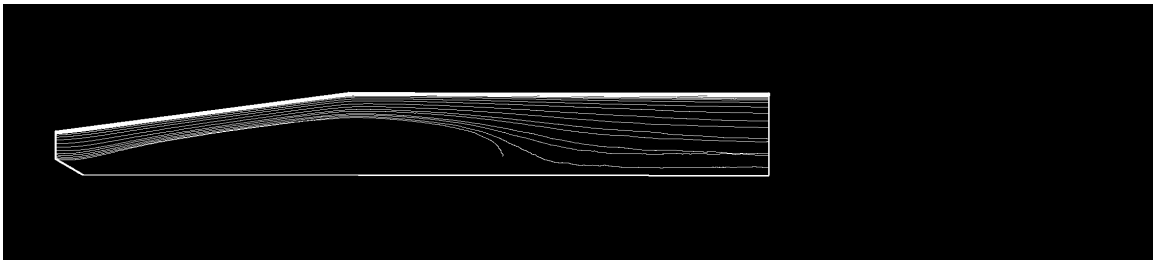

(c) $2\theta_d = 15°$

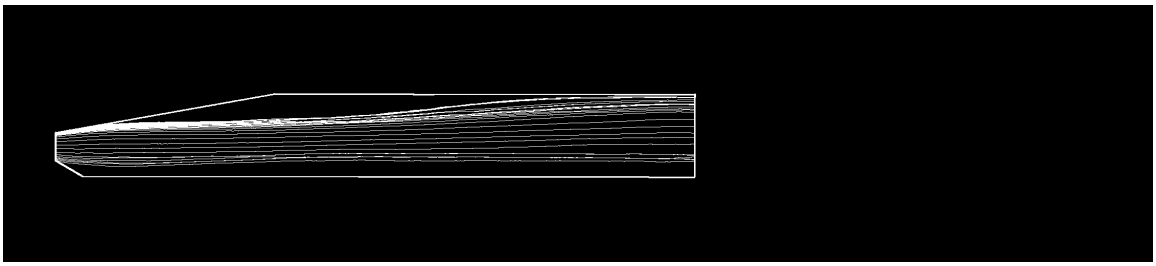

(d) $2\theta_d = 20°$

Figure 3.12: Diffuser streamlines, $B_S = 1$

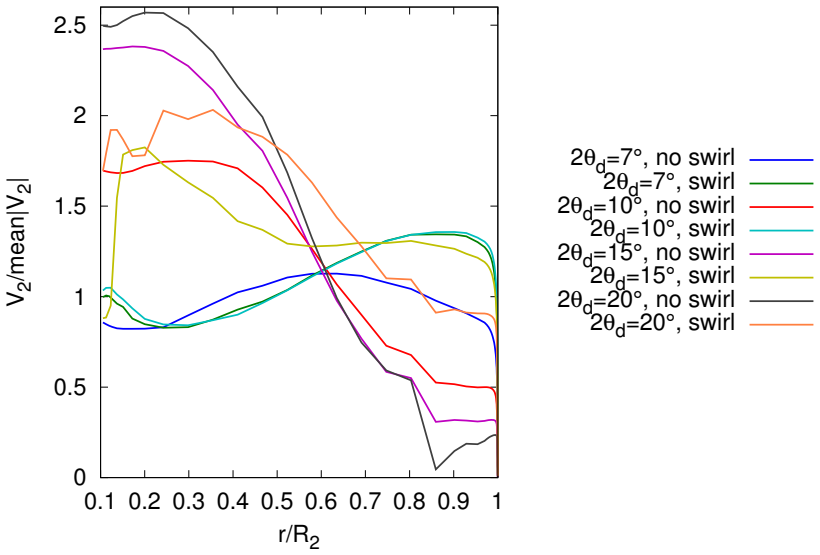

Figure 3.13: Diffuser normalized outlet velocity distributions

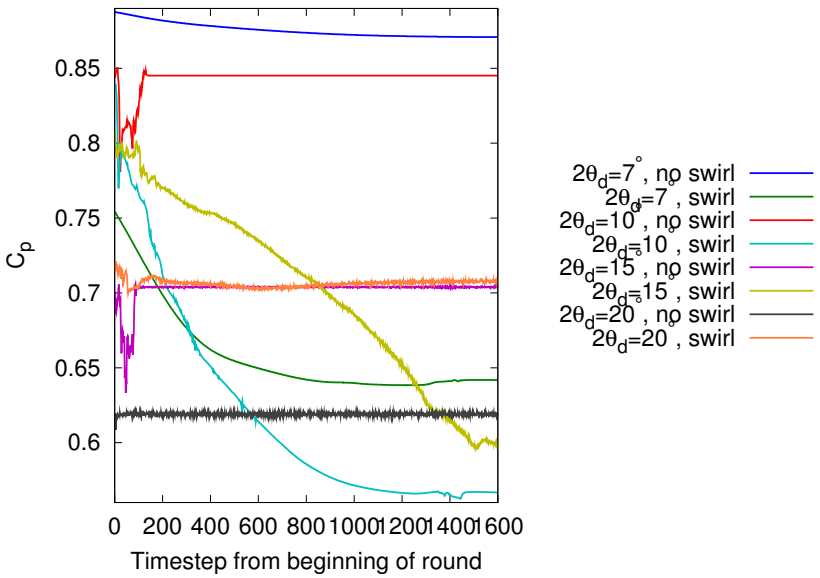

Figure 3.14: Convergence history of pressure recovery over time

3.4 Discussion and conclusions

The general trends in Figures 3.9 through 3.13 were in line with expectations that optimum pressure recovery of a conical diffuser with axial inlet flow would occur near $2\theta_d = 7°$. Furthermore, the hypothesis that swirl may improve the uniformity of outlet velocity distribution at values of $2\theta_d > 7°$ and therefore increase C_p appears somewhat vindicated.

For larger values of $2\theta_d$ where swirl might give real improvement over axial flow, numerical convergence was less than satisfactory. The shape of the predicted outlet velocity distributions in those cases may still be used with caution to infer the effect of swirl. In general, a clear answer to the question of the effect of swirl on diffusing flows remains elusive.

For the N_S650 prototype where higher efficiency was valued over a shorter diffuser, designing for $B_S = 1$ does not appear to have any clear benefits regarding the performance of the diffuser itself. However, swirl bias affects all three main turbine components, so rather than considering the diffuser in isolation, the question remains whether the decision to build a $B_S = 1$ turbine is an improvement overall, considering the sum of effects on all components.

Putting all trust in Figure 3.9, assuming $B_S = 1$, would dictate a diffuser full-angle of about 15°. In fact, Figure 3.9 would suggest that designing the N_S650 prototype for $B_S = 1$ and specifying the traditional $2\theta_d = 7$ degree would give a value of C_p 0.17 less than the maximum value of about 0.89 — a significant loss.

In light of the uncertainties of these computational results, however, a more conservative design has been specified. A conical diffuser of area ratio 4 and $2\theta_d = 7°$ based on existing data will be used in the $B_S = 1$ prototype. During testing of that prototype (see Figure 5.21), although it was not possible to distinguish between the losses attributed to the sudden expansion and the diffuser, the net C_p of the region downstream of the runner was found to be between 0.70 and 0.75. The measured value of C_p was then correlated to the mean inlet swirl angle, which could be varied by changing the runner speed. It showed a decrease with increasing swirl, consistent with a transition between the two left-most points of Figure 3.9. This provided some validation for the two analyses of $2\theta_d = 7°$.

Chapter 4

The flat-bladed runner

In light of conclusions regarding the volute and draft tube, the effects of a non-standard swirl bias on the design and performance of the N_S650 prototype runner were desired. A flat bladed runner in a straight-walled annulus was designed by applying blade element theory along the span of the blade, with a computationally-derived inlet velocity distribution. Computational analysis of the resultant runner at a range of speeds was carried out to characterize runner behavior prior to prototype construction. This analysis highlighted an inherent feature of the high specific speed velocity diagram: the relative magnitudes of axial velocity, blade peripheral velocity, and change in tangential velocity across the runner meant that geometric tolerances required during fabrication and the one-dimensional design method may not be sufficient to design a fixed-geometry microhydro runner.

In contrast to the two preceding chapters, which were essentially non-dimensional and dealt with more generally-applicable components, the runner has been designed specifically for the prototype which is the focus of the proceeding chapter. Given the organization of chapters, there is some unavoidable overlap between this chapter and the one which follows.This chapter steps through the process used to design a flat-bladed runner using the N_S650 runner as an example and presents results of its steady-state computational analysis.

4.1 Design

The runner is generally the most geometrically intricate part of any given turbine. Keeping a turbine simple is largely about keeping the runner simple. In short, at the design speed, the camberline at the leading edge should intercept the stream smoothly, while the trailing edge sets the exit angular momentum. The geometric properties of the intersection of a plane (the blade) and a cylinder (the streamtubes) allowed the correct blade angles to be met by adjusting the positions of the leading and trailing edges in the plane of the blade. A rotating, planar blade has a curved camberline relative to cylindrical streamtubes. Flat blades are especially well-suited to high specific speeds, where the camberline is nearly flat anyway.

The main differences between the prototype runner and a conventional runner were the resulting sweep due to being made from flat material. Whereas conventional blades rely on twist to produce a blade with the correct angles in a relatively compact space, with a span more or less perpendicular to the runner axis, flat blades take on a distinct aft sweep. This is a necessary symptom of their flatness. The process of choosing the blade setup angle, ψ, and shaping the leading and trailing edges will be covered in detail.

Three iterations of the runner design were spawned through design and analysis. The design section of this chapter focuses on the final iteration, **i3**. The comparison of the computationally-predicted performance of **i2** and **i3** is the focus of the second half of the chapter, and justifies **i3**. The differences between the iterations are now summarized.

i1 was designed prior to volute simulation, using an assumed inlet velocity distribution of uniform axial

velocity and zero tangential and radial velocities. No analysis was performed. It was used for checking blade shape.

i2 was designed using the outlet velocity distribution provided by computational analysis of volute.

i3 was the same as **i2** except with trailing edge angle, β_2, decreased by 2° in response to analysis of **i2**. This iteration was built for prototype.

First, several important definitions and assumptions integral to the runner design method are presented here. The leading and trailing edge stations are denoted by a subscript 1 and 2, respectively. Blade hub and tip are represented by a subscript h and t. Figure 4.1 shows a cylindrical hub with a single blade attached, with relative and absolute velocity vectors fixed to both the leading and trailing edge at the blade tip, where: $U = \omega r$ is local blade velocity; β is blade angle, where 90° is facing directly upstream; and δ is the trailing edge deviation, the angle between β_2 and exit velocity relative to the runner, V_2, rel. Other important runner dimensions not shown are the tip diameter, d_t, and hub diameter, d_h. Simplifications which applied to this runner and all of Mr. Giddens's propellers, are enumerated here:

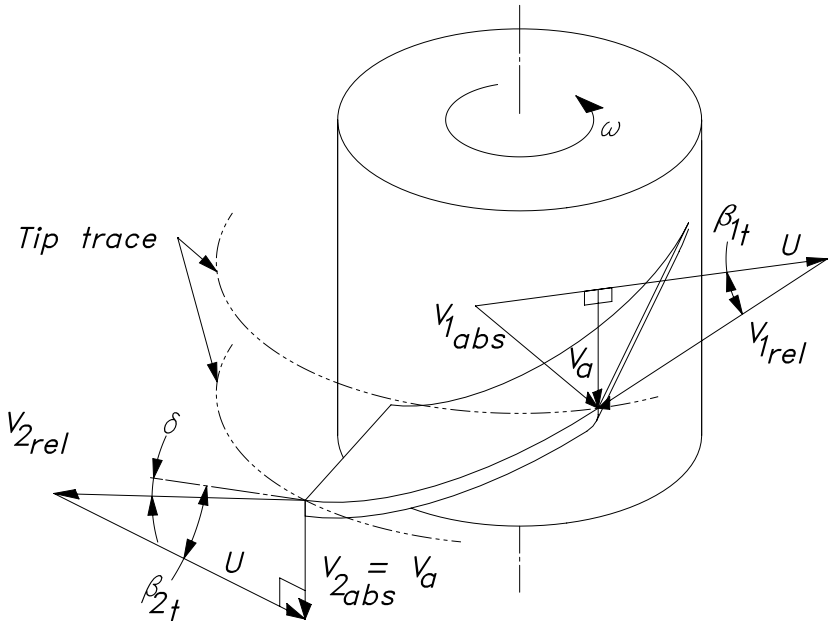

Figure 4.1: Runner velocity diagrams for the blade tip, shown for the more conventional $B_S = 0$

- flat blades, although shaping of the edges is allowed,
- cylindrical hub and casing and negligible radial velocities,
- operating conditions limited to one value of head and speed, where the design speed is set to 1550 rev/min to directly drive a 4-pole induction motor and produce 50 Hz, and
- assume an axial velocity distribution which is unchanged through runner.

Designing a runner for a given duty required several additional pieces of information:

1. dimensions of the bounding envelope,
2. flow conditions along the leading edge,
3. runner torque or desired flow conditions along the trailing edge, and
4. the number of blades.

Parameter	Value
N_S	650
N	1550 rev/min
H_n	2.5 m
η_n	0.8
P_r	1740 W
Q	88 L/s

Table 4.1: N_S650 prototype runner design values

4.1.1 Envelope sizing

The proportions of the runner envelope, its swept space, were determined using empirical data, which is presented as a function of specific speed in Figure 4.2.

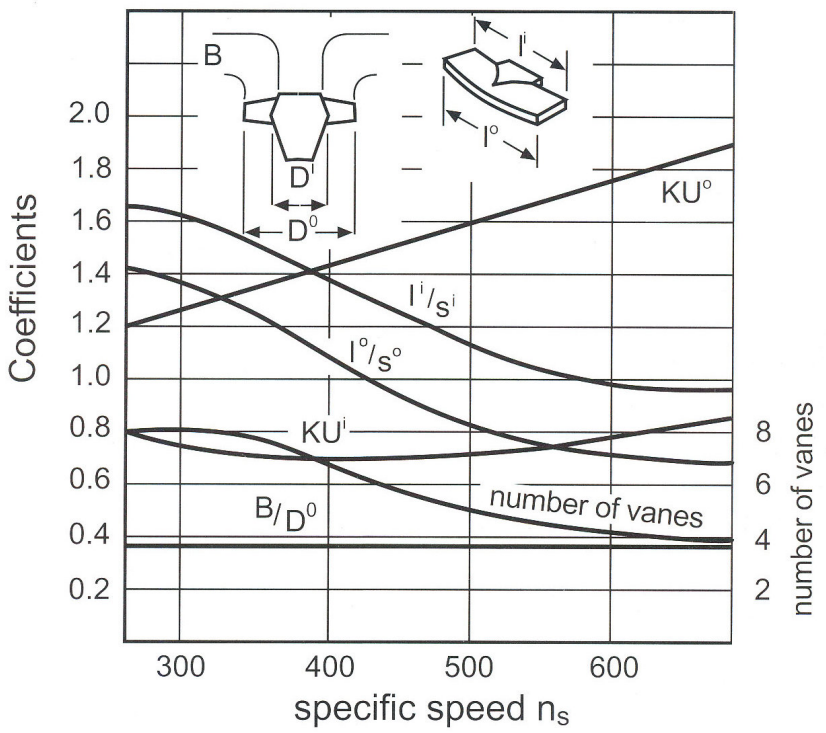

Figure 4.2: Figure 8.5 from Hothersall[30], used for tip and hub diameters but not chord or number of blades. n_s is equivalent to Equation 1.3. Note that $_i$ and o in this figure are equivalent to $_h$ and $_t$ in the text, respectively.

Sizing required dimensional design values, which are given for the N_S650 prototype in Table 4.1. The prototype was sized to fit within the plumbing capacity of the University of Canterbury Civil Engineering Fluids Laboratory.

For an axial flow runner, the runner envelope is straight and annular, being defined by the hub and tip diameters. These diameters were the first part of the turbine to be sized, and the volute and draft tube were subsequently scaled to mate up smoothly. Only the tip and hub diameters are taken from Figure 4.2, as the other parameters are not free to be adjusted within the flat-blade constraint. In hindsight, it may be said that the use of this empirical data was justified. Even though the prototype runner was aesthetically different from those used to create Figure 4.2, it was hydrodynamically similar enough for the purpose of design. The diameters are stated non-dimensionally as the ratio of a peripheral speed to

the spouting velocity equivalent to H_n in Equation 4.1. When $N_S = 650$, $KU_t = 1.83$, and $KU_h = 0.83$.

$$KU = \frac{\pi D N}{60\sqrt{2gH_n}} \tag{4.1}$$

Solving Equation 4.1 for D, when $KU = 1.83$ and 0.83, gave a tip diameter of 158 mm and a hub diameter of 72 mm. These were enlarged to 170 mm and 80 mm to offset the expected higher losses of the prototype turbine as compared to the those used as the basis of Figure 4.2. This enlargement results in a 14 % increase in area.

4.1.2 Geometry of the flat blade

A large part of maintaining a simple design was keeping runner fabrication simple. While twist and precise airfoil sections would no doubt improve efficiency, they would be difficult to communicate and manufacture accurately for a limited workshop. It was decided to use flat blades which would be less efficient in absolute terms, but were easier to communicate clearly. The prototype in Chapter 5 will show that the constraint of flat blades is not as damning as it first appears.

Blade fabrication required cutting each blade to the desired profile from flat plate, positioning against the hub at the specified setup angle ψ, and welding in place. Figure 4.3 illustrates this setup.

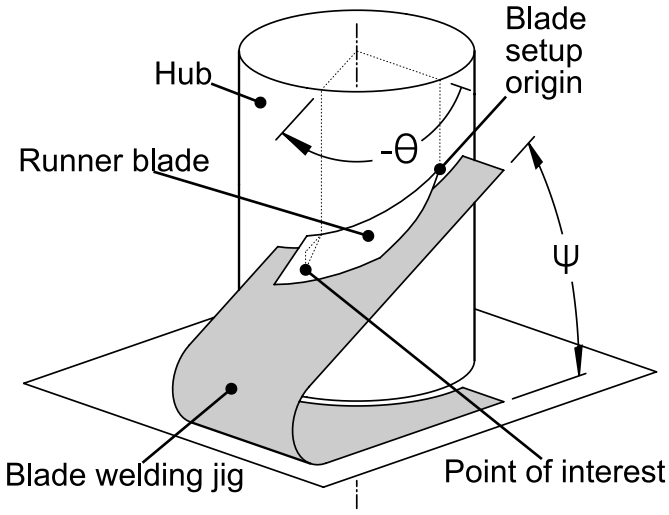

Figure 4.3: Runner blade assembly setup, showing that when the blade is welded in place, the blade setup origin corresponds to $\theta = 0$, where dihedral is zero

Runner speed, N, was fixed due to the constraint of directly driving an induction motor as a generator. A 4-pole motor would deliver 50 Hz at a nominal speed of 1500 rev/min plus 3 % slip, giving a design speed of $N = 1550$ rev/min. The hub-to-tip ratio, $\frac{d_h}{d_t}$, was derived from empirical data, although in the future $\frac{d_h}{d_t}$ appears to be a strong candidate variable for optimizing turbine performance. Notably, reducing the hub diameter would decrease the kinetic energy to be recovered by the draft tube. With flat blades, reducing $\frac{d_h}{d_t}$ would increase the required range of β on the blade, skewing the blade shape.

The runner blades described here were cut from flat steel plate and left unbent and unrolled. The consequence of this geometry was that blade curvature and dihedral were a function of azimuth angle and blade setup angle. The local blade angle, β, as defined in Figure 4.4, at any point on the blade plane was determined using Equation 4.2.

$$\beta = \tan^{-1}\left(\tan\psi\cos\theta\right) \tag{4.2}$$

This is the angle between the blade plane and the runner plane, on a plane tangent to the idealized cylindrical streamtube passing through the point of interest. Local blade angle depends only on azimuth angle, θ, and setup angle, ψ. Equation 4.2 was solved for θ to provide the azimuth angle where the local

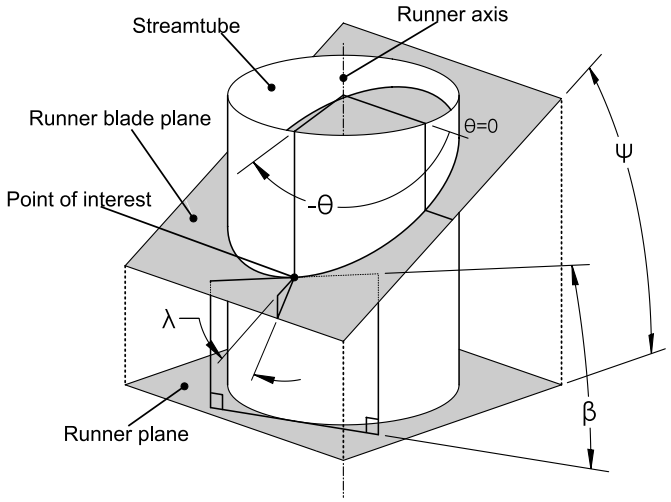

Figure 4.4: Intersection of cylinder and runner blade plane showing definition of local blade angle β on the assumed cylindrical streamtube, local dihedral angle λ, azimuth angle θ, and blade setup angle ψ

blade angle occurs, and this result is presented in Equation 4.3.

$$\theta = \cos^{-1}\left(\frac{\tan\beta}{\tan\psi}\right) \tag{4.3}$$

The leading edges were shaped to efficiently intercept the approaching flow. A velocity triangle was drawn for points along the leading edge of the runner blade based on fluid tangential velocity, V_t, runner peripheral velocity, $U = \omega r$, and fluid axial velocity, V_a, as shown in Figure 4.1. For **i3**, computational data were circumferentially averaged to provide the state of flow at the leading edge. From this, the leading edge blade angle, including a desired angle of attack, α, was determined. The required blade angle β_1 along the leading edge is given in Equation 4.4.

$$\beta_1 = \tan^{-1}\left(\frac{V_a}{U - V_t}\right) - \alpha \tag{4.4}$$

Following a mean streamline along a blade, the camberline curves smoothly to connect β_1 and β_2. Normally, the shape of the camberline is a variable which may be adjusted to affect the distribution of blade loading along an airfoil. Producing a blade from flat sheet resulted in camberline which could not be modified. The trailing edge blade angles were found by constructing a velocity diagram and solving Equation 4.5 to achieve the desired distribution of rV_t, taking into account a reasonable value for deviation, δ. Deviation is the misalignment of a mean streamline through a cascade with the blade camberline, resulting from a finite number of blades. A deviation of 5° is not uncommon in axial flow turbomachinery, and depends on blade loading.[67] For **i2** and **i3**, a δ of 4° and 6° were assumed, respectively. At high specific speeds, $\beta_1 - \beta_2$ and δ may be of comparable size.

$$\beta_2 = \tan^{-1}\left(\frac{V_a}{U - V_t}\right) - \delta \tag{4.5}$$

In conclusion, under the stated geometric constraints and leading edge conditions, leading and trailing edges were found which lie on the setup plane and are connected by smooth camberlines, producing a simple blade with the correct blade angles along the span.

4.1.3 Applying geometry to shape the blade

The design process of this runner was adapted from the work of Mr. Giddens on propeller turbines. The fundamental geometry of constructing the blades—the intersection between a cylinder and plane—has

already been published.[6] This work has made it more rigorous. The process has been expedited by several computer programs written for GNU Octave[20], a language based on the MATLAB (The Mathworks, Inc., Natick, MA, USA) scripting language, and these are summarized below and referred to where relevant. All source code is available.

`circ_avg_rev3b.m` circumferentially averages the velocity distributions from an annular volute outlet surface to give axial velocity and tangential velocity profiles as a one-dimensional function of radius.

`do_circ_avg.m` is a function called by `circ_avg_rev3b.m` to perform the circumferential average.

`swirl_bias_runafter_rev2.m` uses the output of `circ_avg_rev3b.m` to determine leading and trailing edge blade angles. It calculates the shape of a flat blade which achieves the correct angles across the blade span, maximizing blade area. Outputs a parametric description of the runner in a tabular format for use with Solidworks (Dassault Systèmes, Vélizy-Villacoublay, France).

The blade design method used was simplified, one-dimensional, using the blade-element method of dividing a blade into many span-wise slices. Beginning at the leading edge, β was found using trigonometry given the known distributions of peripheral velocity and the absolute velocity of the fluid stream. The absolute velocity at the leading edge was taken from a computational model of the prototype volute, and circumferentially averaged using `do_circ_avg.m` which `circ_avg_rev3b.m` calls near line 38. The contour graphs of Figure 4.5 show the velocity profiles expected at the volute's annular outlet.

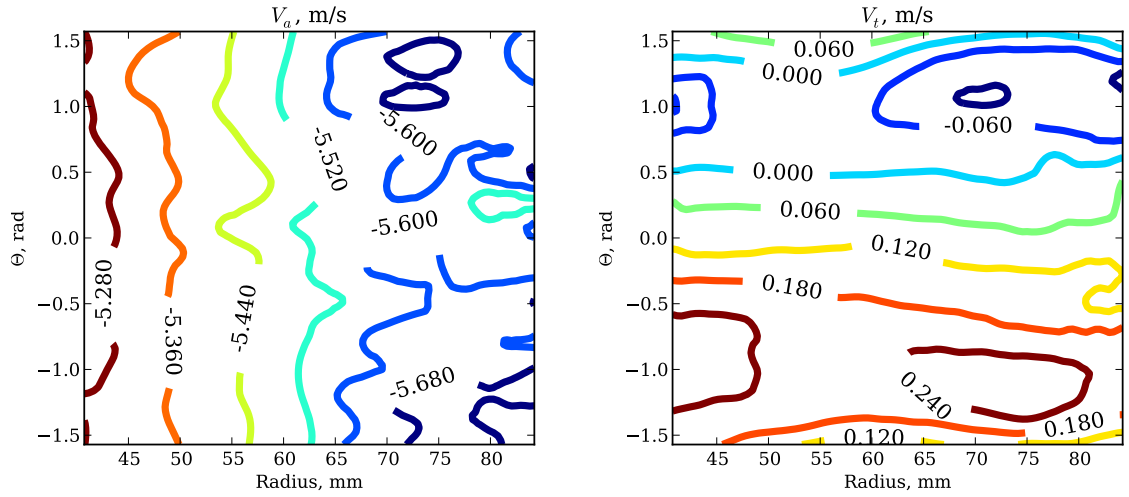

(a) Axial velocity

(b) Tangential velocity

Figure 4.5: Velocity profiles over the prototype volute's outlet annulus used for **i2** and **i3** runner blade design, from `circ_avg_rev3b.m`

Figure 4.6 shows the result of circumferentially averaging those two-dimensional distributions to give profiles as a function of radius only. The maximum and minimum lines indicate the magnitude of circumferential variation.

Along the leading edge, `swirl_bias_runafter_rev2.m`, near line 214, solved Equation 4.4 using the velocity profiles shown in Figure 4.6 to calculate the required blade angle, β_1.

At the trailing edge, the same axial velocity distribution was used as at the leading edge. The assumption of constant axial velocity through the runner was based on constant runner envelope cross-sectional area, the relatively small amount of turning induced by the runner, and that the flow is designed for radial equilibrium along the leading and trailing edges. Before the angles along the trailing edge could be calculated, the desired mean tangential velocity distribution was found. The target distribution was one of uniform rV_t, and the magnitude of that term came directly from the desired runner torque.

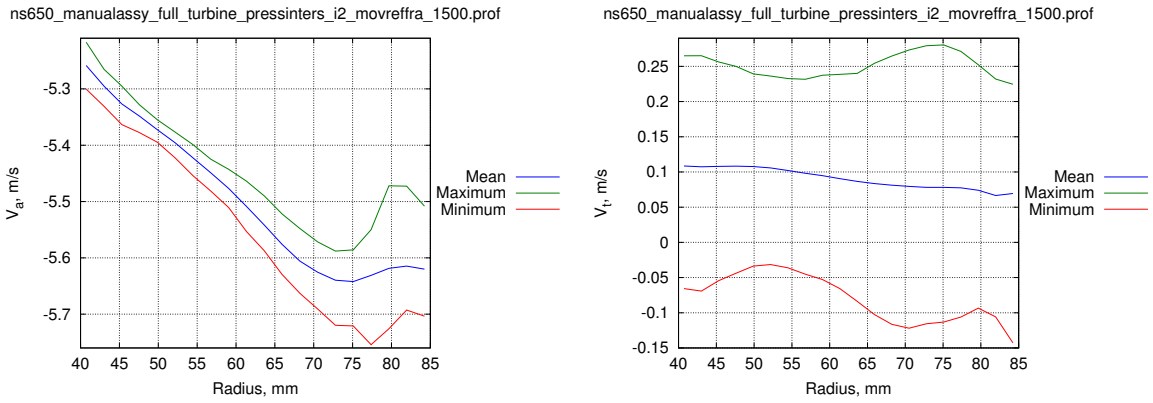

(a) Axial velocity

(b) Tangential velocity

Figure 4.6: Circumferential average of the data in Figure 4.5, from `circ_avg_rev3b.m`

This calculation occurs near lines 106 and 268 in `swirl_bias_runafter_rev2.m`. Now that the tangential, axial, and peripheral velocities are known across the trailing edge, blade angle may be solved for. This calculation occurs near line 269 in `swirl_bias_runafter_rev2.m`.

At that point, although β along the leading and trailing edges were known, their location was undetermined. Figure 4.7 shows the required values of β along the leading and trailing edges.

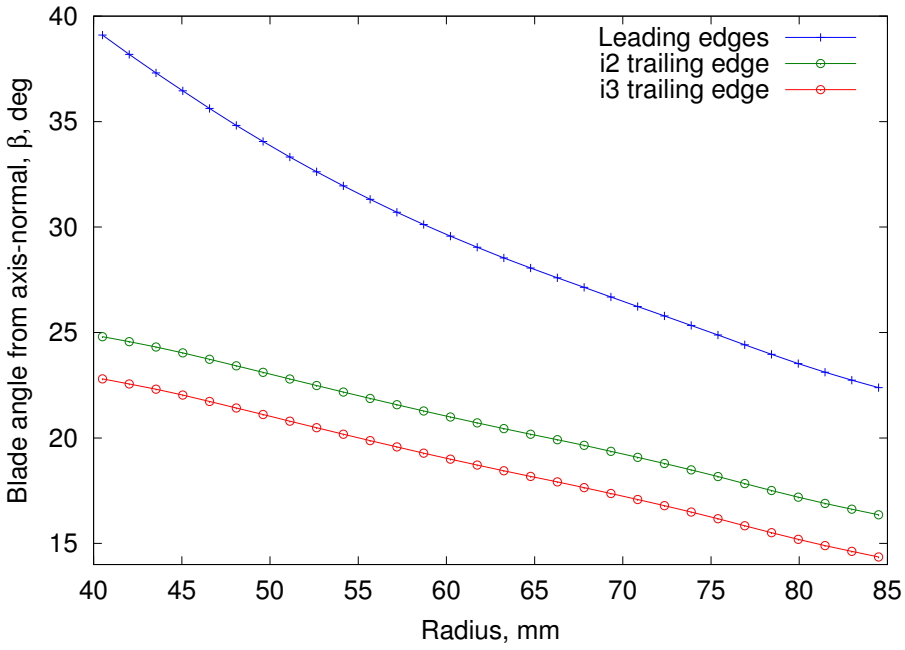

Figure 4.7: **i2** and **i3** leading, and **i2** trailing edge blade angle

For flat blades, one choice remained at this stage: the setup angle, ψ. From Figure 4.7, it was clear that the largest blade angle occurred on the leading edge at the hub. Equation 4.3 dictated that when $\theta = 0°$, $\beta = \psi$, and that $\lim \beta_{\theta \to \pm 90°} = 0°$. Therefore, ψ was set to $\beta_{1,h}$. Choosing a value of $\psi < \max(\beta)$ would have meant that not all blade angles could be met. On the other hand, choosing a value of $\psi > \max(\beta)$ would have been valid, but would have resulted in a smaller blade angle. Since the blade shape was already quite distorted and small, the smallest value of ψ was chosen. For **i2** and **i3**, $\psi = 39.1°$. Finally, Equation 4.3 was solved for all radial locations, fully constraining the geometry of the blade. Relevant parts of the source code are near lines 239, 265, and 274 in `swirl_bias_runafter_rev2.m`. This yielded

Figure 4.8, showing the azimuth coordinate of every point on the leading and trailing edge.

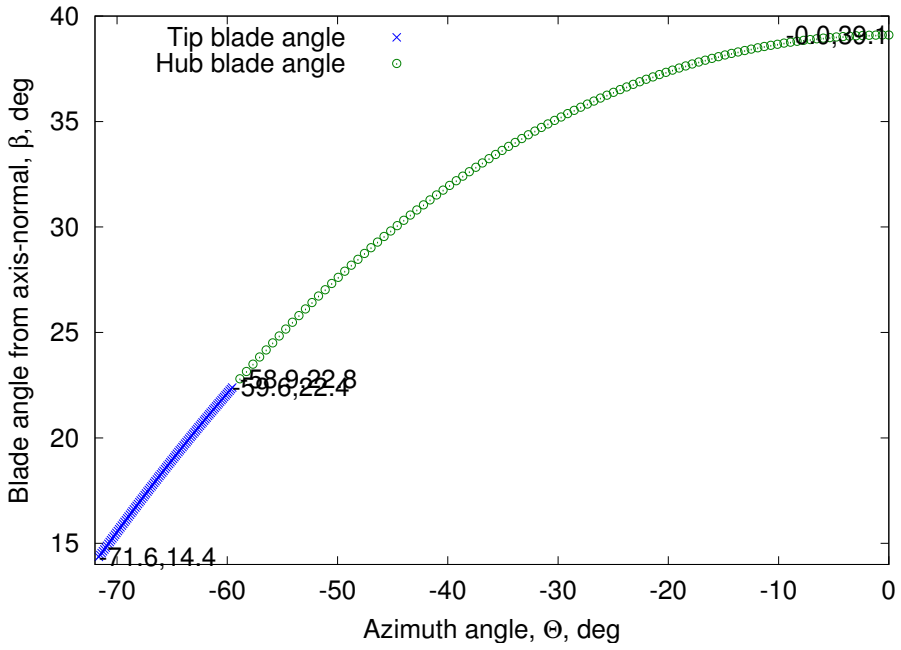

Figure 4.8: Shaping the **i2** flat blade: blade angle β plotted versus azimuth angle θ

Projecting the resulting edge coordinates onto the plane of the blade, which was equivalent to stretching perpendicular to the setup axis by $1/\cos\psi$, gave the view of the flat blade to cut, seen in Figure 4.9. If scaled carefully, this image could be laid over the blade material, traced, and then cut to provide the correct blade shape.

Figure 4.10 shows the cylindrical camberlines at the hub and tip, with relative and absolute velocities indicated by cyan and magenta lines, respectively.

4.1.4 Number of blades

Next, a suitable number of blades was chosen. In an ideal runner all streamlines would follow the blade camberline exactly, however the flow through a real runner with a finite number of blades is subjected to circumferential pressure gradients. The optimum number of blades strikes a balance between the skin-friction losses associated with excessive blade surface area, and the non-uniform exhaust and attendant downstream re-development losses stemming from too few blades. Too few blades would also exacerbate deviation, leading to less turning of the flow than if the flow followed the blade's camberline exactly. Deviation may be addressed by either adding more turning to the blades or increasing the number of blades.

An accepted method for determining an appropriate number of blades for a traditionally shaped axial turbine runner is the Zweifel method. This empirical method specifies the number of blades required to achieve a reasonable blade loading at the hub, where loading is highest. Other methods are the Ackeret and vortex row.[67] The Zweifel coefficient is defined in Equation 4.6, where L is the axial length of the blade, and s is the stagger or circumferential distance between similar points on a blade.[70]

$$\Psi = 2\frac{s}{L}\sin^2\beta_2\left(\cot\beta_2 - \cot\beta_1\right) \tag{4.6}$$

A value of $\Psi = 0.8$ at the hub should be sufficient to avoid excessive deviation.[30]

$$s_h = \frac{\pi d_h}{Z} \tag{4.7}$$

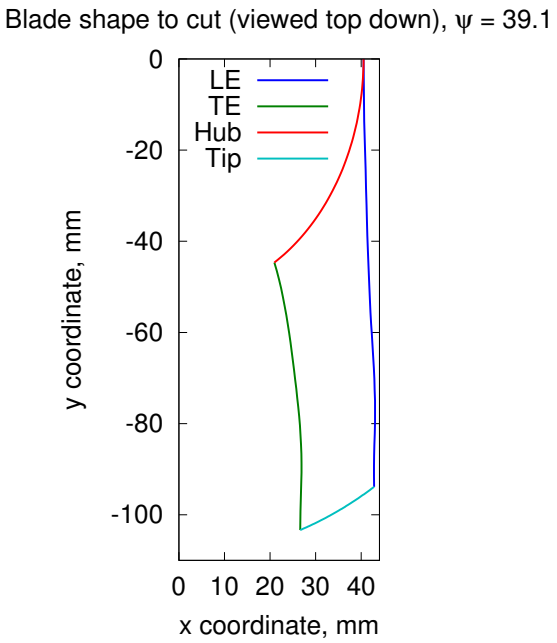

Figure 4.9: N_S650 **i3** blade viewed normal to the blade plane, where ψ is the angle the blade is rotated about the x-axis according to the right hand rule prior to fixing to the hub

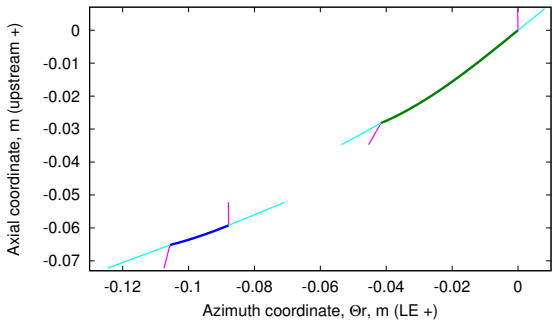

(a) Flat blade hub and tip camberlines and velocity vectors shown with runner axis aligned with Y axis, where flow is from top to bottom, leading edges on the right absolute velocity vectors are magenta, relative velocity vectors are cyan

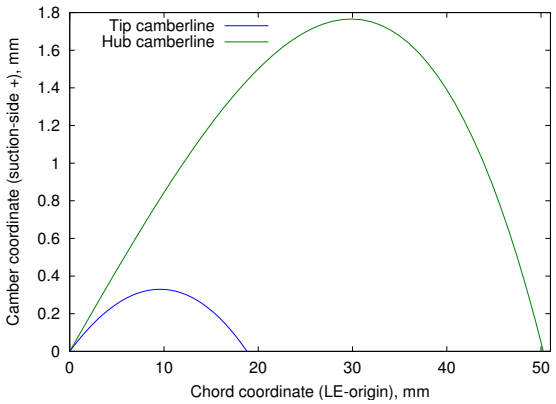

(b) Hub and tip camberlines projected onto surfaces of constant radius, shown in the standard orientation, leading edge to the left, suction face up

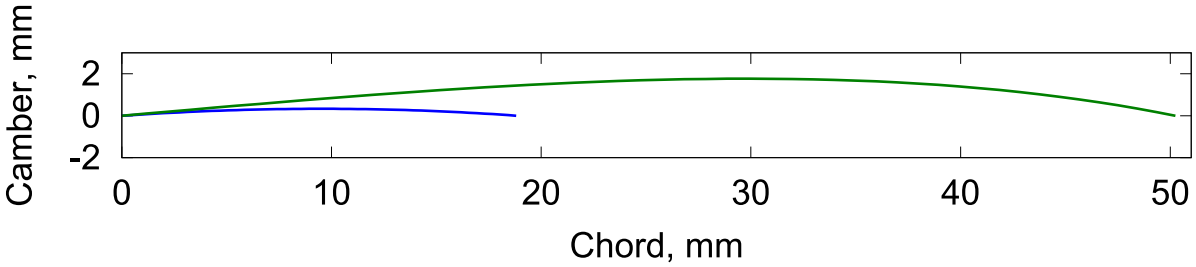

(c) Hub and tip camberlines projected onto surfaces of constant radius, unscaled to show the true shape, where the common left hand point is the leading edge for both

Figure 4.10: Various representations of the **i3** camberline when a blade is cut from flat sheet. Hub camberline is green and tip camberline is blue.

	l/s	
Radius	Prototype	Fig. 4.2
Hub	1.2	1.0
Tip	0.2	0.7

Table 4.2: Blade stagger comparison for a specific speed of 650

Parameter	Value
d_t	170 mm
d_h	80 mm
ψ	39.1°
Z	8

Table 4.3: N_S650 prototype runner geometry

Equation 4.7 was substituted into Equation 4.6, which was then solved for the number of blades, Z, which was then rounded up to the nearest integer. Using this method, $Z = 4$ satisfies a minimum Zweifel coefficient of 0.8 at the N_S650 runner hub. However, the number of blades was doubled to eight to account for the taper of the flat blade, giving a more reasonable stagger at the tip.

With eight blades, the prototype runner stagger at the hub exceeded the suggested minimum of approximately 1.0 given in Figure 4.2, giving confidence that boundary layer separation due to excessive blade loading would be avoided. At the tip, the prototype runner's stagger is 0.2 versus the suggested 0.7, meaning that four times as many blades would be required to satisfy the suggested stagger at the tip. Table 4.2 compares the actual and suggested blade stagger values of Figure 4.2, where l is the length, or chord, of the airfoil along a particular streamtube, and $s = \frac{\pi D}{Z}$ is the stagger, where Z is the number of blades. Eight blades was chosen as a compromise between skin friction losses, effective turning, and ease of fabrication. The runner was shown to produce an adequately uniform outlet velocity distribution in the subsequent computational analysis.

4.1.5 Runner design summary

The runner geometry is now defined in sufficient detail to build or analyze. In summary, first the hub and tip diameters were calculated from empirical data, with some engineering judgment applied. Taking inlet conditions from a CFD model of the prototype volute, the leading edge of the runner rotating at the design speed of was shaped to smoothly intercept incoming flow. The trailing edge was shaped to provide a specific amount of turning with a uniform rV_t distribution across the span. Important runner parameters are summarized in Table 4.3. In the future, the process could be simplified by replacing the CFD-derived velocity profiles with assumed axial velocity and tangential velocity distributions, eliminating the reliance of the design on CFD.

A helpful link between the design and analysis stages was provided by Solidworks (Dassault Systèmes, Vélizy-Villacoublay, France) Design Table functionality. The output in Figure 4.11 was generated by `swirl_bias_runafter_rev2.m`, which contains enough information to configure a parametric CAD (computer aided drafting) model. The hub and tip diameters were calculated as the minimum and maximum radial coordinate of the input velocity profiles and were subject to a rounding error. These were adjusted to 80 mm and 170 mm by hand prior to analysis. In addition to ψ, d_h, and d_t, both the leading and trailing edges are defined in Solidworks by a spline with four control points, labeled `h`, `1`, `2`, and `t` from hub to tip. The `theta_` and `r_` lines determine the placement of these control points with units of ° and mm. Figure 4.12 is an interactive 3D model of the **i3** runner, generated from the data above.

```
Setup angle, Psi = 39.1 deg
Using an aft-swept leading edge
Control-point dimensions for Solidworks Design Table
39.103433 Psi
2.000000 blade thickness
81.000000 d_h
169.000000 d_t
75.183740 downstream length
10.000000 upstream length
148.856121 theta_(point h,TE)
161.640280 theta_(point t,TE)
160.520988 theta_(point 2,TE)
150.084480 theta_(point 1,TE)
90.000000 theta_(point h,LE)
114.201238 theta_(point 1,LE)
147.680993 theta_(point 2,LE)
149.550467 theta_(point t,LE)
44.900000 r_(point 1)
80.100000 r_(point 2)
44.900000 r_(point 1)
80.100000 r_(point 2)
20.000000 taper angle
8.000000 number of blades
```

Figure 4.11: Output for Solidworks Design Table from `swirl_bias_runafter_rev2.m`

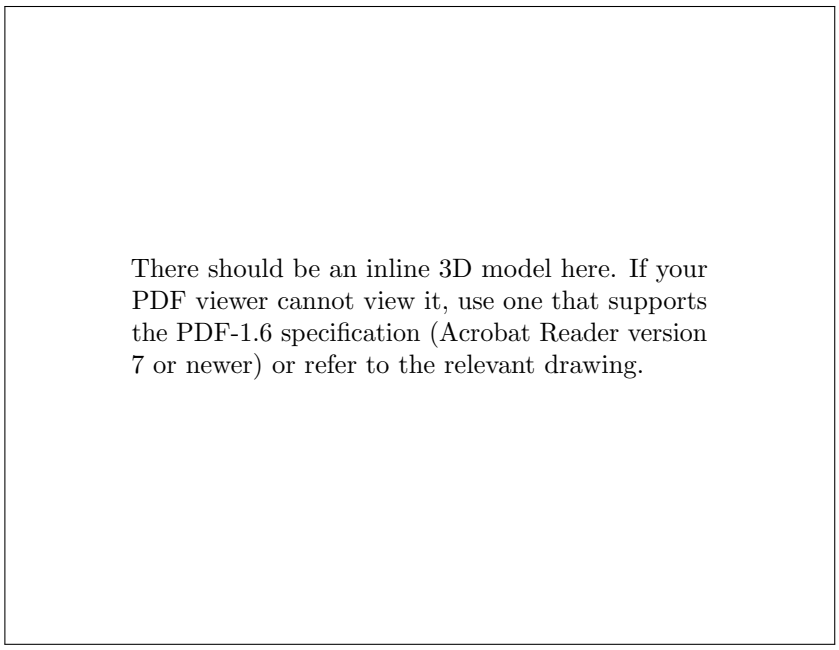

Figure 4.12: **i3** runner model (`../common/runner_to_insert.U3D`) Show controls / Close

4.2 Computational analysis

Given the uniqueness of the N_S650 flat-bladed runner, a computational analysis of its performance was undertaken to uncover pitfalls prior to prototyping. The results present the predicted performance over a range of conditions. These results were first presented at Hidroenergia 2010, a conference held by the European Small Hydro Association. The computational analysis was performed with Fluent. First, the computational setup is introduced, then the results for runner geometry **i2** are given. These results allowed some conclusions to be drawn regarding the most influential modeling choices, and it was noted that due to the proportions of the velocity diagram, which was dominated by the high blade peripheral velocity and small $\Delta(V_t)$, that a small change in predicted turning of the flow had a large impact on the resultant torque. A difference of turning of about 2° in the rotating frame of the blade produced a 50 % change in torque. Since 2° was approximately the difference in turning predicted by the inviscid and $k\omega$ models, β_2 along the trailing edge of the **i2** runner was reduced by 2°, creating **i3**. The **i3** blade was then analyzed to examine the sensitivity of flow angle relative to the blade, β_2', to blade angle, β_2.

4.2.1 Modeling simplifications

Turbines comprise a moving rotor and various other stationary components, and therefore even with a steady flowrate and runner speed the state of flow in them is inherently unsteady. By considering the runner separately from the static components of the turbine, it may be approximated by a steady-state component by adding the radial force terms caused by rotation and adding the effect of the ωr velocity terms to incoming and outgoing flows.

Complimenting this steady-state assumption is the assumption that circumferential variations about the runner inlet do not strongly affect the steady state performance of the runner and that circumferential variations about the runner outlet do not affect the draft tube. Resolving circumferential variations would have required full three-dimensional models of the runner and draft tube, which would have increased the total cell count by an order of magnitude.

These simplifications were implemented in Fluent using its *mixing plane* zone interface. The following passage of the Fluent user guide justifies the assumptions given above.

> In the mixing plane approach, each fluid zone is treated as a steady-state problem. Flow-field data from adjacent zones are passed as boundary conditions that are spatially averaged or "mixed" at the mixing plane interface. This mixing removes any unsteadiness that would arise due to circumferential variations in the passage-to-passage flow field (e.g. wakes, shock waves, separated flow), thus yielding a steady-state result. Despite the simplifications inherent in the mixing plane model, the resulting solutions can provide reasonable approximations of the time-averaged flow field.[1]

Furthermore, since circumferential variations in inlet conditions were averaged out by the mixing plane, and each blade passage was identical, the size of the mesh was considerably reduced by modeling only one blade passage, which was assumed periodic.

Although circumferential variations in conditions were averaged out, it was important to treat the net angular momentum through the system as accurately as possible, since the power output of the turbine is the product of a high speed and a small torque. The mixing plane interface employed to connect the runner zone to the rest of the domain did not by default conserve angular momentum, since the values of tangential and axial velocity, like all the other properties passed through the interface, result from an area weighted, not a mass weighted, circumferential average. This means that in its default configuration, the mixing plane interface could introduce an unrealistic step change in the angular momentum of the fluid stream. A specific modeling option to scale the tangential velocity profile of the downstream mixing plane half in order to conserve angular momentum over the mixing planes was enabled for all cases.

Even though the flow through the volute and draft tube was turbulent and unsteady in general, since the design was resistant to separation and vortex shedding, the assumptions of steadiness remain reasonable. Transient analysis was not undertaken due to the number of cases and the computational requirements of a fully meshed three-dimensional runner.

These conditions allowed the entire turbine to be considered as a three-zone system:

the volute as a fully three-dimensional zone,

the runner reduced to a single three-dimensional, periodic blade passage, and

the draft tube reduced using rotational symmetry to a one-eighth slice.

The remainder of this chapter focuses on results obtained for the runner only.

4.2.2 Boundary conditions

The runner zone was bounded by four types of surfaces, each with its own boundary conditions:

pressure inlet which defined the static pressure and flow direction over the inlet surface which connects the volute to the runner,

pressure outlet which made a similar connection from the runner to the draft tube downstream,

periodic which meant that each pair of facets on this boundary was separated by $360°/8 = 45°$ about the zone axis, and

wall which comprised the cylindrical hub and casing and the blade surfaces.

Conditions at the runner pressure inlet were defined as a function of radius derived from the volute zone outlet upstream. Similarly, the runner zone pressure outlet surface was connected by a mixing plane to the draft tube, which allowed conditions in the draft tube to affect the radial distribution of pressure in the runner. The periodic boundary enforced a zero pressure gradient, and also a zero net circumferential flowrate, which were consistent with rotational symmetry. The walls were assumed no-slip for the $k\omega$ cases and zero-shear-stress for the inviscid cases. The conditions at the runner leading edge for all analyses resembled the data used to design the blade, shown in Figure 4.6.

As mentioned earlier, the runner was one of a three-zone computational domain. The inlet and outlet boundary conditions were a total pressure of 24 476 Pa equivalent to a 2.5 m head of water applied to the volute inlet, and a uniform static pressure of 0 Pa applied to the draft tube outlet. The runner speed was defined by adjusting the rate of rotation of the runner zone reference frame. The effect of the ωr velocity component on incoming and outgoing flow was accounted for by the mixing plane.

Due to the assumed steady nature of flow relative to the runner and the use of a single blade passage, conditions on the volute outlet were circumferentially averaged before being applied to the runner inlet as a function of radius only. Similar averaging connected the runner to the draft tube. Both employed a Fluent mixing plane.

Figure 4.13 summarizes the computational domain high-level topology. Static pressure, p, total pressure, p_t, flow direction, $\hat{V}$, and turbulence scalars k and ω where applicable were passed as functions of radius across the mixing planes in the directions indicated in the figure.

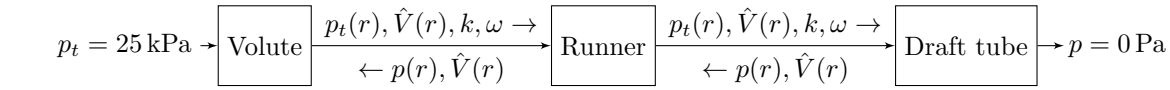

Figure 4.13: High-level mesh topology

4.2.3 Fluid model

The Reynolds numbers of the water flowing through the prototype runner were on the order of 2×10^5, with Mach numbers on the order of 0.01. The fluid was modeled as both turbulent and inviscid. Since the Reynolds numbers were high, and the volute is similar in function to a smooth contraction, the boundary layers entering the runner may be thin enough that assuming the fluid is inviscid is appropriate. Also the static pressure difference across each blade, which produces the resultant torque, is expected to be largely independent of viscous stresses in the fluid. These assumptions were less valid at off-design conditions, where large angles of attack and excessive blade loading may produce boundary layer separation on the suction side which requires more sophisticated models to capture, however the impact of this limitation is offset by the intention to operate the turbine only very near BEP.

On the other hand, high Reynolds numbers guaranteed that flow would be fully turbulent by the time it entered the runner Also, the energy embodied in dynamic head at the runner leading edge was large enough that the effects of energy dissipated by turbulent eddies could require turbulence modeling to produce reasonable predictions of runner efficiency.

The inviscid model had the advantage of simplicity, in terms of both formulation and mesh requirements. Predictions of runner efficiency, on the other hand, were expected to require turbulence modeling to account for total pressure losses.

For the proceeding analysis, results were obtained with the inviscid and standard $k\omega$ fluid models. The inviscid model was a logical choice due to its simplicity of application and lower computational requirements. The standard $k\omega$ model was one implementation of the Reynolds-averaged Navier-Stokes equations, which modeled the velocity fields of turbulent flows as the superposition of a steady field and a field of random fluctuations. It was chosen as a compromise of computational economy and realism. A variant of the standard $k\omega$ model, shear-stress transport (SST), which is recommended in the Fluent user guide was trialled but later abandoned due to convergence issues. More advanced computational models exist, but given the number of cases requiring solution, and the number cells in the mesh, anything beyond two-equation turbulence modeling became intractable. Applying computational fluid dynamics and turbulence to industrial problems such as turbines is very much an active field of research.[63, 68]

4.2.4 Discretization of equations

First and second-order discretization schemes for convection terms were used in analyses to determine the effect of discretization order on predicted runner performance. For first-order cases, this meant using the Fluent standard scheme for pressure and first-order upwind (FOU) schemes for convection terms. For the second-order cases, this meant using the Fluent pressure staggering option (PRESTO!) for pressure and second-order upwind (SOU) schemes for convection terms. Second order schemes were expected to yield better mesh convergence due to the use of unstructured meshes and the presence of highly three-dimensional flows, but at the expense of larger residuals and generally less sure numerical convergence.[1]

4.2.5 Meshes

Two base meshes were prepared for the runner, both meshed from the same input geometry, which is shown in Figure 4.14.

A fully tetrahedral mesh was used with the inviscid model, whereas for the $k\omega$ cases, prismatic cells were added near walls to comply with the y^+ requirements for wall functions. The differences are illustrated in Figure 4.15, which shows in detail the mesh topology around the blade at mid-span. Section 4.2.6 includes the effect of refinement to both meshes, which produced a negligible change in the results compared to the effect of using a different fluid model.

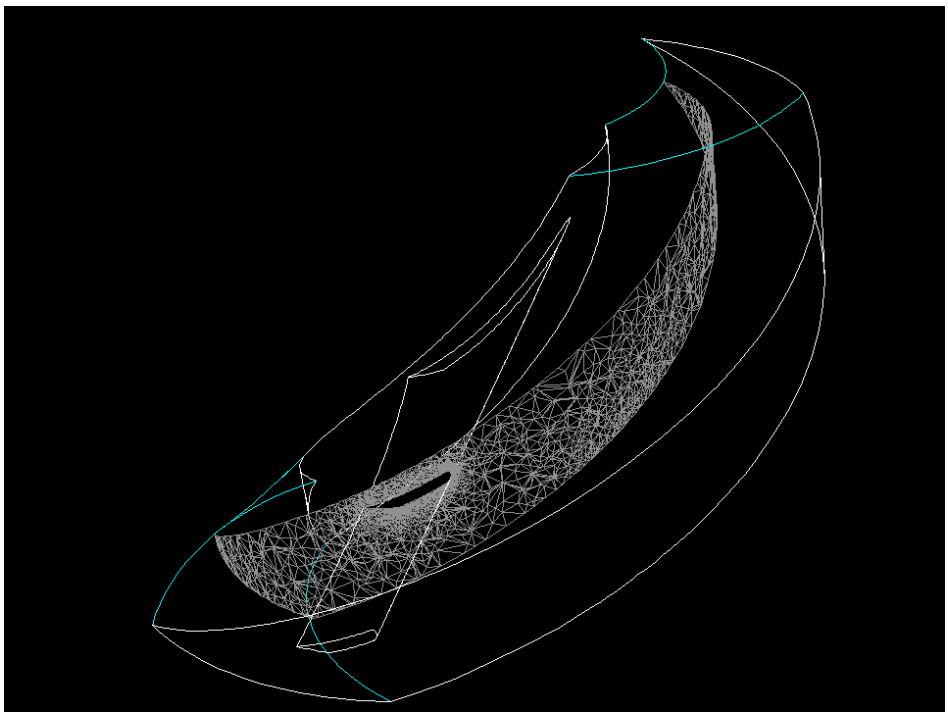

Figure 4.14: Runner domain outline, with a cut at mid-span

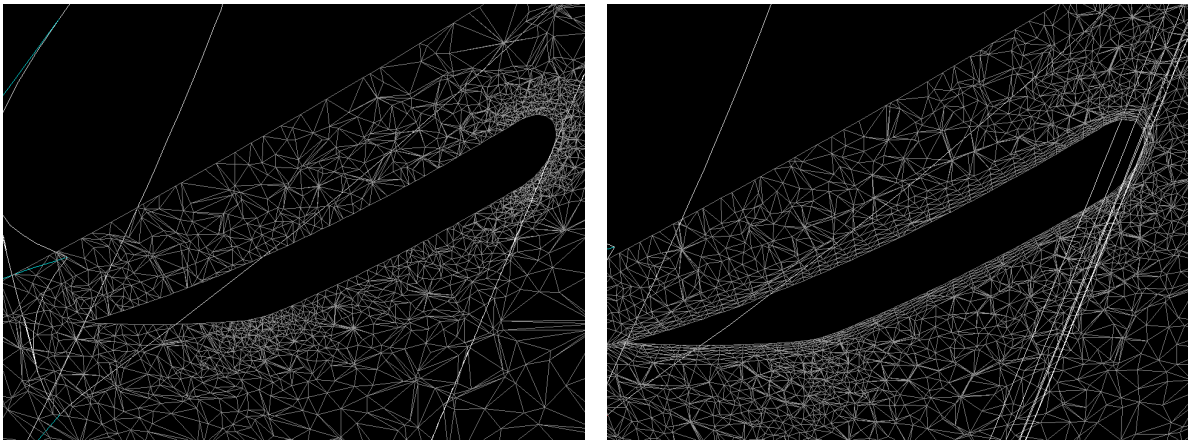

(a) Inviscid (b) $k\omega$

Figure 4.15: **i3** mesh details at mid-span

4.2.6 Analyzing i2

In the absence of best practices for this type of computational analysis, important modeling parameters were varied to study their effects on the results. The total head across the entire three-zone domain was fixed to 2.5 m, while the runner speed was varied between 1000 rev/min and 2000 rev/min. The influence of fluid model, mesh resolution, and discretization schemes for pressure, momentum, and turbulence scalars on predicted performance were analyzed. In all cases, the important outputs were the resultant steady torque, flowrate, and efficiency at a range of speeds under the influence of the design head. Figure 4.16 gives the results from all six cases, including versions with mesh refinements and second order discretization, presented alongside the values used in the design of the **i2** runner.

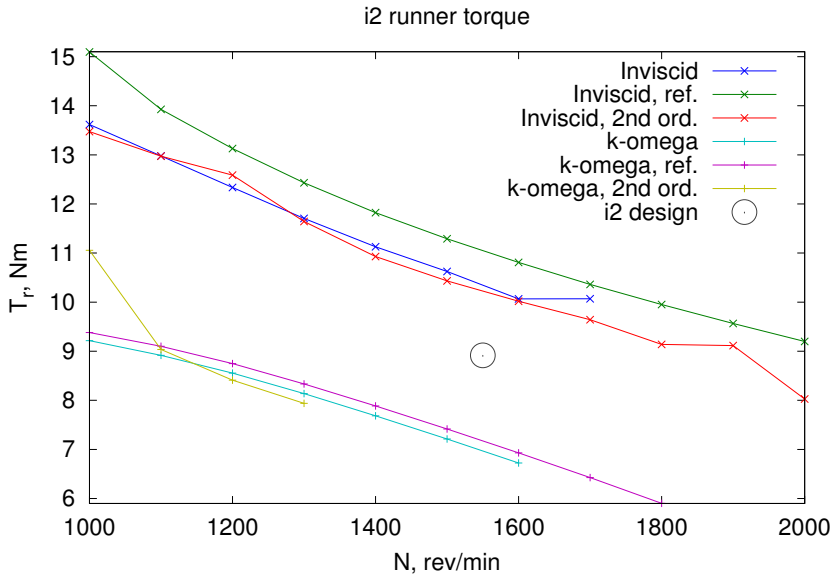

Figure 4.16: Computationally predicted torque on **i2** runner from both fluid models

Fluid model was the most influential modeling parameter affecting predicted torque. Predicted torque at the design speed was approximately 50 % higher for all inviscid cases than any of the $k\omega$ cases. Discretization scheme and mesh resolution were less significant and approximately equal in weight.

Remembering the Euler equation, Equation 1.10, and given that $\dot{m}$, r, and V_{t1} were roughly the same in all cases, it was expected that torque would be proportional to the mean tangential velocity at the trailing edge.

The explanation of the large difference attributed to the choice of fluid model lay in the proportions of the trailing edge velocity diagram, which has been simplified to the spanwise average shown in Figure 4.17. Two velocity diagrams are shown superimposed: the base inviscid and $k\omega$ cases. The proportions of the diagram were such that a small change in the predicted turning effected by the blades, that is, the direction of the fluid velocity relative to the blade, V_{rel}, from one fluid model to the other produced a large change in the predicted torque. In terms of Figure 4.17, this refers to how the difference between ◿ and ◿ affects the magnitude of V_{t2}. This sensitivity was due to the relative size of three velocity components — $\omega r > V_a > \Delta\left(V_t\right)$ — and is an intrinsic property of high specific speed turbines.

The magnitude of this sensitivity may be illustrated through a worked example. The trailing edge blade angle is labeled β_2, and to acknowledge that the flow does not follow the blade camberline exactly, the mean flow relative flow angle at the trailing edge is labeled β_2'. The difference between these two angles is the deviation, δ, and it follows that $\beta_2' = \beta_2 + \delta$. β_2' is defined in Equation 4.8.

$$\beta_2' = \tan^{-1}\left(\frac{V_a}{\omega r + V_t}\right) \tag{4.8}$$

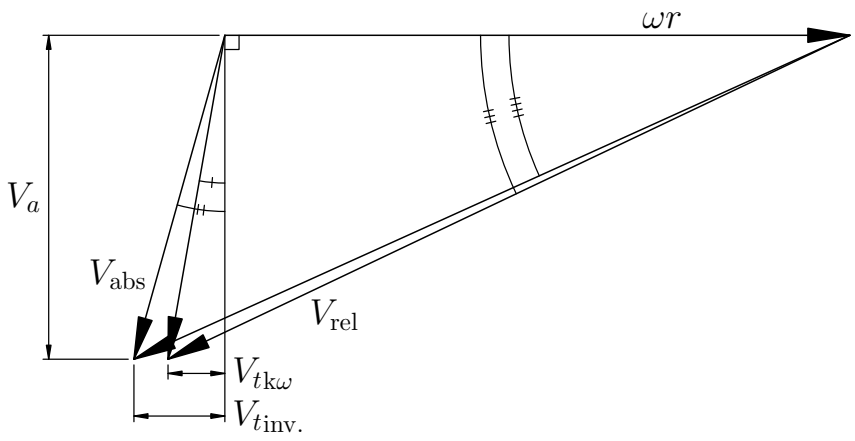

Figure 4.17: High-N_S sensitivity to blade angle highlighted by different flowfields predicted by inviscid and $k\omega$ fluid models

Next, rearranging Equation 4.8 to give V_t in terms of β_2' gives Equation 4.9

$$V_t = \frac{V_a}{\tan(\beta_2')} - \omega r \tag{4.9}$$

and allows analysis of the sensitivity of V_{t2} to changes in β_2'. Inserting values representative of the design, $V_a = 5.3\,\text{m/s}$, $\omega = 162\,\text{rad/s}$, and $r = 62.5\,\text{mm}$, produces Figure 4.18. An increase in β_2' of 5° would reduce

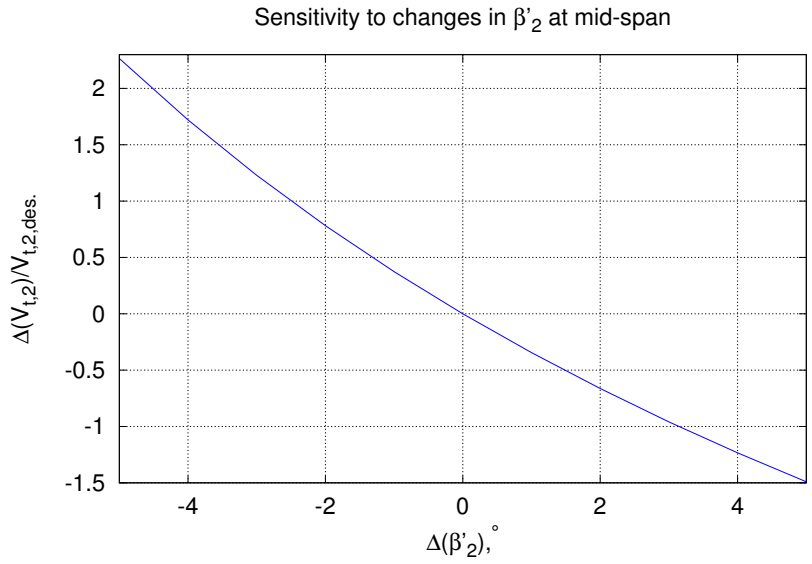

Figure 4.18: Flow turning sensitivity to β_2' at **i2** mid-span, where the x-axis is the change relative to the design value of $\beta_2' = 18°$ and the y-axis is normalized by the design value of V_{t2}

the runner torque to zero. Considering that $\beta_1 - \beta_2 \approx 10°$, and that δ reduces the total turning from that difference by approximately 5°, this is a reasonable figure. Conversely, a reduction in β_2' of 5° would increase the runner torque by one and a half times its design value. A change of 2° in either direction to β_2' produces a change of about 50 % to the resulting torque. These results assume for the sake of argument that flowrate does not change, although the flowrate will be affected by such considerable changes in the force on the runner. Regardless, achieving a precise amount of turning is critical to producing a high specific speed turbine that performs on-design.

Figure 4.19 presents the torque data given in Figure 4.16 in terms of the change in angular momentum. Again, it was quite clear that the choice between the inviscid and $k\omega$ fluid models was more influential

than either mesh refinement or discretization order. Given that the predicted change in the tangential velocity component across the runner varies between the two models by about one third of the design value, seen in Figure 4.16 near the design point, it was expected that the differences in the numerical results would be obvious.

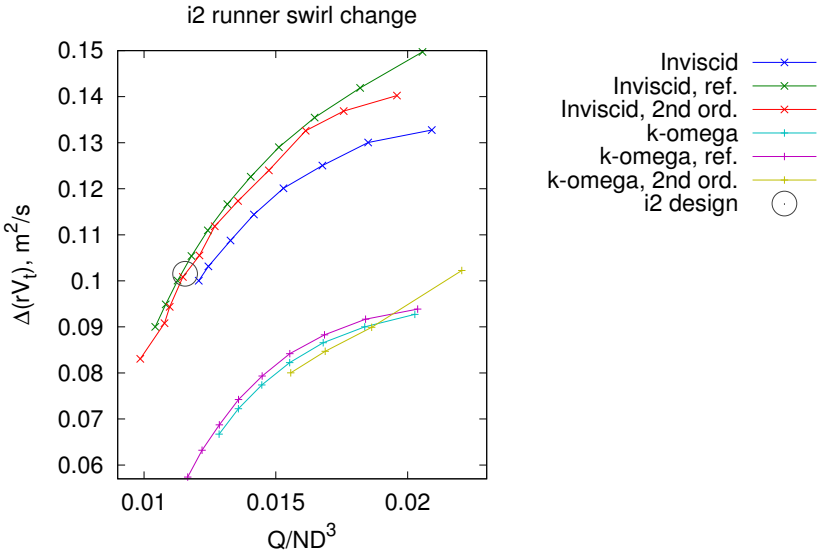

Figure 4.19: Swirl change across **i2** runner

As was shown in the example above, the difference between the two groups of results in terms of the absolute flow angle downstream of the runner is on the order of several degrees. In terms of Figure 4.17, this refers to how the difference between  and  . Figure 4.20 summarizes the average absolute flow angle downstream of the runner.

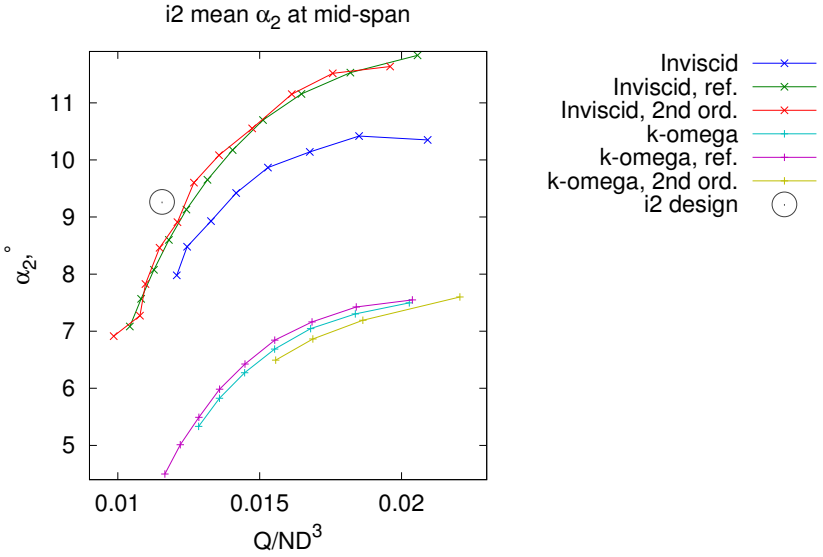

Figure 4.20: Predicted absolute flow angle off axial downstream of **i2** runner

Due to the high speed of the runner, the difference of flow angle through the runner, and relative to it, is several times smaller than the difference of the absolute flow angle in the stationary frame. In terms of Figure 4.17, this refers to how the difference between  and  is significantly greater than and . Figure 4.21 shows the changes in absolute flow angle leaving the runner that would result from a given

variation of the relative flow angle, about the design value of about $\beta_2' = 18°$.

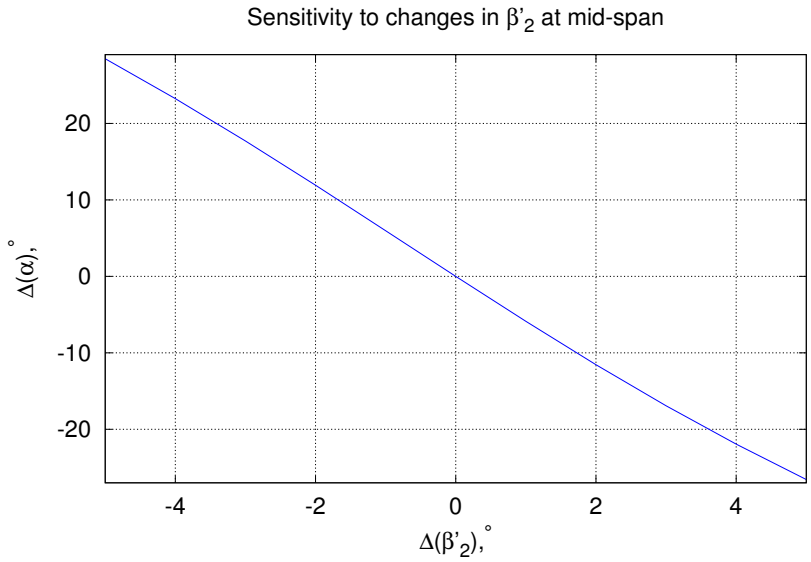

Figure 4.21: Absolute flow angle sensitivity to relative flow angle

Figure 4.22 presents predicted values of β_2'. The grouping by fluid model was visible. The difference between the two groups was less than 0.5° in the rotating frame of the runner, although the effect on predicted torque is approximately one third of the design torque shown in Figure 4.16.

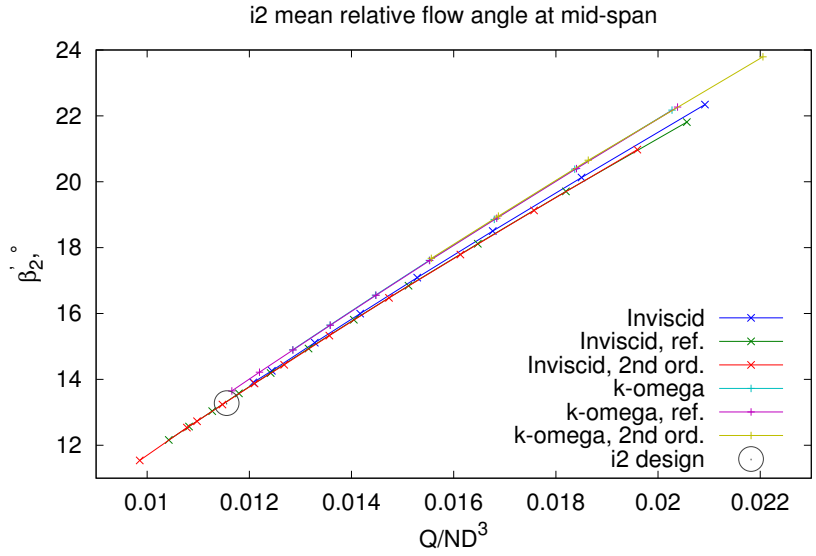

Figure 4.22: Relative flow angle

Since $T_r \propto \Delta(V_t)$, and $\Delta(V_t)$ was very sensitive to β_2', that even a small uncertainty in the predicted amount of turning effected by the blades resulted in a large change to predicted torque.

The **i2** runner head-discharge characteristic curve is given in Figure 4.23. All six variations of the computational model employed agree more closely on the flow characteristic of the runner than its turning performance. This is illustrated by the relatively closer grouping of data series in Figure 4.23 than in Figure 4.20.

It was expected that the inviscid model would predict an efficiency of 1.0, meaning all changes to total energy across the runner would be due to the work extracted by the net static pressure difference across

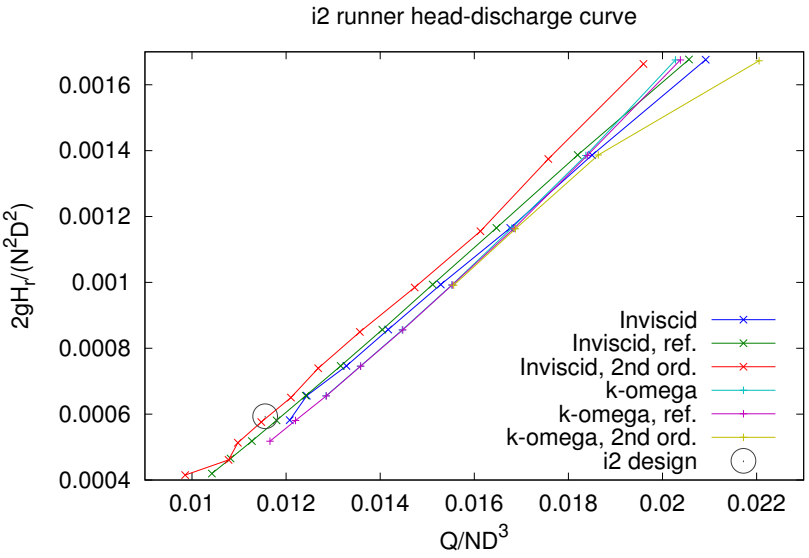

Figure 4.23: **i2** runner non-dimensional head-discharge curve

the spinning blade. This was not the case. As can be seen in Figure 4.24, the inviscid model predicted peak efficiencies of about 0.8, compared to a value of 0.55 to 0.60 for the $k\omega$ cases. Although the linear momentum residuals of the inviscid cases reduced by roughly 10^{-3} all around, this was an insufficient criteria to ensure convergence of angular momentum.

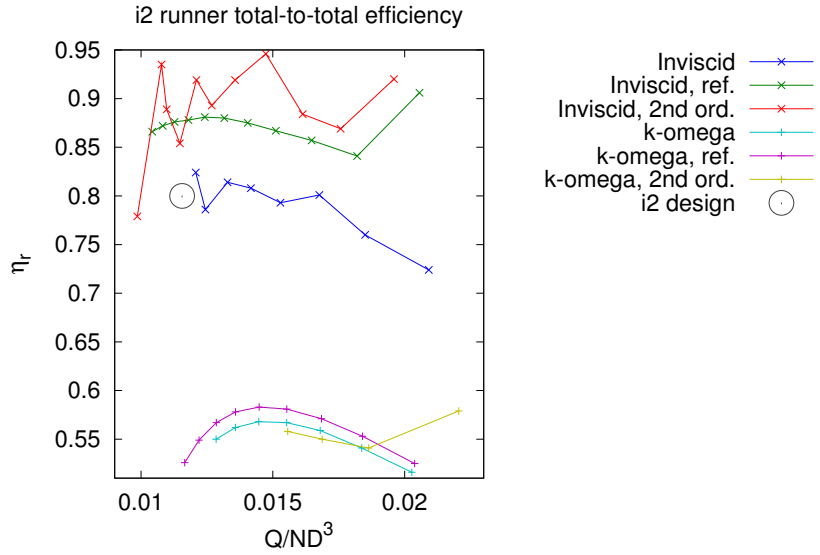

Figure 4.24: **i2** runner predicted total efficiency

Table 4.4 summarizes all the cases whose data has been presented graphically in Figures 4.16 through 4.24.

In conclusion, small differences in the predicted flowfield resulting from modeling options highlighted the intrinsic torque sensitivity of the high specific speed runner. Prior to analysis, a value for η_r of 0.8 was expected, based on comparison with previous Giddens turbines. The measurements of Chapter 5, will show the $k\omega$ model significantly underestimated runner efficiency. The inviscid results, although apparently closer to reality in this regard, were inconsistent with the formulation of the fluid model and should not be trusted to predict efficiency. All cases fell closer together when predicting runner flow

Case set	Fluid model	Cells	Discretization scheme			
			Press.	Mom.	k	ω
Inviscid	inviscid	152×10^3	std.	FOU		
Inviscid, ref.	inviscid	1240×10^3	std.	FOU		
Inviscid, 2nd ord.	inviscid	152×10^3	PRESTO!	SOU		
$k\omega$	$k\omega$	226×10^3	std.	FOU	FOU	FOU
$k\omega$, ref.	$k\omega$	291×10^3	std.	FOU	FOU	FOU
$k\omega$, 2nd ord.	$k\omega$	226×10^3	PRESTO!	SOU	SOU	SOU

Table 4.4: Summary of **i2** runner computational analyses: *Press.* pressure, *Mom.* momentum, k turbulence kinetic energy, ω specific dissipation rate, *std.* standard, *FOU* first order upwind, *SOU* second order upwind, *PRESTO!* pressure staggering option

characteristics, meaning that even though predictions of efficiency were unreliable, the data required for sizing a turbine may be obtained by computational methods such as those employed here.

4.2.7 Introducing i3

Following the results of the analysis of **i2**, the **i2** runner was modified by adjusting β_2 by a uniform $-2°$ along the span, resulting in **i3**. The modifications produces a runner which has slightly more blade area.

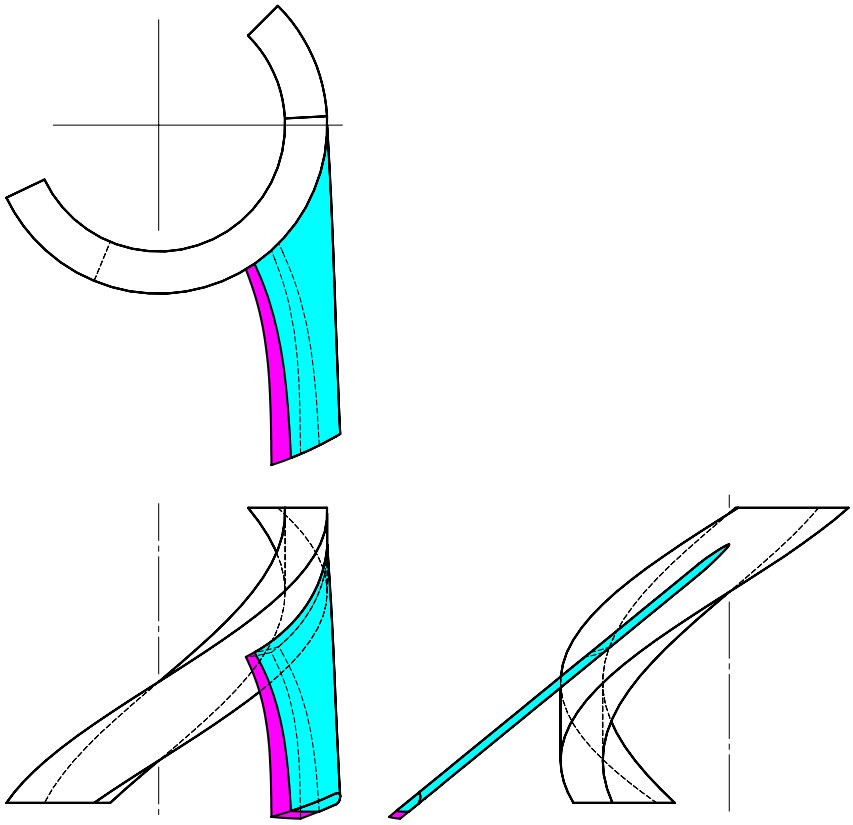

Figure 4.25: **i2** (in cyan) and **i3** (in magenta) N_S650 runner

Analysis of **i3** was carried out primarily to study the effect of β_2 on $N_{\eta_{\max}}$ and also to quantify the relation between β_2 and β_2'. As with **i2**, two fluid models were used to analyze the **i3** runner: inviscid and the standard $k\omega$. Only first-order discretization and base mesh resolution were used Following the conclusions of the previous chapter that discretization order had a lesser effect and the mesh was sufficiently fine. Table 4.5 summarizes the new cases.

Figure 4.26 gives a comparison of the predicted swirl change across the **i2** and **i3** runners at a range of

			Discretization scheme			
Case set	Fluid model	Cells	Press.	Mom.	k	ω
Inviscid	inviscid	415×10^3	std.	FOU		
$k\omega$	$k\omega$	290×10^3	std.	FOU	FOU	FOU

Table 4.5: Summary of **i3** runner computational analyses: *Press.* pressure, *Mom.* momentum, k turbulence kinetic energy, ω specific dissipation rate, *std.* standard, *FOU* first order upwind, *SOU* second order upwind, *PRESTO!* pressure staggering option

inlet conditions, using the base cases. It was expected that the greater turning of the **i3** runner would produce a larger swirl change than the **i2** runner at the same speed. In particular, the adjustment from **i2** to **i3** was an effort to see if the gap in predicted trailing edge flow angle between the **i2** inviscid and $k\omega$ models could be closed by adjusting β_2. Because the change in β_2 from **i2** to **i3** was of a similar magnitude to the difference in β_2' between the inviscid and $k\omega$ **i2** cases, the **i3** $k\omega$ curve was expected to approach that of the the **i2** curve obtained using the inviscid model.

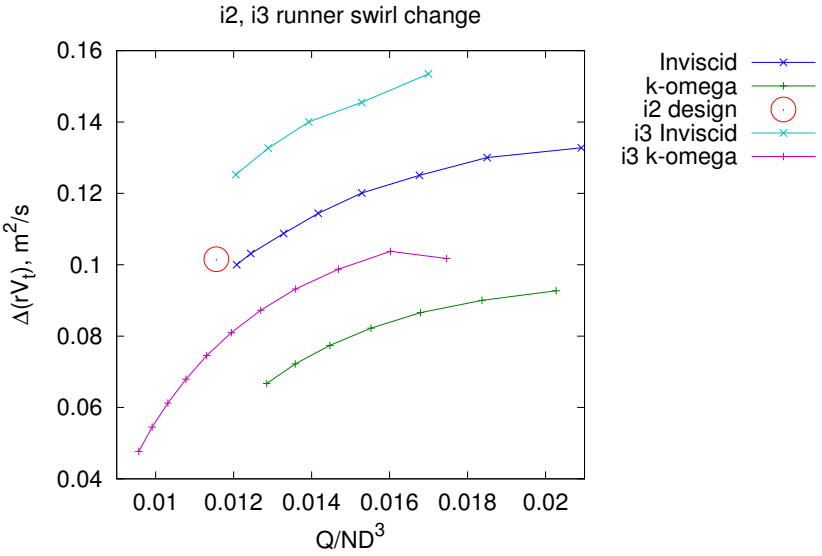

Figure 4.26: Swirl change across the **i2** and **i3** runners

Figure 4.27 illustrates the effect of the 2° change to β_2 on β_2'. A 2° reduction in β_2 was expected to produce a similar change in β_2', since at this point the simple empirical coefficients and blade element theory used to design the runner had been shown to give reasonable results through Figure 4.19 and Figure 4.23. However from Figure 4.27, $\Delta(\beta_2') \approx 0.1\Delta(\beta_2)$, regardless of fluid model. This would seem to indicate that although turbine performance is highly sensitive to flow turning, flow turning is relatively insensitive to blade angle. Quite how β_2' appears so disconnected from β_2 in Figure 4.27 while Figures 4.23 and 4.27 indicate the general agreement of the blade element theory design methods and computational results remains an open question.

Figure 4.28 shows how the **i3** trailing edge adjustment affected the head-discharge characteristic of the runner. From the Euler equation, which relates H_r to T_r, it was expected that the **i3** runner would exhibit a larger head for the same speed, and both fluid models indicated similar and expected changes to the head-discharge characteristic.

Figure 4.29 presents the effect of the **i3** modification on runner efficiency. Since the runner was to operate at fixed conditions, it was important that those conditions occurred as near to the BEP as possible. The design BEP conditions were $Q/(ND^3) = 0.0123$, and Figure 4.24, indicated that BEP of the **i2** runner might occur at a lower speed, or higher $Q/(ND^3)$ than designed. The **i3** adjustment was in part

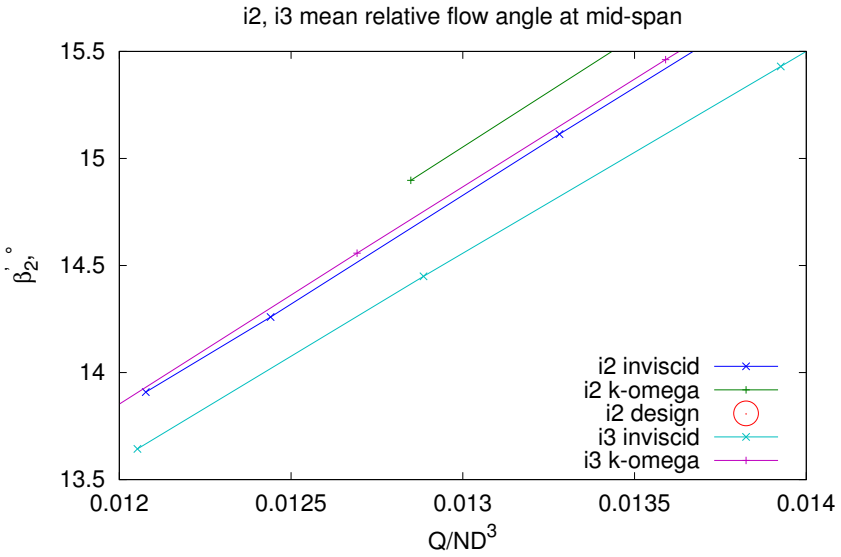

Figure 4.27: Effect of **i2→i3** on mean predicted flow angle relative to runner

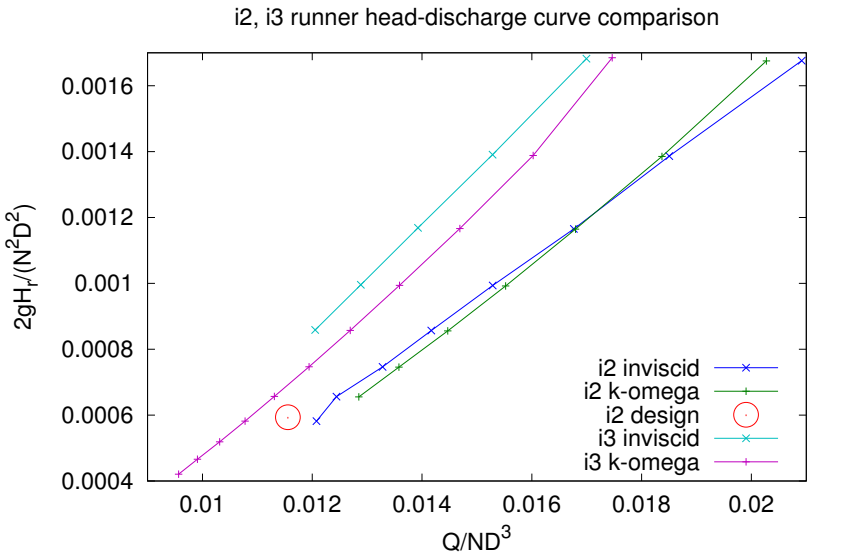

Figure 4.28: **i2-i3** head-discharge curve

made to compensate for this, and the $k\omega$ results show particularly clearly that the conditions for peak efficiency have shifted nearer to the design value.

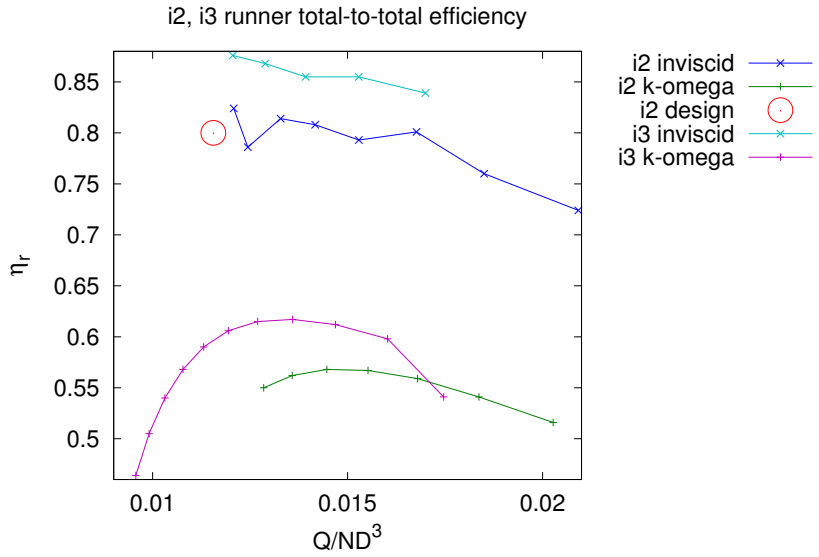

Figure 4.29: **i2-i3** runner efficiency

4.3 Conclusion

This chapter has covered the design of a flat bladed runner to meet a design specific speed of 650 and the computational analysis of that runner using Fluent. The design section showed that although the blade shape is far from standard for this type of turbine, in theory it possessed the correct blade angles for efficient operation. In depth analysis of blade loading, separation, turbulence, and tip leakage was not undertaken. Instead, a single blade passage was modeled with periodic boundaries, first assuming an inviscid fluid, then attempting to model the influence of turbulence with the two-equation $k\omega$ model. The outputs of interest were torque and efficiency, which were calculated over a range of speeds.

The quality of the results was not sufficient to allow confident prediction of the peak efficiency of the runner. The same sensitivity to small changes in the flow field that will challenge the design and fabrication of the runner also plagued these computational analyses.

Although not studied in a comprehensive sense, the effects of mesh refinement, numerical discretization scheme, and fluid model were probed to indicate which modeling choices had the biggest effect. Of these choices, fluid model was most influential. The results fell into roughly two groups depending on whether the inviscid or $k\omega$ fluid model was employed. All other refinements or adjustments produced relatively smaller changes to the output.

The most influential property of the design — the extreme sensitivity of the output torque to variations in trailing edge blade angle at high speed — was revealed only indirectly through the subtly different results of the two fluid models. An eight-bladed runner based on **i3** geometry forms the basis of the N_S650 prototype. The results of this chapter may be carried forward and compared to the dynamometer resulting of the following chapter.

Chapter 5

An N_S650 prototype

The various experimental, computational, and desktop analyses applied to the N_S650 volute, draft tube, and runner cannot definitively predict its real performance. The least uncertainty existed for the volute due to its generally favorable pressure gradient. Its computationally-predicted exit velocity distribution was expected to be a solid starting point for runner design. Concerning the runner, it was expected that the acceleration through the contraction of the volute would lead to thin boundary layers in the runner passage approaching the blades, meaning the inviscid model could closely model the dynamic fluid forces at work. It was expected that peak runner efficiency predicted by the $k\omega$ model of about 60 % would be pessimistic. Finally, the draft tube was the greatest unknown; from the literature and this research, swirl was expected to impact the pressure recovery downstream of the runner, and therefore the net efficiency, and that even a small change in pressure recovery would be significant due to the large fraction of total head embodied in kinetic head leaving the runner.

Measuring performance at a range of heads and speeds revealed the efficiencies and losses of the components. The volute loss coefficient was measured at 0.09, just 0.02 higher than predicted computationally. Runner peak efficiency of 87 % occurred very near design speed, implying that conditions leaving the volute were as intended. Draft tube pressure recovery as a function of mean swirl angle was obtained, with a maximum measured pressure recovery of 0.74. An important open question is what would happen in the expansion from the runner annulus to the circular cross-section of the draft tube. Fluids texts would say to assume the entirety of the difference of dynamic head is lost in a sudden expansion[62], but it was inferred that up to 80 % of this dynamic head was recovered, even when the hub truncates abruptly. This critical region was omitted from the computational model due to its negative effect on numerical convergence, so no comparison with computational results regarding the losses across the expansion were possible. There is a paucity of information in the literature on annular to circular sudden expansions and their sensitivity to swirl. The two-dimensional analog to that geometry is the backward facing step. If experiments have been performed on such flows, they may be in the field of combustors.

This chapter paraphrases the design process for a high specific speed turbine, discloses the prototype details, describes the dynamometer apparatus and the measurement program employed, and finally contextualizes the prototype relative to the Giddens designs it is meant to compliment and evaluates the worth of the computational results presented in previous chapters.

5.1 The design process in brief

The turbine prototype whose evaluation was the basis of this chapter was a mixture of new and old. The starting point was a target specific speed of 650, defined in Equation 1.3 It was intended that the prototype be as large as possible within the constraints of the University of Canterbury Civil Engineering Fluids Laboratory.

Sizing the prototype began with the runner, which was covered in Chapter 4. The runner passage was

limited to cylindrical hub and casing walls. The hub and tip diameters were calculated from empirical coefficients as 72 mm and 158 mm, then enlarged to counter the anticipated higher loss coefficient of the prototype volute relative to the tubular turbines from which the coefficients are derived to 80 mm and 170 mm[30].

After defining the runner annulus, the volute was uniformly scaled to match its dimensions. The 600 mm-wide volute inlet section happened to match that of the fluids lab standard open flume boxes. One of those flume boxes became the prototype intake bay.

While sizing the draft tube, with an area ratio of 4.0, it was noticed that the required length of the conic section of 1.4 m was to be approximately half of the design net head. Regarding the overall configuration of the turbine, it made sense to dispense with a penstock, and use the large rectangular intake of the volute to terminate an open-channel headwater directly. The draft tube was then oriented vertically and descended to the tailwater. This shortened overall plumbed length of the turbine.

Since the N_S650 volute was to terminate an open channel, the available head was limited by the depth of the tailwater pit to about 3 m. Furthermore, maximum flowrate available was 135 L/s. Satisfying those constraints with some margin to test beyond best efficiency point (BEP) led to design conditions of $H_g = 2.5$ m, $Q = 88$ L/s, with a shaft output of about 1.74 kW at 1550 rev/min, and an assumed net efficiency of 80 %.

5.2 Prototype construction details

This section covers prototype fabrication. For details of the testing setup, see Section 5.3. For the definitive reference of prototype geometry as tested, see the latest revision folder for the original Solidworks 2009 documents, as well as drawings in Portable Document Format.

5.2.1 The runner

As concluded in Chapter 4, at high specific speed the shape of the blade and its orientation when fixed to the hub must be carefully controlled to obtain the correct blade angles. Rather than rely on a jig to hold the blade in place while welding to the hub, equispaced slots were cut in the hub into which the blades fit. Minimal welding was required to secure the blade, since the engaged blade material carries any bending load. This also mitigated warping due to unbalanced welds which might have affected blade orientation during cooling. Cutting the slots required three angular degrees of freedom, including the one required to make the eight equispaced slots. Positioning the hub correctly in space in preparation for cutting the slots is an example of Euler angles. The order of the rotations is important to achieving the correct orientation. This positioning was obtained with a tilting bedway and a dividing head mounted at a fixed angle to that bedway. Figure 5.1 shows various stages of runner fabrication and installed in the turbine. Following initial tests with an abruptly truncated tailcone, a conical and an elliptical tailcone were trialled. The conical tailcone gave the best results of these three configurations, and it is these results which will be presented. The prototype was run up to 1950 rev/min with acceptable vibration levels without any special balancing techniques. The use of a taper-lock hub was chosen over alternative options simplicity, symmetry, ease of disassembly, and the ability to reposition the runner axially.

5.2.2 The volute

The volute as built for testing incorporated some flexibility to allow testing of different shapes. A good shape for the downstream end was of the volute was determined through a CFD study to be the "pinch" shown in Figure 5.2, which provided stable and nearly uniform axial outlet flow. The pinch shape was achieved by an insert which could be removed or replaced if other shapes needed to be tested. Also in Figure5.2 is the "flow-fence" insert. Initial computational modeling of the prototype volute showed that

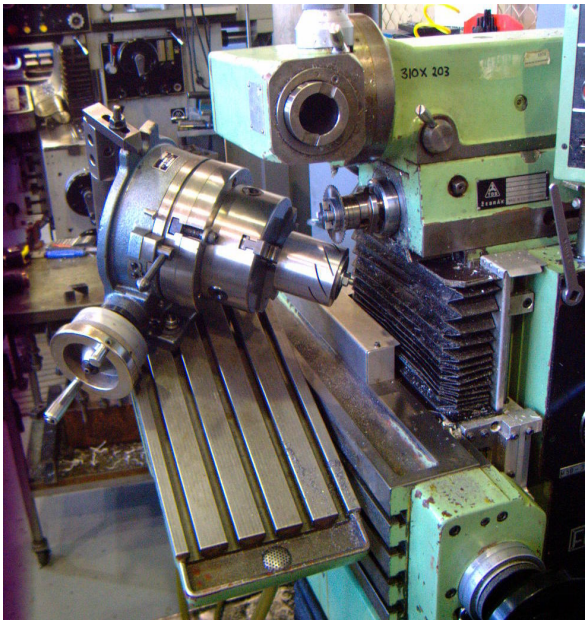

(a) Runner hub mounted on dividing head for cutting of blade slots

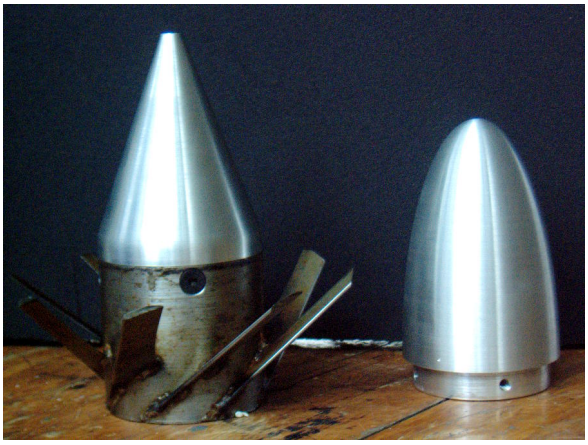

(b) Conical (installed) and elliptical tailcones

(c) Blade connection weld detail

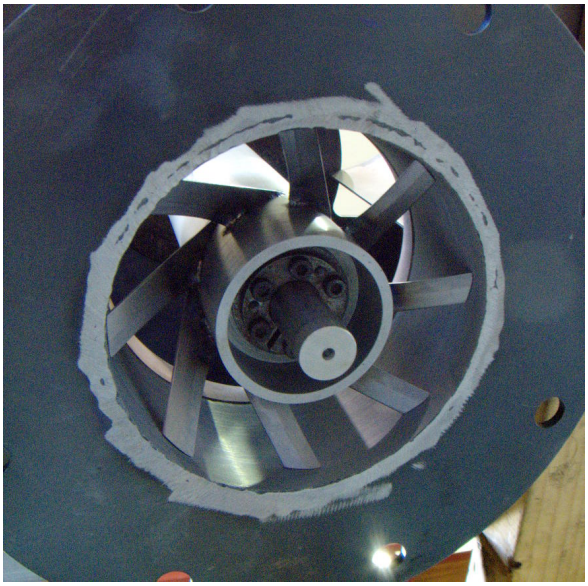

(d) Runner installed in turbine prior to testing

Figure 5.1: Making the flat-bladed runner

without some form of obstruction to encourage flow to the downstream side of the runner hub, a higher axial velocity on the upstream side of the runner hub would result. This would have led to an oscillating angle of attack for the runner when rotating. To achieve the required obstruction with minimal loss, the flow-fence was added. The exit flow resulting from a range of heights and slopes was computationally modeled in Fluentwithin CFX Workbench, and the one with the most uniform flow was implemented in the prototype. The flow-fence was the most complex shape in the entire design, but it was envisioned that in practice, it could be shaped from cement. For purposes of testing its true shape, the prototype made use of a rigid foam insert which used computer numerical control (CNC) machining to produce a part directly from the Solidworks part.

(a) Volute shape inserts: *1* flow-fence insert, *2* "pinch" end insert

(b) Flow fence after machining

Figure 5.2: Volute inserts give some freedom of adjustment to the unproven volute interior shape

5.2.3 The draft tube

The prototype draft tube consisted of a 7° full-angle conical diffuser, with an inlet-to-outlet diameter ratio of 2.0. In the case that priming the turbine would require closing the turbine exit, a parallel "guide" section was added to the end of the cone, allowing a straight outlet pipe to slide up and down on the cone. The turbine was found to prime with the exhaust only slightly submerged. During preliminary testing of the rig, it was noticed that the turbine would reliably prime only if the joint between the cone and outlet pipe was submerged. This leakage issue was solved by packing a fabric seal into the gap and keeping the joint flooded with water during testing, so that any leakage through the joint would be water and not air. The arrangement is shown in Figure 5.3.

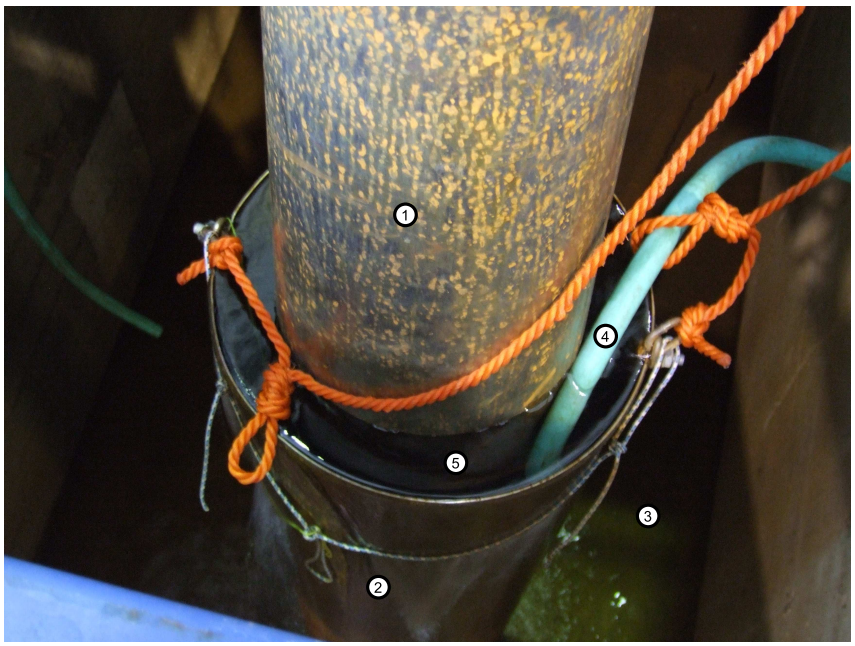

Figure 5.3: Looking down into tailwater pit where the draft tube-outlet pipe joint was flooded to avoid air leakage under suction: *1* conical draft tube, *2* outlet pipe, *3* tailwater, *4* joint flooding water supply, *5* flooded joint

5.3 Executing the experiment

Generating a comprehensive steady-state performance map of the prototype as a whole required measuring torque and flowrate at a range of runner speed and gross head. The runner output was found, along with the net hydraulic potential input, allowing the calculation of net efficiency and specific speed. In addition to overall performance, the performance of each main turbine component was desired. This required knowledge of conditions at intermediate stations. Sections 5.3.1 through 5.3.5 go into more detail about acquiring this data, the operation of the rig in general, and then the dynamometer and hydraulic measurements.

5.3.1 Operational notes

Figure 5.4 gives an overview of the N_S650 prototype and dynamometer, as well as the locations of measurement stations. All dynamometer data was acquired between January 1st to February 10th 2011.

The water originated in the 12 m tower which supplied the lab. The prototype was supplied by several meters of 6-inch steel pipe. Upstream of the prototype inlet, an electromagnetic flowmeter was used for flowrate measurement. Between the flowmeter and prototype, a butterfly valve was used for flowrate control. While the prototype could have been more compactly designed with a closed intake, the free-surface intake formed an integral part of the prototype design, and it was desired to test its operation. As the open flume was only about 2 m long, decelerating the flow with the dissipator shown in Figure 5.5 was required. The key to the success of the dissipator was disallowing any vigorous mixing of air and water on the free surface, while still encouraging swirling underneath. A relatively uniform and bubble-free flow resulted, even at the highest flowrate encountered during testing, as seen in the video clip in Figure 5.6.

The water in the intake flowed under gravity through the turbine and exited through the draft tube into a large pit with a flat floor approximately 2.8 m below the lab floor. At the bottom of the pit there was a large gate valve, which was manually controlled via a lever on the lab floor. Manually controlling the level in the pit proved too tedious for one person to do by hand, so a spillway with removable panels was constructed to allow the valve to be left open, giving a relatively constant water level in the pit. The

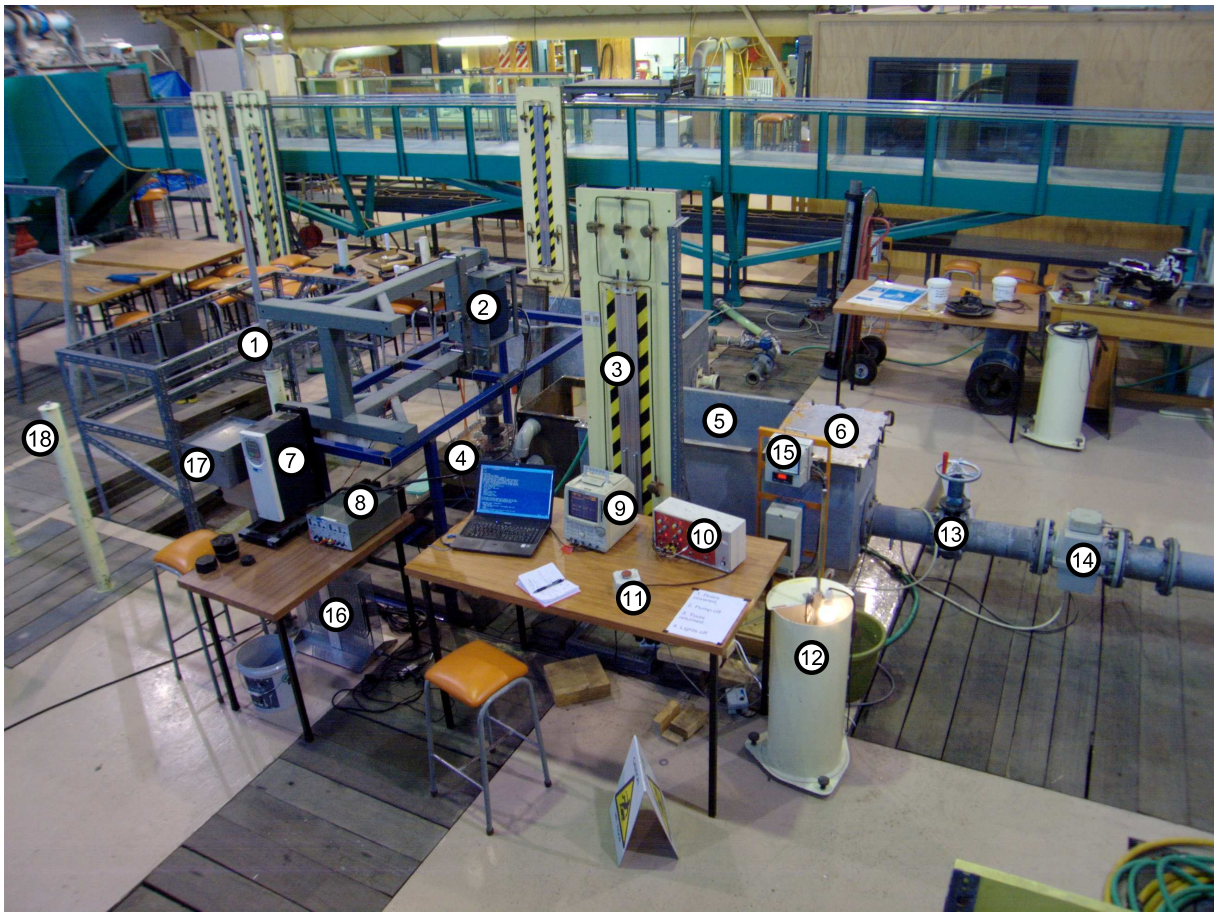

(a) Dynamometer apparatus overview, facing south: *1* tailwater level indicator, *2* dynamometer motor/generator, *3* mercury manometer, *4* volute, *5* open flume, *6* dissipator splash guard, *7* motor speed controller, *8* tachometer power supply, *9* oscilloscope, *10* loadcell amplifier, *11* emergency stop, *12* headwater settling tank, *13* flow control valve, *14* flowmeter, and *15* flowmeter display, *16* motor controller braking dump load (heater), *17* tailwater pit valve control, *18* pit valve position indicator

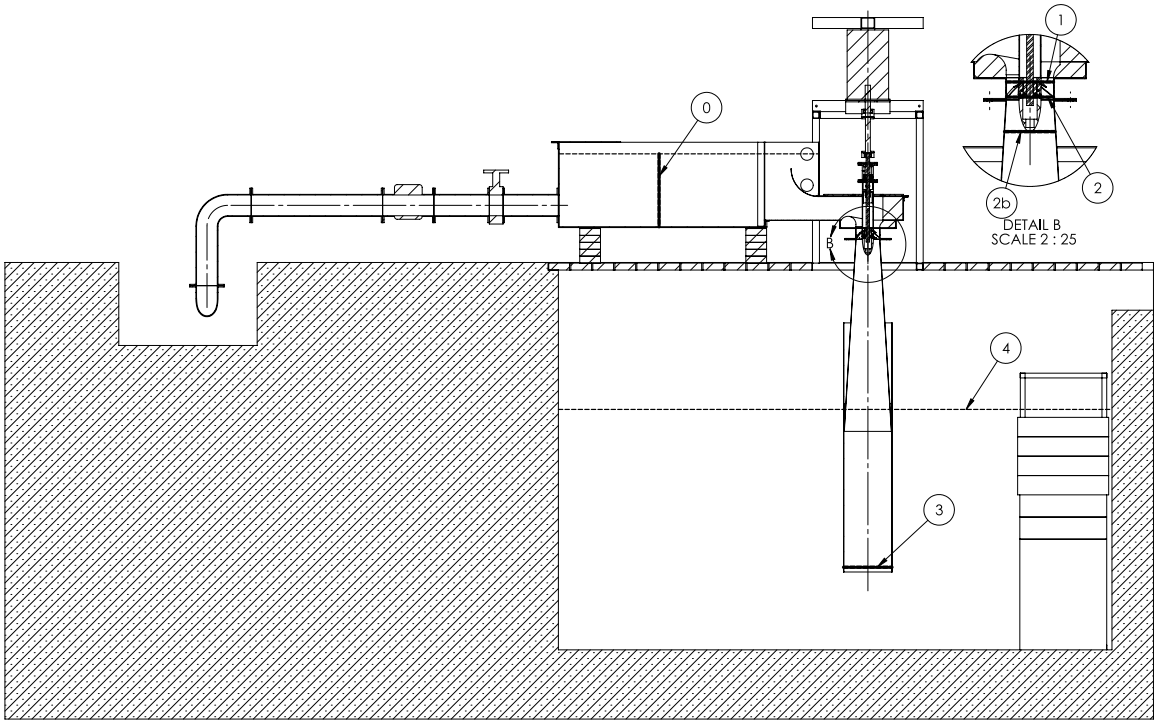

(b) Section view of turbine in lab with numbered stations, facing northeast

Figure 5.4: N_S650 dynamometer setup

(a) Dissipator internals (b) Ready to use

Figure 5.5: Views of the open flume dissipator

There is an inline video here. If your PDF viewer can play inline video, click to activate or use the controls in the caption. Alternatively, open the target video with an external program.

Figure 5.6: Dissipator in operation at maximum flowrate (`../common/DSCF6266.mp4`) Show controls / Play / Pause / Stop / Close

video in Figure 5.7 shows the spillway during operation. Six removable panels of about 15 cm each gave a net head range from 1.8 m to about 2.6 m.

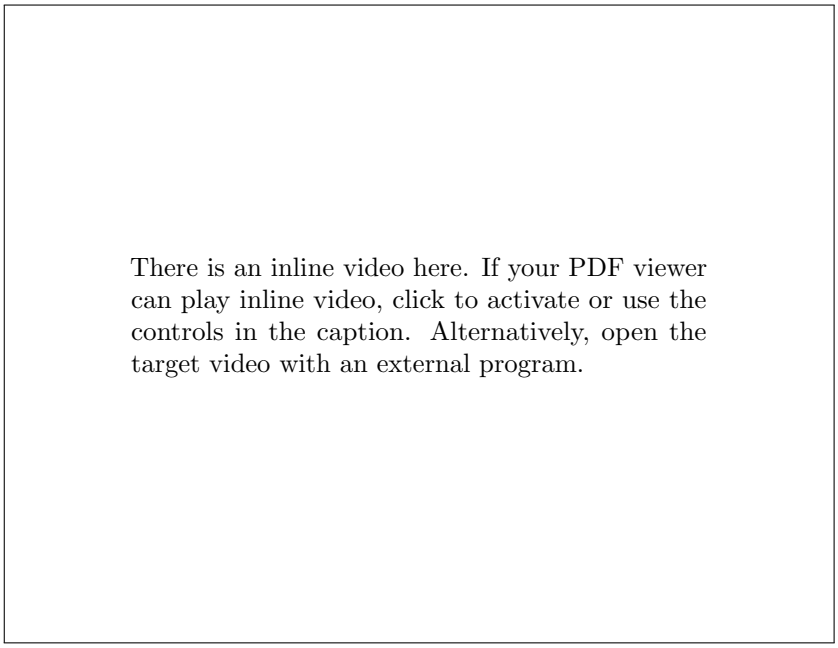

Figure 5.7: Tailwater spillway in operation (`../common/DSCF6267.mp4`) Show controls / Play / Pause / Stop / Close

When beginning a testing session, the first thing was to ensure that all spaces in the turbine were fully primed, that is, free of air pockets, before any measurements were taken. Once the spillway was set to the desired height, the pit was filled quickly by allowing the runner to free-wheel, allowing the largest flowrate. As the water level in the pit rose, decreasing the net head across the turbine, the flowrate gradually decreased until the water breached the spillway. Next, the desired set speed was activated on the motor speed controller, gradually reducing the speed of the runner and further reducing the flowrate. During this entire process, the tester was monitoring the level of the headwater and adjusting the inlet flowrate with the butterfly valve to keep the intake free surface above the volute inlet but below the edge of the flume. Once the set speed was reached, conditions would equilibrate, and smaller valve adjustments were made until the changes were slow enough that measurements could be taken over a period of roughly 20 s which was assumed steady. The video in Figure 5.8 illustrates the start-up process.

Each data point consisted of six individual measurements:

1. runner speed,
2. flowrate,
3. loadcell voltage,
4. headwater level,
5. tailwater level, and
6. station 2 wall pressure.

Data acquisition was done manually, and many times the value was observed to fluctuate, so each recorded measurement was a visual average taken by the author of that fluctuating value. The video in Figure 5.9 illustrates the acquisition of flowrate, station 2 suction head, loadcell voltage, and headwater level near BEP, as well as showing the general state of things at BEP conditions.

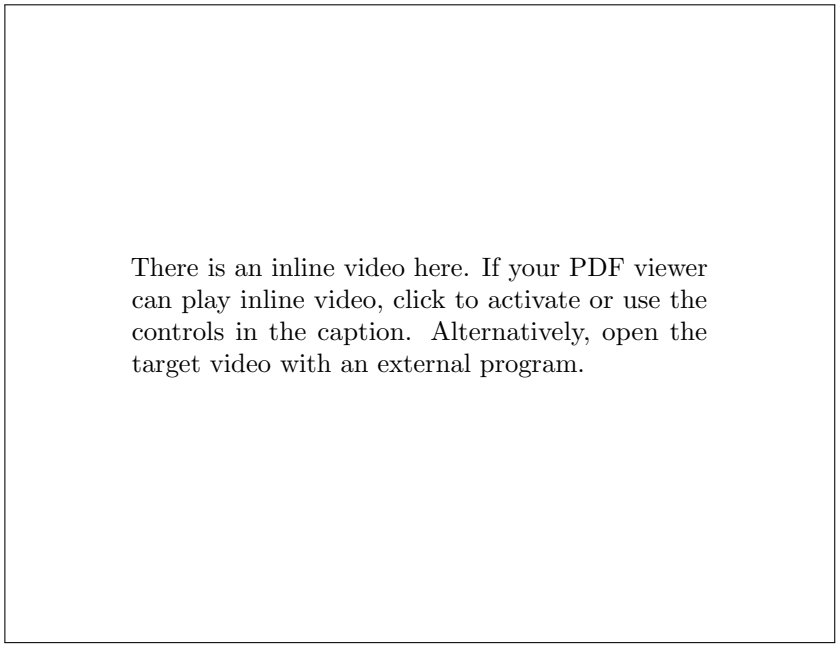

Figure 5.8: Turbine start-up process (`../common/DSCF6273.mp4`) Show controls / Play / Pause / Stop / Close

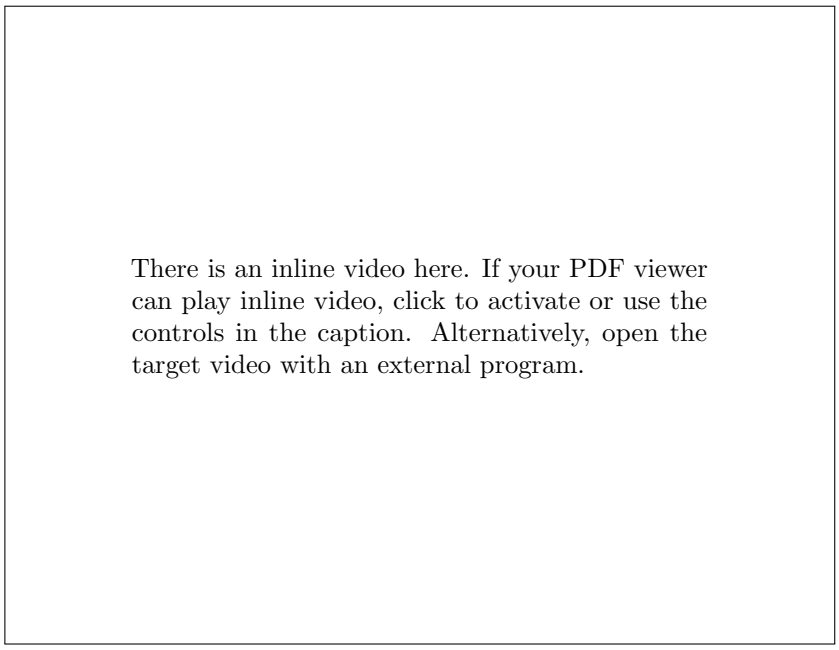

Figure 5.9: Data acquisition process (`../common/DSCF6274.mp4`) Show controls / Play / Pause / Stop / Close

5.3.2 Dynamometer

The dynamometer in this case comprised a 5 kW induction motor, controlled by a variable speed drive, which was equipped with an external resistive load to allow it to brake continuously. To sense torque on the shaft, the motor frame was isolated from its support by two bearings, which supported its weight and allowed it to rotate freely about its centerline. A loadcell mounted to a stationary support resisted the torque on the motor. Figure 5.10b identifies the main elements of the torque measurement apparatus. When torque measurements are being taken, the free body diagram in Figure 5.10a gives the torques on the braking motor chassis, where T_{gross} is the sensed torque, or T_r minus the torque required to overcome mechanical transmission drag.

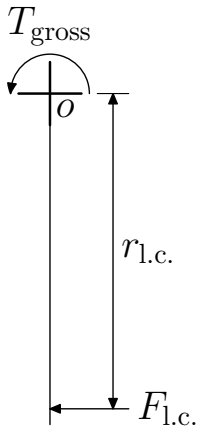

(a) Free body diagram of forces about the braking motor centerline during runner torque measurement

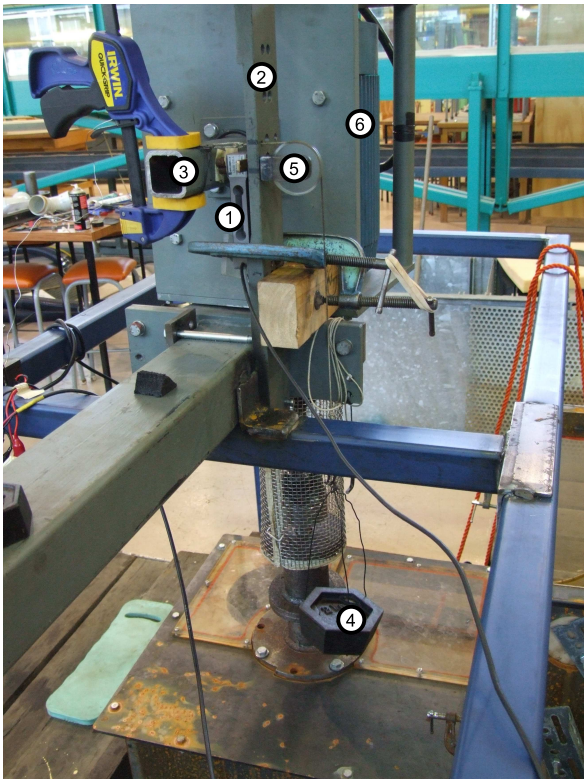

(b) Torque sensing elements of dynamometer: *1* loadcell, *2* loadcell support beam, *3* motor frame reaction arm, *4* 2 kg calibration weight, *5* calibration weight pully, *6* braking motor chassis

Figure 5.10: Dynamometer torque sensing elements

The maximum allowable load for the loadcell was 130 N. The maximum stall torque expected from the turbine was 20 N m. A loadcell arm of greater than 150 mm was required to avoid overloading the loadcell, however calibration accuracy and signal-to-noise ratio would be improved by using more of the available range. Due to construction of the dynamometer support, the loadcell was mounted at approximately 260 mm from the turbine centerline. The loadcell input voltage was approximately 5 V, and the un-amplified output was on the order of a few mV. This signal was amplified such that zero load corresponded to roughly −12 V, and full-load 12 V. The loadcell response was well-approximated by a straight line. This signal was viewed on a Yokogawa digital oscilloscope, whose averaging measurement function provided an approximation of the time-averaged output of amplified loadcell output. Issues of electromagnetic interference and mechanical vibration were overcome by electrically isolating the loadcell from the dynamometer frame and placing a damping material between the reaction arm and loadcell, respectively. Figure 5.11 shows the action of the loadcell damper.

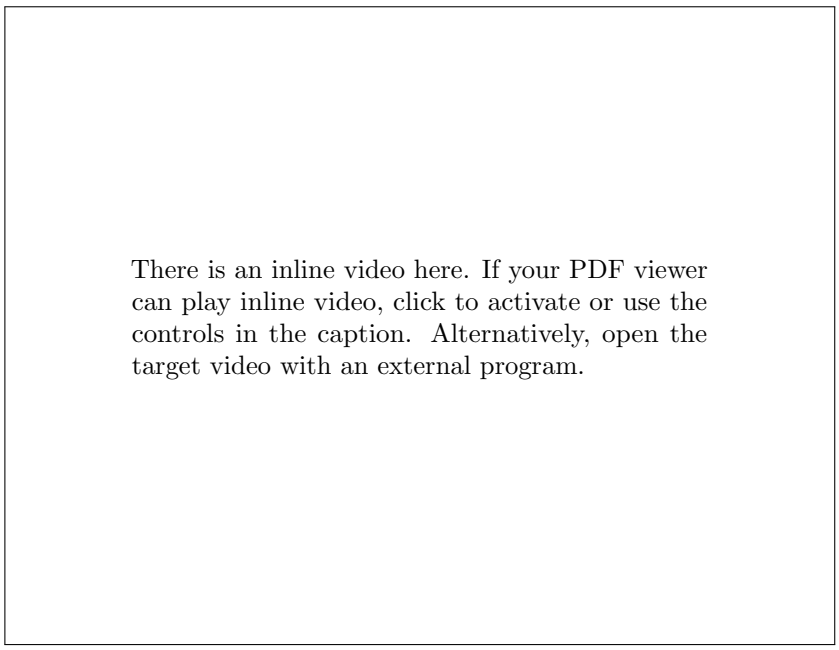

Figure 5.11: Loadcell vibration isolation demonstration (`../common/DSCF6256.mp4`) Show controls / Play / Pause / Stop / Close

As confirmed with a separate optical tachometer, the motor controller set speed was indistinguishable from the measured shaft speed at the range of speeds and loads encountered during testing. The turbine shaft drove the motor by means of a universal shaft. The motor controller set speed was therefore taken as the speed reading for all measurements.

5.3.3 Loadcell calibration

Calibration of the dynamometer loadcell with a known force was critical to obtain trustworthy results. The loadcell was calibrated in place with the turbine dry and with the motor stationary but energized. Calibrating the loadcell in place minimized the possibility of an error due to different conditions when testing versus calibration, however it was also subject to hysteresis in the motor support bearings. To obtain the maximum effect of this hysteresis, the loadcell was gently loaded and unloaded, where the difference in the loadcell output signal across several instances of this test on different days was approximately 200 mV, which corresponded to an error range at BEP of $\pm 0.5\,\%$ of runner torque. The slight vibration throughout testing and the ability of the motor to move slightly due to the aforementioned vibration isolation meant that the actual hysteresis error will be less than $\pm 0.5\,\%$. Figure 5.12 shows the free body diagram of the motor frame as set up for loadcell calibration and a graph of amplified output of the loadcell versus applied force for the run containing BEP. Summing the moments on the braking motor chassis about the motor centerline and neglecting hysteresis yields Equation 5.1.

$$\sum M = 0 = (Fr)_{\text{l.c.}} - (Fr)_{\text{cal.}} - \cancelto{0}{T_{\text{hyst.}}} \tag{5.1}$$

Here, the known calibration force was exerted horizontally by connecting a known mass, $m_{\text{cal.}}$, by string to the motor reaction arm, and running the string over a well-lubricated pully, so the force on the loadcell is given in Equation 5.2.

$$F_{\text{l.c.}} = \frac{r_{\text{cal.}}}{r_{\text{l.c.}}} m_{\text{cal.}} g \tag{5.2}$$

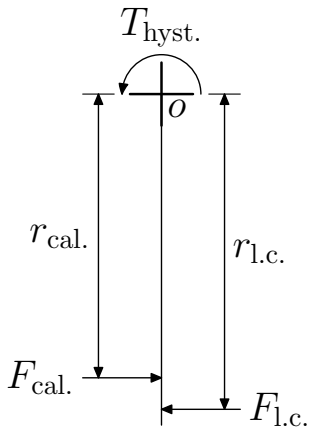

(a) Free body diagram of forces on the braking motor chassis and reaction arm about the motor centerline during loadcell calibration

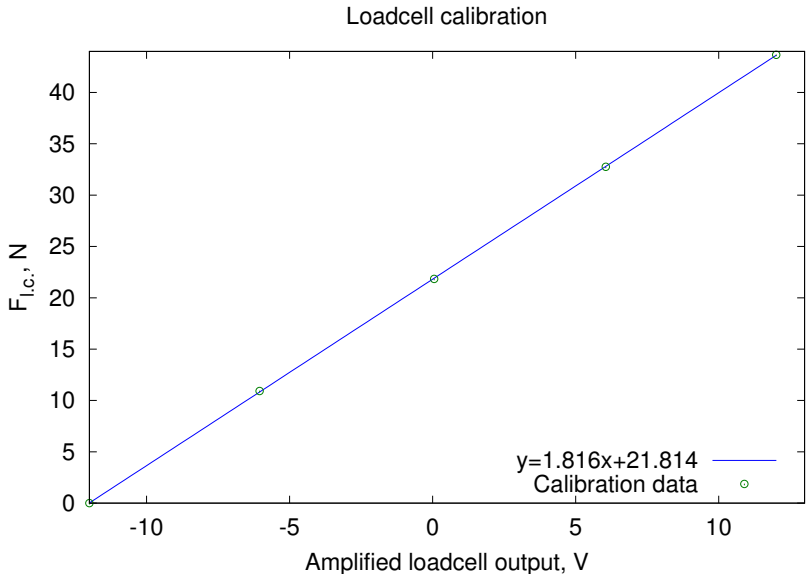

(b) Loadcell calibration for the run containing BEP (`dyno_data_037.m`)

Figure 5.12: In situ loadcell calibration with turbine dry, stationary, and motor energized

5.3.4 Driveline loss estimation

After the loadcell was calibrated, the motor was run at a range of speeds, while the loadcell was used to measure the torque required to overcome bearing drag, allowing bearing drag to be estimated as a function of speed. Spinning the runner in the same direction as during turbine operation produced a resultant torque opposite to that of the calibration weights, so a positive calibration weight, typically 2 kg, was applied so that the net force on the loadcell remained within the calibrated range of the loadcell.

Any time the turbine setup was changed, losses were re-measured, but the values were fairly unchanged from test to test. Above a low speed, the drag torque was relatively constant or increased only slightly with speed. The maximum speed for this test was limited by blade contact with the casing. Although the maximum speed varied with the quality of alignment when mounting the bearing assembly onto the volute, tip scraping would typically occur above 1100 rev/min, worsening with speed.

Figure 5.13 shows the free body diagram of the motor frame as set up for mechanical transmission loss measurement as weel as measurements and the approximating linefit used in subsequent calculations for the run containing BEP.

Equation 5.3 gives the sum of moments on the braking motor chassis about the motor centerline while measuring mechanical transmission drag.

$$\sum M = 0 = (Fr)_{\text{l.c.}} + T_{\text{drag}} - (Fr)_{\text{cal.}} \tag{5.3}$$

After an expression for T_{drag} is adopted, and the dynamometer is configured as in Figure 5.10a, runner torque is the torque sensed by the dynamometer plus estimated bearing drag. Summing the moments on the runner shaft gives Equation 5.4.

$$\sum M = 0 = T_{\text{gross}} + T_{\text{drag}} - T_r \tag{5.4}$$

There were two main weaknesses to this method of bearing drag testing, both stemming from the

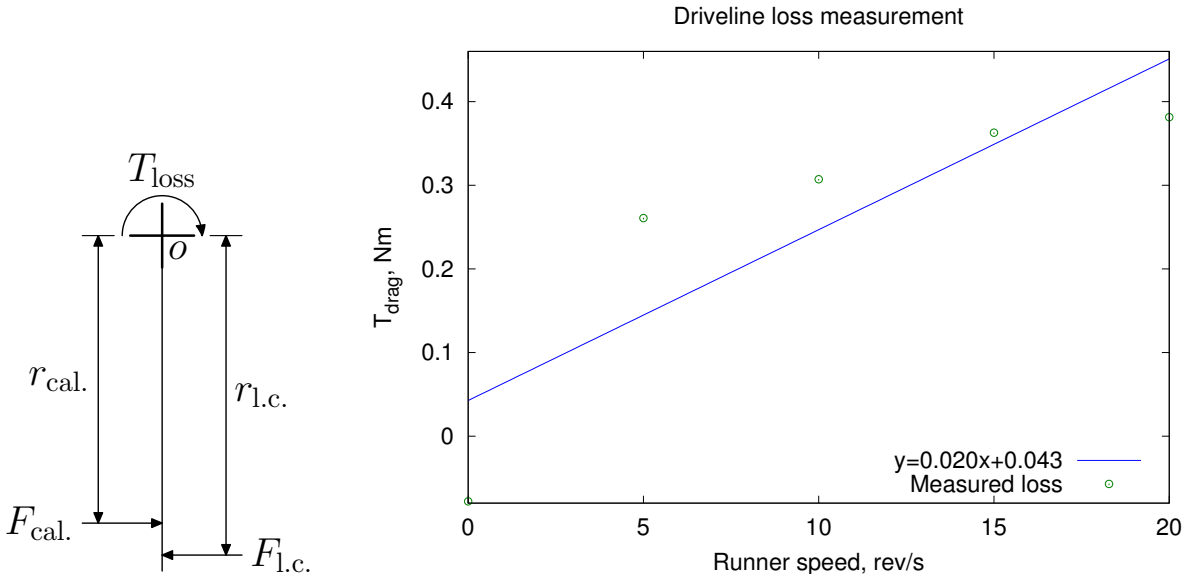

(a) Free body diagram of forces about the braking motor centerline during driveline loss estimation

(b) Measured driveline losses and their approximating linefit

Figure 5.13: Driveline loss estimation

fact that bearing losses were measured under different conditions than those during testing. First, that the turbine was dry for the loss measurement which meant that the axial load due to fluid pressure on the runner while acting as a turbine was absent. This axial load was expected to increase the thrust bearing drag. Therefore the measured loss was only realistic for the two radial bearings, whose load is negligible for either the dry or wet case. Second, while the maximum speed of bearing drag testing was limited by blade tip interference to approximately 1100 rev/min due to centrifugal forces and vibration, the speed obtainable without any noticeable interference during actual turbine testing was higher than the runaway speed, which was at least 2500 rev/min. This led to some uncertainty about the bearing drag at turbine speeds above 1100 rev/min. By observation, blade tip scraping was not present, even at runaway conditions, which made the bearing drag extrapolation more comfortable.

Bearing losses were estimated to be on the order of 5 % of measured torque at BEP, as shown in Figure 5.14, and increased to more than 12 % as the head decreased and speed increased. The uncertainty of bearing drag should be kept in mind when interpreting T_r and other values that depend on it.

5.3.5 Numbered station measurements

Figure 5.4b shows the location of each station where conditions are to be determined. Station 0 was the headwater free-surface, station 1 was just upstream of the runner leading edge, station 2 was just downstream of the runner trailing edge, station 2b was between the runner and the draft tube, station 3 was the draft tube outlet, and station 4 was the tailwater free-surface. All measurements were used to determine the conditions at the station in question, primarily the specific energy measured in meters of water relative to the lab floor and calculated from Equation 5.5. Knowledge of station conditions allowed the losses or efficiencies of the components between stations to be calculated.

$$E = z + \frac{p}{\rho g} + \frac{V^2}{2g} \tag{5.5}$$

Any leakage flows were assumed negligible in comparison to gross flowrate. An electromagnetic

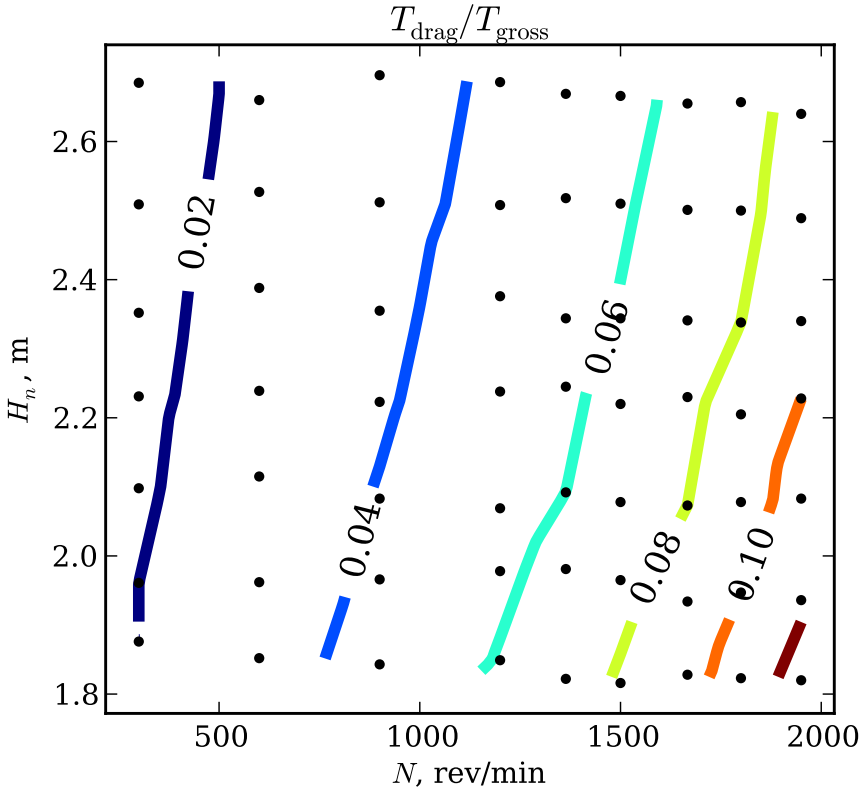

Figure 5.14: Estimated bearing losses as a fraction of measured torque

flowmeter just upstream of the open flume provided all flowrate measurements. When general equilibrium was achieved, the displayed flowrate fluctuated on the order of 1 % of the indicated value, so the recorded flowrate was a visual average over several seconds.

Velocity across station 0 was assumed uniformly horizontal through the rectangular cross-section, and the elevation of the free-surface was obtained from a vernier in a settling tank connected to the open flume by a length of hose. The small mean velocity at station 0 was then calculated from the flowrate and the cross-sectional area of the flow.

The specific energy at station 1 was obtained by subtracting the losses from 0 to 1. The loss coefficient of the volute was measured, and has been expressed as a fraction of the volute outlet dynamic head. The velocity was assumed uniformly axial.

At station 2, the axial velocity distribution was assumed to be the same as at station 1. The tangential velocity distribution was deduced from the measured runner torque, which was assumed equal to $\dot{m}\,(rV_t)_2$. The radial velocity was assumed negligible, as the runner annulus was purely axial, and the turning due to the blades is designed for radial equilibrium at both the leading and trailing edges. The pressure at the wall, relative to atmosphere, was measured with a mercury manometer. A single average pressure measurement was obtained by connecting four equally-spaced wall taps about the periphery of the runner passage to a common line. The radial pressure gradient due to swirling flow was estimated from the assumed $rV_t = \text{const.}$ distribution. This gradient was the used to correct the wall pressure measurement to give the mean static pressure of the flow.

No measurements are taken at station 2b, but it was introduced as the hypothetical boundary between the sudden expansion and the draft tube proper. In this way, the sudden expansion was bounded by stations 2 and 2b, and the draft tube was bounded by stations 2b and 3. Since the only the pressure recovery from station 2 to 3 was measured, an assumption as to the amount of pressure recovered over the sudden expansion from 2 to 2b was required to fairly attribute pressure recovery to the conical diffuser

itself.

Station 3 was assumed far enough downstream of the disturbance of the runner and draft tube to have no radial velocity components. Its pressure was calculated from the hydrostatic equation.

Station 4 was assumed stagnant. The depth of water in the pit was indicated by a buoyant ruler. The marks on the ruler were approximately 30 mm apart, so the uncertainty of estimating a steady reading was very small compared to H_n.

5.4 Measured performance

Results will now be presented that give an objective description of the N_S650 turbine performance. As head and speed were the two independent variables, the natural way to show the data at each point was with a series of contour plots versus these two variables. On these contour plots, a dot indicates where a measurement was taken. All presented measurements were with the conical tailcone installed, because that configuration gave the highest measured net efficiency of 64 %. This was expected from earlier work.[44]

Flowrate increased with increasing head, and except for an anomaly at low speeds it also increased with runner speed as seen in Figure 5.15.

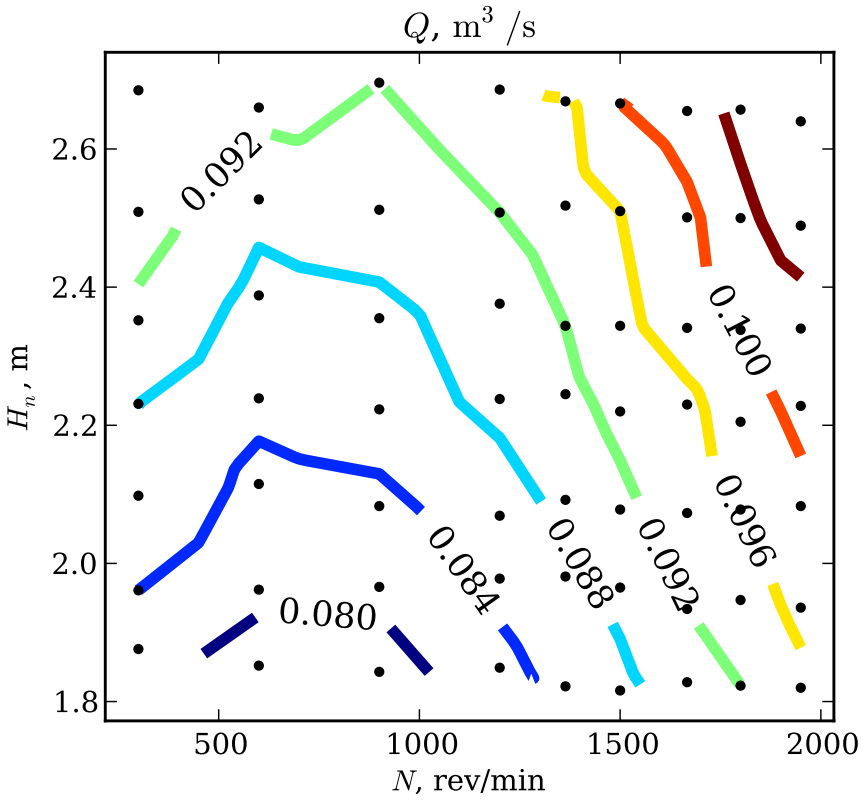

Figure 5.15: Volumetric flowrate

Figure 5.16 gives the runner power measured at a range of H_n and N. Runner output shaft power is defined as ωT_r.

The net efficiency presented in Figure 5.17 was based on the American Society of Mechanical Engineers (ASME) standard, which penalized the draft tube exit velocity, as opposed to the more lenient ISO standard.[8, 15] In terms of the defined stations, $H_n = E_0 - E_4$.

Runner head, defined as $H_r = E_1 - E_2$, was required to calculate the efficiency of the runner alone. Figure 5.18 presents the estimated efficiency of the runner. The net efficiency, η_n, would approach η_r if losses in the volute and draft tube were reduced.

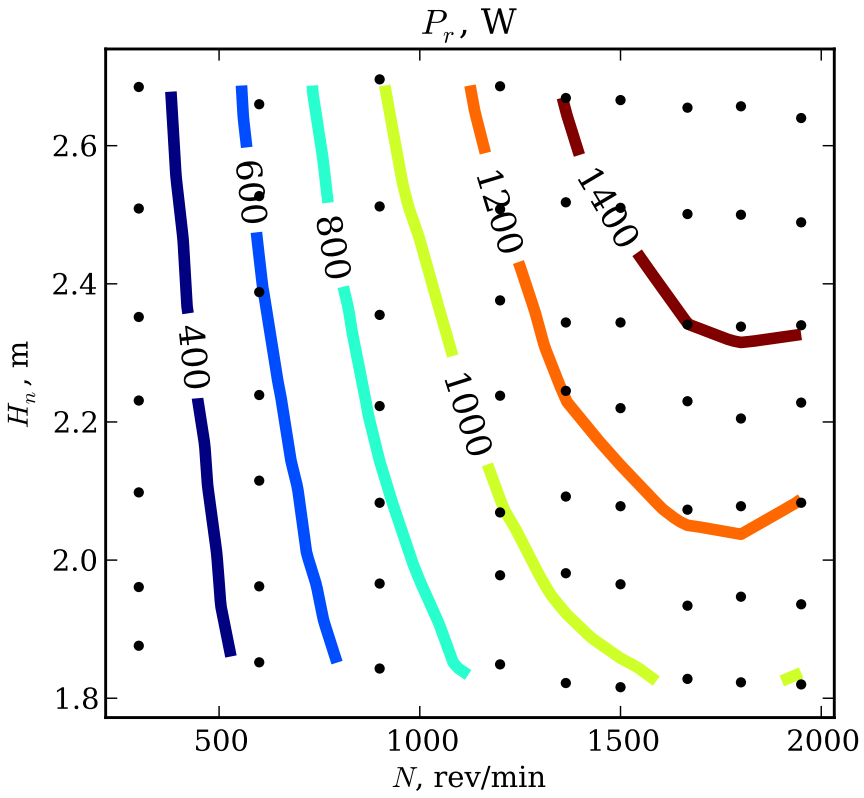

Figure 5.16: Runner power

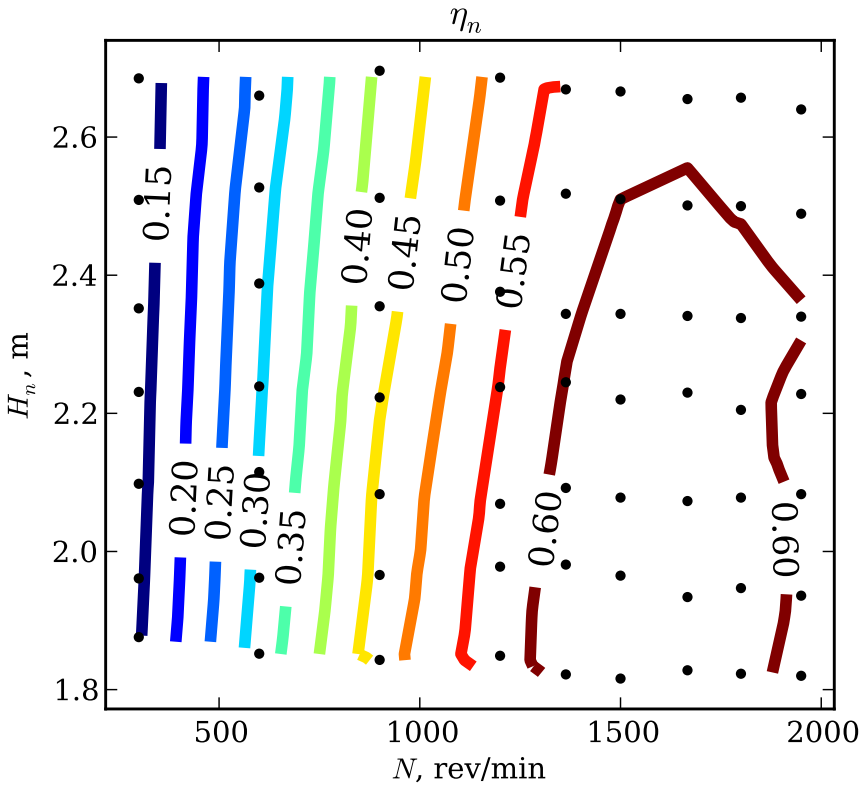

Figure 5.17: Net efficiency (ASME definition)

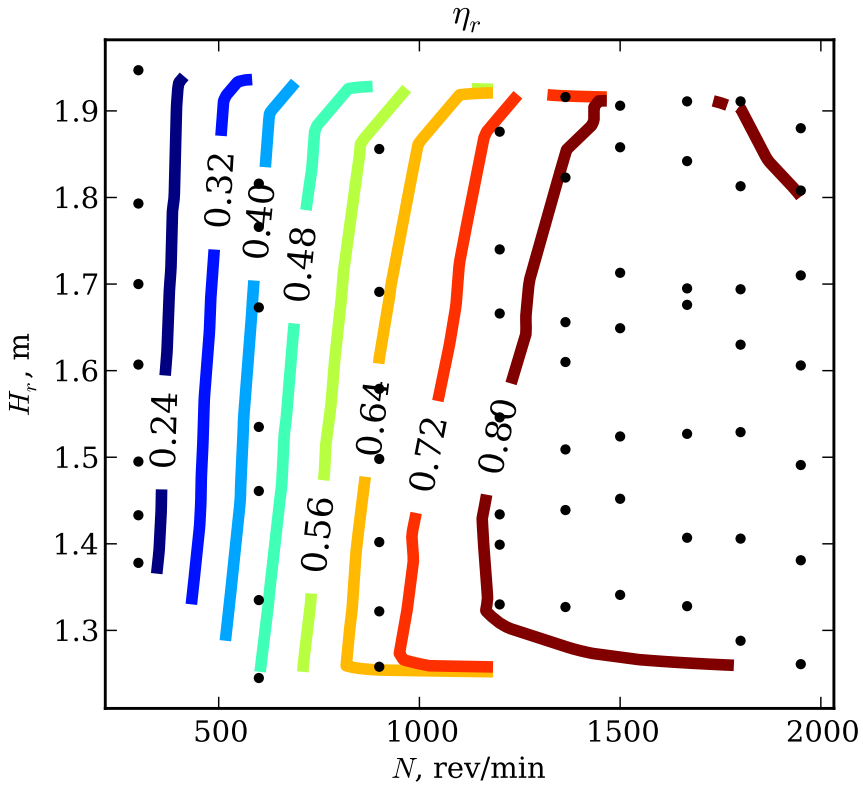

Figure 5.18: Runner efficiency

The turbine efficiency in Figure 5.19 is for direct comparison with results obtained by Mr. Giddens. His head measurement placed the downstream pressure tap upstream of the draft tube, if present. Turbine head was defined as $E_0 - E_{2b}$.

Figure 5.20 shows the dynamic head at the trailing edge, $\frac{1}{2}\rho V_2^2$ as a proportion of H_n.

Recalling Chapter 3, one of the key questions to be answered was the effect of swirl on draft tube pressure recovery. Figure 5.21 gives the measured pressure recovery from the runner trailing edge to the draft tube exit. From the measured torque, the absolute swirl angle of the flow leaving the trailing edge, α_2, may be inferred. Figure 5.21 may be compared directly with the predictions for $2\theta_d = 7°$ in Figure 3.9. It was concluded that the computational model of the diffuser correctly predicted that small amounts of inlet swirl to a $2\theta_d = 7°$ would reduce pressure recovery.

Although not necessarily causal, draft tube inlet swirl and its effect on pressure recovery at high specific speed strongly correlated with overall efficiency, as seen in Figure 5.22.

Figure 5.23 shows the basis of the decision to present the results with the conical tailcone mounted. The linefits help visualize the general trend of pressure recovery over a range of swirl angles only, and should not be used to extrapolate. Somewhat surprisingly, pressure recovery was notably less with the elliptical tailcone installed than with no tailcone at all. The conical tailcone gave a slight improvement over no tailcone at all. This result duplicated earlier measurements by Faulkner, who provided the dimensions for the two tailcones.[22]

While specific speed is often utilized as a shape factor, any turbine may be operated at a range of specific speeds by varying the head and speed, but it is the specific speed at BEP that labels it. Figure 5.24 is the appropriate figure for revealing the this specific speed, and it may be seen that maximum net efficiency occurs at a specific speed of around 740, where N_{Sn} is calculated using H_n. This sounds quite a bit higher than the design target of 650, but note the small difference in efficiency between these two conditions. Consistency with the definition of turbine specific speed would be reason to rename the N_S650

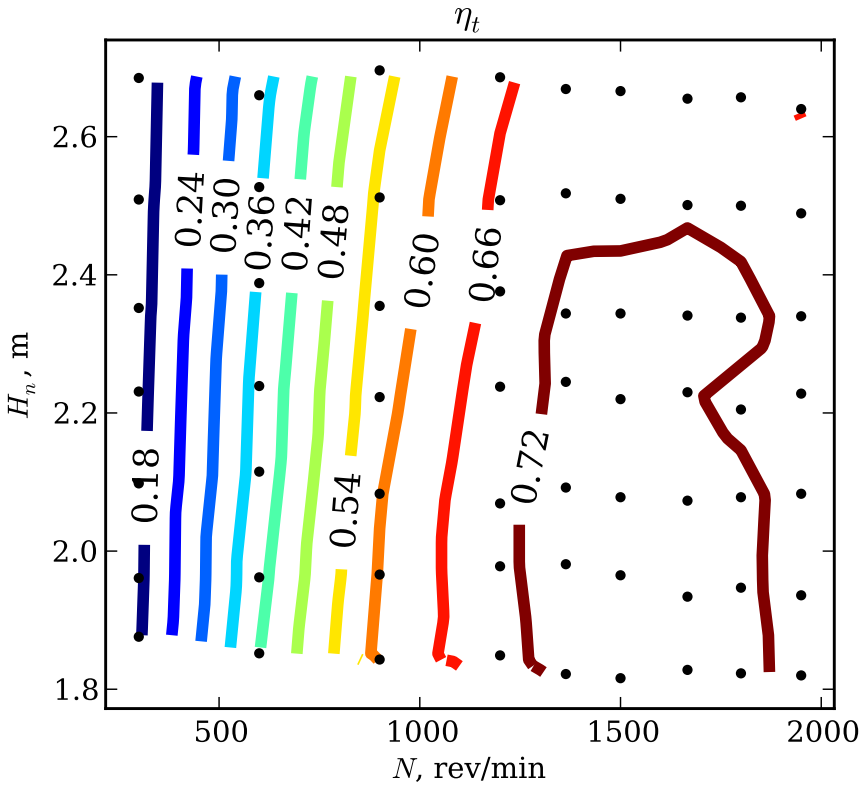

Figure 5.19: Turbine efficiency, for direct comparison with efficiencies reported by Mr. Giddens

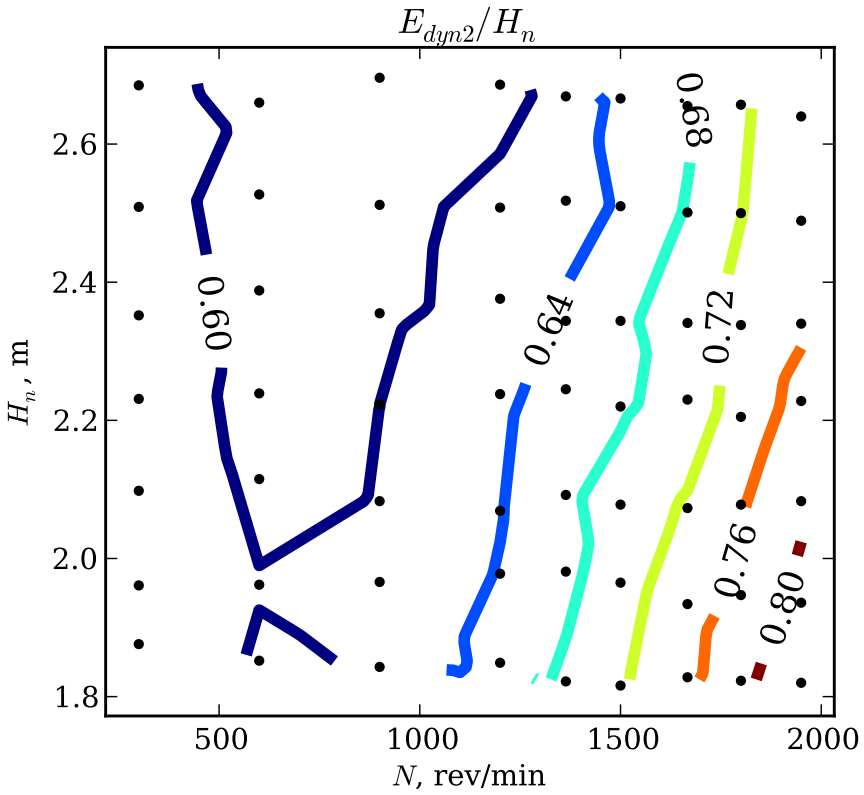

Figure 5.20: Trailing edge (station 2) dynamic head as a fraction of net head

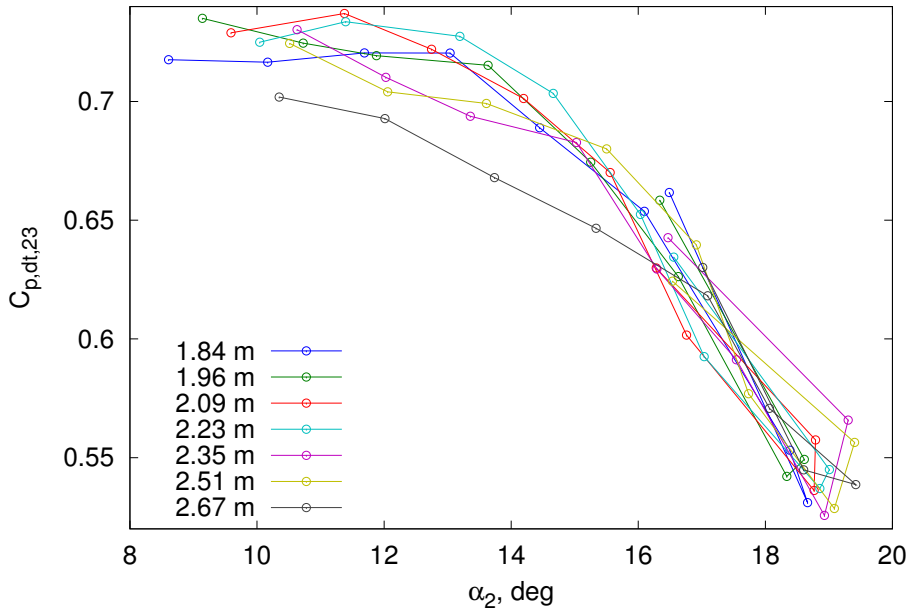

Figure 5.21: Draft tube performance: pressure recovery from station 2 to 3

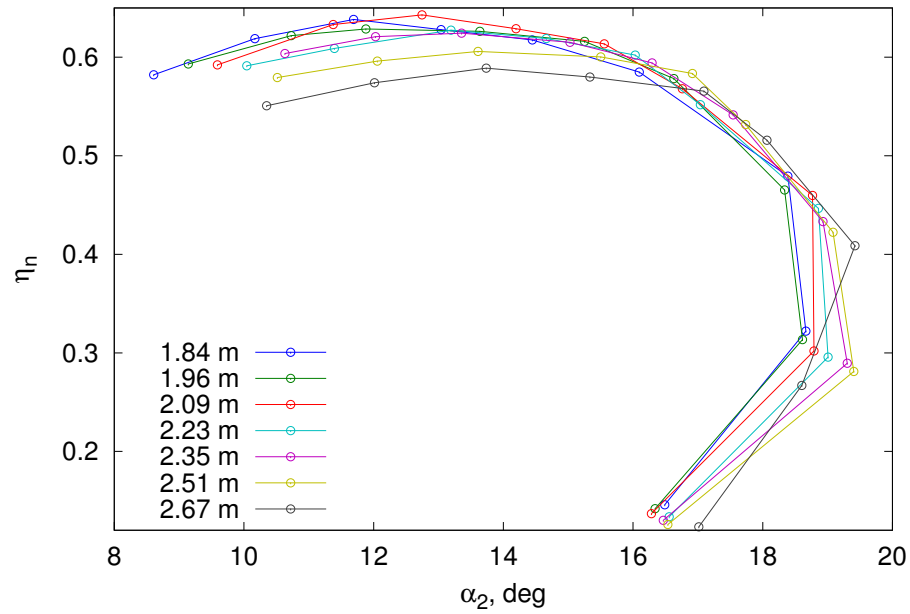

Figure 5.22: The link between runner exit swirl angle and net turbine efficiency

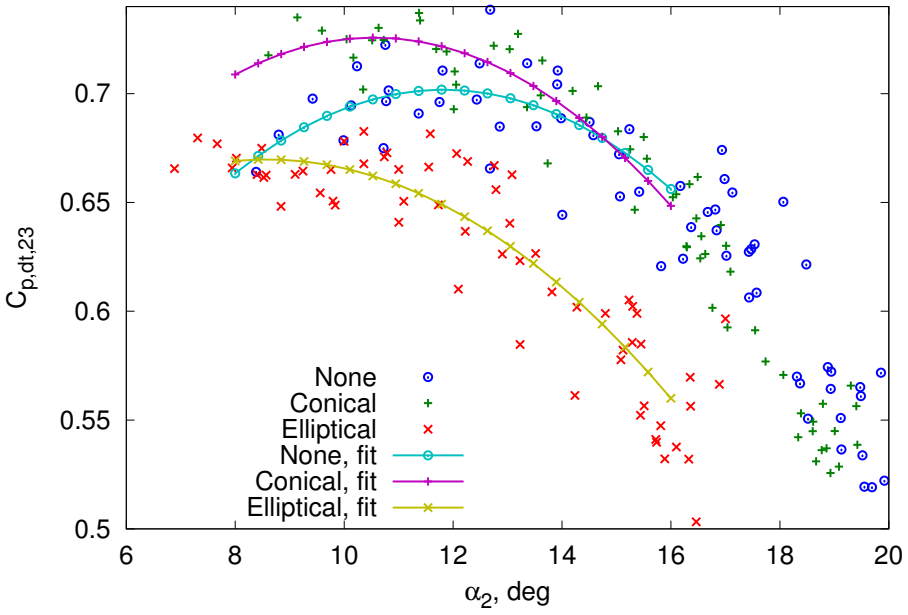

Figure 5.23: Comparison of the effect of runner tailcone on diffuser pressure recovery

Source	K_d
$k\omega$	0.07
Measured	0.09

Table 5.1: N_S650 prototype volute loss coefficient, with data from `dyno_data_008.m`

prototype to N_S740.

Figure 5.25 illustrates the strong relationship between angle of attack and runner efficiency. These values were taken from mid-span.

Due to the Reynolds numbers in the volute being well above 10^5 throughout, total pressure losses were assumed to be driven by turbulent dissipation, and would therefore proportional to the square of flowrate. Prior to the dynamometer measurements, a pressure reading at each of the four taps at station 1 were taken at a constant flowrate. These measurements were taken with the runner removed. This gave an idea of the circumferential variation of flow leaving the volute, and allowed the calculation of a loss coefficient based on mean volute exit dynamic head. Table 5.1 gives the measured loss coefficient alongside the numerically predicted value, and shows that the numerically predicted value was quite realistic. This measured loss coefficient was used to infer the total head loss from station 0 to station 1 for all measurements.

The dimensionless head-flowrate curve in Figure 5.26 succinctly presents the possible operating conditions for the N_S650 turbine. It shows that, as is the case for most turbomachines operating with high Reynolds numbers throughout, kinematic similarity corresponds to dynamic similarity. These clustering of results near the linefit gave assurance that the neglect of viscous forces in favor of inertial forces in the dynamic similarity formulation was well founded. Included on the same plot were the best results from inviscid and $k\omega$ computational models.

The computational results of Figure 5.26 are in best agreement over a limited range of Q/ND^3. From Figure 5.27, this is the region near BEP. The weakness of all computational models trialled was inaccurate prediction of turbine net efficiency.

Similar characteristics for the runner on its own were made by replacing all instances of H_n with H_r, giving Figures 5.28 and 5.29.

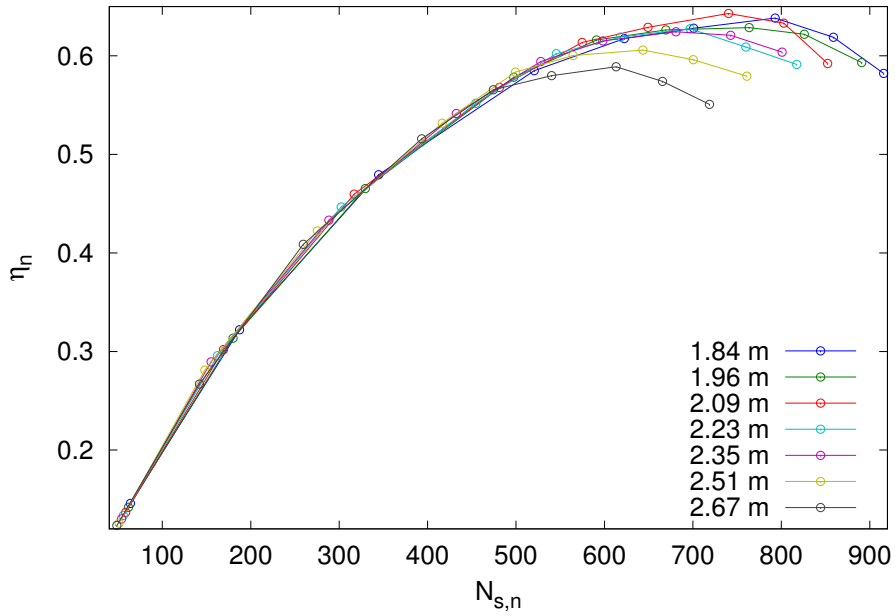

Figure 5.24: Determining prototype specific speed, series labels are nominal H_n

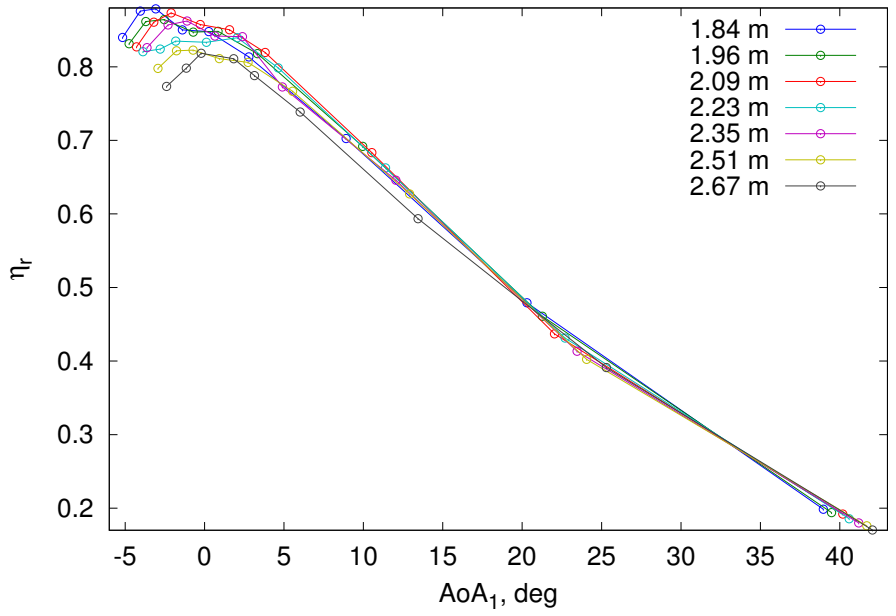

Figure 5.25: Dependency of runner efficiency and mid-span angle of attack, series labels are nominal H_n

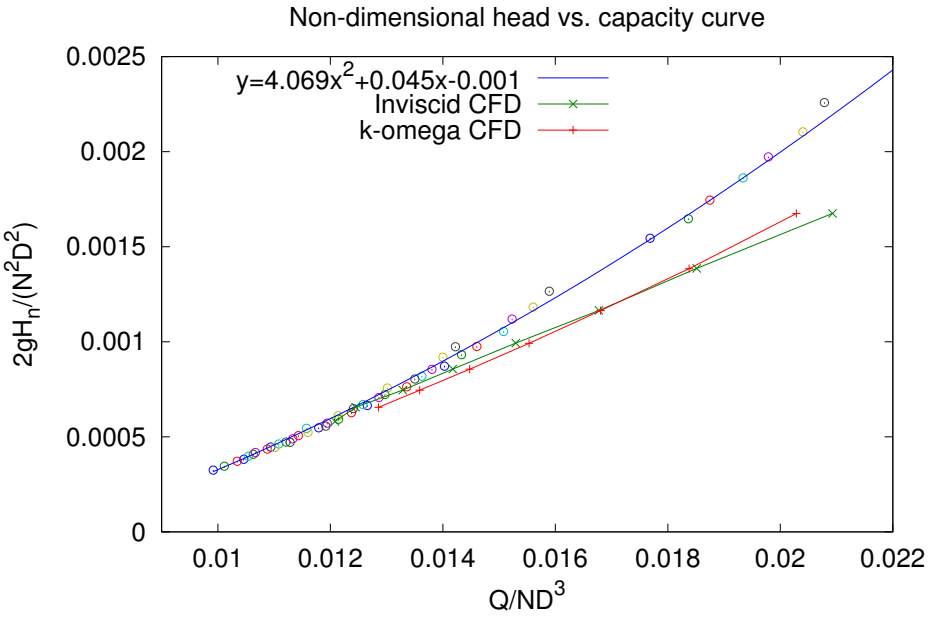

Figure 5.26: The measured and computationally predicted non-dimensional head-flowrate characteristic of the N_S650 turbine. Circles of the same color are values measured at the same nominal H_n.

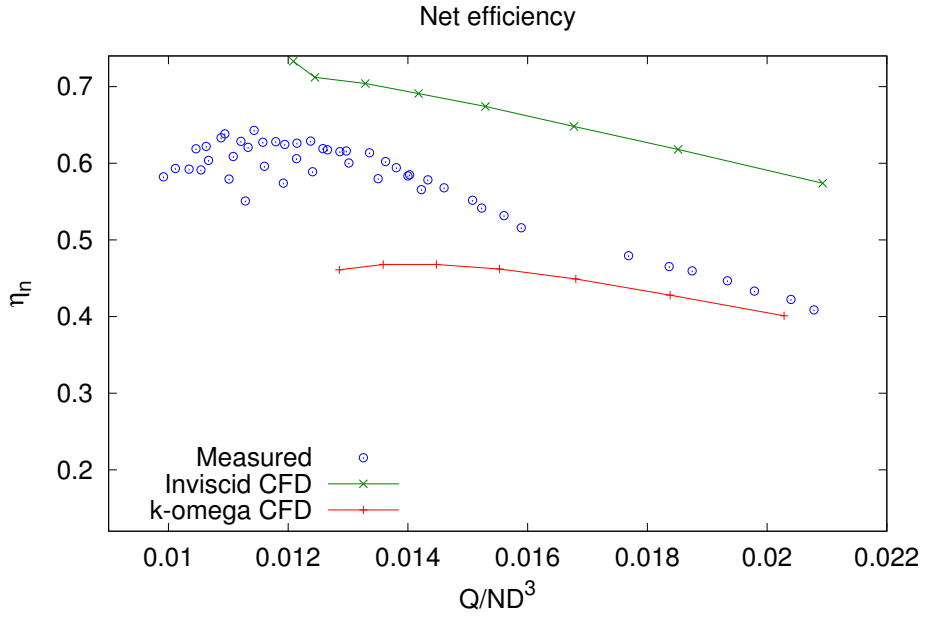

Figure 5.27: The measured and computationally predicted turbine efficiency of the N_S650 turbine

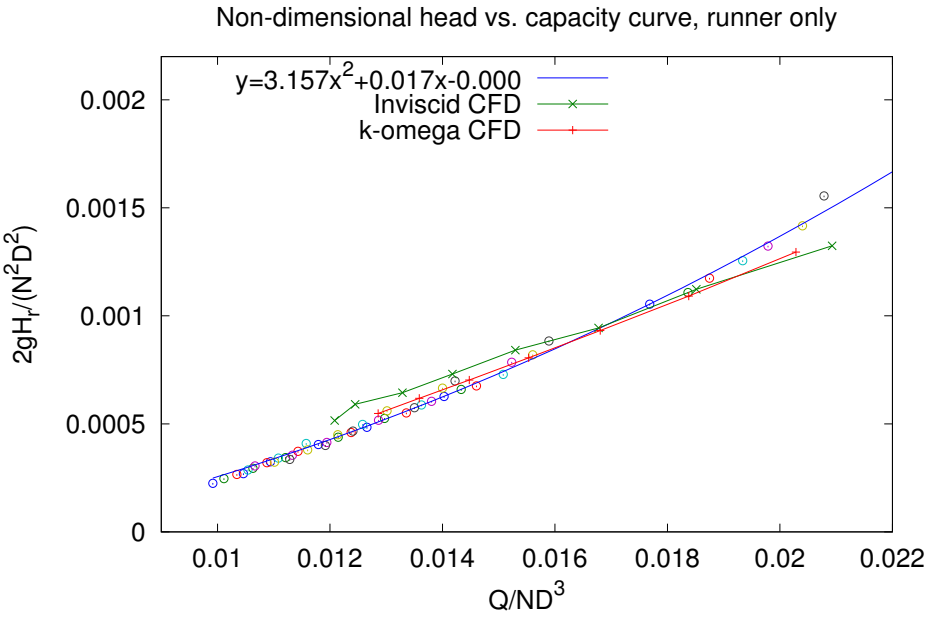

Figure 5.28: the measured and computationally predicted non-dimensional head-flowrate characteristic of the N_S650 turbine runner. Circles of the same color are values measured at the same nominal H_n.

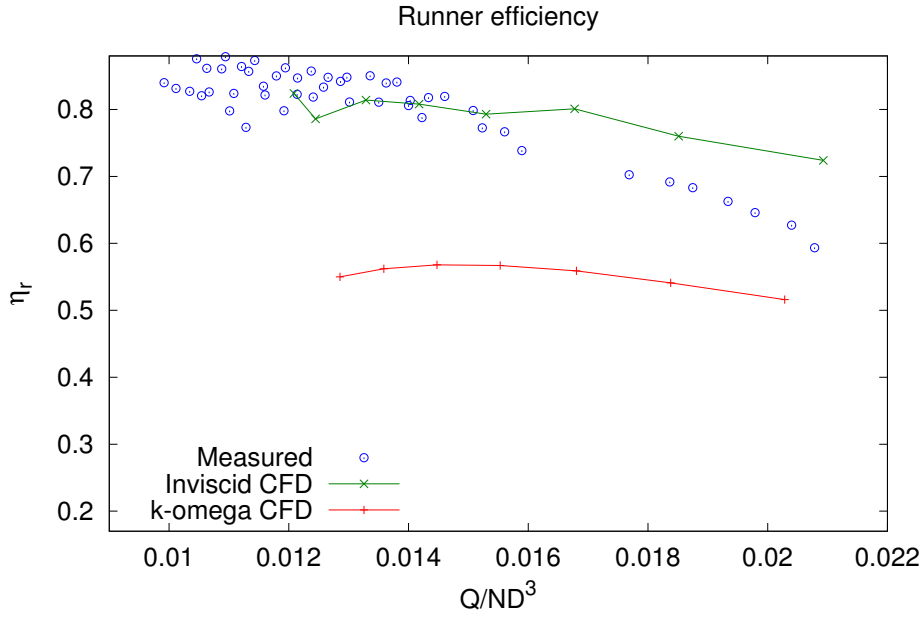

Figure 5.29: Measured and computationally-predicted turbine efficiency of the N_S650 runner

Loss mechanism	Fraction of H_n
Volute	0.062
Runner	0.092
Downstream of runner	0.175
Expansion at 2b	0.058
Draft tube	0.118
Exhaust	0.026
Total	0.357

Table 5.2: N_S650 prototype loss breakdown at BEP. Items in italics depend on an assumed pressure recovery across the sudden expansion of 0.80

Figure 5.30 gives the mean values of the three terms of the Bernoulli equation, Equation 5.5 — elevation, static pressure, and kinetic energy — at each of the named stations detailed in Figure 5.4b, normalized by H_n, for the BEP run.

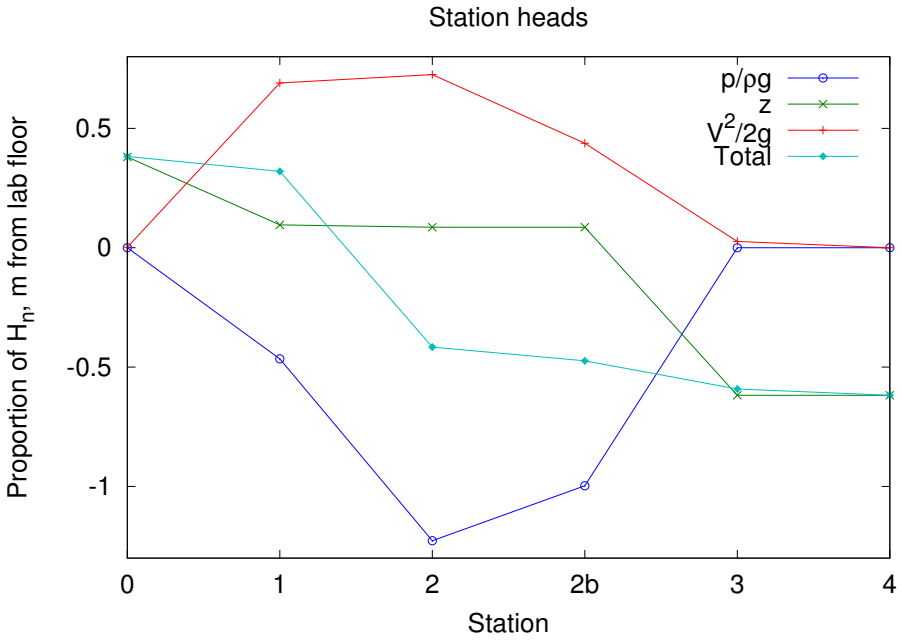

Figure 5.30: Station energy components for the run containing BEP (`dyno_data_037.m`)

Losses may be attributed to regions of the turbine bounded by known stations. A breakdown of component losses near BEP is given in Table 5.2. The losses sum to $1 - \eta_n$ because the components listed covered all stations from 0 to 4. No data existed to attribute losses within the listed components. A partial exception to this was the distinction of losses between stations 2 and 3 into sudden-expansion and draft tube losses. Station 2b was created to distinguish between these two loss mechanisms, and the numbers in Table 5.2 reflect an assumed pressure recovery of 0.80 from station 2 to 2b. Sudden expansions may usually be assumed to have zero pressure recovery, but the value of 0.80 was justified by best agreeing with the pressure recovery from station 2b to 3, which was estimated from data in the literature.[40]

As a measure of the quality of the design method, the design and measured BEP conditions are presented together in Table 5.3. Design values are from Table 4.1. In retrospect, the decision to increase the runner diameter by several percent from the value suggested by the empirical coefficients was unnecessary, and probably contributed to the mismatch between design and BEP conditions.

Parameter	Value		
	Design	BEP	At design
N_S	650	740	588
N, rev/min	1550	1650	1550
H_n, m	2.5	2.1	2.5
η_n	0.8	0.64	0.60
P_r, W	1740	1240	1440
Q, L/s	88	94	97

Table 5.3: N_S650 prototype design values, best measured performance (BEP), and measured performance at design head and speed

5.4.1 Measurement uncertainty

The uncertainty of measurements used in this experiment will now be presented. All measurements used for these results are one of the following:

1. mean static head on a given cross-section of the stream,
2. mean dynamic head on a given cross-section of the stream,
3. volumetric flowrate of the stream,
4. runner rotational rate,
5. loadcell force, or
6. bearing resisting torque.

Knowing the values of each individual component allowed the uncertainty of derived values, such as H_n or P_r or η_n to be calculated.

Uncertainty of the static and dynamic energy as a proportion of net head is given in Figure 5.31 for each numbered station. The uncertainty of H_n, which is defined as $E_0 - E_4$, is the sum of the uncertainty of the total head of stations 0 and 4—less than 1 % of H_n, or about 2.5 cm. Stating the uncertainty as a proportion of H_n is a convenient format for determining the uncertainty of other heads defined as the difference in E between two stations. For example, the uncertainty of H_r, defined as $E_1 - E_2$, is about $0.06H_n$ or 16 cm.

The uncertainty of the flowrate measurement had three sources: the fluctuation of the reading, the ability of the open flume between the flowmeter and turbine to store a variable amount of water, and leakage. The fluctuations of the indicated flowrate for any given reading were approximately ± 0.5 L/s, which was equivalent to the uncertainty. The uncertainty due to the second component was harder to quantify, however it may be estimated. All measurements were recorded only after the author felt that steady conditions had been achieved. This meant waiting until there was no perceptible change in the depth of water in the open flume, or less than 3 mm/s in either direction. The plan dimensions of the open flume were 1.5 m by 0.61 m, so the maximum flowrate which could have been accumulating or leaving the open flume, that is, the maximum possible difference between the metered flowrate and that which is passing through the turbine, was $1.5\,\text{m} \times 0.61\,\text{m} \times 3\,\text{mm/s} = 2.7\,\text{L/s}$. At BEP this is an uncertainty of approximately 3 %.

The uncertainty of the measured runner power had three components:

1. runner speed,
2. torque, and
3. bearing losses

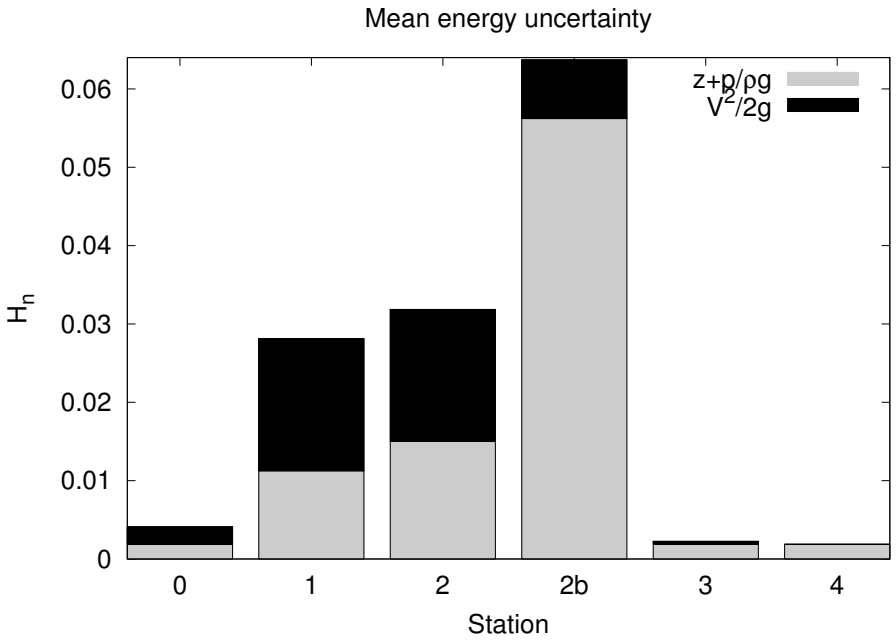

Figure 5.31: Uncertainty of static and dynamic head components at each of the 5 numbered stations given in Figure 5.4b, as a fraction of net head

The motor speed controller was used to control and also indicate runner shaft speed. The indication of speed given by the speed controller was verified against a independent tachometer to be correct within the tachometer precision, which was no worse than 0.3 rev/s. This test was performed at a low speed near peak torque, when the slip, and therefore controller speed error, was expected to be greatest. From then on, the speed indicated by the motor controller was used directly.

Measured torque was the product of the force on a loadcell which resisted the motor shaft torque and its moment arm about the motor centerline. The loadcell was a force transducer which nominally produced a voltage proportional to an applied force. Re-calibration of the loadcell was carried out when any changes were made to the apparatus, if there had been any significant delay since the last calibration, or if there was any other reason to suspect the most recent calibration might be invalid. Figure 5.12 shows a typical calibration result, indicating that there was no significant error in replacing the measurements with a linear approximation. The force of the loadcell near BEP was about 30 N.

Hysteresis in the bearing supporting the motor was observed to affect the torque measurement. This was worst when the loadcell was deliberately loaded or unloaded very slowly which produced a range of about ±200 mV, and was least noticeable when the motor frame was allowed to vibrate and come to rest naturally, giving a range of about ±50 mV. As the entire rig was vibrating slightly during testing, the lower limit seemed the most appropriate figure. The uncertainty due to hysteresis was then $\pm 50\,\text{mV} \times 1.8\,\text{N/V} = 0.09\,\text{N}$, or less than 0.5 % of the measured torque at BEP.

Accurately measuring the radial location of the loadcell was not without its uncertainty. The nominal distance was 255.5 mm, with an uncertainty of ±1.5 mm. This amounted to an uncertainty of 0.6 %, which had a proportional effect on the measured torque.

Finally, estimating the torque required to overcome losses in the two radial roller bearings and one thrust roller bearing in the turbine bearing assembly and the universal driveshaft connecting the turbine to the dynamometer was possibly the most significant source of uncertainty affecting the measurement of power output. Without estimating transmission losses, there was no way to distinguish hydraulic losses in the turbine from friction losses in the bearing. In contrast to the satisfactory curvefit achieved for loadcell calibration, Figure 5.13 indicates the possible magnitude of discrepancy between estimated and real transmission losses. Section 5.3.4 explained why efforts were not made to find a better approximation

than is given in Figure 5.13. Essentially the drag of the thrust bearing was expected to be a function of not only speed, but also axial load, which was not able to be varied during the estimation of mechanical losses. At approximately 27.5 rev/s, where BEP occurred, mechanical losses were estimated to be 0.6 N m, which was 0.2 N m more than the highest bearing loss the author was able to measure due to speed limitations while running dry. This difference may be taken as an approximation of the uncertainty of the transmission loss measurement. This was slightly greater than 2 % of T_r at BEP.

Calculating the uncertainties of two important derived quantities will illustrate the compound impact of these uncertainties. In terms of measured quantities, $P_r = ((Fr)_{\text{l.c.}} + T_{\text{drag}})\,\omega$, and the uncertainty of this quantity was ±4.8 % at BEP. Derived from that, $\eta_n = \frac{P_r}{\rho g Q H_n}$, and the uncertainty of its component measurements gave a maximum range of 70.5 % to 58.6 % at BEP.

5.4.2 A note on tip clearance following testing

It was discovered after the several weeks of testing were completed that the runner tip diameter had shrunk considerably. Originally, the radial clearance between the blade tips and casing was 0.5 mm, which grew to 4 mm by the end of testing, or from 1 % to 9 % of blade span, due to the blades being bent downstream. While running the runner dry at high speeds to measure driveline drag, the blades would occassionally touch the casing. The resulting vibrations exhibited positive feedback on more than one occasion, rapidly and loudly bringing the runner to a stop. One or more of those episodes presumably bent the runner blades inward, since the bending moment due to static pressure during normal operation was well within the elastic range of the blade material. Such an increase in tip clearance could decrease runner efficiency by as much as 10 %.[18] Protecting the runner from this type of extreme would be important for future testing.

5.4.3 Comparison to Giddens propeller turbines and others

To compare the N_S650 to others, Figures 5.32 and Figure 5.33 are provided. Figure 5.33 reproduces Hothersall's Figure 6.4[30], which is a compilation of non-dimensional efficiency curves for a wide variety of reaction turbines, from Francis to tubular propeller. Overlain on the image are measured operating points of the N_S650 as well as the Giddens propeller turbines. Figure 5.32 indicates how η_n and η_t vary with n_{11}, which allows the reader to place BEP on Figure 5.33. The N_S650 operates outside the envelope of existing designs, although peak η_n is less than the other designs in Figure 5.33.

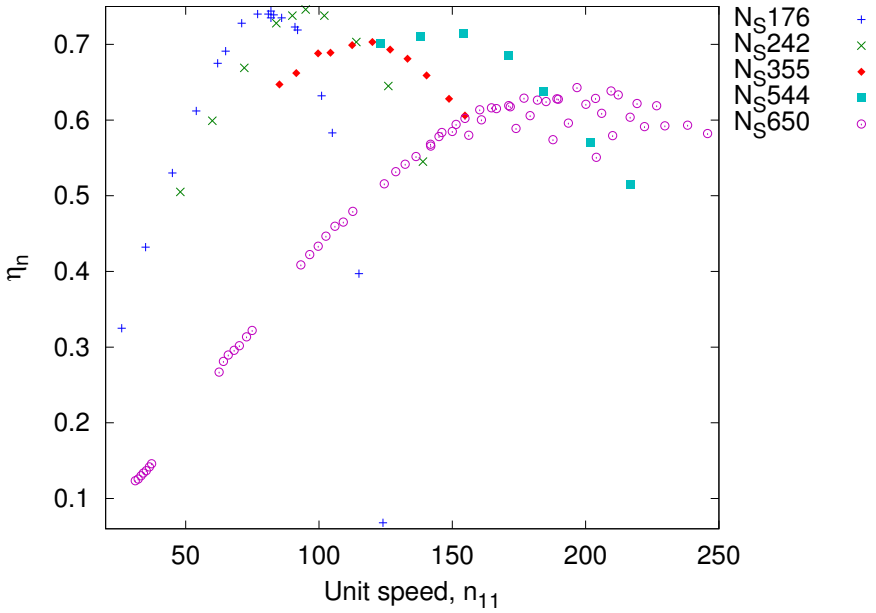

(a) Net efficiency

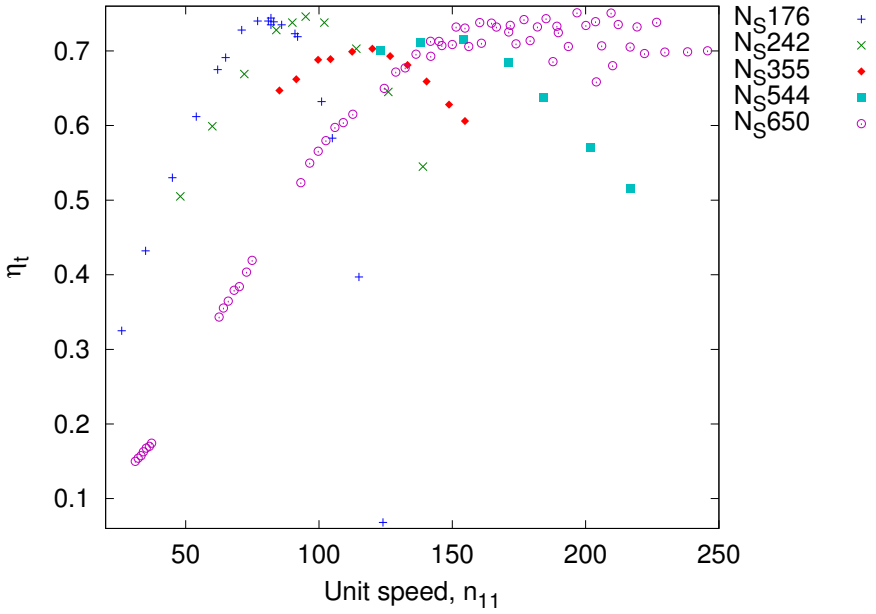

(b) Turbine (Giddens) efficiency

Figure 5.32: Efficiency versus unit speed, for use with Figure 5.33

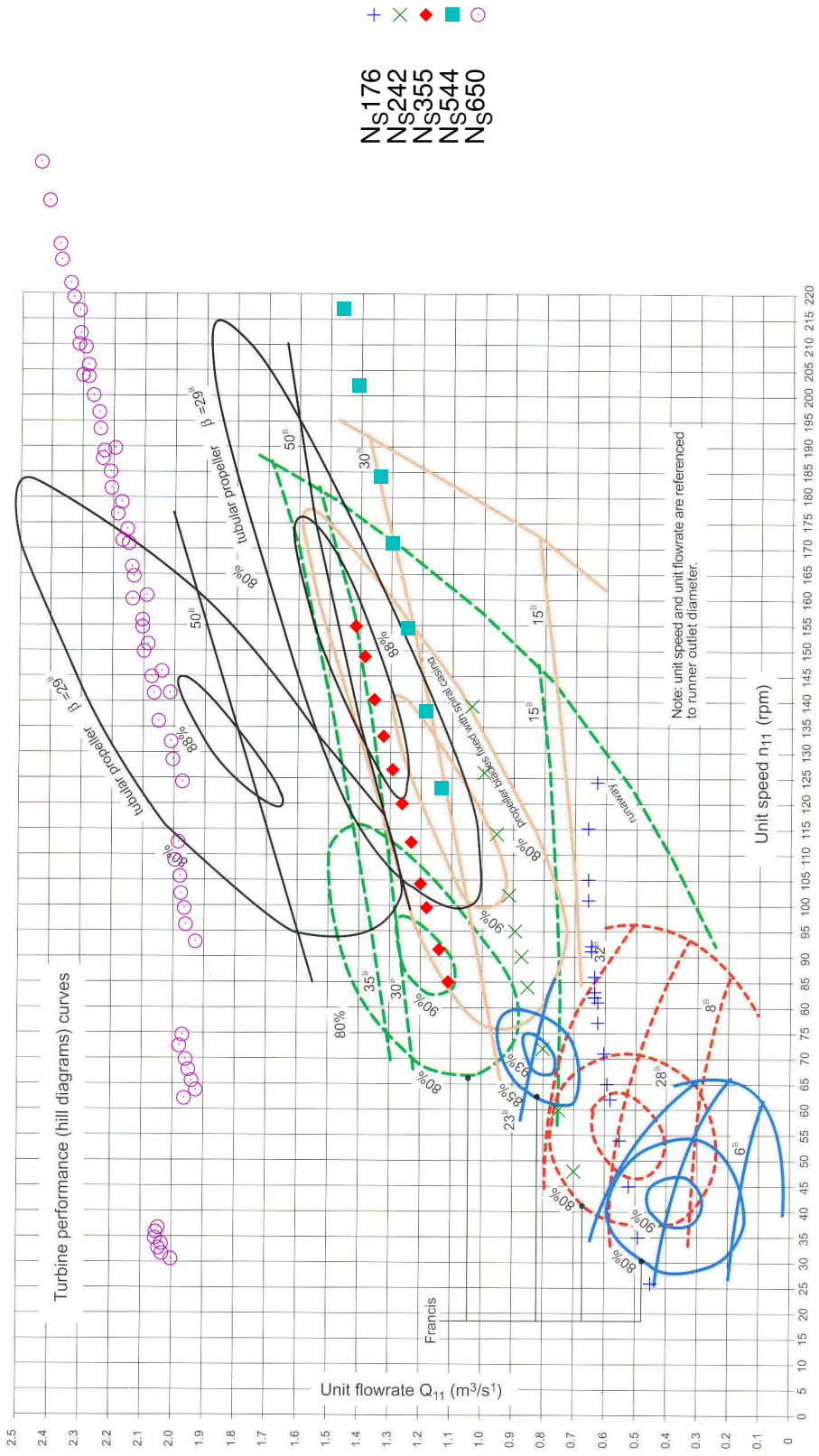

Figure 5.33: Contours of η_n comparing the N_S650 and Giddens propeller turbines with established small-hydro designs, in a figure reproduced from Hothersall[30]

Chapter 6

Conclusions

On volutes Shifting from the STIV to an axial design was a major change from previous designs. The decision was prompted by the measured change in angular momentum through two STIVs. Compared to the N_S176 and N_S544 volutes, the axial-outlet flow volute has a simpler shape, a lower loss, and less uncertainty regarding the outlet flow distribution. Peak measured runner efficiency of the N_S650 prototype efficiency occurred near design conditions, indicating the volute outlet flow was as expected. Losses incurred downstream of the runner by swirling flow were more than compensated by dispensing with the tangential inlet volute.

Flat bladed runner computational analyses Flat blades are particularly well suited to high specific speed turbines due to the high speeds and small amount of turning required. The discrepancy in predicted torque between two computational fluid models highlighted the sensitivity of runner torque to blade angle in such runners. The computational model of the flat bladed runner is not yet a useful tool for obtaining exact efficiencies, although predictions of conditions at which peak efficiency will occur may be of some use to designers. Velocity traverses upstream of the prototype runner would allow validation of volute and runner computational results and improvement of the computational models.

Draft tube swirl computational analyses The effect of an annular stream, with swirl on the order of 20° off-axial entering a conical diffuser was shown by computational methods to affect diffuser pressure recovery. Accurate modeling of this region is important because the fraction of net head embodied in dynamic head at the N_S650 runner exit is over 70 % of net head. Velocity traverses downstream of the runner would give more realistic inlet boundary conditions for analysis of the draft tube. Much of the kinetic energy is lost not only in the draft tube itself but in the sudden expansion downstream of the runner hub. The computational model of the entire region downstream of the runner deserves improvement.

The N_S650 prototype Its stated goals were: achieve a specific speed over 600, an efficiency of at least 70 %, at a speed of 1550 rev/min. However, when those goals were initially laid out, 'efficiency' was not explicitly defined. Efficiency relies on a definition of head. Net head defined by the American Society of Mechanical Engineers (ASME) is ideal for comparing turbines fairly, which requires testing with a full circuit, including a draft tube in place. The tests of the N_S544 that Mr. Giddens performed were done without draft tube in place, and therefore those results excluded the effect of losses due to a real draft tube. In the presented results of Chapter 5, this was the difference between η_n and η_t. The N_S650 prototype reached a maximum η_t of 75 % and an η_n of 64 %, so the success of the N_S650 in terms of achieving its target efficiency of 70 % depends on the definition used. The peak measured efficiency of the prototype runner, η_r, of 87 %, is only 3 % less than the efficiency of the most similar runner found in the literature, which included the additional complication of a rolled leading edge and operated at a lower specific speed.[34]

Opportunities for improvement The additional measurements suggested earlier — velocity traverses at stations 1 and 2 — would give a clearer picture of where improvements could be made. Much of the losses in the prototype stem from the high dynamic head through the runner. The benefit of a naturally high shaft speed and smaller plumbing and equipment typified by high specific speed is penalized by the losses incurred by these high velocities. Exploring reduction of this kinetic energy by reducing the hub diameter or increasing the tip diameter is worthwhile. The downside will be working further away from the empirical coefficients which were used to size the prototype in the first place. Reducing the average velocity through the runner would lower all losses: volute, runner drag, sudden expansion following the runner hub, and draft tube recovery. One negative effect will be an even further flattening and distorting of the runner blade camberlines.

Comparison of the N_S650 to existing designs Despite the large number of low-head designs, the N_S650 has its niche. It has no flow-spanning structures which sets it apart from most of the designs in Section 1.5. The N_S650 shares the same overall 90°-bend form with the siphon design, which is appealing in that it may be slung over an existing weir.[48] Adapting the N_S650 to operate as a siphon design would require the addition of a priming system, rotating the whole apparatus 45°, and mounting to the crest of a weir. When comparing to the Archimedean screw, the advantages of high specific speed become obvious; the size of that design makes it unattractive to remote locations. The volute of the Canadian 'vaneless' turbine developed resembles the design which lacks guide vanes and produces weak swirl which Mr. Giddens was looking for with the N_S544 volute; in the case of the N_S650, however, $B_S = 1$ which simplified the volute altogether seems the easier option. Finally, the simplicity and economy of the sub-kilowatt turbines are appealing apart from their small runner passages and struts which are necessary to support the motor. These features would presumably make them more liable to clog than a design such as the N_S650.

Comparison to an earlier low-head Giddens design The N_S650 prototype deserves some special comparison to a research turbine developed during an earlier Masters thesis at the University of Canterbury.[22] In particular, the research undertaken here has addressed many of the 'Future Work' items listed there. The method of designing blades from flat sheet has been made more rigorous here, calculating the correct flow angle all across the span of the blade, rather than only at the tip. A volute design which avoids the use of guide vanes has been found. The performance of the draft tube in its own right, as well as the importance of minimizing the maximum velocity head in the runner by increasing the cross-sectional area, have both been echoed here. The improvement in efficiency noted with the use of a conical tailcone has been confirmed.

Research Proposal objective The Research Proposal promised the delivery of "a freely available design for an efficient high-specific speed microhydro turbine of simple construction and robust operation". Chapter 5 presents this design.

Bibliography

[1] *Fluent 6.3 user's guide*. Fluent, Inc., 2006.

[2] R B Akhmedov and F K Rashidov. The aerodynamic characteristics of vortex burners with axial-tangential vane units. *Thermal Engineering*, 16(4):78–82, 1969.

[3] R B Akhmedov and F K Rashidov. The hydraulic characteristics of air registers in vortex burners with axial-tangential air intake. *Thermal Engineering*, 16(4):130–133, 1969.

[4] Keith Alexander and E Peter Giddens. Microhydro: cost-effective, modular systems for low heads. *Renewable Energy*, 33(6):1379–1391, 2007.

[5] Keith Alexander and Peter Giddens. Optimum penstocks for low head microhydro schemes. *Renewable Energy*, 33(6):1379–1391, 2008.

[6] Keith Alexander, Peter Giddens, and Adam Fuller. Axial-flow turbines for low head microhydro systems. *Renewable Energy*, 34(1):35–47, 2009.

[7] Keith Alexander, Peter Giddens, and Adam Fuller. Radial- and mixed-flow turbines for low head microhydro systems. *Renewable Energy*, 34(7):1885–1894, 2009.

[8] American Society of Mechanical Engineers. Test code for hydraulic prime movers. Technical report, ASME, 1945.

[9] European Small Hydro Asscociation. Guide on how to develop a small hydropower plant. Technical report, ESHA, 2004.

[10] F S Bhinder. Investigation of flow in the nozzle-less spiral casing of a radial inward-flow gas turbine. *Proceedings of the Institution of Mechanical Engineers*, 184, Part 3G(11):66–71, 1969-1970.

[11] D. Boon, J Groenhof, A M Hens, J P Jansen, J de Kieviet, H Kruik, J A Landstra, L G de Steur, and G G Waasdorp. *Shell flow meter engineering handbook*. Waltman, Delft, The Netherlands, 1968.

[12] M J Cervantes, T F Engström, and L H Gustavsson. Proceedings of the third IAHR/ERCOFTAC Workshop on draft tube flows. In *Turbine-99 III*, Department of Applied Physics and Mechanical Engineering, Division of Fluid Mechanics, 2005. Luleå University of Technology.

[13] J. A. Clarke, G Connor, A. D. Grant, and C. M. Johnstone. Design and testing of a contra-rotating tidal current turbine. *Proceedings of the Institution of Mechanical Engineers, Part A: Journal of Power and Energy*, 221(2):171–179, 2007.

[14] P D Clausen, S G Koh, and D H Wood. Measurements of a swirling turbulent boundary layer developing in a conical diffuser. *Experimental Thermal and Fluid Science*, 6:39–48, 1993.

[15] International Electrotechnical Commission. Hydraulic turbines, storage pumps and pump-turbines — model acceptance tests. International Technical Standard BS EN 60193 : 1999, British Standards Institution, 389 Chiswick High Road, London, W4 4AL, April 2006. English version. This European Standard supersedes EN 60995 : 1994.

[16] D M Demetriades and A A Williams. Low-cost micro-hydro equipment for low head sites. In *UPEC '94*, volume 1, pages 382–385, Galway, Ireland, September 1994. Universities Power Engineering Conference, University College. 29th Universities Power Engineering Conference, 14th, 15th, and 16th September 1995: conference proceedings.

[17] G M Demetriades, A A Williams, and N P A Smith. A simplified propeller turbine runner design for stand alone micro-hydro power generation units. *International Journal of Ambient Energy*, 17(3):151–156, July 1996.

[18] J. Dunham and P. M. Came. Improvements to the ainley-mathieson method of turbine performance prediction. *Journal of Engineering for Power*, 92(3):252–256, 1970.

[19] Mohammed Durali. Design of small water turbines for farms and small communities. Master's thesis, Massachusetts Institute of Technology, Cambridge, Mass., 1976.

[20] John W. Eaton. *GNU Octave Manual*. Network Theory Limited, 2002.

[21] M S Y Ebaid, F S Bhinder, and G H Khdairi. A unified approach for designing a radial flow gas turbine. *Transactions of the ASME*, 125:598–606, July 2003.

[22] Simon Andrew Faulkner. A simplified low head propeller turbine for micro hydroelectric power. Master's thesis, University of Canterbury, Christchurch, New Zealand, 1991.

[23] Adam Fuller and Keith Alexander. Adapting simplified propeller turbines to higher specific speeds. In *Hidroenergia*, Lausanne, Switzerland, 2010. European Small Hydro Association.

[24] Adam Fuller and Keith Alexander. Exit-flow velocity survey of two single-tangential-inlet vaneless turbine volutes. *Experimental Thermal and Fluid Science*, 35(1):48–59, 2010.

[25] E Peter Giddens. An air separator. In *Eighth Australasian Fluid Mechanics Conference*, pages 2C.1—2C.3, University of Newcastle, NSW, 1983. Australasian Fluid Mechanics Society.

[26] A K Gupta, D G Lilley, and N Syred. *Swirl flows*. Abacus Press, Tunbridge Wells, Kent, 1984.

[27] George E. Hecker and Thomas C. Cook. Development and evaluation of a new helical fish-friendly hydroturbine. *Journal of Hydraulic Engineering*, 131(10):835–844, 2005.

[28] Douglas Henderson. An advanced electronic load governor for control of micro hydroelectric generation. *IEEE Transactions on Energy Conversion*, 13(3):300–304, September 1998.

[29] Lee Wing Ho. Manufacture and evaluation of a five-kilowatt axial-flow water turbine. Master's thesis, Massechussetts Institute of Technology, Cambridge, Mass., 1979.

[30] Rik Hothersall. *Hydrodynamic Design Guide for Small Francis and Propeller Turbines*. United Nations Industrial Development Organization, Vienna, Austria, 2004.

[31] M Hussain and F S Bhinder. Experimental study of the performance of a nozzle-less volute casing for turbocharger turbines. Technical Report 840571, Society of Automotive Engineers, 1984.

[32] International Organization for Standardization. ISO 5167-1980 Measurement of fluid flow by means of orifice plates, nozzles and Venturi tubes inserted in circular cross-section conduits running full. In *ISO standards handbook 15: Measurement of fluid flow in closed conduits*. ISO, 1983.

[33] David Japikse and Nicholas C Baines. *Introduction to Turbomachinery*. Concepts ETI and Oxford University Press, 1994.

[34] V Kercan and L Bizjak. Plate blade application for the small hydro-turbine runners. In D R Webb and D N Papadakis, editors, *Small hydro-power fluid machinery*, pages 41–49, United Engineering Center, 345 East 47th Street, NY, NY 10017, 1980. The American Society of Mechanical Engineers (ASME), ASME.

[35] Jordan Ko, Said Zahrai, and Olivier Macchion. Numerical modeling of highly swirling flows in a through-flow cylindrical hydrocyclone. *Fluid mechanics and transport phenomena*, 52(10):3334–3344, October 2006.

[36] P Legentilhomme and J Legrand. The effects of inlet conditions on mass transfer in annular swirling decaying flow. *International Journal of Heat and Mass Transfer*, 34(4/5):1281–1291, 1991.

[37] M F Malak, A Hamed, and W Tabakoff. Three-dimensional flow field measurements in a radial inflow turbine scroll using LDV. *Journal of Turbomachinery*, 109:163–169, 1987.

[38] B S Massey. *Mechanics of fluids*. Van Nostrand Reinhold, Workingham, UK, 5th edition, 1983.

[39] A T McDonald, R W Fox, and R V Van Dewoestine. Effects of swirling inlet flow on pressure recovery in conical diffusers. *AIAA Journal*, 9(10):2014–2018, 1971.

[40] Donald Stuart Miller. *Internal flow systems*. British Hydromechanics Research Association, 1978.

[41] T Morel and R E A Arndt. Potential for reducing kinetic energy lossess in low-head hydropower. In ASME, editor, *Project report no. 221*, volume 1984, pages 57–65, New Orleans, Dec 9-14 1984. ASME, ASME.

[42] Håkan Nilsson. Evaluation of OpenFOAM for CFD of turbulent flow in water turbines. Yokohama, 2006. International Association of Hydraulic Research, IAHR.

[43] Bryan Orchard and Sander Klos. Pumps as turbines for water industry. *World Pumps*, 2009(8):22–23, 2009.

[44] G J Parker. Theoretical analysis of a low-head axial flow turbine for micro-hydro applications. Technical report, University of Canterbury, Christchurch, NZ, 1992.

[45] G J Parker. A theoretical study of the performance of an axial flow turbine for a microhydro installation. *Proceedings of the Institution of Mechanical Engineers, Part A: Journal of Power and Energy*, 210(2):121–129, 1996.

[46] F A Payette, V De Henau, G Dumas, and M Sabourin. Sensitivity of draft tube flow predictions to boundary conditions. Foz do Ignassu, Brazil, 2008. IAHR.

[47] Jr Peter W Runstadler, Francis X Dolan, and Jr Robert C Dean. *Diffuser data book*. Creare Incorporated, Hanover, New Hampshire, USA, 1st edition, 1975.

[48] IT Power. `http://www.itpower.co.uk/Technologies/Hydro`. Internet website.

[49] Graham Pullhan and Neil W Harvey. Influence of sweep on axial flow turbine aerodynamics at midspan. *Journal of Turbomachinery*, 129:591–598, July 2007.

[50] G J Rao, R Prasad, and B S Kulkani. Simplified turbine runner shows good cavitation resistance. *Water power and dam construction*, 40(8):20–22, August 1988.

[51] E Schlemmer, F Ramsauer, X Cui, and A Binder. HYDROMATRIX and StrafloMatrix, Electric Energy from Low Head Hydro Potential. *Clean Electrical Power, 2007. ICCEP '07. International Conference on*, pages 329–334, May 2007.

[52] Yasutoshi SENOO, Nobumasa KAWAGUCHI, and Tetsuzou NAGATA. Swirl Flow in Conical Diffusers. *Bulletin of the Japanese Society of Mechanical Engineers*, 21(151):112–119, 1978.

[53] A T Simpson, S W T Spence, and J K Watterson. A comparison of the flow structures and losses within vaned and vaneless stators for radial turbines. *Journal of Turbomachinery*, 131, 2009.

[54] Robert Simpson and Arthur Williams. The design of cost-effective pico-propeller turbines for developing countries. In *Hidroenergia*, Crieff, Scotland, 2006. European Small Hydro Association.

[55] Punit Singh and Franz Nestmann. Experimental optimization of a free vortex propeller runner for micro hydro application. *Experimental Thermal and Fluid Science*, 33:991–1002, 2009.

[56] S N Singh, V Seshadri, K Saha, K K Vempati, and S Sharani. Effect of inlet swirl on the performance of annular diffusers having the same equivalent cone angle. *Proceedings of the Institution of Mechanical Engineers*, 220(2):129, April 2006.

[57] Leroy H Smith and Hsuan Yeh. Sweep and dihedral effects in axial-flow turbomachinery. *Journal of Basic Engineering*, 85(3):401–416, September 1963.

[58] B H Stark, E Andò, and G Hartley. Modelling and performance of a small siphonic hydropower system. *Renewable Energy*, 36(9):2451–2464, September 2011.

[59] T Ravi Sundar, V Balabaskaran, and E G Tulapurkara. An experimental investigation of flow in an elbow type draft tube with swirl. *International Journal of Fluid Mechanics Research*, 32(1):57–78, 2005.

[60] MJ2 Technologies. `http://www.vlh-turbine.com/EN/html/The_VLH_Range.htm`. Internet website.

[61] Hiroyoshi TERANISHI. Feature of micro hydraulic power unit (Hydro-eKIDS), and its application. *Energy*, 56(266):53–59, 2006.

[62] Frank M White. *Fluid Mechanics*. McGraw-Hill, New York, 5th edition, 2003.

[63] J D White, A G Holloway, and A G Gerber. Predicting turbine performance of high specific speed pumps using CFD. In *Proceedings of FEDSM2005*, pages 125–131, Houston, USA, 2005. ASME fluids engineering division, ASME.

[64] A Whitfield and A B Mohd Noor. Design and performance of vaneless volutes for radial inflow turbines Part 1: non-dimensional conceptual design considerations. *Proceedings of the Institution of Mechanical Engineers*, 208:199–211, 1994.

[65] A Williams. *Pumps as turbines: a user's guide*. ITDG Publishing, Rugby, UK, 2nd edition, 2003.

[66] David Gordon Wilson. *The design of high-efficiency turbomachinery and gas turbines*. MIT, Cambridge, Massachusetts, 1984.

[67] George F Wislicenus. *Fluid mechanics of turbomachinery*. Dover, New York, 2nd edition, 1965.

[68] Jingchun Wu, Katsumasa Shimmei, Kiyohito Tani, Kazuo Niikura, and Joushirou Sato. CFD-based design optimization for hydro turbines. *Journal of Fluids Engineering*, 129:159–168, February 2007.

[69] Y Yassi. *An experimental study of improvement of a micro hydro turbine performance*. PhD thesis, University of Glasgow, Glasgow, Scotland, 1999.

[70] O Zweifel. The spacing of turbomachine blading, especially with large angular deflection. *Brown Boveri Review*, 32(12):436–444, December 1945.